UNIVERSITY OF AMSTERDAM

UvA-DARE (Digital Academic Repository)

The Dark that Shapes the Light

Silverwood, H.G.M.

Link to publication

Citation for published version (APA):
Silverwood, H. G. M. (2016). *The Dark that Shapes the Light*.

General rights
It is not permitted to download or to forward/distribute the text or part of it without the consent of the author(s) and/or copyright holder(s), other than for strictly personal, individual use, unless the work is under an open content license (like Creative Commons).

Disclaimer/Complaints regulations
If you believe that digital publication of certain material infringes any of your rights or (privacy) interests, please let the Library know, stating your reasons. In case of a legitimate complaint, the Library will make the material inaccessible and/or remove it from the website. Please Ask the Library: https://uba.uva.nl/en/contact, or a letter to: Library of the University of Amsterdam, Secretariat, Singel 425, 1012 WP Amsterdam, The Netherlands. You will be contacted as soon as possible.

UvA-DARE is a service provided by the library of the University of Amsterdam (http://dare.uva.nl)

Download date: 05 Nov 2020

THE DARK THAT SHAPES THE LIGHT | Hamish Silverwood

studioLIN.nl

THE DARK THAT SHAPES THE LIGHT

Hamish Silverwood

The Dark that Shapes the Light

This work has been accomplished at the Gravity and AstroParticle Physics in Amsterdam (GRAPPA) center of excellence and the Institute for Theoretical Physics (ITFA) of the University of Amsterdam (UvA).

Cover: Milky Way composite image courtesy of ESO/S. Brunier. Cover design by StudioLIN. Inside covers: Fermi-LAT 60 month gamma-ray image of the Milky Way, courtesy of NASA/DOE/Fermi-LAT Collaboration.

© Hamish Silverwood, 2016

All rights reserved. Without limiting the rights under copyright reserved above, no part of this book may be reproduced, stored in or introduced into a retrieval system, or transmitted, in any form or by any means (electronic, mechanical, photocopying, recording or otherwise) without the written permission of both the copyright owner and the author of the book.

The Dark that Shapes the Light

Academisch Proefschrift

ter verkrijging van de graad van doctor

aan de Universiteit van Amsterdam

op gezag van de Rector Magnificus

prof. dr. ir. K.I.J. Maex

ten overstaan van een door het college voor promoties

ingestelde commissie,

in het openbaar te verdedigen in de Agnietenkapel

op woensdag 5 oktober 2016, te 12.00 uur

door

Hamish George Miles Silverwood

geboren te Timaru, Nieuw-Zeeland

Promotiecommissie

Promotor

prof. dr. J. de Boer	Universiteit van Amsterdam

Co-Promotores

dr. G. Bertone	Universiteit van Amsterdam

Overige leden

dr. D. Berge	Universiteit van Amsterdam
prof. dr. M.P. Decowski	Universiteit van Amsterdam
dr. F. Donato	University of Turin
prof. dr. F.L. Linde	Universiteit van Amsterdam
prof. dr. J.I. Read	University of Surrey
dr. G. van de Ven	Max Planck Institute for Astronomy
prof. dr. R.A.M.J. Wijers	Universiteit van Amsterdam

Faculteit der Natuurwetenschappen, Wiskunde en Informatica

Publications

This thesis is based on the following publications:

[1] C. Arina, G. Bertone, and H. Silverwood, *Complementarity of direct and indirect dark matter detection experiments*, *Phys. Rev. D* **88** (July, 2013) 013002, arXiv:1304.5119.

Presented in Chapter **2**.

All authors participated in the planning of the project. CA focused on the direct detection part of the analysis code, and HS focused on the IceCube section. CA and HS were both responsible for the overarching MultiNest *-based code, launching runs and the analysis of the output. CA, GfB, and HS all contributed to the writing of the paper.*

[2] H. Silverwood, C. Weniger, P. Scott, G. Bertone, *A realistic assessment of the CTA sensitivity to dark matter annihilation*, *JCAP* **3** (Mar., 2016) 055, arXiv:1408.4131.

Presented in Chapter **3**.

All authors participated in the planning of the project. The analysis code was written by HS under the supervision of CW. The paper was written by primarily by HS with input from CW, PS and GfB.

[3] H. Silverwood, S. Sivertsson, P. Steger, J. Read, G. Bertone, *A non-parametric method for measuring the local dark matter density*, *MNRAS*, **459** (Apr., 2016) 4191-4208, arXiv:1507.08581.

Presented in Chapter **4**.

All authors participated in planning the project. The analysis code was based upon work by PS, heavily modified by HS and SS. The paper was written primarily by HS with input from JR, GfB, and SS.

Other publications by the author:

[4] M. G. Aartsen, K. Abraham, M. Ackermann, J. Adams, J. A. Aguilar, M. Ahlers et al., *Improved limits on dark matter annihilation in the Sun with the 79-string IceCube detector and implications for supersymmetry*, *JCAP* **4** (Apr., 2016) 022, arXiv:1601.00653.

HS contributed benchmark points from MSSM25 parameter scans.

[5] S. Horiuchi, O. Macias, D. Restrepo, A. Rivera, O. Zapata, H. Silverwood, *The Fermi-LAT gamma-ray excess at the Galactic Center in the singlet-doublet fermion dark matter model*, *JCAP* **3** (Mar., 2016) 048, arXiv:1602.04788.

HS contributed customised CTA detection limits, and editing work on the paper text.

Contents

1 Introduction

1.1 Overture

What we normally consider ordinary matter - the Earth we live on, the Sun and stars around us, the very atoms of which we are composed - is actually, in the wider scheme of things, very special. It comprises only a small portion of the total amount of matter in the Universe. The remainder is made up of *dark matter* (DM), an as-yet-unknown particle responsible for holding galaxies like our very own Milky Way together, weaving threads of galaxies into the web of structure we see throughout the Universe, and shaping the tiny ripples in cosmic microwave background (CMB) that fills the cosmos.

This thesis is about searching for DM, from the directions of both particle physics and astronomy. It is based on three papers, which are presented in Chapters 2, 3, and 4. While each chapter will have its own more detailed introduction to the relevant material, this chapter will set the scene. We will first look briefly at the astrophysical motivations and evidences for DM, followed by an overview of the relevant particle physics aspects, and then an account of the so-called Λ-CDM cosmological model and the role of DM in it. After this we give a short introduction to the three DM detection techniques which will feature in the first two papers of this thesis; direct detection, indirect detection with neutrinos from solar capture and annihilation of DM, and indirect detection with gamma-rays. The third paper, presented in Chapter 4, is concerned with astrometrics, galactic dynamics, and the local density of DM, and so we will save the relevant introductory material until then.

1.2 Motivations for Dark Matter

The presence of unseen mass within the galaxy and the wider Universe has been recognized for almost a century, though it has only become clear more recently that it consists of a new type of matter. Early work by Ernst Öpik [6], Jacobus Kapteyn [7], and James Jeans [8] searched for missing mass in the local region of our galaxy, and while not revealing an excessive deficit, the work of Kapteyn and Jeans laid the groundwork for much subsequent research. Later, the movements of galaxies in the Coma cluster led Fritz Zwicky to conclude that there was significant additional unseen mass present there [9, 10]. In the 1970s further evidence of missing mass emerged from the rotation curves of galaxies outside our own, measured using optical spectroscopy by Vera Rubin and Kent Ford [11, 12, 13], and at larger radii by radio observations of neutral hydrogen emission (*e.g.* Fig. 1.1) [14, 15, 16, 17, 18, 19, 20, 21]. The rotation curves were above those which would be generated if the gravitational attraction was provided solely by the visible matter - unseen mass was providing extra gravitational pull, allowing the outer parts of the galaxies to spin faster while still remaining bound.

However at this point it was not clear that this missing mass was due to a new type of matter, or even that these phenomena at greatly disparate length scales were linked. That latter idea took until the mid-1970s to emerge [22, 23], while the former began to crystalize from the early 1980s onwards. James Peebles argued that, in light of the upper limit on anisotropies in the Cosmic Microwave Background found by early observations, a new ingredient was required to seed the perturbations that would go on to form the structures seen in the Universe [24, 25]. Numerical simulations of a universe dominated by neutrinos yielded cosmological structures too large to agree with observations, ruling out neutrinos from the Standard Model (SM) of particle physics as a source of the DM [26]. Due to their relativistic speed these neutrinos were termed *hot dark matter* (HDM). The competing model of slower moving *cold dark matter* (CDM) correctly predicted the cosmological structure, and soon gained favour. But a candidate particle to fill the role of CDM was, and remains, lacking.

Another attempt at accommodating DM within the realm of baryons[1] was the idea of Massive Compact Halo Objects (MACHOs). These were objects comprised of baryons, which were compact like stars but emitted only negligible radiation, such as black holes, neutron stars, brown, red and white dwarf stars, and planets. These MACHOs could be detected by searching for *microlensing* events, where the MACHO would gravitationally lens the light from a background star, briefly increasing the brightness of that star. However microlensing surveys starting in the 1990s did not

[1] Within the DM community 'baryon' is often used to describe all SM matter, be it baryon or fermion. This is because the baryons have higher particle masses, and hence dominate any mass sum of baryons and fermions.

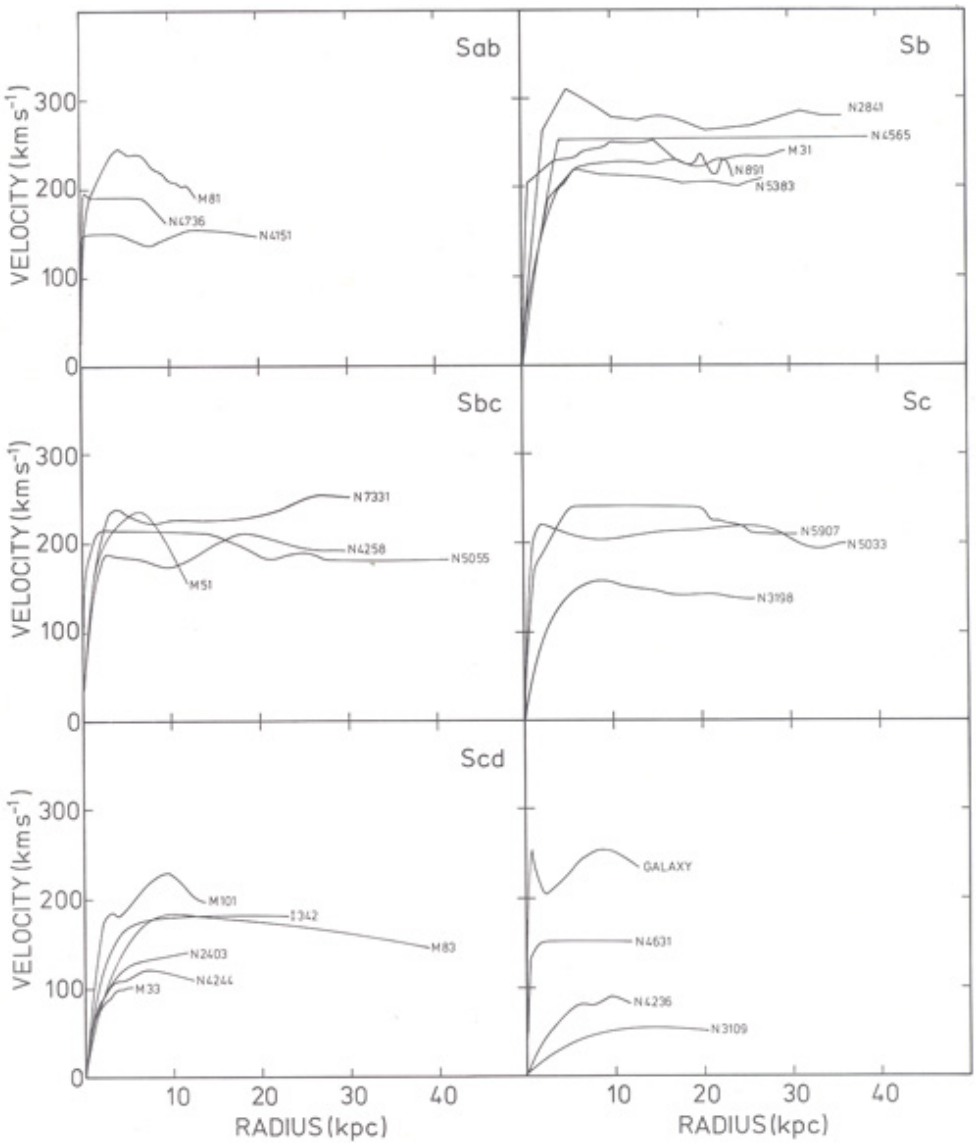

Figure 1.1: Rotation curves for 25 galaxies measured using radio observations, presented in the PhD thesis of Albert Bosma [21].

find these events at a rate high enough to fit the required amount of DM [27, 28, 29], disfavouring yet another baryonic DM candidate.

Emphatic evidence for non-SM DM has been derived from the anisotropies of the Cosmic Microwave Background (CMB) measured first by COBE [30], and later by WMAP [31, 32] and Planck [33]. Prior to its emission the electrons, protons, and photons of the Universe are coupled in a plasma. The photons are energetic enough to photodisintegrate any hydrogen atoms that form from the protons and electrons, and the photons also frequently scatter off the free electrons, making the Universe opaque. However as the Universe expands and cools, the photon energy drops to the point where neutral hydrogen can form, a process known as *recombination*. The electrons and protons bind into hydrogen atoms, drastically reducing the photon-electron scattering rate and clearing the opaque fog of electrons. This allows the photons to stream unimpeded through the Universe, and we now detect these very same photons, redshifted to microwave frequencies, as the CMB. At the point when the CMB is produced the plasma is oscillating acoustically, and clumps of DM have begun to form, leaving a subtle imprint on the energy of these photons: peaks of the plasma sound waves will be hotter and so produce higher energy photons, and troughs will thus produce lower energy photons; and overdensities of matter will create gravitational wells out of which some photons will have to climb, loosing energy and thus having a slightly lower frequency compared to the other photons. Detailed analysis of these imprints, which will be discussed further in Section 1.4, shows that of the total mass energy budget of the Universe, 26.5% is dark matter, 4.9% is normal matter, and the remainder is the *dark energy* which is driving the current acceleration of the expansion of the Universe [33].

Finally, observations of galaxies in galaxy clusters, which provided Zwicky with early signs of DM, have also more recently furnished us with further evidence that DM cannot consist of SM particles. Observations of what has been dubbed the Bullet Cluster, shows the outcome of two galaxy clusters that have collided with each other [34, 35]. The mass distribution is mapped out using *weak lensing*, which looks for the correlated warping of the shapes of background galaxies due to gravitational lensing. Individual galaxies in the cluster can be seen optically, while the hot diffuse gas between them, the intracluster medium, radiates x-rays and can be mapped thusly. The x-ray emission also tells us that the intracluster medium dominates the baryonic mass of the cluster. From these three elements, depicted in Fig. 1.2, one can deduce the story of these two colliding clusters. The two bodies of hot x-ray emitting gas, shown in pink, have interacted with each other, forming a distinct bow shock formation on the right which gives the Bullet Cluster its name. The majority of the mass however, mapped via weak lensing and shown in blue, is displaced from the dominant baryonic component, the hot intracluster gas. The constituent galaxies of the clusters, which

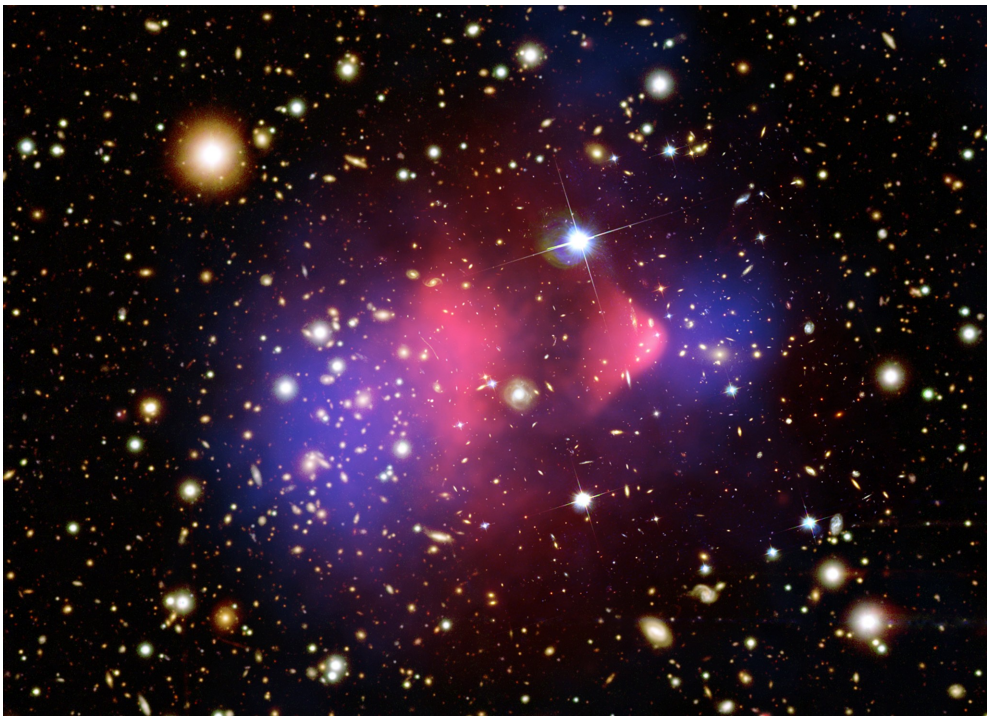

Figure 1.2: The Bullet Cluster. The hot intracluster medium emits in X-rays, which is depicted in pink. The blue distribution is derived from weak lensing, which maps out the total mass distribution. Composite Credit: X-ray: NASA/CXC/CfA/ [37]; Lensing Map: NASA/STScI; ESO WFI; Magellan/U.Arizona/ [35] Optical: NASA/STScI; Magellan/U.Arizona/D.Clowe et al.

make up some of this displaced mass, have naturally passed through each other - the individual galaxies are tightly bound objects with a small size compared to the entire cluster, and so are unlikely to interact with each other. The smooth DM halos have also passed through each other, giving further evidence that DM is non-baryonic - if it were baryonic the two halos would have interacted with each other as the gas did, and the distribution of mass would match that of the gas. Analysis of the Bullet Cluster allows us to set limits on the strength of self interactions between DM particles of $\sigma/m_{\mathrm{DM}} \lesssim 1\,\mathrm{cm}^2\,\mathrm{g}^{-1}$ [36].

The astrophysical observations that reveal the presence of DM also place restrictions on its particle nature. A brief summary of these are:

- it should be (nearly) electrically neutral. Exotic models with fractionally charged DM are possible, but experimental searches for this so-called milli-charged DM

yeild strong limits (see *e.g.* [38]);

- sufficient amounts of it must be produced in the early Universe to match observations of the CMB, discussed further in Section 1.4.5;
- it must be stable on cosmological time scales in order to play a role in events ranging from the CMB at a redshift of $z \simeq 1100$ to the motions of galaxies and galaxy clusters in the present time;
- it must mesh with other cosmological measurements, such as the abundances of light elements produced during Big Bang Nucleosynthesis (BBN), which is discussed further in Section 1.4.4;
- it should be cold enough to form the galaxies, galaxy clusters, and larger filamentary structures seen in the Universe, as discussed further in Section 1.4.6;
- and finally, it should evade the self-interaction limits imposed by the Bullet Cluster, as discussed earlier.

Nothing from the SM fits all of the imposed constraints. However, just as problems from the Cosmos demanded new particles, so too did problems with the SM. In the next section we will discuss several of these new particles, born out of particle physics yet finding support from cosmology.

1.3 Dark Matter in Particle Physics

The SM of particle physics, developed in the 1970s, has been remarkably successful in describing the sub-atomic realm. It organized and unified a panoply of particles and forces, and correctly predicted a trifecta of new ones, namely the top quark [39, 40, 41], the tau neutrino [42, 43], and the Higgs boson [44, 45, 46, 47, 48]. Yet we know it to still have puzzles, holes, and shortcomings. Here we explore several compelling extensions to SM physics which not only provide redress for some of these problems, but also supply us with a DM candidate particle.

Axions are a class of particles now covering several different models which produce a pseudoscalar (*i.e.* acquires negative sign under parity transformation), pseudo-Goldstone (produced by spontaneous and explicit symmetry breaking) bosons [49]. The first axion model arose as a solution to the strong-CP problem. Quantum Chromodynamics (QCD), the theory that describes the strong force, admits a term in its Lagrangian which violates the Charge-Parity (CP) symmetry for strong interactions, and one manifestation of this is an electric dipole moment (EDM) for the neutron of $d_n \sim 3.6 \times 10^{-16} \theta_{\rm QCD} e\,{\rm cm}$ with a naively expected value of $\theta_{\rm QCD} \sim 1$ [50]. The

observed limits for the neutron EDM are $|d_n| < 2.9 \times 10^{-26} e\text{cm}$ [51], 10 orders of magnitude less. To solve the strong-CP problem and explain the lack of observed CP violation in the strong sector Roberto Peccei and Helen Quinn introduced a new, global chiral U(1) symmetry which was spontaneously broken [52]. This in turn generates a massive particle, as pointed out by Steven Weinberg and Frank Wilczek [53, 54], which was then identified as a DM candidate [55, 56, 57].

While the original Peccei-Quinn-Weinberg-Wilcek model has been ruled out by beam-dump experiments at particle colliders [58], several other axion models have been put forward in the context of the Strong-CP problem. In the broader category of axions this particular subset is known as a QCD-axion. Further axions (or axion like particles) arise from a host of other extensions of the standard model, including string theory. For a review of the QCD axions and other models see *e.g.* [49].

Another DM candidate arises from the incongruous fact that while all other particles of the SM come in both left and right chiralities, the neutrinos found so far have only left handed chirality. The right-handed neutrinos that would solve this discrepancy would not interact via the weak force, and thus are called *sterile neutrinos*, in contrast to the *active* left-handed neutrinos. Sterile neutrinos were proposed as a DM candiate in 1993 [59], and due to the Tremaine-Gunn bound, discussed in Section 1.4.6, have a mass of at least keV scale (see *e.g.* [60, 61] for reviews). The introduction of sterile neutrinos can also provide non-zero masses to the active neutrinos, something that is experimentally verified via neutrino oscillations yet not accommodated within the SM. Processes such as the seesaw mechanism [62, 63, 64] would give the active neutrinos their small but non-zero masses while giving the sterile neutrinos much higher masses. Despite not interacting via the weak force the sterile neutrinos would still mix with the left-handed neutrinos, and also produce x-rays through radiative decays to active neutrinos. These x-rays offer an avenue for detecting sterile neutrinos, with an anomalous x-ray line feature at 3.5 keV observed in a variety of astrophysical bodies already being investigated as a possible signal of a 7 keV sterile neutrino DM particle [65, 66] (see also *e.g.* [67] and references therein).

Supersymmetry (SUSY) is currently the leading paradigm for beyond the standard model physics. SUSY has gained prominence for several reasons, including its ability to solve a number of problems in the SM, namely the *hierarchy problem* and *gauge coupling unification*. Here we work within the paradigm of the *Minimally Supersymmetric Standard Model* (MSSM), which is the SM with a minimum of new particle states and interactions necessary to make the theory supersymmetric and fulfil current phenomenology.

At its core the hierarchy problem is the question of why the electroweak scale, $E_{\text{weak}} \sim v_{\text{Higgs}} = 246$ GeV, which set the masses of the Higgs, $W^{\pm}$, and Z^0 bosons, is so

dramatically lower than the Planck scale, $E_{\text{Planck}} \sim 10^{19}$ GeV, the scale where the effects of gravity become important in particle physics interactions. This disparity is not an issue in the limited scope of the SM, but can lead to instability in the mass of the Higgs boson if any extension to the SM is added. Such extensions are inescapable given that, at the very least, the SM cannot describe gravity.

The physical mass of the Higgs boson m_H, measured as 125 GeV by the LHC [68, 69], is a combination of the bare scale mass $m_{H,0}$ and radiative corrections δm_H [70]:

$$m_H^2 = m_{H,0}^2 + \delta m_H^2 \tag{1.1}$$

The bare scalar mass is set by the vacuum expectation value generated by the spontaneous breaking of electroweak symmetry, and gives a contribution on the order of the weak scale. The radiative corrections arise from loop contributions of all the particles that interact with the Higgs boson, and the contribution of these corrections is proportional to the cutoff scale Λ where new physics takes over from the SM [71]:

$$\delta m_H^2 = -\frac{|\lambda_f|^2}{8\pi^2}\Lambda^2 + ... \tag{1.2}$$

A priori there is nothing stopping Λ being equal to the Planck scale, and thus increasing the Higgs mass far beyond its measured value at the weak scale. One potential solution is to fine tune the elements $m_{H,0}^2$ and δm_H^2 in Eq. 1.2, but such solutions are considered highly unnatural, and such coincidences often point to a deeper symmetry as a root cause [71].

SUSY solves this problem by introducing for each SM particle a new SUSY superpartner with a half-integer spin difference. SM bosons get fermionic partners called *bosinos* and with 'ino' appended (*e.g.* Higgs*ino*), and SM fermions get spin-0 scalar boson partners, called *sfermions* and with an 's' prepended for 'scalar' (*e.g. s*quarks and *s*leptons). The left- and right-handed parts of the fermions each get their own complex scalar partner as they are described by separate Weyl fermions with different SM gauge transformation properties. The single Higgs doublet of the SM is replaced by two separate Higgs doublets, because the supersymmetric Yukawa interactions cannot involve both a complex scalar field and its hermitian conjugate while remaining invariant under SUSY. These two Higgs doublets are known as H_u and H_d, as they couple to the up and down-type quark/squark supermultiplets. The new SUSY particles also contribute to the radiative corrections of the Higgs mass seen earlier, with the same magnitude as their SM counterparts but with *opposite sign*. This cancellation thus stabilises the Higgs mass against quadratic divergences.

The fact that we have not detected these SUSY particles at the same masses of their SM counterparts indicates that SUSY must be a broken symmetry. The scale at which this symmetry breaking occurs is currently unknown, and could potentially even be

at the Planck scale [*e.g.* 72]. However there are reasons to hope that this scale is much closer to the weak scale. The so-called *soft* SUSY breaking schemes [73] break SUSY yet maintain their ability to solve the hierarchy problem. Under soft SUSY breaking the Higgs mass correction is

$$\delta m_H^2 = -m_{\text{soft}}^2 \left[\frac{\lambda}{4\pi^2} \ln \left(\frac{\Lambda}{m_{\text{soft}}} \right) + ... \right] \tag{1.3}$$

The high energy cutoff of the theory, Λ is now natural log-scaled and sub-dominant. The main quantity driving the scale of the Higgs mass corrections is now the energy scale of soft SUSY breaking, m_{soft}. In order to keep corrections to the Higgs mass limited to the weak scale, the soft SUSY breaking scale must also be approximately weak scaled. As the soft-SUSY breaking scale increases the ability of SUSY to remedy the hierarchy problem decreases. This intimation of roughly weak scaled SUSY suggests the possibility of finding evidence at the LHC, and also dovetails with evidence from cosmology as to the nature of DM, in a concept known as the *WIMP Miracle*, which will be discussed further in Section 1.4.

SUSY has the added attraction of facilitating gauge coupling unification. The coupling constants that govern the strengths of the electromagnetic, weak and strong interactions change with energy, a process known as *running*. It is hoped that at high energies the strong, weak, and electromagnetic forces combine into a single Grand Unified Theory (GUT), much like the weak and electromagnetic forces unify into the electroweak force above an energy scale of $\mathcal{O}(100\,\text{GeV})$. As part of any GUT we would expect the gauge coupling constants for the three forces should intersect at high energies. Extrapolating these constants upwards in energy with only SM physics included does not result in the desired intersection; however the addition of SUSY helps make this intersection possible [*e.g.* 74].

The energy scale of SUSY is beyond that of electroweak symmetry breaking, and so the weak gauge bosons $W^{\pm}$, Z^0, and the photon γ have unified and mixed into the W^+, W^0, W^-, and B^0 gauge bosons. These have *gaugino* superpartners $\tilde{W}^+$, $\tilde{W}^0$, $\tilde{W}^-$, and $\tilde{B}^0$, known as the *winos* and the *bino*. The charged electroweak gauginos combine with the charged parts of the two Higgs gaugino doublets to form the *charginos*, while their neutral counterparts mix to form the *neutralinos*. The charginos and neutralinos mix amongst themselves, forming four mass eigenstates each: $\tilde{\chi}_1^{\pm}$, $\tilde{\chi}_2^{\pm}$; and $\tilde{\chi}_1^0$, $\tilde{\chi}_2^0$, $\tilde{\chi}_3^0$, $\tilde{\chi}_4^0$.

If the lightest of the neutralinos, $\tilde{\chi}_1^0$ (generally referred to as *the* neutralino) is also the lightest superpartner overall, it is a candidate for the DM particle. The neutralino is also the archetypal member of the DM category known as *Weakly Interacting Massive Particles*, or WIMPs, which have become the dominant paradigm for DM. The physics underpinning Chapters 2 and 3 rely on WIMPs, and so in these chapters DM will be

almost synonymous with WIMP. The neutralinos are Majorana fermions - they are their own anti-particle, and so can self-annihilate. They are rendered stable against decay by R-parity, which is introduced to enforce proton stability. Additional terms in the SUSY Lagrangian allow for protons to decay into lepton meson pairs, and these terms are suppressed by the conservation of R-parity at the interaction vertices, with R defined as

$$R = (-1)^{3B+L+2s}, \tag{1.4}$$

where B is the baryon number, L is the lepton number, and s is the spin of the particle. Calculating R for all SM particles gives $R = 1$, while all superpartners receive $R = -1$. Thus stability of lightest superparticle is ensured - the multiplicative conservation of R means that superparticles can decay into a particle-superparticle pair ($-1 = 1 \times -1$), but not into a SM particle alone ($-1 \neq 1 \times 1 \times ...$).

However conservation of R-parity still allows for the annihilation of two superparticles into SM particles:

$$\chi + \chi \rightarrow SM + SM + ... \tag{1.5}$$

$$R : -1 \times -1 = 1 \times 1 \times ... \tag{1.6}$$

This allows for neutralinos to be produced by the high energy SM particles present in the early Universe, and to subsequently follow the process of *dark matter freezeout* which will be discussed in Section 1.4.2. The thermally averaged annihilation cross-section multiplied by the relative velocity is $\langle \sigma v \rangle$, and can be expanded as [75]

$$\langle \sigma v \rangle = a + bv^2 + \mathcal{O}(v^4). \tag{1.7}$$

In the galactic halo and in DM populations captured in the Sun and the Earth the DM velocity distribution peaks around $\mathcal{O}(10^{-3}c)$, and thus generally only the velocity independent a term must be considered. At the time of DM freezeout (Section 1.4.2) the relative velocities are higher ($\sim 0.5c$), and so for the calculation of the freezeout process the bv^2 term can become important.

Depending on the particular SUSY model and the parameter values used, the neutralino annihilation will produce a variety of different initial SM particles, some of which will be unstable and undergo further decay and hadronization processes until stable particles are produced. These final stable particles are the basis for indirect detection of DM, of which two types, using neutrinos and gamma-rays, are discussed further in Sections 1.6 and 1.7.

For the types of indirect detection discussed in this thesis, annihilation of WIMP DM directly into to two neutrinos or two gamma-rays would be ideal, producing a near mono-chromatic line signal with energy equal to the DM mass (assuming annihilation at low velocity). However, for gamma-rays, this process can only take place with an

intervening loop, as there is no direct interaction between neutral DM and photons [76, 77], and so is loop suppressed relative to annihilations occurring at the tree level. The cross-section for annihilations into fermion final states receive a helicity suppression on the order of m_f^2/m_χ^2 [75]. Given that the neutrino masses are at most a few eV [78] and that neutralinos are typically MeV scale and above, annihilation into neutrino final states is massively suppressed.

The main source of gamma-rays and neutrinos will therefore be from the processes involving the unstable fermions and bosons produced. The range of initial particles that can be produced is limited by the mass of the DM particle, which, as they are annihilating at relatively low velocity, can only produce particles of lower masses. The helicity suppression mentioned earlier will bias the fermion-antifermion annihilation products towards heaviest available states, such as top quarks ($t\bar{t}$), bottom quarks ($b\bar{b}$), charm quarks ($c\bar{c}$), and taus ($\tau^+\tau^-$). Other important channels are the W^+W^- and Z^0Z^0 gauge boson pars, and those containing Higgs bosons [79]. Quarks and gluons produced in the annihilation will undergo the process of hadronization, whereby they produce hadrons by combining with quarks and gluons drawn out of the vacuum due to colour confinement. These hadrons, such as neutral pions, will then decay into gamma-rays. The hadronization process is complex and so must be simulated using Monte Carlo tools.

1.4 Dark Matter in the Cosmos

The dominant paradigm of cosmology is the Λ-Cold Dark Matter (ΛCDM) model. It has achieved its preeminence by virtue of its ability to effectively and concisely describe a wide range of phenomena and observations. Here we will give a brief introduction to the ΛCDM model, highlighting the features salient to the subsequent chapters of this thesis. Additionally, we will focus on WIMP Cold Dark Matter, as this is the model used in Chapters 2 and 3.

1.4.1 Inflation

In cosmology *inflation* refers to a period of very rapid expansion at the start of the Universe after which the standard Hubble expansion takes over, postulated to solve several observational puzzles. The Universe we see today is remarkably flat, isotropic, and homogeneous, enough so to be problematic within a Big Bang expansion history lacking inflation. A flat Universe is an unstable solution of the Friedmann equations, and the Universe will become increasingly curved as time progresses. As the Universe is measured to be very close to a flat geometry currently, it must have been even

flatter initially.

The isotropy and homogeneity of the Universe, as shown by the smoothness the CMB, is problematic due to the horizon problem. Variations in the temperature of the CMB across the entire sky are very small, on the order of 10^{-5} [33]. This would be tenable if the entire Universe had reached a state of thermal equilibrium at the time the CMB was emitted, which is however impossible in a expansion history sans inflation. Volumes of the Universe in causal contact (causal patches) expand at the speed of light, yet the Universe is expanding faster than the speed of light, moving separate causal patches away from each other faster they are themselves expanding. Due to this effect points in the CMB sky separated by more than approximately two degrees would have never been in causal contact in an inflation-less universe.

Inflation was proposed as a solution to these problems in the early 1980s [80, 81, 82, 83, 84, 85, 86]. Any curvature of the Universe is flattened out by this rapid expansion, giving the extremely flat initial condition required by the standard expansion. The horizon problem is solved by taking a region of the Universe in causal contact and expanding it to encompass all the regions of the sky we see today. What were previously separate casual patches are now pieces of a single causal patch greatly expanded. The mechanism by which inflation is generated is still unknown and hotly debated.

Fields present during the period of inflation will have quantum fluctuations, and as the expansion occurs these fluctuations will be stretched out. These fluctuations are continually produced, so their imprint on the matter in the Universe will be present at all scales. After inflation ends these fluctuations will remain, and those thrown beyond the causal horizon by inflation will re-enter as the horizon expands. These fluctuation are the seeds from which the vast web of structure we see in the Universe grows, as will be discussed later in Section 1.4.6.

1.4.2 Dark Matter Freeze-out and the WIMP Miracle

Since the Big Bang, the Universe has been expanding and cooling. We generally work in a coordinate system which follows this expansion, known as *comoving coordinates*, with quantities such as *comoving distance* and *comoving volume*. As the Universe expands the physical distance between two stationary objects increases, but the comoving distance does not[2]. Physical and comoving coordinates are linked by the *scale factor* $a(t)$; *e.g.* physical distance $\mathbf{r}$ and comoving distance $\mathbf{x}$ are linked as $\mathbf{r} = a(t)\mathbf{x}$,

[2]An apt analogy would be two points drawn onto a balloon which is then inflated. The points themselves are not moving over the surface of the balloon, but the physical distance between them is increasing because the very surface of the balloon is expanding. Comoving coordinates are like a grid drawn onto the balloon and so expanding with balloon as it inflates. Physical coordinates are akin to an separate fixed ruler being used to measure the distance between the points.

while a physical volume $V_{\rm phys}$ and a comoving volume $V_{\rm comoving}$ would be linked as $V_{\rm phys} = a(t)^3\, V_{\rm comoving}$.

The initial state of the Universe was one of a hot, dense, homogeneous plasma. The WIMP DM particles χ were in chemical equilibrium with rest of the components of the Universe, denoted ℓ and $\bar{\ell}$:

$$\chi + \overline{\chi} \leftrightarrow \ell + \bar{\ell}. \tag{1.8}$$

However, as the Universe cools, the average energy of the ℓ particles drops, reducing the rate at which the right-to-left reaction of Eq. 1.8 occurs. This means equilibrium abundance of WIMPs starts to drop. This could continue unabated until all the WIMPs had annihilated, but at some point the annihilation rate drops below the expansion rate of the Universe. The equilibrium is broken as the left-to-right reaction of Eq. 1.8 stops, and the number of WIMPs per comoving volume remains constant. This process is known as *freezeout*, and is of much importance as it sets the amount of DM that is produced in the early Universe under the dominant WIMP paradigm. For a full treatment see *e.g.* [87, 88].

To quantify this process we take $\ell\bar{\ell}$ as one species of essentially massless particles coupled to the rest of the cosmic plasma [87]. The WIMPs χ annihilate with their anti-particles $\overline{\chi}$ to produce particles ℓ and $\bar{\ell}$, but the latter are energetic enough to collide and create WIMPs, balancing the equation. The abundance of WIMPs, n_χ, is described by the Boltzmann equation,

$$\frac{1}{a^3}\frac{\mathrm{d}(n_\chi a^3)}{\mathrm{d}t} = n_\chi^{\rm eq} n_{\bar{\chi}}^{\rm eq} \langle\sigma v\rangle \left[\frac{n_\ell n_{\bar{\ell}}}{n_\ell^{\rm eq} n_{\bar{\ell}}^{\rm eq}} - \frac{n_\chi n_{\bar{\chi}}}{n_\chi^{\rm eq} n_{\bar{\chi}}^{\rm eq}}\right], \tag{1.9}$$

where superscript 'eq' denotes their equilibrium value. As the light particles ℓ remain in equilibrium with cosmic plasma, $n_\ell = n_\ell^{\rm eq}$. Furthermore, assuming that the WIMP is Majorana we have $\chi = \overline{\chi}$, and the equation describing the abundance of WIMPs, n_χ, becomes

$$\frac{1}{a^3}\frac{\mathrm{d}(n_\chi a^3)}{\mathrm{d}t} = \langle\sigma v\rangle \left[(n_\chi^{\rm eq})^2 - n_\chi^2\right]. \tag{1.10}$$

We now introduce the total entropy density for the plasma,

$$s = \frac{2\pi^2}{45} g_{\star S}(T) T^3. \tag{1.11}$$

where $g_{\star S}(T)$ is the effective number of degrees of freedom in entropy, which changes throughout the thermal history of the Universe. Later in the thermal history $g_{\star S}(T)$ diverges from the number of relativistic degrees of freedom $g_\star(T)$, but for the era of WIMP freezeout we can assume $g_{\star S}(T) = g_\star(T)$. Entropy density is conserved and so will be diluted as the Universe expands, scaling as $s \propto a^{-3}$. A consequence of Eq. 1.11 and the conservation of entropy density is that, along with the Friedman

equations, we can derive an expression for the Hubble constant that will be be useful later:

$$H(T) \simeq \frac{\pi}{3}\sqrt{\frac{g_\star(T)}{10}}\frac{T^2}{M_{\rm Pl}}. \tag{1.12}$$

Using the $s \propto a^{-3}$ scaling relation to replace a with s in Eq. 1.10 gives us[3]

$$s\frac{\mathrm{d}}{\mathrm{d}t}\left(\frac{n_\chi}{s}\right) = \langle\sigma v\rangle\left[(n_\chi^{\rm eq})^2 - n_\chi^2\right]. \tag{1.13}$$

We now define N_χ, the number of WIMPs in a comoving volume,

$$N_\chi \equiv \frac{n_\chi}{s} \propto n_\chi a^3, \tag{1.14}$$

and thus,

$$\frac{\mathrm{d}N_\chi}{\mathrm{d}t} = s\langle\sigma v\rangle\left[(N_\chi^{\rm eq})^2 - N_\chi^2\right]. \tag{1.15}$$

We then introduce new time variable x with a Jacobian,

$$x \equiv \frac{m_\chi}{T} \quad \text{and} \quad \frac{\mathrm{d}x}{\mathrm{d}t} = Hx, \tag{1.16}$$

where m_χ is the mass of the WIMP. At the time of WIMP freeze-out $g_{\star S}$ is constant, so from Eq. 1.12 we have $H \propto T^2$, and thus $H = H(m_\chi)/x^2$. Applying this and the new time variable to Eq. 1.15 gives us the *Riccati equation*,

$$\frac{\mathrm{d}N_\chi}{\mathrm{d}x} = \frac{\lambda}{x^2}\left[(N_\chi^{\rm eq})^2 - N_\chi^2\right] \tag{1.17}$$

$$\text{where } \lambda = \frac{2\pi^2}{45}g_{\star s}(T)\frac{m_\chi^3\langle\sigma v\rangle}{H(m_\chi)}. \tag{1.18}$$

The Riccati equation is not analytically solvable, but can be solved numerically. We can also make some simplifications to extract the general properties of the solution. As time progresses $N_\chi^{\rm eq}$ drops rapidly and after freeze out will be much less than N_χ, simplifying Eq. 1.17 to

$$\frac{\mathrm{d}N_\chi}{\mathrm{d}x} \simeq -\frac{\lambda}{x^2}N_\chi^2. \tag{1.19}$$

Integrating this from the time of freeze out x_f until a much later time $x = \infty$ yields

$$\frac{1}{N_\chi^\infty} - \frac{1}{N_\chi^f} = \frac{\lambda}{x_f}. \tag{1.20}$$

[3]Any constant of proportionality from inside the derivative will cancel with that found in the $1/a^3$ term.

Furthermore, N_χ^∞ is generally much lower than N_χ^f, giving

$$N_\chi^\infty \simeq \frac{x_f}{\lambda}. \tag{1.21}$$

The abundance of WIMPs after freeze out is inversely proportional to the self annihilation cross-section $\langle\sigma v\rangle$ via the λ term. Increasing $\langle\sigma v\rangle$ will delay freeze out and result in a lower WIMP DM density - the chance of two WIMPs meeting each other is dropping, but the chance that they annihilate each other when they do meet is higher. A lower $\langle\sigma v\rangle$ will result in a higher WIMP density after freeze out as the particles are less likely to annihilate when they encounter each other.

Using the expression for the abundance from Eq. 1.21 we can derive the relic density of WIMP DM, $\Omega_{\rm DM}$. A detailed calculation is presented in [89] and shown in Fig. 1.4. An approximate solution is given by [75]:

$$\Omega_{\rm DM}h^2 \approx \frac{3\times10^{-27}\,{\rm cm}^3\,{\rm s}^{-1}}{\langle\sigma v\rangle}. \tag{1.22}$$

Inserting the relic density as measured by Planck of $\Omega_{\rm DM}h^2 = 0.1197$ we find the canonical value for the annihilation cross-section, also known as the *thermal* cross-section (as it arises from thermal production of WIMPs):

$$\langle\sigma v\rangle \approx 3\times10^{-26}\,{\rm cm}^3\,{\rm s}^{-1}. \tag{1.23}$$

This annihilation cross-section is weak scaled, implying a weakly interacting DM particle, *i.e.* the WIMP. In comparison, an electromagnetic scale cross-section is $\mathcal{O}(10^{-21}\,{\rm cm}^3\,{\rm s}^{-1})$, while a cross-section of the strong scale is $\mathcal{O}(10^{-15}\,{\rm cm}^3\,{\rm s}^{-1})$ [89]. This is the *WIMP miracle*: extensions to the SM such as SUSY predict DM particles with weak scale interactions, and such DM particles naturally produce the relic abundance required by cosmology. In contrast DM particles produced in the above manner with electromagnetic or strong interactions would undershoot the relic density by five and 11 orders of magnitude respectively.

Equation 1.22 along with results from particle theory can also give an approximate upper limit on the WIMP mass. Partial wave unitarity of the S-matrix imposes an upper bound on the self annihilation cross-section of

$$\langle\sigma v\rangle_{\rm max} \approx \frac{1}{M_X^2}. \tag{1.24}$$

Combining this with Eq. 1.22 yields an upper bound on the WIMP mass, known as the *unitarity bound* [90]. Scaling the original value derived in [90] to the current Planck relic density value of $\Omega_{\rm DM}h^2 = 0.1198$ yields an upper bound of $m_X \lesssim 120$ TeV.

Similar arguments can be made to derive an approximate lower limit on the WIMP mass, known as the *Lee-Weinberg bound* [91]. Here the annihilation cross-section is approximated by $\langle \sigma v \rangle \approx G_F^2 m_\chi^2$. Combining this with Eq. 1.22 gives a lower bound on the WIMP mass, which after scaling to current relic density value gives $m_\chi \gtrsim 4$ GeV. Thus from these two bounds we have an approximate range for the WIMP mass of

$$\mathcal{O}(1\,\mathrm{GeV}) \lesssim m_\chi \lesssim \mathcal{O}(100\,\mathrm{TeV}). \tag{1.25}$$

Both the unitarity and Lee-Weinberg bounds give only an approximate range for possible WIMP masses, and in practice specific models can potentially evade the bounds.

Following freeze-out the WIMPs can still undergo elastic scattering with other particles in the primordial plasma, *e.g.*

$$\chi + \ell \leftrightarrow \chi + \ell \tag{1.26}$$

This process will keep the WIMPs in kinetic equilibrium until its rate drops below the expansion rate of the Universe, a point known as kinetic decoupling. The effect of being kinetically coupled to the plasma will be to inhibit the formation of DM structures below a certain scale through collisional damping [92, 93]. This scale is positively correlated with the strength of the interaction between the DM and the plasma [94] - stronger (weaker) interactions will lead to larger (smaller) minimum structure size. The kinetic decoupling temperature T_{kd} and time will be dictated by the WIMP-plasma interaction and WIMP mass, with most WIMP models having $T_{\mathrm{kd}} \gtrsim$ MeV [95, 96, 97]. Following kinetic decoupling the WIMP DM will act like a collisionless fluid.

1.4.3 Neutrino decoupling

The next component to be removed from the thermal bath by the inexorable expansion and cooling of the Universe are the SM neutrinos. Initially they coupled to the plasma via weak interactions such as

$$\nu_e + \bar{\nu}_e \leftrightarrow e^+ + e^- \quad \text{and} \quad e^- + \bar{\nu}_e \leftrightarrow e^- + \bar{\nu}_e. \tag{1.27}$$

As the temperature drops, the reaction rate of Eq. 1.27 drops below the expansion rate of the Universe. The neutrinos *decouple* from the thermal bath. These neutrinos, like the WIMPs discussed above, are still present in the Universe. They have a relic density of

$$\Omega_\nu h^2 = \frac{m_\nu}{92\,\mathrm{eV}} \quad \text{where} \quad m_\nu = \sum_{i=1}^{3} m_{\nu_i} \tag{1.28}$$

It is also possible to calculate their *free streaming length*, the mean distance travelled by the neutrino before it interacts:

$$\lambda_{\mathrm{FS},\nu} \sim 20 \left(\frac{30\mathrm{eV}}{m_\nu} \right) \mathrm{Mpc}. \tag{1.29}$$

Neutrino oscillation experiments prove that neutrinos do have mass [98, 99, 100, 101, 102, 103, 104, 105, 106], and these have given us measurements of the mass differences between the three neutrinos. The largest of these mass splittings is $\sim 0.05\,\mathrm{eV}$ [78]. However so far direct measurements of the absolute neutrino mass have only yielded upper limits. The most stringent of these limits is on the anti-electron neutrino mass from tritium decay experiments, with $m_{\bar{\nu}_e} < 2.0$ eV [78]. Combining this upper limit with mass splitting measurements we can derive an upper bound on the sum of neutrino masses of $m_\nu \lesssim 6$ eV, and so by direct measurement alone we have via Eq. 1.28

$$\Omega_\nu h^2 \lesssim 0.0652, \tag{1.30}$$

just over half of the required DM density of $\Omega_{\mathrm{DM}} h^2 = 0.1197$. Furthermore, results from the measurements of the CMB anisotropy power spectrum place even more stringent limits on Ω_ν and m_ν. The Plank temperature power spectrum (TT) measurement alone gives

$$m_\nu = \sum_{i=1}^{3} m_{\nu_i} < 0.715\mathrm{eV} \implies \Omega_\nu h^2 < 0.0079, \tag{1.31}$$

while combining this with additional data (Planck polarization data, weak lensing of the CMB, observations of the baryon acoustic oscillations (Section 1.4.5), supernova data, and H_0 measurements gives [33]

$$m_\nu = \sum_{i=1}^{3} m_{\nu_i} < 0.23\mathrm{eV} \quad \text{and} \quad \Omega_\nu h^2 < 0.0025. \tag{1.32}$$

Thus SM neutrinos could at most contribute $\sim 2\%$ of the DM relic density.

1.4.4 Big Bang Nucleosynthesis

A few minutes after the Big Bang, the neutrons and protons are in equilibrium with each other via the weak interactions:

$$n + \nu_e \leftrightarrow p^+ + e^- \quad \text{and} \quad n + e^+ \leftrightarrow p^+ + \bar{\nu}_e. \tag{1.33}$$

The equilibrium ratio between protons and neutrons is [87]

$$\frac{n_p^{\mathrm{eq}}}{n_n^{\mathrm{eq}}} = \exp\left(\frac{Q}{T} \right), \tag{1.34}$$

where $Q = m_n - m_p$ and T is the temperature. At early times when $T \gg Q$ we have $n_p^{\rm eq} = n_n^{\rm eq}$, but as T begins to approach the proton-mass difference Q, then the number of neutrons will decline relative to the number of protons. If the processes of Eq. 1.33 remained efficient then this equilibrium ratio would continue to rise until no neutrons remained. However these equilibrium processes at some point stop, and so the neutron abundance freezes out, just as the WIMPs did previously. While WIMP freeze-out was caused by the annihilation rate dropping below the expansion rate of the Universe, the neutron freeze-out is initiated by the decoupling of the neutrinos described above, which causes the processes of Eq. 1.33 to cease. Neutrino decoupling and neutron freeze-out occurs at $T \sim 0.8$ MeV, leaving us with a proton to neutron ratio of ~ 5. But we are not yet done with neutrons.

A free proton is stable, but a free neutron will decay into a proton p^+ by emitting an electron e^- and electron anti-neutrino $\bar{\nu}_e$. The only way to preserve a neutron is to bind it into a nucleus, but at the point of neutron freeze out the temperature of the thermal bath is still too high to allow nuclei to form. Until the temperature drops sufficiently the neutrons decay into protons, and the neutron abundance decreases. After approximately 330 seconds of cooling there are no longer enough photons of high enough energy to prevent nuclei forming. First protons and neutrons bind to form deuterium, most of which then quickly undergo additional reactions to form more stable helium-4 nuclei. Further reactions produce smaller quantities of lithium-6, lithium-7, and beryllium-7, the latter decaying back into lithium-7 via electron capture [107], and traces of deuterium, and helium-3 also remain. The bulk of the baryon abundance remains in neutral hydrogen (lone protons). This process is known as *big bang nucleosynthesis* (BBN). Any nuclei heavier than lithium must be formed much later, inside the first generation of stars.

In the Standard BBN (SBBN) framework the relative abundances of the nuclei produced during BBN are linked by the baryon to photon ratio

$$\eta = \frac{n_N}{n_\gamma}, \tag{1.35}$$

where n_N and n_γ are the nucleon and photon densities respectively. Measurements of any two of the BBN relics can be used to determine η, and combined with the photon density a figure for Ω_b can be derived. For instance it is possible to measure deuterium to hydrogen ratios in gas clouds by observing absorption features in the spectra of distant quasars lying behind the gas cloud. Such measurements combined with SBBN and the photon density give $\Omega_b h^2 = 0.0222 \pm 0.0013$ [108], in close agreement with that derived from Planck measurements of the CMB of $\Omega_b h^2 = 0.02225 \pm 0.00016$ [33].

The outcome of BBN is also sensitive to the addition of new physics in the early Universe. One example is the possibility of WIMP DM annihilations continuing after

freeze-out, injecting additional energy during BBN and thus producing lithium-6 at rates 10^7 times larger than under SBBN [109, 107]. Thus BBN provides another set of constraints upon the physics of DM and the early Universe in general, and reinforces the inability of baryons to account for DM.

1.4.5 Recombination and the Cosmic Microwave Background

So far we have been working under the assumption of a smooth and homogeneous Universe, but now we begin to investigate deviations from this. The source of the inhomogeneities are the quantum fluctuations generated during inflation that were stretched out beyond the horizon. As the Universe expands these fluctuations re-enter the horizon, continuously generating perturbations in matter and radiation of the Universe.

Until this point the Universe has been dominated by radiation, *i.e.* photons. As the Universe expands the matter energy density drops as a^{-3} simply from the volume expansion of space. The radiation energy density also falls due to the volume expansion of space, but the energy of individual photons also falls as a^{-1} from their expanding wavelengths. Thus the radiation energy density drops as a^{-4}, much faster than that of matter, and eventually the Universe will reach the point of matter-radiation equality. At this point the Universe has a temperature of $T \sim \mathcal{O}(\text{eV})$, and about 60,000 years have elapsed since the Big Bang.

Well before matter-radiation equality the WIMP DM has frozen out, and at a temperature of $\sim$ MeV has kinetically decoupled from the SM plasma. Following matter-radiation equality the radiation was no longer dominant, and perturbations in the DM density field could begin to grow. At this point the baryons were still combined with photons in a hot plasma. As this plasma began to fall into the DM overdenstities its pressure would increase, pushing the plasma outwards again. These two opposing forces of gravitational attraction and the repulsion of pressure set up acoustic oscillations within the plasma.

The plasma was sustained by the equilibrium equation $e^- + p^+ \leftrightarrow \text{H} + \gamma$. The electrons and protons would form hydrogen and photons, but the surrounding soup of photons was energetic enough to disintegrate the hydrogen back into electrons and protons. However the unrelenting expansion of the Universe continues to cool the plasma and reduce the energy of the photons, to the point where the right-to-left reaction slows down and eventually stops. Protons and electrons can now form neutral hydrogen - this is known as *recombination*. As the plasma separates the repulsive pressure disappears, and the oscillations cease.

Recombination sets the photons of the plasma free. Before this time the Universe was opaque - photons would scatter off the large number of free electrons in the plasma. As these electrons are now bound into neutral hydrogen atoms, this scattering drops precipitously, dropping below the rate of expansion of the Universe. Like the neutrinos before them the photons *decouple*, and can now pass through the Universe largely unimpeded. As the Universe expands further their wavelengths are stretched out and increased. Today they have a wavelength in the microwave band, and are detectable as the *cosmic microwave background* (CMB).

As mentioned earlier, the plasma from which the CMB photons are produced is oscillating, with regions of compression and rarefaction. When the plasma separates out into baryons and photons both of these components will inherit an imprint of the oscillations. For the photons this imprint is seen through temperature anisotropies in the CMB - regions where the plasma was in compression at the time of recombination will be hotter while regions where it was in rarefaction will be cooler. The CMB anisotropies give us a snapshot of the oscillations in the plasma at recombination.

The CMB anisotropies are generally analysed by way of power spectrum, which broadly speaking is a description of the amount of power in each frequency component of a signal. We start with the temperature fluctuations as a function of position on the sky $\hat{\mathbf{n}}$ [110],

$$\Theta(\hat{\mathbf{n}}) = \frac{T(\hat{\mathbf{n}}) - \overline{T}}{\overline{T}}, \tag{1.36}$$

where $\overline{T}$ is the average temperature of the CMB over the whole sky. The fluctuations can be decomposed into spherical harmonics $Y_{\ell m}$,

$$\Theta(\hat{\mathbf{n}}) = \sum_{\ell m} \Theta_{\ell m} Y_{\ell m}(\hat{\mathbf{n}}), \tag{1.37}$$

and the power spectrum is then derived from the coefficients $\Theta_{\ell m}$ of each of these harmonics,

$$\langle \Theta^*_{\ell m} \Theta_{\ell' m'} \rangle = \delta_{\ell\ell'} \delta_{mm'} C_\ell. \tag{1.38}$$

If the fluctuations $\Theta(\hat{\mathbf{n}})$ are Gaussian, then the power spectrum contains all the statistical information of the field [110]. Large ℓ corresponds to small physical scales, while small ℓ corresponds to larger scales. Figure 1.3 shows the temperature power spectrum measured by the Planck satellite [33], where $\mathcal{D}_\ell = \ell(\ell+1)C_\ell/2\pi$ [111], and the normally dimensionless C_ℓ has been multiplied by $\overline{T}^2$.

From this power spectrum and other data from the CMB we can extract information about the baryon-photon plasma from whence the CMB came and the wider state of the Universe at the time of emission. For instance, the baryons are initially coupled to the photons and so add mass (and thus momentum) to the plasma. Changing the baryon to photon ratio η will change how the plasma oscillates before decoupling,

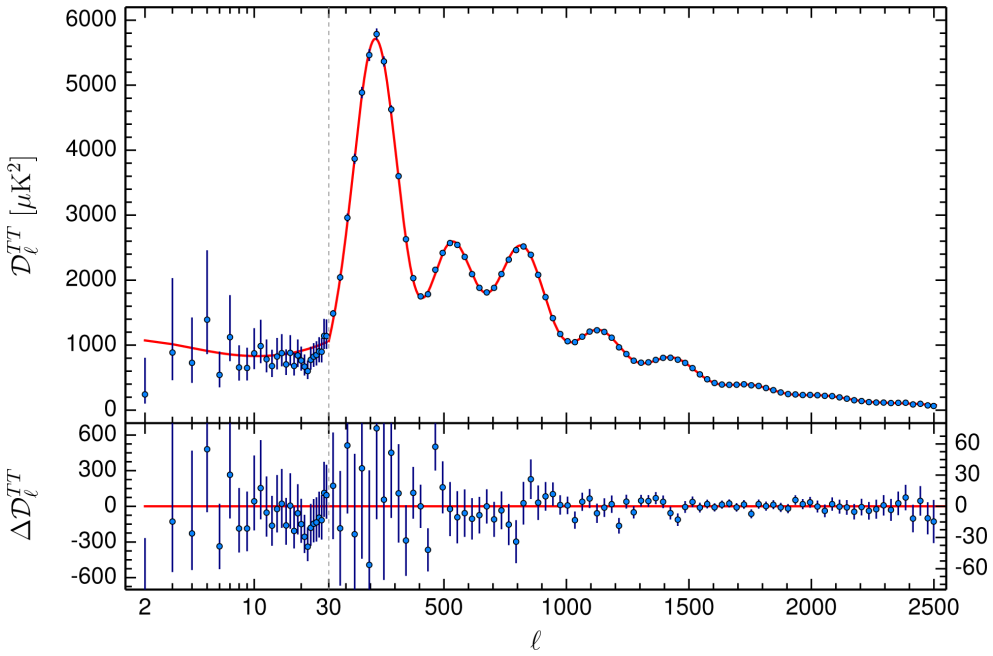

Figure 1.3: Planck CMB temperature anisotropy power spectrum [33].

which manifests itself as changes in the relative heights of the even and odd peaks in the CMB power spectrum. As decoupling occurs well after the point of matter domination the primary source of density perturbations is DM. Thus the DM to radiation ratio controls the amplitudes of the peaks in the CMB, with less DM leading to higher peaks. Additional temperature variations are caused by the *Sachs-Wolfe effect* [112]: at the point of decoupling the photons that find themselves within the gravitational wells of the DM clumps will loose energy climbing out. When we observe the CMB these photons will have slightly lower energy compared to the average energy.

Further information can be drawn out from the polarization of the CMB photons, generated through effects such as Thomson scattering of electrons in the photon field during decoupling, first detected by the DASI experiment [113]; graviational lensing, first detected by the South Pole Telescope [114], and also later detected by Planck [115]; and finally primordial gravitational waves produced by inflation, a detection of which was claimed by the BICEP2 collaboration [116], but later ruled out by a joint BICEP2, Keck Array, and Planck analysis [117].

Figure 1.4: *(Opposite)* Canonical WIMP annihilation cross-section (black dashed), along with the more precise calculation given in [89]. Also shown are the limits on the annihilation cross-section derived from Planck data (blue) [33], those from gamma-ray observations of dwarf spheroidal galaxies using *Fermi*-LAT and MAGIC (red) [122], and the Galactic Centre observations by HESS (magenta) [123], discussed further in Section 1.7.

Analysis of the temperature and polarization anisotropies in the CMB yield the following values for the relative amounts of baryons, dark matter, and dark energy in the Universe [33]:

$$\text{Baryons} \quad \Omega_b h^2 = 0.0225 \pm 0.00016 \quad \Rightarrow \quad \Omega_b = 0.04917 \pm 0.00035 \tag{1.39}$$

$$\text{Cold Dark Matter} \quad \Omega_c h^2 = 0.1198 \pm 0.0015 \quad \Rightarrow \quad \Omega_c = 0.2647 \pm 0.0033 \tag{1.40}$$

$$\text{Dark Energy} \quad \Omega_\Lambda = 0.685 \pm 0.013 \tag{1.41}$$

where $\Omega_i = \rho_i/\rho_c$, ρ_c is the critical density of the Universe, and Ω_b and Ω_c are derived using $h = 0.6727$, also from [33].

The CMB can yield not only information on how much DM there is in the Universe, but it can also place limits on the properties of DM. The annihilation of DM particles during the phase of recombination would inject energy into the photon-baryon plasma, altering the course of recombination and the production of the CMB [118, 119, 120, 121]. Thus limits can be set on the self-annihilation cross-section $\langle \sigma v \rangle$ multiplied by a red-shift dependent efficiency factor $f_{\text{eff}} \simeq [0.01, 1.0]$, which quantifies the fraction of energy from the annihilation that is injected into the plasma. These limits are shown in Fig. 1.4.

The other part of the plasma - the baryons - also receive an imprint of the oscillations before recombination. When the plasma breaks down the baryons will be concentrated at the acoustic peaks, *i.e.* regions of compression. By this time the DM density perturbations have been growing for some time and are much larger than any baryon perturbations. The baryons will be attracted by the DM overdensities and fall into their gravitational wells. However remnants of the initial baryon perturbations will survive this infall, and today are visible as patterns in the clustering of galaxies. This phenomena, known as *baryon acoustic oscillations* (BAO), was seen first in 2005 by the Sloan Digital Sky Survey (SDSS) [124] and 2dFGRS [125], and has been detected in several subsequent surveys [126, 127, 128]. The values of the cosmological parameters from BAO match those from the CMB - for instance the first measurement from SDSS gave $\Omega_m h^2 = 0.130 \pm 0.011$, within 1σ mutual uncertainty from the Planck measurement of $\Omega_m h^2 = 0.1426 \pm 0.0020$ [124, 33].

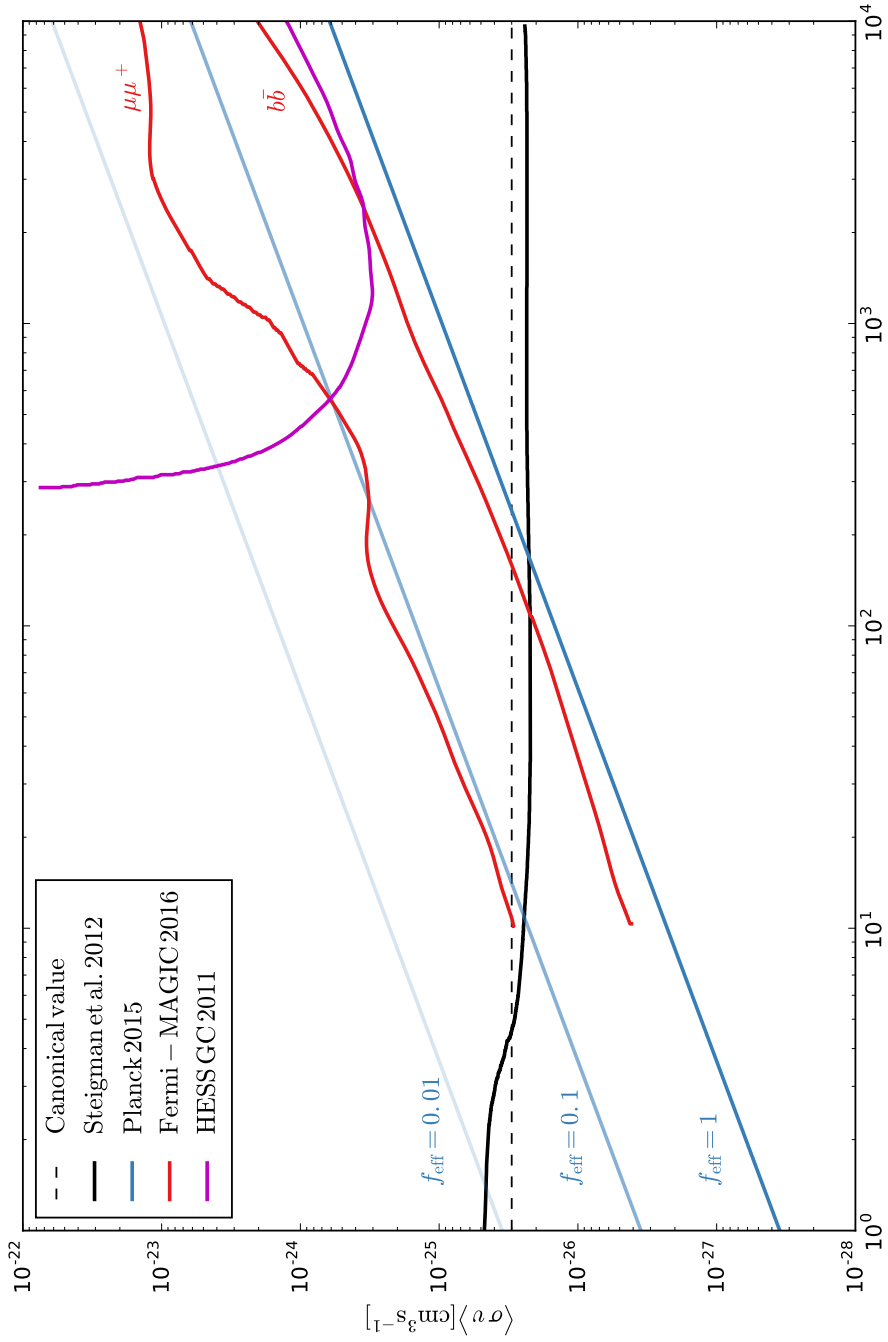
Canonical value
Steigman et al. 2012
Planck 2015
Fermi – MAGIC 2016
HESS GC 2011
$\mu\mu^+$
$b\bar{b}$
$f_{\rm eff} = 0.01$
$f_{\rm eff} = 0.1$
$f_{\rm eff} = 1$
$\langle\sigma v\rangle[\mathrm{cm}^3\mathrm{s}^{-1}]$
DM Mass m_χ [GeV/c^2]
10^{-22}
10^{-23}
10^{-24}
10^{-25}
10^{-26}
10^{-27}
10^{-28}
10^0
10^1
10^2
10^3
10^4

Figure 1.4

1.4.6 Large Scale Structure formation

The DM density perturbations, seeded by the stretched quantum fluctuations generated from inflation, continue to grow as time progresses, with the accompanying subdominant baryons following suit. While the DM component plays the dominant role in structure formation, it is the attendant baryons which coalesce into visible galaxies and allow us to see the structure. Small clumps merge with each other to form larger clumps, which in turn merger with other clumps to become even larger. This process of building bigger and bigger conglomerations of DM from smaller pieces is known as *hierarchical structure formation*. The integrity of the smaller chunks is not entirely destroyed by the merging process - some of the DM particles will be stripped off and merge into a smooth component of the larger unit, but remnants of the chunks will remain intact[4]. This formation process leads to the hierarchy of structure seen in the Universe: the small clumps host small satellite galaxies, which orbit larger conglomerations of DM hosting larger galaxies such as the Milky Way. These larger clumps themselves form the building blocks of nodes and filaments which extend across the Universe and host galaxy clusters. This can be seen in Fig. 1.5, which shows both results from the Millennium Simulation [129], and observations from the CfA2 [130], 2dFGRS [131], and SDSS [132] surveys [133]. Hierarchical structure formation is a non-linear process, and so must be simulated using a large number of DM clumps each moving under the combined gravity of the other clumps.

The formation of this large scale structure places further limits on the nature of DM. The scale of structures possible for a given DM candidate are controlled via the collisional damping prior to kinetic decoupling, as discussed earlier in Section 1.4.2, and also their free-streaming length $\lambda_{\rm FS}$. DM particles with larger $\lambda_{\rm FS}$ will stream out of overdensities and 'wash out' structures smaller than a given scale. For example, the free streaming length for SM neutrinos is given earlier by Eq. 1.29. Taking only direct limits on the sum of neutrino masses calculated earlier ($m_\nu \lesssim 6$ eV) we have $\lambda_{{\rm FS},\nu} = 100\,{\rm Mpc}$. Thus with only SM neutrinos as DM the smallest structures that could initially form would be on the order of galaxy superclusters. This would imply so-called *top-down* structure formation, whereby supercluster-scale objects would form first, and smaller structures such as galaxies would form later through fragmentation. The resulting distribution of galaxies is much more highly clustered than that found in observations of the Universe [134, 135].

On the other hand, WIMP cold dark matter, such as the SUSY neutralino, has a very small free streaming length and can form much smaller structures. The minimum size of the DM structures is set by a combination of collisional damping and the small

[4] A culinary equivalent would be chunky peanut butter. It's all peanuts, but there is a smooth component interspersed with peanut fragments

free streaming, and is estimated to be in the range $10^{-11} - 10^{2}\,\mathrm{M}_{\odot}$, depending on the exact parameters of the DM model [96, 97]. This ability to form small DM structures in the early Universe agrees with the paradigm of hierarchical structure formation.

The inability of neutrinos to form the inferred DM structures can be seen another way, via the Tremaine-Gunn bound [136]. Neutrinos (and WIMPs) are fermions, and so the Pauli Exclusion Principle sets a limit on their number density - *i.e.* how many particles can be packed into a given volume. An even stronger bound can be placed by the conservation of phase space density, as the neutrinos are non-interacting. With this number density lower limit it is possible to calculate the minimum mass per neutrino required to make up the total mass of the halo. For a galactic halo Reference [136] found that $m_{\nu} \gtrsim 16$ eV (assuming $g_{\nu} = 2$). This limit is inversely proportional to the velocity dispersion of the bound object, and so becomes even more restrictive for dwarf spheroidal galaxies, rising to $\sim 0.1 - 2$ keV [*e.g.* 137, 138, 139, 140]. This mass lower limit is at odds with even the neutrino mass upper limits from tritium decay experiments ($m_{\nu_e} \lesssim 2$ eV, [78]), let alone those from Planck ($\sum m_{\nu} < 0.492$ eV, [33]), firmly ruling out SM neutrinos as the DM particle. The proposed right-handed sterile neutrinos introduced earlier in Section 1.3 can, however, have masses that evade the Tremaine-Gunn bound, making them a viable DM candidate.

With keV scale masses the sterile neutrinos would be an example of *warm dark matter* (WDM), which has larger free streaming lengths than CDM but does not violate observed limits on structure formation. WDM would still generate hierarchical structure formation, but the smallest possible structures would be larger than those possible from CDM models. Motivation for WDM has come from the need to address discrepancies between observations of satellite galaxies orbiting the Milky Way and the results of numerical simulations. Simulations of CDM haloes predict far more satellites than are observed, known as the *missing satellites problem* [141, 142], and also a population of satellites so massive as to have been guaranteed to form stars and thus be visible, dubbed the *too big to fail problem* [143, 144, 145, 146]. WDM would solve these problems by limiting the minimum size of the DM clumps that could form, and so limiting the number of satellite haloes that could form. These problems are still, however, undergoing rigorous debate, with inclusion of baryonic physics being a potential solution [147].

1.4.7 Modelling of Dark Matter Halos

The question now becomes how to describe the DM haloes in which galaxies such as our own are embedded focusing on the smooth component. Early simulations of CDM alone yielded a universal profile, known as the *Navarro, Frenk, and White* (NFW) profile, that described halos ranging in size from micro-halos to galaxy clusters

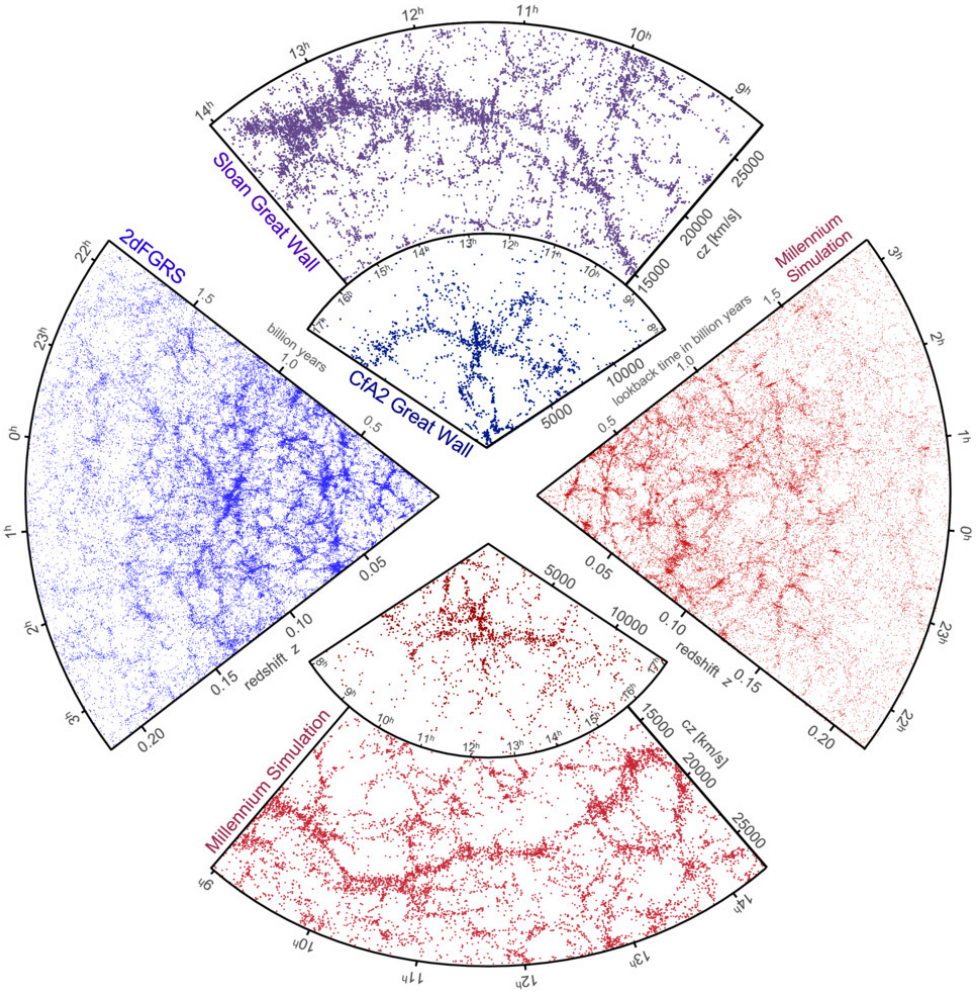

Figure 1.5: Comparison by Ref. [133] of the observed distribution of galaxies throughout the Universe (blue and purple) with the results of large scale structure formation simulations (red). Observational data is drawn from the CfA survey [130] (with Coma cluster in the middle), 2dFGRS [131], and the SDDS survey [132]. The simulated galaxy distributions are produced by the Millennium simulation [129].

[148, 149]. The now generalised form of this equation is

$$\rho_{\rm NFW}(r) = \frac{\rho_s}{\left(\frac{r}{r_s}\right)^{\gamma}\left(1+\frac{r}{r_s}\right)^{3-\gamma}}, \tag{1.42}$$

where ρ_s and r_s are the scale density and scale radius respectively, and $\gamma = 1$ gives the original, classic NFW profile. The classic NFW profile features a *cusp* at the center, *i.e.* as $r \to 0$, $\rho(r) \to \infty$, and so naturally some minimum cutoff radius must exist. The γ parameter primarily affects the inner slope of the profile - in the regimes of $r < r_s$ and $r_s < r$ the profile can be approximated as

$$\rho(r) \approx \frac{\rho_s}{\left(\frac{r}{r_s}\right)^{\gamma}} \qquad \text{for } r \ll r_s \tag{1.43}$$

$$\rho(r) \approx \frac{\rho_s}{\left(\frac{r}{r_s}\right)^{3}} \qquad \text{for } r_s \ll r \tag{1.44}$$

Altering the inner slope of the profile can be useful in accommodating the effects of interactions between the baryons and DM. For instance, the high concentration of baryons in the centre of the galaxy can pull in the DM and steepen the profile in a process known as *adiabatic contraction* [150, 151]. On the other hand, outflows of material from star formation and supernovae can alter the gravitational potential enough to reduce the density of DM at the centre [152, 153, 154, 155, 156]. The classic NFW profile is shown in Fig. 1.6.

Later simulations [157] suggested the use of a profile which was later realised to have been proposed many decades earlier by Jan Einasto [158, 159, 160]. This Einasto profile is

$$\rho(r)_{\rm Ein} = \rho_s \exp\left(-\frac{2}{\alpha}\left[\left(\frac{r}{r_s}\right)^{\alpha} - 1\right]\right) \tag{1.45}$$

In the vicinity of the Sun the Einasto and classic NFW profiles are similar, but they begin to diverge towards the Galactic Centre (GC) as illustrated by Fig. 1.6. Note that as $r \to 0$ the Einasto profile gently increases, remaining finite at $r = 0$. However it is not considered to have a *core*, which is generally considered to be a large central region with a flat profile. Also shown in Fig. 1.6 are the density profiles for a range of MW analogue galaxies drawn from the EAGLE HR [161, 162] and APOSTLE IR [163, 164] simulations, which include both DM and baryonic physics. These MW analogues were identified by searching through the simulation results to find galaxies which were close to the MW's shape, rotation curve, and total stellar mass [165]. These results show that for halos analogous to the MW there can be appreciable spread in density profiles and deviations from NFW and Einasto profiles.

Just as rotation curves of external galaxies gave early evidence for DM, so too can they be used to look for DM in our own galaxy. However such endeavours are hampered by

Figure 1.6: *(Opposite)* Comparison of the classic NFW radial DM profile (Eq. 1.42) with $\gamma = 1$ (green), the Einasto (Eq. 1.45, magenta), both of which have been normalised to $\rho_{\mathrm{DM},\odot} = 0.4\,\mathrm{GeV\,cm^{-3}} = 10.54 \times 10^{-3}\mathrm{M_\odot\,pc^{-3}}$, and also density profiles for MW analogues [165] identified in the EAGLE HR [161, 162] and APOSTLE IR [163, 164] DM plus baryons simulations.

the fact that we reside inside the baryonic disc itself. Our own motion around the MW is uncertain, much is obscured by dust, and for many tracers we have radial velocity information (*i.e.* towards or away from us), but the distance determination needed to convert this into a rotational velocity is lacking. The data used to reconstruct the MW rotation curve can be divided into three broad categories; stellar kinematics, gas kinematics, and astrophysical masers (microwave band lasers). A comprehensive catalogue of such tracers was compiled and presented in [166]. This data was then used, along with permuted combinations of models describing the MW's baryonic disc, bulge, and gas components, to fit generalized NFW and Einasto DM profiles to the MW [167]. Variation in the baryon models produced a wide spread of parameter values. Assuming $r_s = 20$ kpc, both have $\rho_\odot \sim [0.4, 0.55]\,\mathrm{GeV\,cm^{-3}}$, while the generalised NFW profile has $\gamma \sim [0, 1.5]$ and the Einasto profile has $\alpha \sim [0.1, 1]$. The authors of [167] found that the main source of uncertainty at and inside the solar position was the uncertainty on the spatial distribution of the baryons. This is a theme that will resurface later in Chapter 4 - the motions of objects in the galaxy are dictated by the *total* potential and are agnostic to whether this potential is generated by baryons or DM. Knowledge of the distribution of DM in the MW is utterly dependent on knowledge of the distribution of baryons.

1.4.8 Departures from Spherical Symmetry

So far we have assumed that the DM halo is spherically symmetric. More generally, the DM halo can be described by triaxial ellipsoid, the general Cartesian form of which is

$$\frac{x^2}{a^2} + \frac{y^2}{b^2} + \frac{z^2}{c^2} = 1 \tag{1.46}$$

A sphere is described by $a = b = c$, while a fully triaxial ellipsoid has $a > b > c$. The intermediate cases are $a = b > c$, describing an oblate ellipsoid (a flattened sphere, similar to an M&M candy), and $a = b < c$, describing a prolate spheroid (an elongated sphere, akin to a rugby ball). Early DM-only simulations found triaxial halos, with most finding a preference towards a prolate shape [168, 169, 170, 171]. Further simulations found that the inclusion of baryons yielded spherical or oblate halos [172, 173, 174, 175, 176].

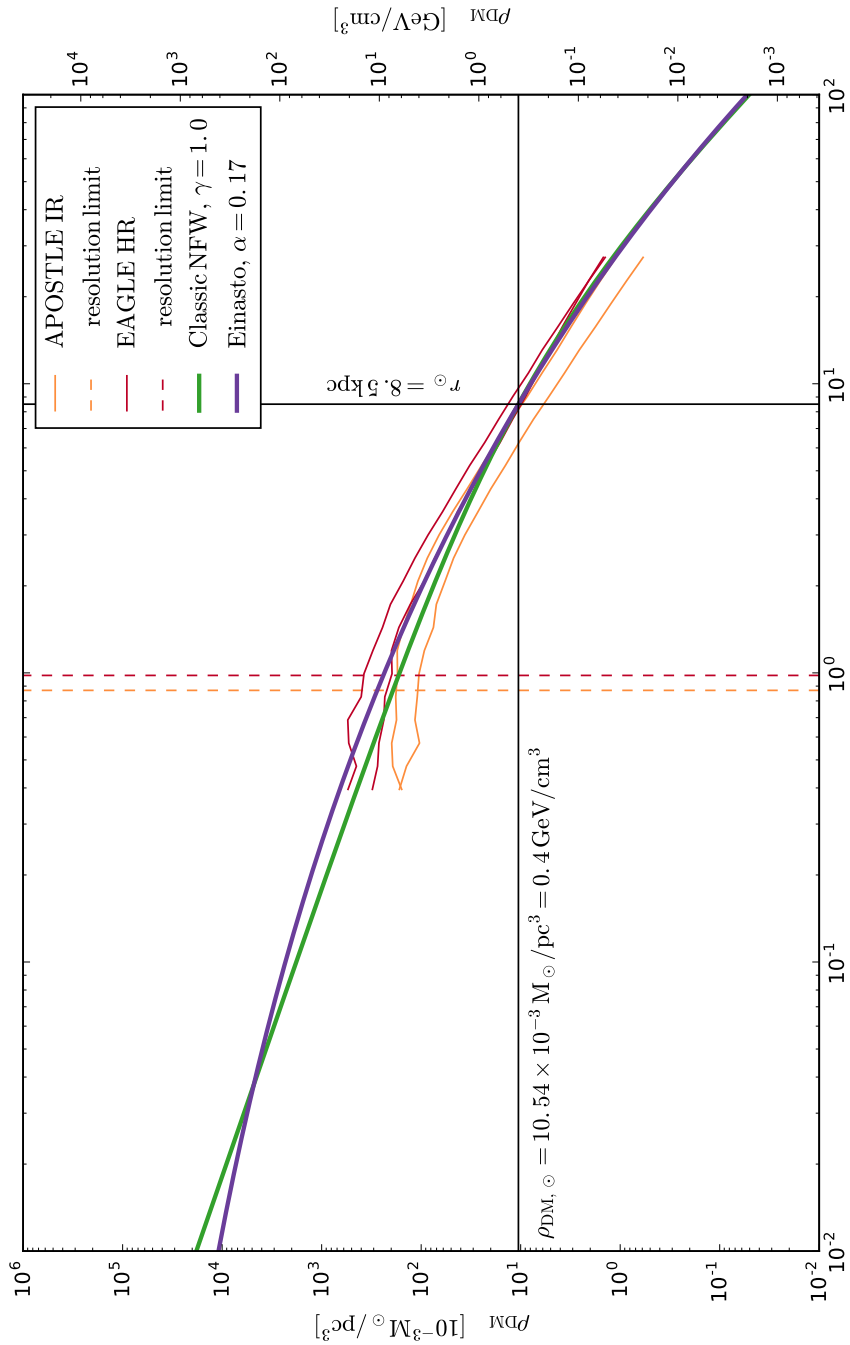
APOSTLE IR
resolution limit
EAGLE HR
resolution limit
Classic NFW, $\gamma = 1.0$
Einasto, $\alpha = 0.17$
$r_\odot = 8.5\,\mathrm{kpc}$
$\rho_{\mathrm{DM},\odot} = 10.54 \times 10^{-3}\,\mathrm{M}_\odot/\mathrm{pc}^3 = 0.4\,\mathrm{GeV/cm}^3$
ρ_{DM} $[10^{-3}\mathrm{M}_\odot/\mathrm{pc}^3]$
ρ_{DM} $[\mathrm{GeV/cm}^3]$
r [kpc]

Figure 1.6

Another departure from a spherically symmetric DM component is the addition of a disc-shaped component of DM, known as a *dark disc*. These can arise from both the standard CDM paradigm, and also from more exotic scenarios such as the proposed Double Disc Dark Matter (DDDM) that delivered deadly destruction to the doomed Dinosaurs [177, 178, 179]. In the standard CDM cosmology dark discs are formed at late times by in-falling clumps of DM interacting with and then accreting onto an already formed baryonic disc. They are first dragged down into the baryonic disc by dynamical friction [180, 181] and then torn apart by tidal disruption, leaving a disc shaped distribution of DM [182, 183, 184]. DM clumps that are rotating in the same direction as the baryon disc are more readily accreted because the dynamical friction force is given by [185]

$$F_{\rm dyn} \propto \frac{1}{v_{\rm rel}^2} \tag{1.47}$$

where $v_{\rm rel}$ is the relative velocity between the DM clump and the baryonic disc. Thus the resulting dark disc will co-rotate with the baryonic disc, leading to interesting effects in DM detection experiments. Direct detection experiments, discussed more in Section 1.5, detect the deposition of energy from WIMPs scattering off nuclei, with faster WIMPs leaving more energy and yielding more scattering events above the detector's low energy threshold, thus giving higher total signal. These experiments would detect a lower signal from the dark disc particles due to their slower speed relative to the Earth. Other experiments rely on the capture of slower moving WIMPs in the Sun, as discussed further in Section 1.6, and these would experience a boost in signal from the dark disc DM particles.

Gravitationally a highly oblate halo and a dark disc are indistinguishable and degenerate[5]. One method to distinguish the two is to hunt for the chemically and kinematically distinct stars born inside the DM clumps that would accompany the accreted dark disc, but not the contracted DM halo. Recent Gaia-ESO observational data find no evidence for such stars [186, 187], suggesting that the rate of sub-halo mergers within the Milky Way has been low since its disc formed, and therefore the MW does not host a significant accreted dark disc. If correct, then any gravitationally detected non-sphericity must imply a non-rotating locally oblate halo.

The radial profile of the MW halo, be it a cusped NFW or a flatter Einasto, whether it is prolate, oblate, or spherical, and the presence or absence of a dark disc, are all imprints of the how the MW formed. Thus unravelling the properties of the DM distribution in the MW will not only aid in the search for DM, but also tell us how our galaxy came to be.

[5]Sometimes an oblate halo is erroneously referred to as a dark disc, leading to some confusion. Throughout this work we use the unmodified term 'dark disc' to refer to a co-rotating dark disc formed through DM accretion.

1.4.9 Velocity distribution of Dark Matter in the Milky Way

In addition to describing the distribution of cold DM particles in position space, we must also investigate how they are distributed in velocity space. In the standard halo model (SHM) the velocities of the DM particles are isotropic (*i.e.* the same in all directions), and their speeds are described by a Maxwell-Boltzmann distribution [188]

$$f(v)\mathrm{d}v = 4\pi \left(\frac{3}{2\pi\sigma_v^2}\right)^{3/2} v^2 \exp\left(-\frac{3v^2}{2\sigma_v^2}\right) \mathrm{d}v. \tag{1.48}$$

The peak of this distribution is $v_0 = \sqrt{2/3}\,\sigma_v$, with $v_0 = 220\mathrm{km\,s^{-1}}$ taken as the standard value [*e.g.* 189, 190]. The Maxwell-Boltzmann distribution corresponds to a singular isothermal sphere profile, whose density profile is

$$\rho(r)_{\mathrm{SIS}} \propto \frac{1}{r^2}. \tag{1.49}$$

This profile has the advantage of being simple, and giving a flat rotation curve, but is disfavoured by observations and simulations.

More complex speed distributions are possible, such as those using Eddington's formula [191, 192, 193], which gives a one-to-one relationship between any isotropic distribution and a spherically symmetric density profile; the logarithmic ellipsoidal model [194], which generalises the isothermal sphere to the triaxial case; and Osipkov-Merritt models [195, 196], which feature radially dependent anisotropic distributions. Another approach is to use distribution functions fitted to simulations. Some early work found significant deviations from the Maxwell-Boltzmann distribution, in cases of DM-only simulations [197, 198], and simulations including baryons [199]. However the recent work of Ref. [200] analysed the DM velocity distributions of MW-like halos from the EAGLE and APOSTLE simulations, finding them well described by a Maxwell-Boltzmann distribution with peak speed in the range of $v_0 = [223, 289]\,\mathrm{km\,s^{-1}}$.

The velocities of DM particles will have an upper limit set by the escape speed of the MW at the solar position, *i.e.* the speed a particle (or star) would need to escape the MW starting from the vicinity of the Sun. This was measured to be $v_{\mathrm{esc}} = 544^{+64}_{-46}\,\mathrm{km\ s^{-1}}$ by the RAVE survey in 2007 [201], and updated to $v_{\mathrm{esc}} = 533^{+54}_{-41}\,\mathrm{km\ s^{-1}}$ in 2014 [202].

1.5 Direct Dark Matter detection

The effort to detect DM is proceeding on three broad fronts - direct detection, indirect detection, and collider searches. In direct detection the signal is that of a DM particle interacting within our detector and depositing energy. Indirect detection methods look for SM particles produced by DM decay or annihilation in astrophysical structures, such as in the Sun, the centre of the galaxy, or in galaxy clusters. Collider production aims to produce the new beyond the Standard Model (BSM) particles discussed earlier in Section 1.3, and while this will not directly probe the DM content of the Universe, it could potentially give us precise information on DM candidate particles and thus help inform the analysis of direct and indirect detection searches.

In this section we discuss direct detection of WIMP DM, and in Sections 1.6 and 1.7 we discuss indirect detection via two signals, neutrinos from the Sun and gamma-rays from the GC respectively. Collider production is a distinct and complex undertaking, and is beyond the scope of this thesis.

As described earlier, the Galaxy is embedded within a DM halo, and thus the Earth is surrounded and permeated by DM particles. We can potentially detect these DM particles via the energy they deposit within our detector on the rare occasion they interact with SM particles. For axion DM this energy deposition would be in the form of monochromatic photons, produced by the conversion of an DM axions in the presence of a strong magnetic field [203, 204, 205]. However for the WIMP DM that is the focus of this thesis, the energy is deposited as the recoil of a nucleus [206]. How that energy manifests a detectable signal will depend on the material and experimental setup. The three basic signals are the production of heat, via phonons in cryogenic crystals or the rapid expansion of superheated liquid whose transition to a gaseous state is triggered by the WIMP energy deposition; the production of light through the excitation of a nucleus which releases scintillation light upon returning to its de-excited state; and production of charge through the ionization of the target atom [207].

Given a detector of mass $M_{\rm det}$, running for a length of time T, the number of signal counts observed over an energy range $[E_0, E_1]$ is [208]

$$S_{\rm DD} = M_{\rm det}\, T \int_{E_0/q}^{E_1/q} {\rm d}E\, \epsilon(qE)\, \frac{{\rm d}R}{{\rm d}E}\,. \tag{1.50}$$

The quantity $\epsilon(qE)$ is an energy dependent efficiency function, while q is the quenching factor, describing the fraction of the recoil energy that is ultimately seen in a given detection channel, *e.g.* $E_{\rm det} = qE_{\rm rec}$. The quenching factor is dependent on the nuclear target used and the detector setup itself. Some experiments will calibrate their energy scales such that $E_{\rm det} = E_{\rm rec}$ and $q = 1$ [209]; we will adopt this assumption

later in Chapter 2. E_0 will have a lower limit given by the detector's low energy threshold, below which the energy deposition is too small to be detected.

The last term in Eq. 1.50 is the differential event rate

$$\frac{\mathrm{d}R}{\mathrm{d}E} = \frac{\rho_{\mathrm{DM},\odot}}{m_\chi m_\mathcal{N}} \int_{v_{\min}}^{v_{\mathrm{esc,MW}}} \frac{\mathrm{d}\sigma}{\mathrm{d}E}(E,v)\, v\, f\left(\mathbf{v}(t)\right)\, \mathrm{d}^3 v, \tag{1.51}$$

where E is the energy transferred during the interaction. The elements of this equation can be separated into two categories: particle physics and astrophysics. In the former are m_χ, the WIMP mass; $m_\mathcal{N}$, the mass of the target nucleus; and $\mathrm{d}\sigma/\mathrm{d}E$, the differential scattering cross-section between the DM particle and the nucleus, which is a function of E and the WIMP speed v. Kinematics gives us the lower limit on the integral $v_{\min}$, the minimum velocity necessary to produce a recoil of energy E on a given nuclei,

$$v_{\min} = \sqrt{\frac{m_\mathcal{N} E}{2\mu}}\,, \tag{1.52}$$

where μ is the WIMP-nucleus reduced mass,

$$\mu = \frac{m_\chi m_\mathcal{N}}{(m_\chi + m_\mathcal{N})}. \tag{1.53}$$

From astrophysics we have the local density of WIMP DM at the solar position[6] $\rho_{\mathrm{DM},\odot}$, and the WIMP velocity distribution $f(\mathbf{v}(t))$, introduced in Section 1.4.9. The velocity distribution is a crucial input to the direct detection rate - a faster (slower) WIMP will deposit more (less) energy in the detector, and will be more likely to be above (below) the detector's low energy threshold, giving higher (lower) overall signal. Astrophysics also gives us the upper limit of the integral - the escape velocity of the Milky Way, $v_{\mathrm{esc,MW}}$. WIMPs with velocities higher than this will escape from the halo and thus not pass through the detector volume. The effects of uncertainties in these astrophysical parameters are significant [*e.g.* 210, 211, 212, 213, 214], but can potentially be dealt with by marginalizing over them [215, 216, 217], working in quantities where the astrophysical uncertainties have already been integrated out [218], or by using halo-independent analysis methods (see Ref. [219] and references therein).

When we introduced the cold DM velocity distribution $f(\mathbf{v})$ in Section 1.4.9 we neglected the motion of the detector through the halo. The primary component of this velocity is due to the motion of the Sun through the halo, as part of the MW's baryonic disc, resulting in a 'head wind' of WIMP particles. Futhermore, the Earth is rotating around the Sun, with its orbit inclined approximately 60° to the galactic

[6]The measurement of the local DM density $\rho_{\mathrm{DM},\odot}$, discussed further in Chapter 4, is agnostic to the particle DM model used.

disc [220]. This will add a variable velocity component with a time period of one year. In June the Earth will be heading in the same direction as the Sun, pointed into to the WIMP wind, increasing the average speed of the WIMPs and boosting the signal. Six months and half an orbit later in December, the Earth will be travelling in the opposite direction as the Sun, decreasing the average WIMP speed and reducing the signal. This is known as *annual modulation*, and can be an important tool in detecting a WIMP signal and discriminating it from background [188, 221]. The rotation of the detector along with the Earth's surface will also give a daily modulation, however the magnitude of this modulation will be ~ 60 times smaller [221].

Note the degeneracy between the local DM density $\rho_{\mathrm{DM},\odot}$, and the WIMP-nucleus scattering cross-section $\frac{\mathrm{d}\sigma}{\mathrm{d}E}$. The latter is a quantity describing BSM physics, and is of great interest to the particle physics community. In the absence of a signal from direct detection experiments, limits are placed on the cross-section, which in turn are used to place constraints on a variety of BSM theories such as supersymmetry [e.g. 222, 223, 224, 225, 226]. Yet this limit on the cross-section is dependent on an accurate determination of the local DM density $\rho_{\mathrm{DM},\odot}$. Moreover, it is also crucial to have an accurate determination of the *uncertainty* in the $\rho_{\mathrm{DM},\odot}$ measurement, with the minimum of assumptions made. An erroneous assumption could artificially reduce the uncertainty on $\rho_{\mathrm{DM},\odot}$, which propagates into overly strong limits on the cross-section, and finally resulting in incorrect limits being placed on theoretical parameter spaces. This fact serves as motivation for the last chapter of this thesis, where a new method is presented to use the motions of stars in the MW to determine the local DM density, with the potential to reduce assumptions to a bare minimum.

If there is indeed a dark disc component present in the MW, as discussed earlier in Section 1.4.8, then this will also impact the signal rates seen in direct detection experiments. As the dark disc is co-rotating with the baryonic disc, the relative speed between the dark disc WIMPs and the Sun is smaller, and the direct detection signal produced by the dark disc particles would be lower. Given that direct detection experiments have a low-energy threshold the dark disc WIMPs could escape detection completely.

The effect of a dark disc on the overall signal rate in direct detection experiments is more subtle. The velocity dispersion function $f(\mathbf{v})$ is generally defined such that it normalizes to 1, *i.e.*:

$$\int \mathrm{d}^3\mathbf{v} f(\mathbf{v}) = 1. \tag{1.54}$$

If we instead consider a 6-dimensional distribution function $f(\mathbf{x}, \mathbf{v})$ where $\mathbf{x}$ is position, integrating over velocity would give

$$\int \mathrm{d}^3\mathbf{v} f(\mathbf{x}, \mathbf{v}) = \rho(\mathbf{x}). \tag{1.55}$$

The density $\rho(\mathbf{x})$ is the density of DM particles regardless of velocity, and so is the sum of the dark disc and the spherical halo contribution:

$$\rho(\mathbf{x}) = \rho(\mathbf{x})_{\rm DD} + \rho(\mathbf{x})_{\rm Sph}. \tag{1.56}$$

If there is a dark disc, then its mass has already contributed to measurements of the local DM density, *e.g.* the widely used value of $\rho_{\rm DM,\odot} = 0.4\,{\rm GeV\,cm^{-3}} = 10.5 \times 10^{-3}{\rm M_\odot\,pc^{-3}}$. As we will discuss later in Chapter 4, there are two broad methods of determining the local DM density: extrapolating a value from spherically symmetric halo profiles fit to rotation curve data, or measuring the vertical motions of stars near the Sun up and down out of the disc plane. Vertical measurements generally assume a constant vertical DM density profile, which is a good approximation to the spherical halo (see Fig. 4.2), and so a dark disc component would simply boost this constant value, as seen later in Fig. 4.16.

Thus we can see that current DM density measurements should already include at least a partial contribution of any dark disc. For simplicity we take the maximal case, and say,

$$\rho(\mathbf{x}) = \rho(\mathbf{x})_{\rm DD} + \rho(\mathbf{x})_{\rm Sph} = 0.4\,{\rm GeV\,cm^{-3}}. \tag{1.57}$$

Combining this with Eq. 1.55 gives us

$$\int {\rm d}^3\mathbf{v} f(\mathbf{x},\mathbf{v}) = \rho(\mathbf{x}) = 0.4\,{\rm GeV\,cm^{-3}}. \tag{1.58}$$

When we introduce a dark disc, the velocity distribution function is subdivided into parts describing the dark disc and the standard halo model:

$$f(\mathbf{x},\mathbf{v}) = f(\mathbf{x},\mathbf{v})_{\rm DD} + f(\mathbf{x},\mathbf{v})_{\rm Sph}, \tag{1.59}$$

and so we find

$$\int {\rm d}^3\mathbf{v} f(\mathbf{x},\mathbf{v})_{\rm DD} + \int {\rm d}^3\mathbf{v} f(\mathbf{x},\mathbf{v})_{\rm Sph} = 0.4\,{\rm GeV\,cm^{-3}}. \tag{1.60}$$

Eqs. 1.57 and 1.60 show that if we include a dark disc component, there must be a decrease in the spherical halo to compensate. As the particles in the co-rotating dark disc component yield lower signal than those from the spherical halo, including a dark disc would *reduce* the overall signal. If we add low speed, low signal dark disc particles we have to subtract high speed, high signal spherical halo particles.

In other words, for a fair comparison between the halo-only scenario and the halo plus dark disc scenario, we must take the measured value for the local DM density, and in the first case, set the local halo DM density to this value, and in the latter

case, determine how much of the putative dark disc has been incorporated into the local DM measurement, and reduce the halo DM density by this ammount.

This dissection of the issue stands in contrast to that of Ref. [227] in the context of direct detection, and Refs. [228, 229] in the context of WIMP capture in the Sun and Earth. These references include the dark disc mass contribution as a previously unseen excess over the spherical halo and considers the currently measured local DM density as originating solely from the spherical halo, *i.e.* taking the value used here[7] they would have $\rho(\mathbf{x})_{\rm Sph} = 0.4\,{\rm GeV\,cm^{-3}} = 10.54 \times 10^{-3}\,{\rm M_\odot\,pc^{-3}}$ and $\rho(\mathbf{x})_{\rm DD} = \alpha\rho(\mathbf{x})_{\rm Sph}$ where α is number between 0.5 and 2. The inclusion of the dark disc thus simply increases the local DM density, and while for direct detection the dark disc particles contribute comparatively little signal due to their slower speed, the overall signal still receives an increase. For WIMPs heavier than 50 GeV/c^2 Ref. [227] found a factor of three increase in recoil energy range of 5 - 20 keV. For comparison the XENON1T experiment discussed below and in Chapter 2 has a recoil energy threshold of 1 keV [230], and CRESST-II discussed below has a threshold of 307 eV [231]. However, for the reasons stated above, it is our opinion that this approach overlooks some of the subtlety of the situation.

The interaction between the WIMP and the nuclei can be divided into two components, one *spin independent* (SI), and the other *spin dependent* (SD):

$$\frac{{\rm d}\sigma}{{\rm d}E} = \frac{{\rm d}\sigma_{\rm SI}}{{\rm d}E} + \frac{{\rm d}\sigma_{\rm SD}}{{\rm d}E}. \tag{1.61}$$

As the name suggests the SD interaction is a function of the total nuclear spin of the nucleus, which varies up and down as one progresses through the periodic table adding protons and neutrons. The SI interaction is a function of the total mass of the nuclei, and so is larger for heavier nuclei. This means that it is easier to probe the SI interactions, as heavier atoms can be used, compared to SD interactions, where the maximum nuclear spin is 6 for vanadium-50. In Fig. 1.7 the SI and SD interactions for a range of SUSY models drawn from [232] are shown in green, along with the strongest $\sigma_{\rm SI}$ and $\sigma_{\rm SD}$ limits available for any WIMP mass. Note that the limits on $\sigma_{\rm SI}$ are at least four orders of magnitude stronger than that on $\sigma_{\rm SD}$ from the IceCube Neutrino Observatory (see Section 1.6). Further details on this topic can be found in Section 2.2.1.

No reliable WIMP DM signal has yet been seen in direct detection, and so experimental collaborations are only able to derive upper limits on the strength of the WIMP-nucleon interactions. Comparisons of limits set by various experiments are shown in Fig. 1.8 for SI interactions and Fig. 1.9 for SD interactions. For SI interactions, at the lowest WIMP masses ($0.5 - 1.7\,{\rm GeV/c^2}$) the strongest limits come

[7] Refs. [227, 228, 229] take the local DM density to be $\rho_{\rm DM,\odot} = 0.3\,{\rm GeV\,cm^{-3}} = 7.90 \times 10^{-3}{\rm M_\odot\,pc^{-3}}$.

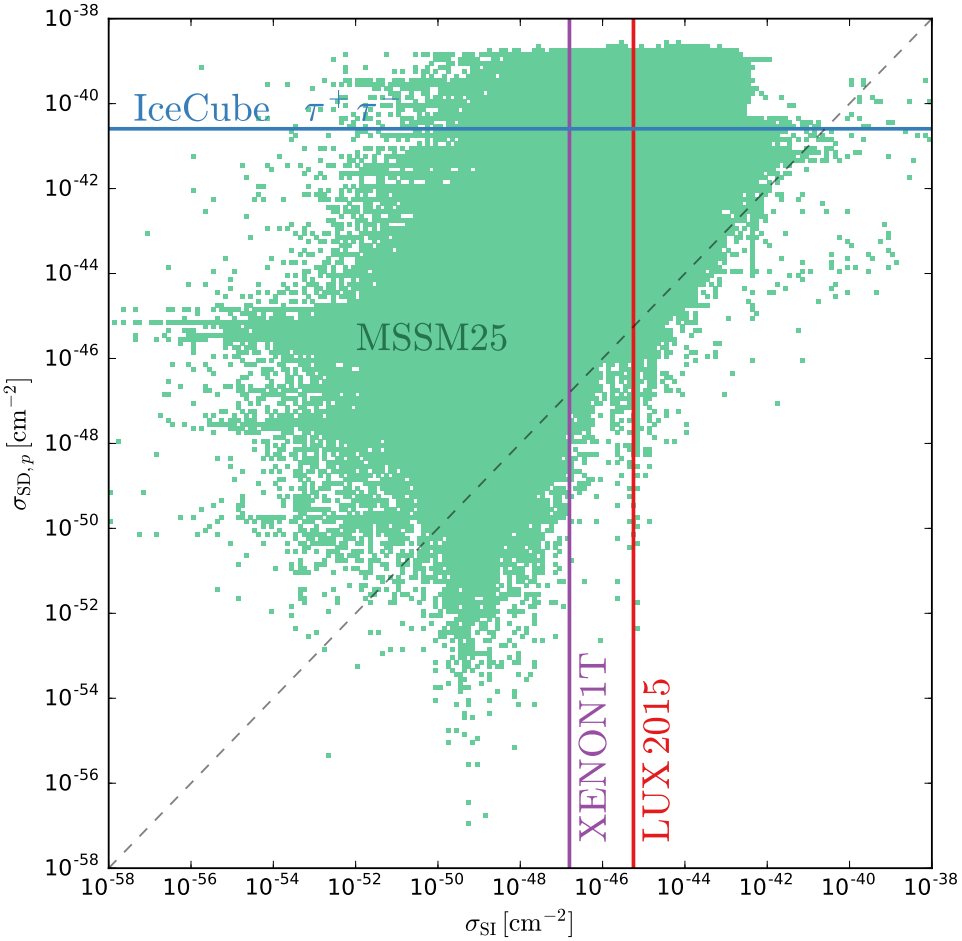

Figure 1.7: Maximum reach of experiments probing SI interactions independent of WIMP mass, LUX [189] and XENON1T [230], and the IceCube experiment, which probes SD-proton interactions experiments [4]. Shown in green is the a range of possible $\sigma_{\mathrm{SI,\,nucleon}}$ and $\sigma_{\mathrm{SD,\,proton}}$ cross-sections from models produced by 25-parameter MSSM scans [232].

from the CRESST-II experiment, which uses cryogenic crystals of $CaWO_4$ to detect both scintillation light and phonons [231]. For slightly higher masses ($1.7-6\,\mathrm{GeV/c^2}$) CDMSlite sets the strongest limits using cryogenic germanium crystals and detecting only the phonon signal, although the usual mode of operation is to detect both phonons and ionization [233]. Above $\sim 6\,\mathrm{GeV/c^2}$ the LUX experiment sets the most stringent limits, derived from 85.3 live-days of exposure [189]. LUX is a two-phase time projection chamber (TPC) that detects both scintillation light and the ionization signal. The experimental setup of LUX is similar to that of the recently commissioned XENON-1T experiment, also shown in Fig. 1.8, which is expected to over take LUX after only 5 days of operations due its larger detector volume [230]. The XENON-1T experiment will be discussed in greater depth in Chapter 2.

The grey region of Fig. 1.8 is known as the neutrino floor. This is the region where astrophysical neutrinos become detectable in direct detection experiments, and hence become a background for WIMP searches [234]. These neutrinos come from nuclear reactions in the Sun, cosmic ray interactions in the atmosphere, and also a diffuse background of neutrinos from supernovae throughout the Universe (diffuse supernova neutrino background - DSNB). Once this sensitivity is reached separating any WIMP signal from the neutrino background becomes increasingly difficult. Strategies to overcome this background include using the annual modulation of the WIMP signal [235, 236], combined analyses of data from detectors made from different target materials [237], increasing energy resolution [238], and new detector concepts such as the use of polarised helium-3 [239]. A further avenue is to build detectors capable of measuring not only the energy but also the direction of the nuclear recoil [240, 241, 242, 243, 244, 245]. The solar neutrino background could be reduced by rejecting recoils originating from the Sun's direction. Additionally, WIMP induced recoils have a directional anisotropy due to the Earth's motion through the halo, making the WIMP signal potentially visible above the isotropic atmospheric and diffuse supernova neutrinos.

For SD interactions the strongest direct detection limits are placed by LUX using neutron interactions [189]. Also competitive are the limits from PICO60 [246] and PICO-2L [247], which watch and listen for WIMP induced bubble formation in superheated liquids (CF_3I and C_3F_8 respectively). However the strongest limit on SD interactions comes not from direct detection, but from the IceCube Neutrino Observatory, which we will discuss in the next section.

In the coming years even larger direct detection experiments are planned. Many components of XENON1T were built to enable an easy upgrade to XENONnT, which is planned to begin operations around 2018 and have a target mass of up to 7 tonnes of liquid xenon [248]. The LUX and ZEPLIN teams have combined to build the LUX-ZEPLIN (LZ) detector, with a detector mass of 10 tonnes of liquid xenon and

Figure 1.8: *(Overleaf)* Comparison of $\sigma_{\mathrm{SI,\,nucleon}}$ limits from direct detection experiments: XENON100 (purple) [190], XENON1T (projected, purple shaded) [230], LUX (red) [189], CRESST-II (green) [231], and CDMSLite (pink) [233]. Also shown in grey is the 'neutrino floor' generated by coherent scattering of solar and cosmological neutrinos [234].

Figure 1.9: *(Overleaf)* Comparison of $\sigma_{\mathrm{SD,\,nucleon}}$ limits from direct detection experiments and solar capture and annihilation to neutrinos: LUX-neutron (dashed red), LUX-proton (solid red) [251], XENON100 neutron (dashed purple), XENON100 proton (solid purple) [252], PICO60 [246] and PICO-2L [247] (yellow), and IceCube-79 proton [4].

---

a planned operational start date of 2021 [249]. An even larger detector, DARWIN, is currently in planning [250]. Also, the Cryogenic Dark Matter Search (CDMS) collaboration is planning a 1.5 tonne solid state germanium detector called GEODM. These new detectors will push even further down in the $(m_\chi, \sigma_{\mathrm{SI}}, \sigma_{\mathrm{SD}})$ parameter space, potentially ruling out that area, discovering WIMP DM there, or providing more data on any WIMP signal detected with the upcoming generation of experiments such as XENON1T.

1.6 Indirect Dark Matter detection with Neutrinos from Capture and Annihilation

The same WIMP-nuclei scatterings that deposit energy in direct detection experiments will also occur when the WIMPs pass through the bulk mass of celestial bodies such as the Earth and Sun. During this scattering, energy is deposited into the baryonic matter, and energy is lost by the WIMP, reducing its speed. If the energy loss is large enough, the DM particle will become gravitationally bound to the celestial body and begin to orbit it. This greatly increases the chances that the particle will pass through the body and interact again, loosing further energy, and becoming bound tighter and tighter to the celestial body. With enough interactions and enough energy loss the DM particle's orbit will sink to the core of the celestial body, joining a population of similarly captured particles [253, 254, 255, 256, 257]. Given its gravitational dominance in the solar system we henceforth only consider capture in the Sun.

While WIMP particles are individually stable, when they interact with one another they can annihilate into SM particles. If WIMPs are indeed captured by the Sun and

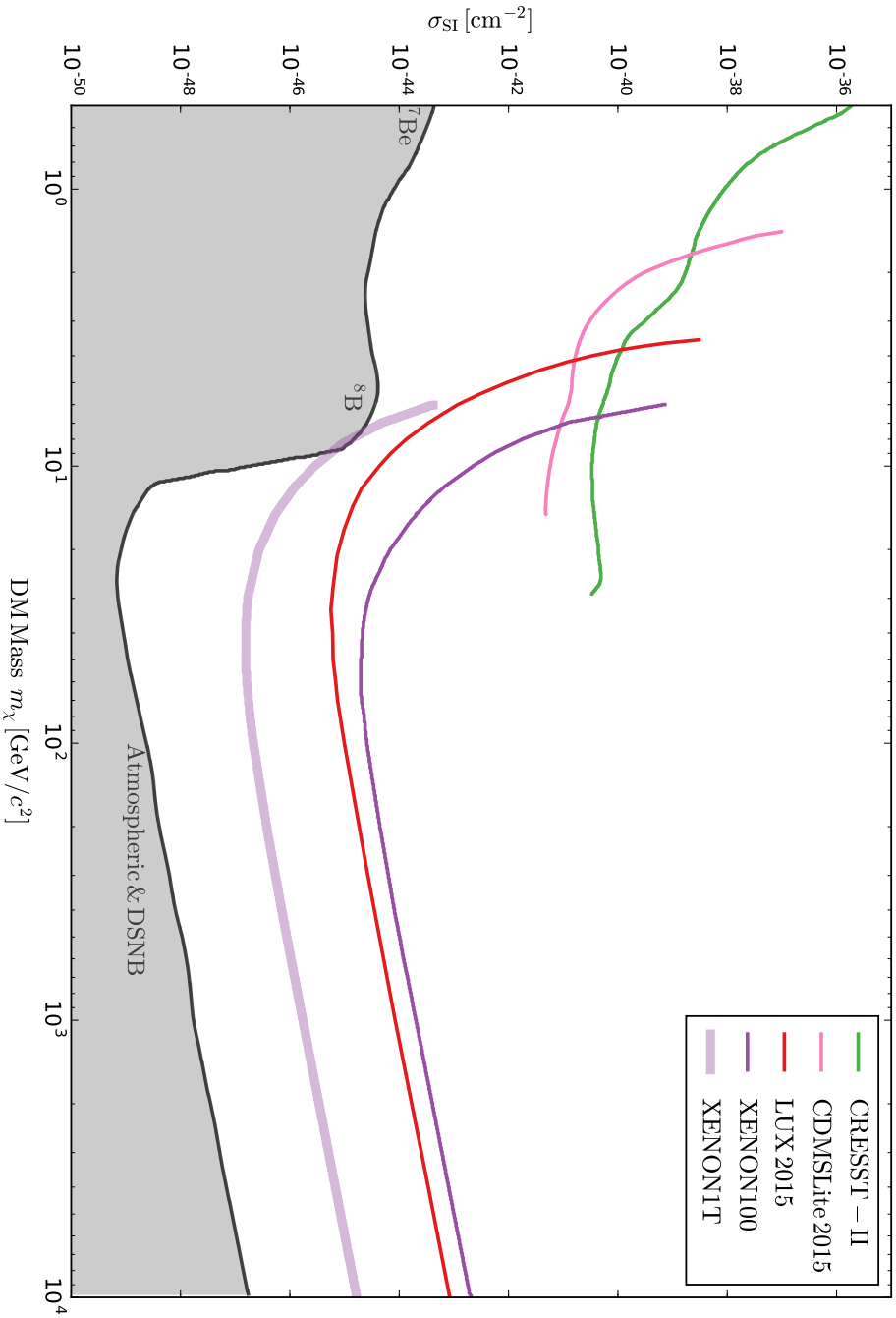
$\sigma_{\mathrm{SI}}\,[\mathrm{cm}^{-2}]$
10^{-36}
10^{-38}
10^{-40}
10^{-42}
10^{-44}
10^{-46}
10^{-48}
10^{-50}
^{7}Be
^{8}B
Atmospheric & DSNB
CRESST – II
CDMSLite 2015
LUX 2015
XENON100
XENON1T
10^{0}
10^{1}
10^{2}
10^{3}
10^{4}
DMMass $m_{\chi}\,[\mathrm{GeV}/c^{2}]$

Figure 1.8

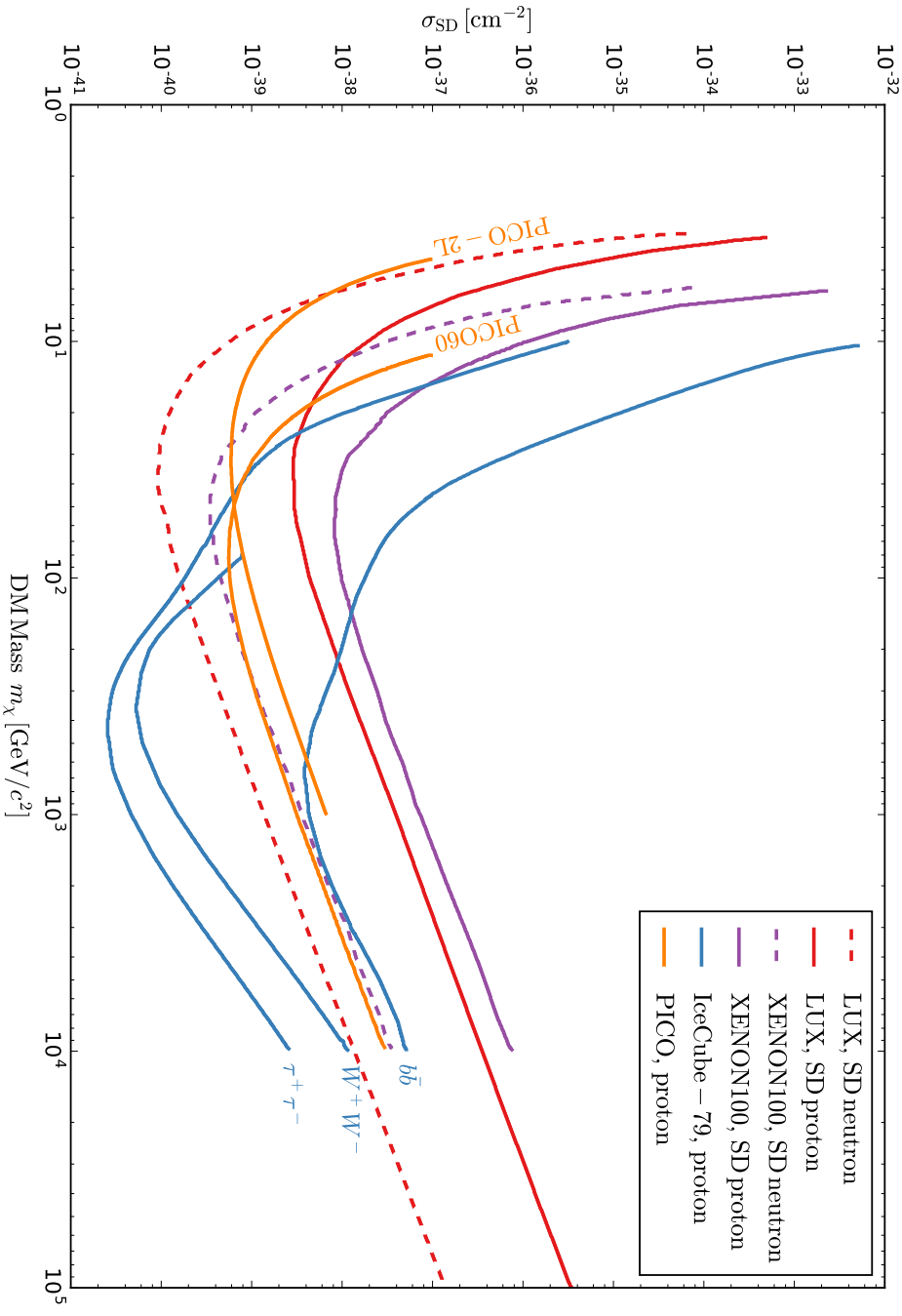
$\sigma_{\mathrm{SD}}\,[\mathrm{cm}^{-2}]$
10^{-32}
10^{-33}
10^{-34}
10^{-35}
10^{-36}
10^{-37}
10^{-38}
10^{-39}
10^{-40}
10^{-41}
10^{0}
10^{1}
10^{2}
10^{3}
10^{4}
10^{5}
DM Mass $m_\chi\,[\mathrm{GeV}/c^2]$
LUX, SD neutron
LUX, SD proton
XENON100, SD neutron
XENON100, SD proton
IceCube − 79, proton
PICO, proton
PICO − 2L
PICO60
$b\bar{b}$
W^+W^-
$\tau^+\tau^-$

Figure 1.9

concentrated at its core, then the number of WIMP annihilations there will increase and eventually an equilibrium between capture and annihilation will be reached. As mentioned earlier in Section 1.3, annihilation of WIMPs directly to neutrinos is helicity suppressed, but neutrinos will generally be produced as part of the decay chains of the particles that are produced. All the particles produced by these decay chains will be quickly absorbed by the matter surrounding them, except for neutrinos, which interact so weakly they can pass largely unimpeded through the entire bulk of the Sun. A small fraction of the neutrinos will either be absorbed through charged current ($W^{\pm}$ boson) interactions, producing a charged lepton, or neutral current (Z^0) interactions, which reduce the energy of the neutrino. The neutrinos will also undergo neutrino oscillations as they travel between the solar core and detectors on Earth, including contributions from the Mikheyev-Smirnov-Wolfenstein (MSW) effect given their long passage through matter [258, 259, 260]. These oscillations will alter the flavour ratio of the neutrinos that reach Earth, and so must be taken into account when calculating the flavour dependent rates expected at neutrino detectors. Software packages such as `DarkSUSY`, used in Chapter 2, include this effect when modelling neutrino detection rates.

Detecting this signal of neutrinos is challenging, as the very property that allowed them to escape from the Sun - very weak interactions with other matter - makes the chances of them interacting within a detector very small. Hence neutrino detectors are generally very large: the ANTARES telescope in the Mediterranean has an instrumented volume of approximately $35 \times 10^6\,\mathrm{m}^3$, the IceCube Neutrino Observatory in Antarctica is $1\mathrm{km}^3 = 1 \times 10^9\,\mathrm{m}^3$, and the upcoming KM3NeT detector, also in the Mediterranean, will have a similar volume. Neutrino observatories such as IceCube detect these neutrinos via the muons produced when muon neutrinos undergo charged current interactions in or near the detector volume. The resulting muon is travelling above the local speed of light and thus emits Cherenkov radiation, which is detectable through the ice or water of the detector. Muons can propagate for large distances through the detector and so create a distinct track that is closely aligned with the incoming neutrino direction, allowing the determination of the neutrino origin. This direction information is useful because it helps to disentangle the signal from DM annihilations in the sun from isotropic atmospheric neutrino backgrounds. Electron and tau neutrinos undergoing the same charged current interactions produce electron and tau neutrinos, but electron neutrinos quickly induce a electromagnetic cascade, and tau neutrinos rapidly decay. Neither of these produce distinct direction information for the incoming neutrino. Given that it is primarily the muon neutrinos which are detected, calculation of the oscillation processes which link the flavour ratios at Earth with the ratios at production is especially important [261, 262].

While the full formalism of WIMP capture and annihilation will be given in Section

2.2.2, several key equations are worth mentioning here. The number of WIMPs in the Sun can be described by

$$\frac{\mathrm{d}N(t)}{\mathrm{d}t} = C_c - \Gamma_a(t) \tag{1.62}$$

where C_c is the capture rate, $\Gamma_a(t) = \frac{1}{2}C_a N^2(t)$ is the annihilation rate, and the parameter C_a is a function of the WIMP annihilation cross-section $\langle\sigma_{\mathrm{ann}}v\rangle$ and the velocity distribution of the WIMPs in the Sun. The capture rate is often approximated by

$$\begin{aligned} C_c \approx & 1.3 \times 20^{21}\,\mathrm{s}^{-1} \left(\frac{\rho_{\mathrm{DM},\odot}}{0.3\mathrm{GeV\,cm}^{-3}}\right)\left(\frac{270\,\mathrm{km\,s}^{-1}}{\bar{v}_{\mathrm{local}}}\right) \\ & \times \left(\frac{100\,\mathrm{GeV}}{m_\chi}\right)\sum_i \left(\frac{A_i\,(\sigma_{\mathrm{SD},i}+\sigma_{\mathrm{SI},i})\,S\,(m_\chi/m_{\mathcal{N},i})}{10^{-6}\mathrm{pb}}\right) \end{aligned} \tag{1.63}$$

where $\bar{v}_{\mathrm{local}}$ is the local root mean squared velocity of the WIMPs, index i runs across the species of target nuclei involved, A_i parameterises relative abundances and nuclear form factors for each species, and S encodes dynamical information about the Sun. The quantities $\sigma_{\mathrm{SD},i}$ and $\sigma_{\mathrm{SI},i}$ are the same that we saw in Eq. 1.61, but for a specific nuclei i and integrated over energy. As the Sun is primarily composed of hydrogen the dominant interaction will be SD interactions with protons. Solving Eq. 1.62 to find the annihilation rate $\Gamma_a(t)$ allows us to then, after modelling the decay chains, calculate the rate of neutrinos that would pass through our detector for a given WIMP model.

First note that the capture rate, and hence the rate of neutrinos, is dependent on the spin independent and spin dependent WIMP-nuclei cross-sections, $\sigma_{\mathrm{SD},i}$ and $\sigma_{\mathrm{SI},i}$. These are same quantities used previously when calculating the rate for direct detection experiments. Second, again note the degeneracy between the WIMP-nuclei interaction strength and the local DM density $\rho_{\mathrm{DM},\odot}$. The same issues that arose from this degeneracy in direct detection will repeat themselves here - an accurate determination of $\rho_{\mathrm{DM},\odot}$ and its uncertainty is crucial for a reliable determination of the WIMP DM properties. This serves as yet more motivation for the work presented in Chapter 4, where a new method for such a determination of the local DM density is presented.

Both ANTARES and IceCube have performed searches for these neutrinos, and having not detected them, drawn limits on the WIMP-proton cross-sections [263, 264, 4]. The strongest limits from this method were derived from a re-analysis of IceCube-79 data which we presented in Ref. [4], and are shown on Fig. 1.9.

The departures from sphericity such as triaxiality discussed earlier in Section 1.4.8 also impact the DM capture rate. The solution to Eq. 1.62 is

$$\Gamma_a(t) = \frac{C_c}{2} \tanh^2 \left(\frac{t}{\tau} \right). \tag{1.64}$$

The quantity $\tau = 1/\sqrt{C_c C_a}$, and is known as the capture-annihilation equilibrium time scale, or equilibration time: for $t \gg \tau$ Eq. 1.64 simplifies to the steady state solution of $\Gamma_a(t) = \frac{1}{2} C_c$. However this assumes a constant capture rate C_c. If the DM halo is significantly triaxial, then as the Sun orbits around the galaxy it will pass through regions of higher and lower DM density, with the instantaneous capture rate increasing or decreasing accordingly. The annihilation rate (and hence signal rate) however is sensitive to the historical capture rate; if we are, for instance, just moving out of an underdense region and the equilibration time is long, the annihilation rate will be suppressed with respect to the steady state solution. A shorter equilibration time would relieve this suppression. This effect will be discussed further in Section 2.7.1.

In contrast to direct detection, the capture rate of WIMPs in the Sun is inversely proportional to the WIMP velocity, as seen in Eq. 1.63. The rate would therefore be boosted by the presence of a co-rotating dark disc, regardless of whether it included as an additional component on top of the standard halo, increasing the total local DM density above the observed value, or as a component which cannibalizes a fraction of the standard halo density, leaving the total observed density unchanged. References [228] and [229] studied the impact of a dark disc on the WIMP capture rate in the Sun, and like Ref. [227] considered it an additional component which increased the local DM density above the measured value. The presence of a dark disc was found to boost the capture rate, up to a factor of 50 for one extreme case of Ref. [229] where the dark disc doubled the local DM density.

It is also possible to detect neutrinos from annihilations in other concentrations of DM around the MW, such as the GC and dwarf spheroidal galaxies (dSphs) orbiting the Milky Way. Searches for these have been conducted using a range of neutrino detectors [265, 266, 267, 268, 269, 270, 271], though with no detection. IceCube has however confirmed detections of astrophysical neutrinos [272, 273], including three at in the PeV energy range, named 'Bert' (1.04 PeV), 'Ernie' (1.14 PeV), and 'Big Bird' (2.00 PeV). A relationship between dark matter and these astrophysical neutrinos has been proposed, but the validity of these claims is currently unclear [274, 275, 276, 277, 278, 279, 280].

1.7 Indirect Dark Matter detection with Gamma-rays

As mentioned in the previous Section, WIMP DM particles can annihilate with each other to produce SM particles. When these annihilations take place in the centre of the Sun, as discussed previously, the only particles to escape are neutrinos. However if these annihilations take place outside of celestial bodies such as the Sun, then an entire gamut of SM particles could be detected. Neutrinos again offer such a signal candidate, as mentioned above. Antimatter particles could also provide evidence of dark matter [281, 282, 283, 284], though much directional information is lost due to their random diffusion though the magnetic fields of the MW. Several experiments have found an anomalous rise in the positron fraction above normal background expectations [285, 286, 287]. This excess can be interpreted as a DM signal, but production of positrons by a local pulsar remains a more likely scenario [288, 289, 290].

A powerful channel to search for these annihilations is gamma-rays [291, 292]. They are easier to detect than neutrinos, and are not deflected by the magnetic field permeating the galaxy like charged cosmic rays. This channel does however suffer from significant contamination from background sources of gamma-rays, complicating the search for WIMP DM.

The flux of gamma-rays in our detector produced by annihilating WIMPs is given by

$$\frac{\mathrm{d}\Phi}{\mathrm{d}E} = \frac{\langle\sigma v\rangle}{8\pi\, m_\chi^2} \frac{\mathrm{d}N_\gamma}{\mathrm{d}E}\, J\left(\Delta\Omega\right). \tag{1.65}$$

In this equation we again have the WIMP mass m_χ and the WIMP self-annihilation cross-section $\langle\sigma v\rangle$. For a signal coming from galactic WIMPs we take $\langle\sigma v\rangle$ in the limit of $v \to 0$, as the average WIMP speed is $\mathcal{O}(220\,\mathrm{km\,s^{-1}}) \ll c$ (see Section 1.4.9). Additionally we have $\mathrm{d}N_\gamma/\mathrm{d}E$, the average number of photons produced per annihilation per energy, which depends on the annihilation channel. All these quantities describe the particle physics that goes into to the calculation of flux. The astrophysical aspect is described by the *J-factor*, which is

$$J\left(\Delta\Omega\right) = \int_{\Delta\Omega} \mathrm{d}\Omega \int_{\mathrm{l.o.s}} \mathrm{d}l\, \rho_{\mathrm{DM}}(r)^2. \tag{1.66}$$

This is the integral of the DM density $\rho_{\mathrm{DM}}(r)$ squared (as two particles are required for an annihilation), integrated over the line of sight (l.o.s.), within a cone $\Delta\Omega$ that covers the region of the sky we are observing. The density of DM in the equation is no longer just the local density $\rho_{\mathrm{DM},\odot}$, but is instead a varying quantity $\rho_{\mathrm{DM}}(r)$, where r runs along the line of sight.

The dependence of Eq. 1.66 on $\rho_{\rm DM}(r)^2$ immediately suggests that the best place to look for gamma-rays from annihilating DM is in nearby regions that have higher DM density compared with the wider Universe, namely the centre of the MW, and in dSphs. While the density in the GC is significantly higher than that of the dSphs, the GC also has a large background of gamma-rays produced by the interaction of high energy cosmic ray particles with the interstellar medium. This background is part of the Galactic Diffuse Emission (GDE), and will play an important role in the analysis presented in Chapter 3. The dSphs on the other hand, are thought to contain no significant astrophysical gamma-ray emission as they contain old, low luminosity stellar populations, which do not produce high energy cosmic rays, and have negligible amounts of gas for any cosmic rays to interact with ([293], and *e.g.* Ref. [294] and references therein). Observations of 15 of these dSphs by the *Fermi*-LAT and MAGIC gamma ray telescopes currently set the most stringent limits on the annihilation cross-section [122] below $m_\chi = 3$ TeV, while for $m_\chi > 3$ TeV the strongest limits are set by HESS observation of the GC [123]. These limits from *Fermi*-LAT, MAGIC, and HESS were shown previously in Fig. 1.4.

The inverse square dependence of the differential flux on the WIMP mass m_χ in Eq. 1.65 reflects the fact that our knowledge of the local DM density is only a mass density rather than a number density. A higher DM particle mass will mean fewer particles are needed to fulfil the required energy density, and a lower DM particle mass will mean more are needed.

The observation of gamma-rays can be done with either space-based observatories or ground based telescopes. The *Fermi*-Large Area Telescope (*Fermi*-LAT) mentioned above falls in the former, and is preeminent in that category. Launched in 2008, *Fermi*-LAT is a pair-conversion telescope - gamma-rays interact by producing e^+e^- pairs, which are then tracked as they pass through the detector layers that make up the LAT [295]. The direction and energy of the original gamma-ray can be determined from the reconstruction of the e^+ and e^- tracks and the energy they deposit in the calorimeter at the end of their passage through the LAT.

In 2009 *Fermi*-LAT data revealed an excess of emission above modelled backgrounds in the direction of the GC, consistent with the WIMP DM annihilation scenario and since confirmed by many independent studies [296, 297, 298, 299, 300, 301, 302, 303, 304, 305, 306, 307]. This has become known as the *Fermi* GeV Excess. If interpreted as a DM signal, the spatial distribution of the excess suggests a DM density profile described by a generalised NFW profile with $\gamma = 1.1 - 1.3$ [308].

However, the inner galaxy contains many other gamma-ray sources, and it can be difficult to disentangle a WIMP DM signal from this background [309]. These backgrounds can be from diffuse sources, or from point sources that are below the resolving

power of the detector. The GDE, which we will encounter again in Chapter 3, traces the distribution of molecular clouds in the inner MW, and includes contributions from relativistic electrons producing gamma-rays via bremsstrahlung and inverse-Compton, and the decay of neutral pion generated high energy proton-proton collisions. Studies using the spatial morphology and energy spectra of the excess have found it to be robust against variations in the standard background models [305, 306], suggesting the need for either WIMP DM, or for additional components to be included in the background. Such additional elements could include extra electron injection from supernova remnants [310], changes to the cosmic-ray propagation in the inner MW [311], or a burst of high energy electrons produced $\mathcal{O}(10^6)$ years ago [312]. While these ingredients would alter the diffuse emission, it is also possible that a population of unresolved point sources such as rapidly spinning millisecond pulsars (MSPs) are responsible for this excess [313, 301]. Recent analysis of the *Fermi* data has suggested that such a population of point sources exists just below the resolution limit of *Fermi* [314, 315]. The *Fermi* GeV excess remains an open and hotly debated topic within the community.

The alternative method of observing gamma-rays is to look for the light emitted when they interact with the Earth's atmosphere. High energy gamma-rays will initiate electromagnetic cascades in the atmosphere, tearing apart an atom and imparting each fragment with sufficient energy to cause multiple stages of further disintegration. This cascade of charged particles will be travelling faster than the speed of light in air and so create a focused cone of Cherenkov light. By observing the brightness, shape, and orientation of this cone using optical telescopes on the ground it is possible to to reconstruct the energy and direction of the incoming gamma-ray. This type of detector is known as an Imaging Air Cherenkov Telescope (IACT) [316, 317]. Around the world there are currently three IACTs in operation: HESS II in Namibia [318], VERITAS in Arizona, USA [319], and MAGIC in La Palma in the Canary Islands, Spain[8]. These three collaborations have joined forces to build the next generation IACT, the *Cherenkov Telescope Array* (CTA). CTA will be split across a northern hemisphere site at La Palma, and a southern hemisphere site at Paranal in Chile [320].

Space- and ground-based methods of detecting gamma-rays from WIMP DM annihilations are complementary as they each cover the failings of the other. IACTs suffer from a large background of cosmic ray protons and electrons at lower energies (see Section 3.4), but can be constructed to have very large effective areas, *e.g.* CTA will have an effective area $\sim 100\,\mathrm{m}^2$ at its threshold energy of 20 GeV, rising to $\mathcal{O}(10^6\,\mathrm{m}^2)$ at 10 TeV. Thus IACTs are well suited to detecting the rare but high energy gamma-rays from higher mass WIMPs. *Fermi*-LAT and other space-based observatories do

[8] `http://magic.mpp.mpg.de/`

not have this cosmic ray background, and so can probe the lower energy gamma-ray spectrum. However their effective area is limited by the cost of launching large satellites into orbit - *e.g.* *Fermi*-LAT has an effective area of $\sim 1\text{m}^2$. Thus *Fermi*-LAT is suited to detecting the large number of lower energy gamma-rays produced by lower mass WIMPs.

***

2 Complementarity of Direct and Indirect Dark Matter Detection

2.1 Introduction

The experimental effort to probe the σ_{SI} and σ_{SD} WIMP-nucleon interactions is proceeding apace, using both direct detection and indirection detection via neutrinos from solar capture and annihilation. A slew of direct detection experiments are currently taking data, and the XENON1T[1] experiment will also be taking data before the end of 2016. ANTARES[2] and IceCube[3] are both looking for the neutrinos produced by captured WIMPs annihilating in the Sun, and KM3NeT[4] will join them within the decade.

However, even if new particles are convincingly discovered by these experiments, reconstructing the properties of these putative DM particles, such as their mass and the scattering cross-sections with nuclei, will be a complex task. First, the rate calculation will be impacted by uncertainties in astrophysical quantities such as the local DM density and velocity dispersion, as discussed earlier in Section 1.5. Second, the spectrum of nuclear recoils is insensitive to the WIMP mass when the latter is much larger than that of the nuclei of the target material, making a mass determination impossible for WIMPs heavier than approximately 100 GeV [*e.g.* 321, 322]. Third, as

[1] `http://www.xenon1t.org/`
[2] `http://antares.in2p3.fr/`
[3] `https://icecube.wisc.edu/`
[4] `http://www.km3net.org/`

pointed out in Ref. [323], not only it is impossible to disentangle SI and SD couplings with a single direct detection experiment, but the large uncertainties associated with the nuclear structure function might lead to an error of about one order of magnitude on the reconstructed SD coupling [323, 252].

Uncertainties and degeneracies in the parameter space can fortunately be reduced with a careful combination with other DM searches, *e.g.* combining the information arising from direct detection experiments with different targets [324, 217, 325, 326, 327], or combining direct detection with accelerator searches or indirect searches [328, 329, 330, 331, 332]. In this chapter we explore the degree of complementarity between DM direct searches and indirect detection via neutrinos produced by the capture and annihilation of WIMPs in the Sun's core (see also Refs. [333, 334] for a similar analysis in the framework of supersymmetric models). To quantify this complementarity we investigate the combination of an upcoming direct detection experiments such as XENON1T, and the IceCube neutrino telescope in the 86-string configuration including the DeepCore array. We start by assessing the reconstruction capabilities of XENON1T [335] for 3 benchmark DM candidates close to current and upcoming bounds: XENON1T is expected to reach 10^{-47}cm^2 in sensitivity for the SI interaction, and 10^{-42}cm^2 for the SD interaction (the same sensitivity to SD interaction as is expected for IceCube in a similar time period [336]).We will demonstrate that even if one of the detectors does not see a signal the reconstruction of the physical parameters is still improved by utilizing both experiments. We will then assess the impact of uncertainties from astrophysics and from the nuclear structure functions in the reconstruction of the WIMP parameters. Our final results will be obtained by marginalizing[5] over all these nuisance parameters[6], assessing the degradation of the reconstruction of physical properties, such as the DM mass and the WIMP-nuclei cross-sections with respect to the scenario with fixed nuisance parameters.

This chapter is organized as follows. We first elaborate upon the signals theoretically expected for DM scattering off nuclei in underground detectors, Section 2.2.1, and for the neutrino flux from the Sun, Section 2.2.2. Section 2.3 describes the phenomenological approach we use in studying the WIMP signal as well as the statistical framework. Section 2.4 describes the setup of the XENON1T experiment, and its sensitivity for detecting WIMP signals. On the same lines, in Section 2.5 we describe the prospect for detection with IceCube and its sensitivity in reconstructing WIMP parameters. Section 2.6 illustrates the effectiveness of combining different search strategies for reconstructing the benchmark models. We subsequently discuss the uncertainties that affect the signal reconstruction in Section 2.7: we first describe

[5] By *marginalizing* we mean to integrate over all other parameters than the WIMP mass and cross-sections.

[6] A nuisance parameter is any parameter which is not of immediate interest but which must be accounted for in the analysis of those parameters which are of interest.

the impact of astrophysical uncertainties over the Galactic parameters, then the effect of undetermined nuclear structure functions, and lastly comment on the velocity distribution parametrization. Finally, we summarize our findings in Section 2.8.

2.2 Predicted signals from WIMPs

In this section we review the theoretical predictions for the direct detection rate and for the neutrino flux arising from annihilation of DM particles in the Sun. The scope of this brief summary is to introduce the key model parameters of our phenomenological analysis and underline the (different) dependence of the expected rates in direct and indirect detection experiments.

2.2.1 Theoretical rate for direct detection

Direct detection experiments aim to detect nuclear recoils arising from the scattering of WIMPs off target nuclei. The differential spectrum of a DM particle recoiling off a nucleus, in units of events per time per detector mass per energy, has the form

$$\frac{\mathrm{d}R}{\mathrm{d}E} = \frac{\rho_{\mathrm{DM},\odot}}{m_{\mathrm{DM}} m_{\mathcal{N}}} \int_{v>v_{\mathrm{min}}} \mathrm{d}^3 v \, \frac{\mathrm{d}\sigma}{\mathrm{d}E}(E,v)\, v\, f(\mathbf{v})\,, \tag{2.1}$$

where E is the energy transferred during the collision, $\rho_{\mathrm{DM},\odot} \equiv \rho_{\mathrm{DM}}(R_\odot)$ is the WIMP density in the solar neighborhood, m_{DM} is the WIMP mass, $\mathrm{d}\sigma/\mathrm{d}E$ is the differential cross-section for the scattering, and $f(\mathbf{v}(t))$ is the normalized WIMP velocity distribution in the Earth's rest frame. The integration in the differential rate is performed over all incident particles capable of depositing a recoil energy of E. For elastic scalar interactions, this implies a lower integration limit of

$$v_{\mathrm{min}} = \sqrt{\frac{M_{\mathcal{N}} E}{2\mu^2}}\,, \tag{2.2}$$

where $M_{\mathcal{N}}$ is the mass of the target nucleus, and $\mu = m_{\mathrm{DM}} M_{\mathcal{N}}/(m_{\mathrm{DM}} + M_{\mathcal{N}})$ is the WIMP-nucleus reduced mass. As for the velocity distribution $f(\mathbf{v})$, we use the MB parametrization [337, 338] and neglect the time dependent modulation due to the Earth's motion around the Sun. We defer to Section 2.7.1 and 2.7.3 the discussion about the role of astrophysical uncertainties.

The differential cross-section $\mathrm{d}\sigma/\mathrm{d}E$ encodes the particle and nuclear physics information and is in general separated into the SI and SD contributions as

$$\frac{\mathrm{d}\sigma}{\mathrm{d}E} = \frac{\mathrm{d}\sigma_{\mathrm{SI}}}{\mathrm{d}E} + \frac{\mathrm{d}\sigma_{\mathrm{SD}}}{\mathrm{d}E}. \tag{2.3}$$

Spin-independent interaction

$$\frac{\mathrm{d}\sigma_{\mathrm{SI}}}{\mathrm{d}E} = \frac{m_{\mathcal{N}}\sigma_n^{\mathrm{SI}}}{2\mu_n^2 v^2} \frac{\Big(f_p Z + (A-Z) f_n\Big)^2}{f_n^2} \mathcal{F}_{\mathrm{SI}}^2(E)\,, \tag{2.4}$$

where $\mu_n = m_{\mathrm{DM}} m_n/(m_{\mathrm{DM}} + m_n)$ is the WIMP-nucleon reduced mass, σ_n^{SI} is the SI zero-momentum WIMP-nucleon cross-section, Z (A) is the atomic (mass) number of the target nucleus used, and f_p (f_n) is the WIMP effective coherent coupling to the proton (neutron). We assume the WIMP couples equally to the neutron and the proton ($f_n = f_p$), so that the differential cross-section $\mathrm{d}\sigma_{\mathrm{SI}}/\mathrm{d}E$ is sensitive only to A^2. The nuclear form factor $\mathcal{F}_{\mathrm{SI}}(E)$ characterizes the loss of coherence for nonzero momentum transfer, and is well parametrized by the Helm form factor [339, 340] for all nuclei [341]

$$\mathcal{F}_{\mathrm{SI}}(E) = 3e^{-q^2 s^2/2} \frac{\sin(qr) - qr\cos(qr)}{(qr)^3}, \tag{2.5}$$

where $s = 1$ fm, $r = \sqrt{R^2 - 5s^2}$, $R = 1.2\ A^{1/3}$ fm, and $q = \sqrt{2 M_{\mathcal{N}} E}$.

Spin-dependent interaction

$$\frac{\mathrm{d}\sigma_{\mathrm{SD}}}{\mathrm{d}E} = \frac{4 m_{\mathcal{N}} \sigma_n^{\mathrm{SD}}}{3\mu_n^2\, v^2} \frac{J+1}{J} \left(\langle S_p\rangle + \frac{a_n}{a_p}\langle S_n\rangle\right)^2 \mathcal{F}_{\mathrm{SD}}^2(E)\,, \tag{2.6}$$

where σ_n^{SD} is the SD zero-momentum WIMP-nucleon cross-section, a_p (a_n) are axial WIMP-proton (neutron) couplings, J is the total spin of the nucleus and $\langle S_p\rangle$ ($\langle S_n\rangle$) is the proton (neutron) spin averaged over the nucleus. The nuclear form factor for SD is usually defined as

$$\mathcal{F}_{\mathrm{SD}}^2(E) = \frac{S(E)}{S(0)}\,, \tag{2.7}$$

and

$$S(q) = a_0^2 S_{00}(q) + a_0 a_1 S_{01}(q) + a_1^2 S_{11}(q)\,, \tag{2.8}$$

with $a_0 = a_n + a_p$ ($a_1 = a_p - a_n$) being the isoscalar (isovector) coupling. Furthermore we assume equal coupling to neutron and proton ($a_n = a_p$), hence only the structure factor S_{00} will be relevant for our analysis. This assumption is motivated by the fact that theoretical models of WIMPs typically predict a similar cross-section to proton and neutron [326, 342].

For the xenon-based detector we will consider there are two isotopes that have a nonzero total spin because of the unpaired neutrons: ^{129}Xe, with $J = 1/2$ and abundance 26.44%, and ^{131}Xe, with $J = 3/2$ and abundance 21.18%.

The structure functions $S_{00}(q)$ and $S_{11}(q)$ are related to the transverse electric and longitudinal projections of the axial current. These functions can be computed in a

shell-model for the atomic nucleus, and the spin of the nucleus is computed by means of the wave functions of the unpaired nucleons. Assuming a particular interaction between nucleons, these are placed in energy levels according to the exclusion principle. As many excited levels as possible are included, making this kind of computation difficult. Finally the projected currents are computed by evaluating the matrix elements of the many-nucleon model. Nuclear shell models are more reliable for heavy nuclei, but even in this case there can be significant deviations at zero momentum transfer or at high momentum. To bracket the uncertainties in the case of the xenon nucleus, for both isotopes we consider two parametrizations for the structure functions: the first (NijmegenII hereafter) was computed in 1997 by Ressell and Dean [343], while the second is based on a very recent computation using chiral effective field theory formalism and accounting for two body interactions [344] (from now on CEFT). In the first part of our discussion we assume nuclear structure functions from CEFT formalism, while in Section 2.7.2 we discuss the effect of marginalizing over various realizations of the nuclear structure functions. The structure functions presented in [344] were updated in [345], released soon after our work was published [1], and the updated limits are now used in the LUX SD analysis [251].

The total number of recoils expected, as a function of the DM parameters, in a detector of mass $M_{\rm det}$ in a given observed energy range $[E_{\rm min}, E_{\rm max}]$ over an exposure time T is obtained by integrating Eq. (2.1) over energy

$$S_{\rm Xe}(m_{\rm DM}, \sigma_n^{\rm SI}, \sigma_n^{\rm SD}) = \epsilon\, M_{\rm det}\, T \int_{E_{\rm min}}^{E_{\rm max}} {\rm d}E \frac{{\rm d}R}{{\rm d}E}\,, \tag{2.9}$$

where we have accounted for an energy independent efficiency factor ϵ and a finite energy resolution $\sigma(E)$ for the detector:

$$\frac{{\rm d}R}{{\rm d}E} = \int_0^\infty \frac{{\rm d}R}{{\rm d}E'} \frac{{\rm e}^{\frac{-({\rm E}'-{\rm E})^2}{2\sigma({\rm E}')^2}}}{\sqrt{2\sigma(E')^2\pi}}\, dE'\,. \tag{2.10}$$

For this analysis we will focus on the future XENON1T experiment, the details of which are outlined in Section 2.4.

As noted earlier in Section 1.5, a degeneracy exists between $\rho_{\rm DM,\odot}$ and the DM-nuclei interaction cross-section ${\rm d}\sigma/{\rm d}E$. As we split this latter term into SI and SD pieces (Eq. 2.3, and then reduce each piece into a function based on DM-nucleon interactions $\sigma_n^{\rm SI}$ and $\sigma_n^{\rm SD}$ (Eqs. 2.4 and 2.6), we acquire additional degeneracies, first between $\sigma_n^{\rm SI}$ and $\sigma_n^{\rm SD}$, and then also between the combination of these two and $\rho_{\rm DM,\odot}$.

A further degeneracy will form as $m_{\rm DM}$ increases beyond the mass of nuclei $M_{\mathcal{N}}$. To see this, consider Eq. 2.1 and the places where $m_{\rm DM}$ enters in the case where $m_{\rm DM} \gg M_{\mathcal{N}}$. First, it enters ${\rm d}\sigma/{\rm d}E$ via the $\mu_n = m_{\rm DM} m_n/(m_{\rm DM} + m_n)$ term in

Eqs. 2.4 and 2.6. Naturally $m_{\rm DM} \gg M_{\mathcal{N}}$ implies $m_{\rm DM} \gg m_n$, and so in this case $\mu_n \simeq m_n$. Second, it enters via the $v_{\rm min}$ limit integration limit (Eq. 2.2), again via a reduced mass, $\mu = m_{\rm DM} M_{\mathcal{N}}/(m_{\rm DM} + M_{\mathcal{N}})$. In the case under consideration $\mu \simeq M_{\mathcal{N}}$, and $v_{\rm min}$ becomes

$$v_{\rm min} \simeq \sqrt{\frac{E}{2M_{\mathcal{N}}}}. \tag{2.11}$$

Thus the only remaining input for $m_{\rm DM}$ is in the denominator of the initial fraction in Eq. 2.1, leaving it degenerate with $\rho_{\rm DM,\odot}$, $\sigma_n^{\rm SI}$, and $\sigma_n^{\rm SD}$. This matter will be illustrated and further discussed in Section 2.4.

2.2.2 Muon signal in neutrino telescopes

The method of indirect DM detection with neutrino telescopes we use here involves four processes: capture of WIMPs by the Sun, annihilation of these WIMPs, production of neutrinos following the annihilation event, and finally detection of these neutrinos. The formalism described in this section is encoded in the `DarkSUSY 5.0.6` software package which we use in our analysis [346].

Capture of WIMPs in the Sun occurs when WIMPs elastically scatter off nuclei in the Sun and lose enough energy to reduce their velocity to below the solar escape velocity. Subsequent scattering events reduce the velocity of the captured WIMPs further, until they concentrate and thermalize in the core of the Sun. In Chapter 1 an approximate formula for the capture rate was given (Eq. 1.63). Here we present a more detailed elucidation of this rate. The capture rate is [347]

$$C_c = \frac{\rho_{\rm DM,\odot}}{m_{\rm DM}} \int_0^R {\rm d}r \sum_i \frac{{\rm d}C_i}{{\rm d}V} 4\pi r^2, \tag{2.12}$$

where

$$\frac{{\rm d}C_i}{{\rm d}V} = \int_0^{u_{\rm max}} {\rm d}u \frac{f(u)}{u} w \Omega_{v,i}^-(w) \tag{2.13}$$

is the capture rate per unit shell volume, R is the solar radius and index i runs across nuclear species present in the Sun. The variable w is the velocity of the WIMP at the shell, and $w = \sqrt{u^2 + v^2}$, where u is the velocity at an infinite distance away from the shell (*i.e.* where the influence of the shell's gravitational potential is negligible) and v is the escape velocity at the shell. The integration limit $u_{\rm max}$ is given by

$$u_{\rm max} = \frac{\sqrt{4 m_{\rm DM} m_{\mathcal{N}_i}}}{m_{\rm DM} - m_{\mathcal{N}_i}} v. \tag{2.14}$$

The term $w\Omega_{v,i}^-(w)$ quantifies the probability that a WIMP will scatter to a velocity less than the escape velocity, and is proportional to $\sigma_i n_i$, where n_i is the number

density of nuclei i in the shell and σ_i is the total interaction cross-section between the WIMP and nuclei i. This calculation, the default in `DarkSUSY 5.0.6`, does not include the effects of diffusion and planets as these have been shown to be minimal [348].

The WIMP-nuclei cross-section σ_i can be expressed as [349, 350]

$$\sigma_i = \beta^2 \left[\sigma_n^{\mathrm{SI}} A_i^2 + \sigma_n^{\mathrm{SD}} \frac{4(J_i+1)}{3J_i} \left| \langle S_{\mathrm{p,i}} \rangle + \langle S_{\mathrm{n,i}} \rangle \right|^2 \right], \tag{2.15}$$

where

$$\beta = \frac{m_{\mathcal{N}_i}(m_\chi + m_{\mathrm{p}})}{m_{\mathrm{p}}(m_\chi + m_i)}. \tag{2.16}$$

The Sun is composed overwhelmingly of spin-$\frac{1}{2}$ hydrogen and spin-0 helium, with only small quantities of heavier elements. The increased atomic number of these heavier elements will compensate for their lower abundance via the A_i^2 term and give appreciable contributions to the SI part of σ_i. However no such enhancement occurs for the SD part, with total spin being related to the number of unpaired nucleons. Thus we can consider only a SD contribution from hydrogen nuclei, reducing Eq. (2.15) to

$$\sigma_i = \begin{cases} \sigma_n^{\mathrm{SI}} + \sigma_n^{\mathrm{SD}} & \text{for } i = 1, \\ \beta^2 \sigma_n^{\mathrm{SI}} A_i^2 & \text{for } i \geq 2. \end{cases} \tag{2.17}$$

While SI interactions are taken into account in the capture rate calculation, in practice the SD interaction is dominant. As the SD process occurs directly on protons, the theoretical rate is not affected by nuclear structure functions describing the coherence of the nucleus.

As shown in Eq. (2.12) the capture rate is dependent upon the density of WIMPs. However as WIMP capture is a continuous process it is sensitive not to the local density at the Sun's current position but instead samples the local density along the prior path of the Sun around the galaxy [351]. For this analysis, however, we assume a constant local DM density $\rho_{\mathrm{DM},\odot}^{\mathrm{obs}}$, and we will discuss the uncertainties related to this assumption in Section 2.7.1.

Acting against the accumulation of WIMPs is the process of DM annihilation. We can describe the total population of WIMPs in the Sun $N(t)$ [352] by the equation

$$\frac{\mathrm{d}N(t)}{\mathrm{d}t} = C_c - \Gamma_a(t) \tag{2.18}$$

where $\Gamma_a(t) = \frac{1}{2} C_a N^2(t)$ is the annihilation rate. The parameter C_a is dependent on the distribution of WIMPs in the Sun and $\langle \sigma_a v \rangle$, the zero velocity WIMP annihilation cross-section [349].

Solving Eq. (2.18) gives us an expression for the annihilation rate:

$$\Gamma_a(t) = \frac{C_c}{2} \tanh^2 \left(\frac{t}{\tau} \right) \tag{2.19}$$

where $\tau = 1/\sqrt{C_c C_a}$ is the capture-annihilation equilibrium time scale. In the case of $t \gg \tau$, Eq. (2.19) reduces to $\Gamma_a(t) = \frac{1}{2} C_c$, and equilibrium between capture and annihilation is reached. For this study we assume this *steady state* scenario; it allows us to take a more model independent approach by eliminating the dependence on $\langle \sigma_a v \rangle$.

WIMPs which have accumulated in the Sun can annihilate with each other and produce Standard Model particles. The majority of the decay products of these particles are absorbed almost immediately and without consequence in the core of the Sun. However, certain classes of WIMPs can decay directly into neutrinos, and in other cases the Standard Model decay products can themselves decay into neutrinos, which can escape from the Sun and potentially be detected on Earth. The differential flux of neutrinos of flavour $\ell = (e, \mu, \tau)$ at Earth is given by [353]:

$$\frac{\mathrm{d}\Phi_{\nu_\ell}}{\mathrm{d}E_{\nu_\ell}} = \frac{\Gamma_a}{4\pi D_\oplus^2} \sum_f B^f_{\chi\chi} \frac{\mathrm{d}N^f_{\nu_\ell}}{\mathrm{d}E_{\nu_\ell}}, \tag{2.20}$$

where $D_\oplus$ is the Earth-Sun distance, $B^f_{\chi\chi}$ is the branching ratio of DM self annihilation to a final state f, and $\mathrm{d}N^f_{\nu_\ell}/\mathrm{d}E_{\nu_\ell}$ is the number of neutrinos of flavour ℓ per energy produced from the final state f.

Detection of these neutrinos by neutrino telescopes occurs via the observation of the Čerenkov radiation emitted by the particles produced following the weak force interactions between the neutrinos and the matter in and around the telescope. Of particular interest are muons created by the charged current interactions of muon neutrinos, as their range is such that they create long, relatively detectable tracks compared to other leptons [354]. Optical detection of the Čerenkov radiation in a transparent medium such as water or ice then allows the incoming neutrino's energy and origin to be reconstructed. Taking into account neutrino oscillations the differential flux of muon neutrinos is:

$$\frac{\mathrm{d}\Phi_{\nu_\mu}}{\mathrm{d}E_{\nu_\mu}} = \sum_{\ell=e,\mu,\tau} P_{\nu_\ell \to \nu_\mu}(E_{\nu_\ell}, D_\oplus) \frac{\mathrm{d}\Phi_{\nu_\ell}}{\mathrm{d}E_{\nu_\ell}}, \tag{2.21}$$

where $P_{\nu_\ell \to \nu_\mu}(E_{\nu_\ell}, D_\oplus)$ is the probability of a neutrino of type ℓ and energy E_{ν_ℓ} oscillating to a muon neutrino after travelling a distance $D_\oplus$ to the Earth. The flux of muons in the detector is then [353]

$$\frac{\mathrm{d}\Phi_\mu}{\mathrm{d}E_\mu} = N_A \int_{E_\mu^{\mathrm{th}}}^{\infty} \mathrm{d}E_\nu \int_0^\infty \mathrm{d}\lambda \int_{E_\mu}^{E_\nu} \mathrm{d}E'_\mu P(E_\mu, E'_\mu; \lambda) \frac{\mathrm{d}\sigma_\nu(E_\nu, E'_\mu)}{\mathrm{d}E'_\mu} \frac{\mathrm{d}\Phi_\nu}{\mathrm{d}E_\nu}, \tag{2.22}$$

where to save the reader's eyesight from multiple subscripts we assume $\nu = \nu_\mu$. N_A is Avogadro's number, $E_\mu^{\rm th}$ is the detector threshold energy, λ is the muon range in the detector medium, $P(E_\mu, E'_\mu; \lambda)$ is the probability of a muon of initial energy E'_μ having a final energy E_μ having passed through a length λ of the detector medium, and $\mathrm{d}\sigma_\nu(E_\nu, E'_\mu)/\mathrm{d}E'_\mu$ is the weak interaction cross-section for a parent muon neutrino of energy E_ν producing a muon of energy E'_μ. The final number of signal events S_μ for a counting only experiment between times t_0 and t_1 would then be:

$$S_\mu = \int_{t_0}^{t_1} \mathrm{d}t \int_{E_\mu^{\rm th}}^{\infty} \mathrm{d}E_\mu \, A(E_\mu) \frac{\mathrm{d}\Phi_\mu}{\mathrm{d}E_\mu} \tag{2.23}$$

This rate calculation is incorporated into the `DarkSUSY 5.0.6` software package, which we use for this analysis [346, 353]. For this analysis we will focus on the IceCube neutrino telescope, the details of which are outlined in Section 2.5.

2.3 Statistical framework and benchmark WIMP models

To illustrate the capabilities of reconstruction and complementarity of future direct detection experiments and neutrino telescopes we consider three benchmark models, described in Table 2.1. These WIMP models represent a phenomenological approach in the description of the theoretical parameters $\Theta = \{m_{\rm DM}, \sigma_n^{\rm SI}, \sigma_n^{\rm SD}\}$ we are interested in, and capture the relevant aspects of the analysis:

(i) *Benchmark A* is characterized by a light mass of 60 GeV and its cross-section on nucleons is dominated by the SD component.

(ii) *Benchmark B* has an intermediate DM mass of 100 GeV and sizeable WIMP-nuclei cross-sections for both SI and SD interactions.

(iii) *Benchmark C* is characterized by a heavy mass of 500 GeV and significant SI but negligible SD cross-sections.

These benchmark points are shown in Figures 2.1 and 2.2, along with the limits previously seen in Section 1.5. We have checked that our conclusions are robust and hold for benchmarks with same behaviour of the cross-sections but different masses as well. These benchmark WIMP models are representative of well-motivated neutralino configurations arising in scans of the MSSM25 [232] parameter space, which is a phenomenological parametrization of the minimally supersymmetric Standard Model (MSSM) with 25 free parameters defined at the electroweak scale.

At the time this work was conducted in 2013, all benchmark points were below the

	Benchmark A	Benchmark B	Benchmark C
$m_{\rm DM}$ [GeV]	60	100	500
$\sigma_n^{\rm SI}$ [cm^2]	3.7×10^{-49}	8.8×10^{-46}	1.1×10^{-45}
$\sigma_n^{\rm SD}$ [cm^2]	2.0×10^{-40}	2.0×10^{-40}	9.6×10^{-45}
$S_{\rm Xe}^{\rm SI}(\Theta)$	1.1	252.8	74.4
$S_{\rm Xe}^{\rm SD}(\Theta)$ (CEFT)	422.8	356.1	4.4×10^{-3}
$S_{\rm Xe}^{\rm SD}(\Theta)$ (NijmegenII)	170.9	122.3	1.5×10^{-3}
$S_{\mu}(\Theta)$	24.9 ($\tau^+\tau^-$)	66.0 (W^+W^-)	7.8 ($\nu_\mu\bar{\nu}_\mu$)

Table 2.1: Above are listed the parameters and predicted signals for the three benchmark models used in the analysis. In descending order are: their masses; SI and SD interaction cross sections with nucleons, $\sigma_n^{\rm SI}$ and $\sigma_n^{\rm SD}$; counts predicted in XENON1T for the SI interaction, $S_{\rm Xe}^{\rm SI}(\Theta)$; counts predicted in XENON1T from the SD interactions assuming the CEFT and NijmegenII structure functions (see text for further details); and the expected muon signal in IceCube-86 for the WIMP annihilation signal given in brackets. The prediction for XENON1T signals assumes an effective exposure of $\epsilon_{\rm eff} = 2{\rm ton} \times {\rm year}$, while the predicted signal for IceCube assumes an exposure of five 180 day austral winter observing seasons, for a total of 900 days. The first benchmark is characterized by a light DM mass and large SD contribution, the second has intermediate mass and both sizable SI and SD cross-sections, while the third has a large mass and dominant SI contribution.

limits currently available. However Benchmarks A and B are now just inside the SD-neutron exclusion limits set by LUX [251], as seen in Figure 2.2. Additionally, Benchmark B is just below the LUX SI limits [189], and inside the IC79 exclusion region if one assumes a $\tau^+\tau^-$ annihilation channel instead of the W^+W^- channel we assign it. Nonetheless, the conclusions we draw here remain valid, as they are based on signal rates (Eqs. 2.9 and 2.23) which are proportional to the WIMP-nucleon interaction cross section multiplied by an exposure. Similar outcomes for this analysis could be gained by reducing the interaction cross section of the benchmark point and increasing the exposure to compensate.

For each benchmark model we generate mock data, using the experimental likelihoods $\mathcal{L}(\Theta)$, from the true model, *i.e.* without Poisson scatter [355]. These theoretical signals expected in the detectors, which are the number of recoiling nuclei in XENON1T arising from both SI and SD part and the number of up-going muons N_μ in IceCube, are given in Table 2.1 and will be described in detail in Secs. 2.4 and 2.5, respectively.

For the sampling of the theoretical parameter space we adopt the Bayesian methodol-

Figure 2.1: *(Overleaf)* Comparison of of our Benchmark points A, B, and C, with current and projected direct detection limits on $\sigma_{\mathrm{SI,\,nucleon}}$: XENON100 (purple) [190], XENON1T (projected, purple shaded) [230], LUX (red) [189], CRESST-II (green) [231], and CDMSLite (pink) [233]. Also shown in grey is the 'neutrino floor' generated by coherent scattering of solar and cosmological neutrinos [234].

Figure 2.2: *(Overleaf)* Comparison of of our Benchmark points A, B, and C, with current limits on $\sigma_{\mathrm{SI,\,nucleon}}$ from direct detection experiments and solar capture and annihilation to neutrinos: LUX-neutron (dashed red), LUX-proton (solid red) [251], XENON100 neutron (dashed purple), XENON100 proton (solid purple) [252], PICO60 [246] and PICO-2L [247] (yellow), and IceCube-79 proton [4].

---

ogy. We employ the public code `MultiNest v2.12` [356, 357], which uses an ellipsoidal and multimodal nested-sampling algorithm to estimate the posterior probability over the full parameter space:

$$\mathcal{P}(\Theta|d) \propto \mathcal{L}(\Theta)\pi(\Theta)\,, \tag{2.24}$$

where $\pi(\Theta)$ is the prior probability density function (pdf). The priors for the three theoretical parameters m_{DM}, σ_n^{SI} and σ_n^{SD} are chosen to be flat on a logarithmic scale so as not to favor any particular order of magnitude, and are defined as follows:

$$\begin{aligned}
\log_{10}(m_{\mathrm{DM}}/\mathrm{GeV}) &: 1 \to 3\,,\\
\log_{10}(\sigma_n^{\mathrm{SI}}/\mathrm{cm}^2) &: -60 \to -43\,,\\
\log_{10}(\sigma_n^{\mathrm{SD}}/\mathrm{cm}^2) &: -55 \to -38\,.
\end{aligned}$$

We set $n_{\mathrm{live}} = 25000$, and use an efficiency factor of 10^{-4} and a tolerance factor of 0.01 [356], which ensure that the sampling is accurate enough to have a parameter estimation similar to Markov chain Monte Carlo sampling methods [358]. The resulting chains are analyzed with an adapted version of the package `GetDist`, supplemented with `MATLAB` scripts from the package `SuperBayeS` [359, 360]. Two-dimensional posterior probability distribution functions (pdfs), $\mathcal{P}_{\mathrm{marg}}$, marginalized over the nuisance parameters and the remaining $n-2$ theoretical parameters, are obtained from the chains by dividing the relevant parameter subspace into bins and counting the number of samples per bin. An x% credible interval or region containing x% of the total volume of $\mathcal{P}_{\mathrm{marg}}$ is then constructed by demanding that $\mathcal{P}_{\mathrm{marg}}$ at any point inside the region be larger than at any point outside. The inferred pdfs are sensitive to the choice of the mass prior range, which we have checked by increasing the upper bound of the prior range to 100 TeV: the x% contours suffer from volume effects related to the behavior of the likelihood at very large mass, above 10 TeV, and we will comment upon this more in Section 2.6. We however argue that these effects are not relevant

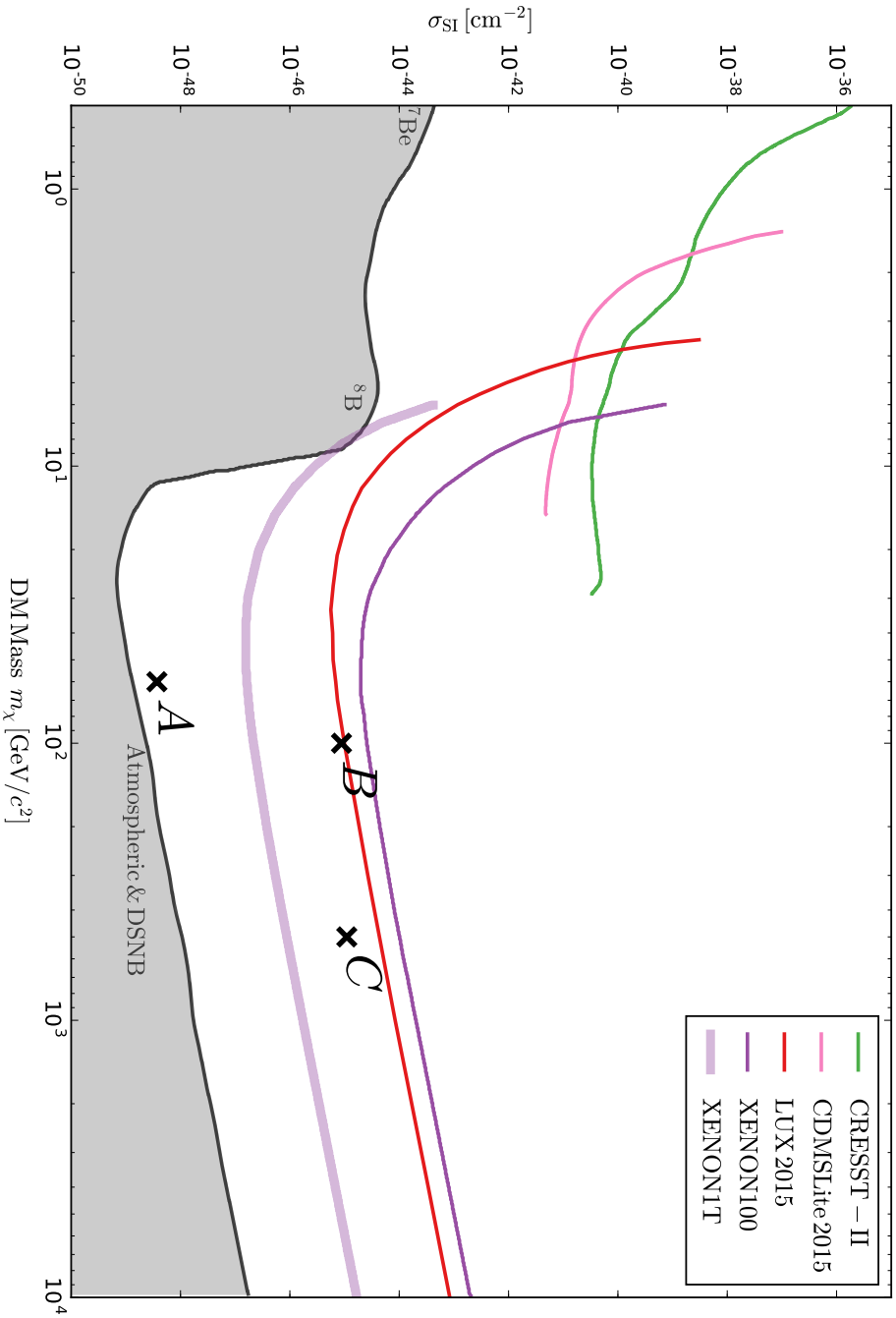
$\sigma_{\mathrm{SI}}\,[\mathrm{cm}^{-2}]$
10^{-36}
10^{-38}
10^{-40}
10^{-42}
10^{-44}
10^{-46}
10^{-48}
10^{-50}
10^{0}
10^{1}
10^{2}
10^{3}
10^{4}
DMMass $m_\chi\,[\mathrm{GeV}/c^2]$
CRESST – II
CDMSLite 2015
LUX 2015
XENON100
XENON1T
^{7}Be
^{8}B
Atmospheric & DSNB
A
B
C

Figure 2.1

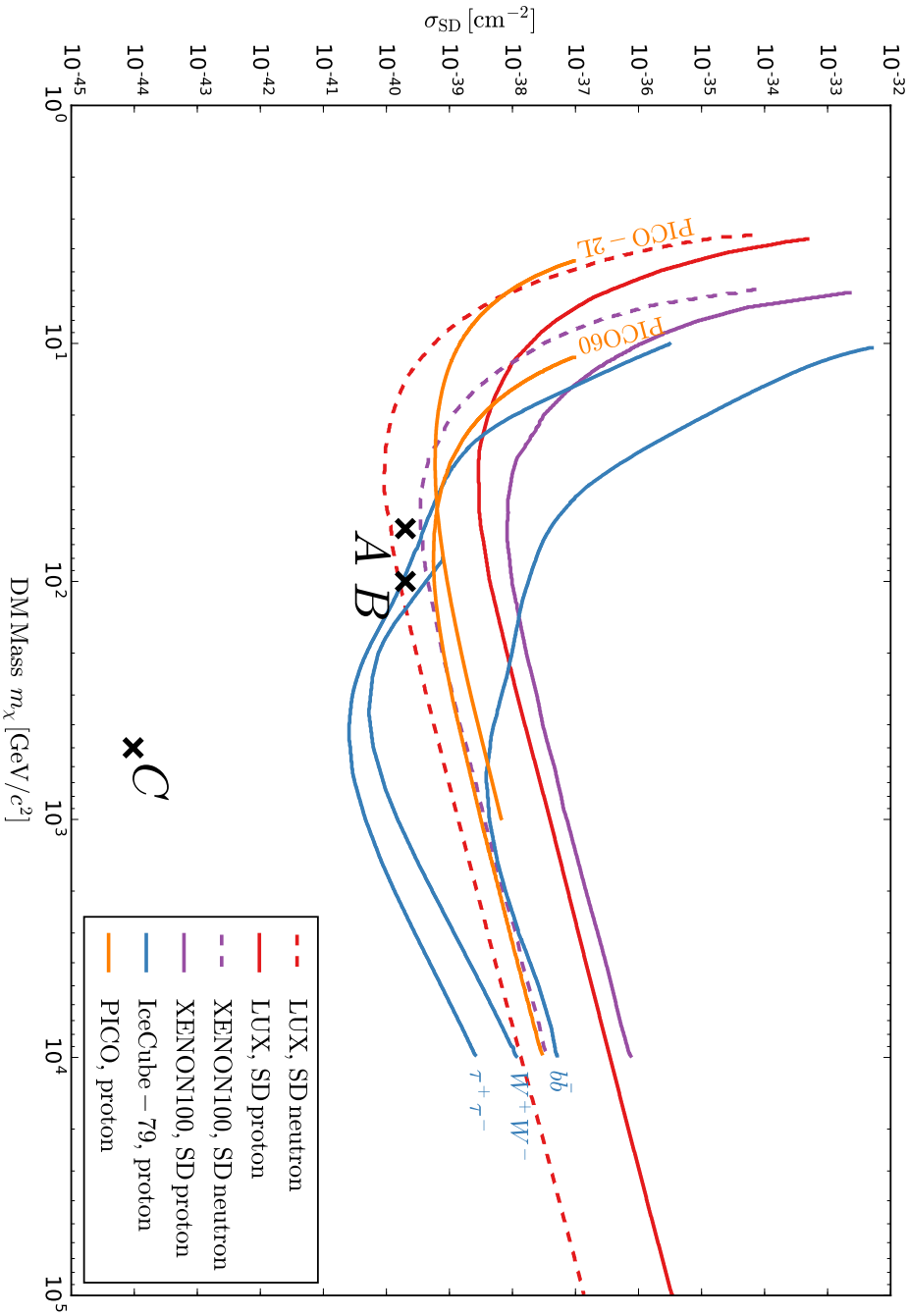
$\sigma_{\mathrm{SD}}\,[\mathrm{cm}^{-2}]$
DM Mass $m_\chi\,[\mathrm{GeV}/c^2]$
LUX, SD neutron
LUX, SD proton
XENON100, SD neutron
XENON100, SD proton
IceCube − 79, proton
PICO, proton
PICO − 2L
PICO60
$b\bar{b}$
W^+W^-
$\tau^+\tau^-$
A
B
C

Figure 2.2

for our analysis, since for these high masses the DM most likely does not meet the WIMP requirements anymore. Hence the mass prior range used here is driven by the standard mass range for WIMPs.

The astrophysical parameters describing the DM halo and the DM in the solar neighbourhood are regarded as nuisance parameters. These parameters are the local standard of rest velocity v_0, the DM escape velocity in the halo $v_{\rm esc}$, and $\rho_{\rm DM,\odot}$. We do not include the effects of a co-rotating dark disc, but later in Section 2.7.1 we discuss the effects of a triaxial halo on DM capture in the Sun. Here we use the following central values and uncertainties for the astrophysical parameters, as used in previously in [361, 362, 208]:

$$\begin{aligned} v_0^{\rm obs} &= 230 \pm 24.4 \text{ km s}^{-1}\,, \\ v_{\rm esc}^{\rm obs} &= 544 \pm 39 \text{ km s}^{-1}\,, \\ \rho_{\rm DM,\odot}^{\rm obs} &= 0.4 \pm 0.2 \text{ GeV cm}^{-3} = (10.5 \pm 5.27) \times 10^{-3}\,{\rm M}_\odot\,{\rm pc}^{-3}. \end{aligned}$$

These ranges are broadly in line with the current state of the art. Since publication of the work presented in this Chapter the RAVE collaboration have revised their measurement of the escape velocity downwards to $v_{\rm esc} = 533^{+54}_{-41}$ km s^{-1} [202]. In the first part of our analysis we keep these nuisance parameters fixed to their observed value, while in Section 2.7.1 we present the final results marginalizing over them. The uncertainty over the nuclear structure function for SD interactions is also treated as a nuisance parameter in Section 2.7.2.

2.4 Reconstruction with XENON1T

XENON1T is the ton scale continuation of the XENON100 detector, and has been constructed underground at the Laboratori Nazionali del Gran Sasso in Italy. It is currently in the commissioning phase, with data taking planned to start sometime in 2016.

We consider the energy window for DM searches to be from 10 to 45 keV, divided into 7 bins. In this range, the XENON1T likelihood function is given by the product of independent Poisson likelihoods describing the probability of observing the predicted events for a given WIMP signal over the energy bins labeled by the index i:

$$\ln \mathcal{L}_{\rm XENON1T}(\Theta) = \sum_{i=1}^{7} \ln P\left(N_i^{\rm obs} | S_i(\Theta) + \theta_{{\rm BG},i}\right)\,. \tag{2.25}$$

$N_i^{\rm obs}$ is the observed number of events in each bin and $\theta_{{\rm BG},i}$ is the total background in each bin, described below. The detector energy resolution is $\sigma(E) = 0.6\,{\rm keV}\sqrt{E/{\rm keV}}$.

The effective exposure $\epsilon_{\rm eff} = 2\,\text{ton} \times \text{year}$ comes from $\epsilon \times \eta_{\rm cut} \times A_{\rm NR} = 5 \times 0.8 \times 0.5$, where ϵ is the total exposure, $\eta_{\rm cut}$ is the cut efficiency, and $A_{\rm NR}$ is the nuclear recoil acceptance. As XENON1T is expected to be almost background free [335], we consider a background of 4×10^{-8} counts/kev/day/kg, which accounts for a total of $\theta_{{\rm BG},i} = 0.02$ events per bin after integrating over the exposure time. With this assumption we can safely consider it to be an energy independent background.

The expected number of recoiling nuclei for our benchmark models are shown in Table 2.1. Benchmark A has a negligible SI cross-section of about 10^{-49}cm^2, which is well below the expected sensitivity of XENON1T of $\sim 10^{-47}\text{cm}^2$: the theoretical predictions are compatible with the background in this case. All the signal comes from the SD contribution, which can range from 200 to 400 events, depending on the nuclear structure function adopted for describing the xenon nuclei. In this case $\sigma_n^{\rm SD} = 2.0 \times 10^{-40}\text{cm}^2$ is close to the upper bound of XENON100 for SD interaction on neutron [252] and in the sensitivity range of XENON1T for SD which is expected to be around 10^{-41}cm^2 [363]. Since the publication of this work [1] the SD-neutron limit from LUX has just passed Benchmark A, thus excluding this point (see Section 2.3).

Benchmark B is similar to A as far as it concerns the SD contribution, with a number of events ranging from 100 to 350 depending on the structure function model. As with Benchmark A it has been ruled out by recent LUX SD-neutron results, but is also ruled out by IC79 results if an alternative $\tau^+\tau^-$ annihilation channel is assumed [364]. In contrast to Benchmark A however, B has a large contribution of 252 events from the SI interaction, which has a cross-section of $\sigma_n^{SI} = 8.8 \times 10^{-46}\text{cm}^2$, just below the exclusion bound of XENON100 [365] and LUX SI results [189].

The last model, Benchmark C, has a negligible contribution from the SD interaction, accounting for zero events, while the SI interaction predicts about 70 events. This point is within reach of XENON1T SI limits, but escapes SD limits by several orders of magnitude.

Figure 2.3 shows the reconstruction of our benchmark models with XENON1T only, with the Galactic parameters fixed at their observed values and with the CEFT nuclear structure function in use. Hence no nuisance parameters are included in this part of our analysis. The left panels show the 2D marginal posterior pdf in the $\{m_{\rm DM}, \sigma_n^{\rm SI}\}$-subspace, the central panels show the 2D marginal posterior pdf in the $\{m_{\rm DM}, \sigma_n^{\rm SD}\}$-subspace, while the rightmost panels show the 2D marginal posterior pdf in the $\{\sigma_n^{\rm SI}, \sigma_n^{\rm SD}\}$-subspace, for Benchmarks A, B and C in the first, second and third rows respectively.

If we allowed the DM particle to have only one interaction, SI or SD, contributing to the observed events, we would expect the reconstruction of the WIMP-nucleon

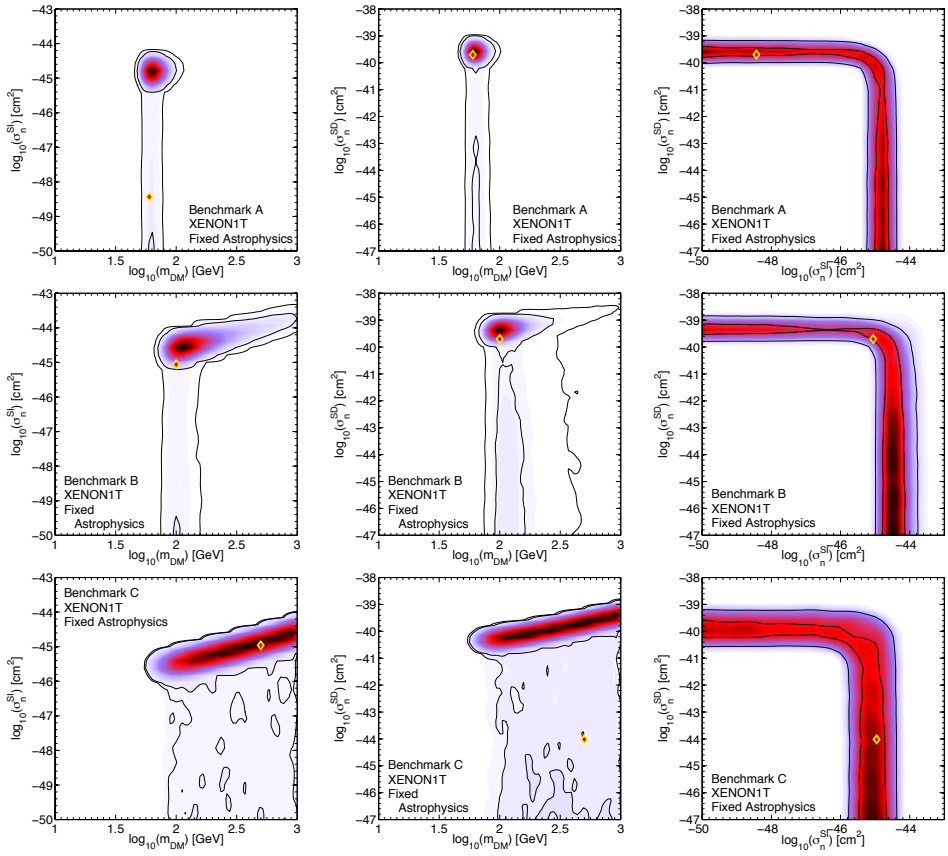

Figure 2.3: The reconstruction with XENON1T of the A (top), B (middle) and C (bottom) benchmark models with fixed astrophysics. No nuclear uncertainties are taken into account. The left, central and right plot shows the 2D marginal posterior pdf in the $\{m_{\rm DM}, \sigma_n^{\rm SI}\}$-plane, $\{m_{\rm DM}, \sigma_n^{\rm SD}\}$-plane and $\{\sigma_n^{\rm SI}, \sigma_n^{\rm SD}\}$-plane respectively. The contours denote the 68% and 95% credible regions and the diamond point shows the parameter values of the benchmark models.

cross-section to be effective, namely to select only a closed region in the parameter space. However, as soon as both cross-sections are allowed to vary the marginal posterior pdf exhibits a tail towards very small values, since each parameter can compensate for the other to achieve the observed number of events. In other words, as the signal in XENON1T receives contributions from both SI and SD interactions a degeneracy can occur [323, 326]. This is apparent from all plots, where the 95% credible region does not exhibit a closed contour. The effect is more pronounced for the SD interaction, while in the case of SI scattering the 68% credible region is denoted by a closed contour around the Benchmark A point, or always bounded from below in the B and C cases. This is due to the fact that XENON1T is more sensitive to SI interactions than SD interactions. In addition a low signal for one interaction will cause the corresponding true value to be poorly reconstructed: for example, for A the SI interaction is very small and close to zero observed events, hence the signal in XENON1T at 68% confidence level (CL) is attributed to the largest cross-section that accounts for such events, and the true value is contained only in the 95% CL. This effect is mirrored for Benchmark C, where again the true value for the SD interaction is only contained in the 95% credible region, which are as well upper bound for that interaction.

In the reconstruction of the DM mass parameter, we encounter the usual limitation of direct detection: after the WIMP mass matches and then exceeds the target nuclei mass, the mass reconstruction becomes progressively worse, as the slope of the differential cross-section becomes essentially insensitive to WIMP mass for $m_{\rm DM} \gg m_{\mathcal{N}}$. The degeneracy in the mass reconstruction can be seen as we move to the higher mass B and C points, as denoted in the left and central panel of Fig. 2.3 by the tail extending towards large masses. The only exception is Benchmark A, whose posterior pdf does not exhibit this mass degeneracy and appears to be a closed contour around the benchmark model point at both 68% and 95% CLs. A viable solution to ameliorate the DM mass reconstruction is to combine different target materials, typically with different atomic number, as described in [217, 326]. However heavy WIMPs still exhibit a tail in the posterior pdf extending towards high mass values. We will show in Section 2.6 that it is possible to break this degeneracy by complementing the signal seen in XENON1T with the signal of IceCube, or even with the nondetection of a signal.

It is worth commenting on the features appearing in the marginal posterior pdf contours at the 95% CL, in particular affecting Benchmark C of Fig. 2.3. These features are not physical, but are an indication that the posterior pdf is flat, which makes it a challenge to sample effectively. This also occurs with IceCube alone or when the likelihood is poorly constrained by the data.

2.5 Reconstruction with IceCube

The IceCube neutrino telescope consists of 5160 digital optical modules (DOMs) arranged vertically along 86 strings embedded in a cubic kilometre of extremely transparent natural ice below the South Pole [366]. Included in IceCube is the DeepCore subarray, which consists of six strings arranged at the centre of IceCube with closer horizontal spacing and instrumented with DOMs of higher sensitivity and closer vertical spacing along the string. DeepCore has been designed to reduce the energy threshold of IceCube from 100 GeV down to 10 GeV [367].

The WIMP annihilations can produce a wide variety of final states, whose subsequent decays can produce high energy neutrinos, with the branching ratios to each state dependent on the properties of the DM particle and the underlying theory that generates it. In our phenomenological approach we consider three annihilation final states with branching ratio equal to one, as labeled in Table 2.1. For Benchmark A we consider the $\tau^+\tau^-$ final state, which gives a harder neutrino signal than the $b\bar{b}$ channel. Benchmark B annihilates into W^+W^-, which is the dominant channel for a common fermionic WIMP with a mass above the W threshold. Finally we consider the $\nu_\mu\bar{\nu}_\mu$ channel for Benchmark C. The annihilation directly into neutrinos is heavily suppressed for Majorana particles (*e.g.* neutralinos) [368] but can occur for vector WIMPs, such as the Kaluza-Klein photon [369, 324].

For each benchmark model and its annihilation channel we first calculate the theoretical signal rate using the default routines in `DarkSUSY 5.0.6` [346, 353] (which employ the methods outlined in Section 2.2.2) with a slight modification to enforce the *steady state* scenario. The MSSM25 models we build upon for our benchmark WIMP models (see Table 2.1) have equilibration times of the order of $1 - 4 \times 10^8$ years, *e.g.* an order of magnitude smaller than the age of the Sun, making our assumption of a *steady state* scenario a valid one. We use an exposure time of five 180 day austral winter observing seasons (*e.g.* 900 days), and an angular cut around the solar position of $\phi_{\rm cut} = 3^\circ$. The predicted muon signals $S_\mu(\Theta)$ for each benchmark model and annihilation channel are given in Table 2.1. From the background files included in the `DarkSUSY 5.0.6` release we extracted the number of background events within the 3° angular cut. For a 180 day season the number of background events was 41, yielding 205 background events for our 900 day exposure time. With this background estimation we have an estimate of the number of events needed for a detection within 5 seasons of data taking in IceCube, which is approximately 50 events, depending on the annihilation channel. This is compatible with the analysis released by the IceCube collaboration [264] prior to the publication of [1]: by analyzing the data from one winter season with up-going muons plus one summer season with down-going muons, taken using 79 strings (including the six DeepCore strings),

the strongest exclusion bounds are for a WIMP mass of 250 GeV annihilating into gauge bosons and with a spin dependent cross-section on proton of about $10^{-40}\mathrm{cm}^2$ producing ~ 15 events per season.

The use of DeepCore allows the limit to be extended down to a mass of 20 GeV but the sensitivity rapidly diminishes, and at this mass only a SD cross-section of approximately $10^{-38}\mathrm{cm}^2$ can be excluded. For a WIMP with a mass of 50 GeV the current exclusion bound is close to $10^{-40}\mathrm{cm}^2$, comparable with the bound obtained with XENON100. For our benchmark models the expected number of events range from ~ 66 muons for Benchmark B to 7.8 muons produced by the $\nu_\mu\bar{\nu}_\mu$ final state for C. Benchmark A annihilating to the $\tau^+\tau^-$ final state is intermediate with 22 expected muons. Comparing these to Table I of [264] we can see that all our benchmarks have signal rates compatible with the exclusion limits at the time this work was published in [1].

The likelihood function we use for the IceCube experiment, Eq. (2.26), is presented in [370] and included in `DarkSUSY 5.0.6`. The likelihood of observing N_{tot} events given a background rate of θ_{BG} and a theoretical model Θ, which has a true expected signal $S_{\mathrm{true}}(\Theta) = \alpha S_\mu(\Theta)$ events, is

$$\mathcal{L}_{\mathrm{IC86}}(\Theta) \equiv \mathcal{L}\left(N_{\mathrm{tot}}|\theta_{\mathrm{BG}}, S_\mu\right) \tag{2.26}$$

$$\equiv \frac{1}{\sqrt{2\pi}\sigma_\alpha}\int_0^\infty \frac{\left(\theta_{\mathrm{BG}} + \alpha S_\mu(\Theta)\right)^{N_{\mathrm{tot}}} e^{-(\theta_{\mathrm{BG}}+\alpha S_\mu(\Theta))}}{N_{\mathrm{tot}}!}\exp\left[-\frac{1}{2}\left(\frac{\ln\alpha}{\sigma_\alpha}\right)^2\right]\mathrm{d}\alpha. \tag{2.27}$$

The variable α quantifies potential systematic errors between the true expected signal $S_{\mathrm{true}}(\Theta)$ and the nominally predicted signal $S_\mu(\Theta)$. The relative fractional error on $S_\mu(\Theta)$ is then $\alpha - 1$, and this is then marginalized over in a semi-Bayesian way, assuming a log-normal probability distribution and with standard deviation σ_α. This likelihood takes into account only the total number of signal events. A likelihood function taking into account the energy of the signal muons is also presented in [370] and encoded into `DarkSUSY 5.0.6`, but this requires an accurate description of the energy response function of IceCube, which is not publicly available for the 86 string configuration. We recently presented further improvements of this likelihood in [4], which took into account a non-negligible opening angle between the paths of the incoming neutrino and outgoing muon. The opening angle is larger for lower energy neutrinos, and so this likelihood reduces the neutrino energy threshold for this DM detection technique from 50 GeV to 10 GeV. The likelihood function of [4] produced limits up to an order of magnitude better than those produced with a simple counts-based likelihood, as we use for this analysis.

There are several experimental aspects of IceCube that are salient to our discussions. First, the effective area of IceCube, which quantifies the sensitivity of the detector,

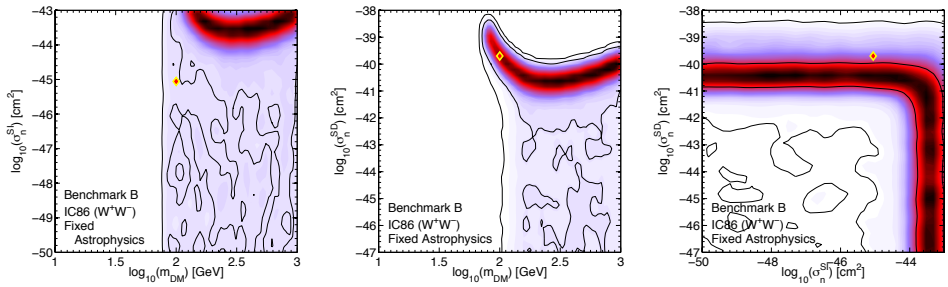

Figure 2.4: Reconstruction using IceCube (denoted IC86), with fixed astrophysics, for benchmark model B with annihilation channel W^+W^-. The left, central and right plot shows the 2D marginal posterior pdf in the $\{m_{\rm DM}, \sigma_n^{\rm SI}\}$-plane, $\{m_{\rm DM}, \sigma_n^{\rm SD}\}$-plane and $\{\sigma_n^{\rm SI}, \sigma_n^{\rm SD}\}$-plane respectively. The contours denote the 68% and 95% credible regions and the diamond point shows the parameter values of the benchmark model.

increases with energy [371]. Thus higher mass WIMPs will tend to produce stronger signals as they will, in general, produce higher energy neutrinos and thus higher energy muons. Second, as neutrino energy increases the mean angular error for the reconstructed muon track decreases [371]. If the calculation of the signal in IceCube is made using an angular cut ($\phi_{\rm cut}$) around the solar position, lower mass WIMPs will produce lower signals as the muons they produce can potentially have greater angular deviation from the solar position and so fewer will survive the angular cut. Conversely the higher energy muons will be more densely clustered around the solar position, and so more will pass the angular cut, increasing signal for the higher mass WIMPs. The energy dependent error on the reconstructed muon track would also impact the improved likelihood from Ref. [4], feeding into a greater uncertainty on the arrival angle of the incoming neutrino.

Given these limitations in the number likelihood of IceCube, there exists a degeneracy between WIMP mass and WIMP-nuclei cross-section $\sigma_{\rm tot} = \sigma_n^{\rm SI} + \sigma_n^{\rm SD}$. Consider two scenarios, one with a WIMP of high mass and low cross-section $\sigma_{\rm tot}$, and another with a WIMP of low mass but high $\sigma_{\rm tot}$. The first scenario will have a low capture rate, as this is dependent on $\sigma_{\rm tot}$ and inversely dependent on WIMP mass, Eq. (2.12). Assuming capture-annihilation equilibrium, this scenario will feature a lower muon flux, but the muons will be of a higher energy and so hence produce higher signal due to the features of IceCube outlined above. The muons of the second scenario will be of lower energy, but they will have a higher flux as their capture rate is higher. This can compensate the lower muon energy and generate a high signal. As the energy spectrum, which could be used to determine the DM mass, is not defined in the number likelihood, these two scenarios cannot be distinguished from each other. As with direct detection signals, there is a degeneracy between $\sigma_n^{\rm SI}$ and

$\sigma_n^{\rm SD}$. The solar capture rate, given in Eq. (2.12), receives contributions from both SI and SD interactions, however the sensitivity of IceCube to the two type of interactions is different, as shown in [264]: the SI is poorly constrained and the actual exclusion limits are one or two orders of magnitude less constraining than the XENON100 ones, while for the SD cross-section the exclusion limits are competitive with XENON100 at high masses.

Figure 2.4 shows the reconstruction of benchmark model B with IceCube only, and exemplifies the discussion above. In the left panel, which shows the 2D marginal posterior pdf in the $\{m_{\rm DM}, \sigma_n^{\rm SI}\}$-plane, the signal clearly exhibits an almost independent behaviour with respect to SI interaction. On the contrary, the SD cross-section as a function of the DM mass is both lower and upper bounded at 68% CL (middle panel). The mass degeneracy is a result of the missing spectral information. The degeneracy between $\sigma_n^{\rm SD}$ and $\sigma_n^{\rm SI}$ is similar to the case of direct detection, as shown in the right panel and in Fig. 2.3. As far as it concerns Benchmarks A and C, the muon signal produced by WIMP annihilations in the Sun cannot be disentangled from the background, leading to a flat and featureless marginalized posterior pdf and underlining that there is not detection in IceCube. Once again, the features in the pdfs have no physical meaning and are merely artefacts of a flat likelihood.

2.6 Combined XENON1T and IceCube analysis

Figure 2.5 shows how the future detection/constraint from IceCube complements a detection in XENON1T, for fixed astrophysical parameters. The top row of Fig. 2.5 illustrates the combined reconstruction of Benchmark A. Even though this benchmark would produce only 12 events in IceCube, hence too small a signal to claim a detection, it still has the ability to improve the reconstruction. Comparing to the top row of Fig. 2.3 the 68% and 95% CLs have shrunk. The reconstruction of $\sigma_n^{\rm SI}$ and $\sigma_n^{\rm SD}$ exhibits the same trend as the case of XENON1T only, except that now the 68% CL for SD cross-section in the right panel is upper bounded, because of the IceCube upper bound. The mass determination remains unchanged, demonstrating the good reconstruction capability of XENON1T and the reduced sensitivity of IceCube.

Benchmark model B (second row of Fig. 2.5) fully exploits the properties of complementarity between DM search strategies and is the principal illustration of the main point of our analysis, as it can be detected by both experiments. Comparing with Figs. 2.3 and 2.4 we can see that the combination of the two experiments allows for the SD cross-section (middle panel) to be well determined at the 68% CL. The mass degeneracy is also significantly reduced and it is well determined at the 68% CL. The contours for the SI cross-section as a function of $m_{\rm DM}$ have been contracted sensibly

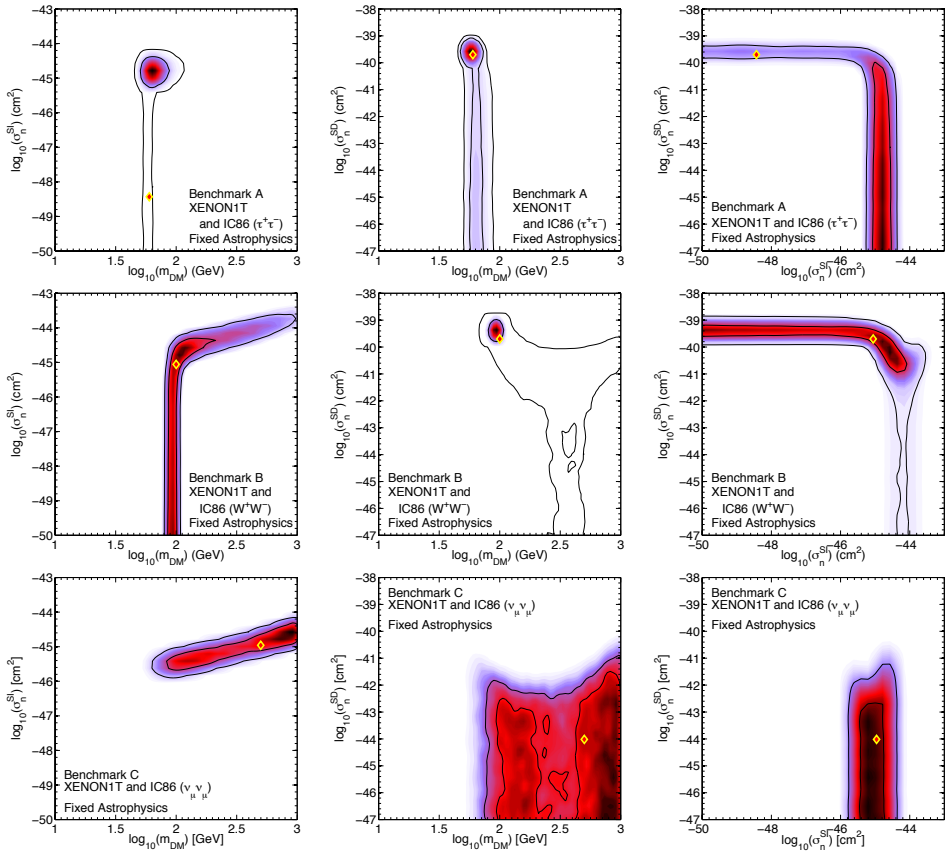

Figure 2.5: Reconstruction using XENON1T combined with IceCube (denoted IC86), with fixed astrophysics, for benchmark models A, B and C with annihilation channels $\tau^+\tau^-$ (top), W^+W^- (centre) and $\nu_\mu\bar{\nu}_\mu$ (bottom). The left, central and right plot shows the 2D marginal posterior pdf in the $\{m_{\rm DM}, \sigma_n^{\rm SI}\}$-plane, $\{m_{\rm DM}, \sigma_n^{\rm SD}\}$-plane and $\{\sigma_n^{\rm SI}, \sigma_n^{\rm SD}\}$-plane respectively. The contours denote the 68% and 95% credible regions and the diamond point shows the parameter values of the benchmark model.

with respect to the separate experiments, but at 68% CL the SI cross-section is only upper bounded, as can be seen as well from the third panel: the SD cross-section is determined within one order of magnitude at most and contains the true value, while the SI cross-section cannot be larger than 10^{-44}cm^2. Therefore if a WIMP is detected by both experiments, meaning that it has sizeable cross-sections, the SD cross-section and the mass can be well reconstructed, while a precise reconstruction of SI interaction would require the use of a further experiment; in this case a direct detection experiment with different target material would be the optimal choice [326].

Benchmark C is illustrated in the last row of Fig. 2.5 and shows remarkably the constraining power of IceCube, even with only 8 events from high energy neutrinos. The most dramatic improvement is in the determination of σ_n^{SI}: where previously the 68% and 95% CLs extended from the upper bound all the way down to the bottom of our prior range, they are now bounded from below as well. As expected, only an upper limit can be set on σ_n^{SD}: the 95% CL is clearly bounded from above at values of $\sigma_n^{\text{SD}} \approx 10^{-42}\text{cm}^2$. The effect of the SD upper bound is much more striking than for Benchmark A, signalling the fact the IceCube is more likely to be sensitive to high WIMP masses. Note that in this analysis we assumed, in absence of published information on the energy response function of the 86-string configuration, that nothing can be said on the energy of the neutrinos measured by IceCube. It is known that the energy resolution of IceCube is poor; for a muon of energy $10^4 - 10^8$ GeV in the core of the detector there is an uncertainty of a factor of two [372]. Nonetheless, including the spectral information on observed events would certainly improve the mass determination, one of the main weaknesses of the reconstruction procedure from XENON1T data only, and substantially reduce the degeneracy in the DM particle parameter space. As the mass cannot be well reconstructed by either XENON1T alone or by adding the upper bound of IceCube, this last benchmark model is affected by the prior range choice on the DM mass: this will be visible in all two-dimensional projections of the dark matter parameter space as an increase of confidence levels, hence volume effect.

2.7 Role of uncertainties in the reconstruction of WIMP parameters

In this section we first assess the effect in the combined reconstruction of benchmark models when DM Galactic parameters vary within their uncertainties (see Section 2.3) and discuss the effective DM density probed by the capture rate (see Section 2.2.2). We then account as well for our lack of knowledge on the true form of the nuclear structure function (see Section 2.2.1). At the end of this section, we return to the

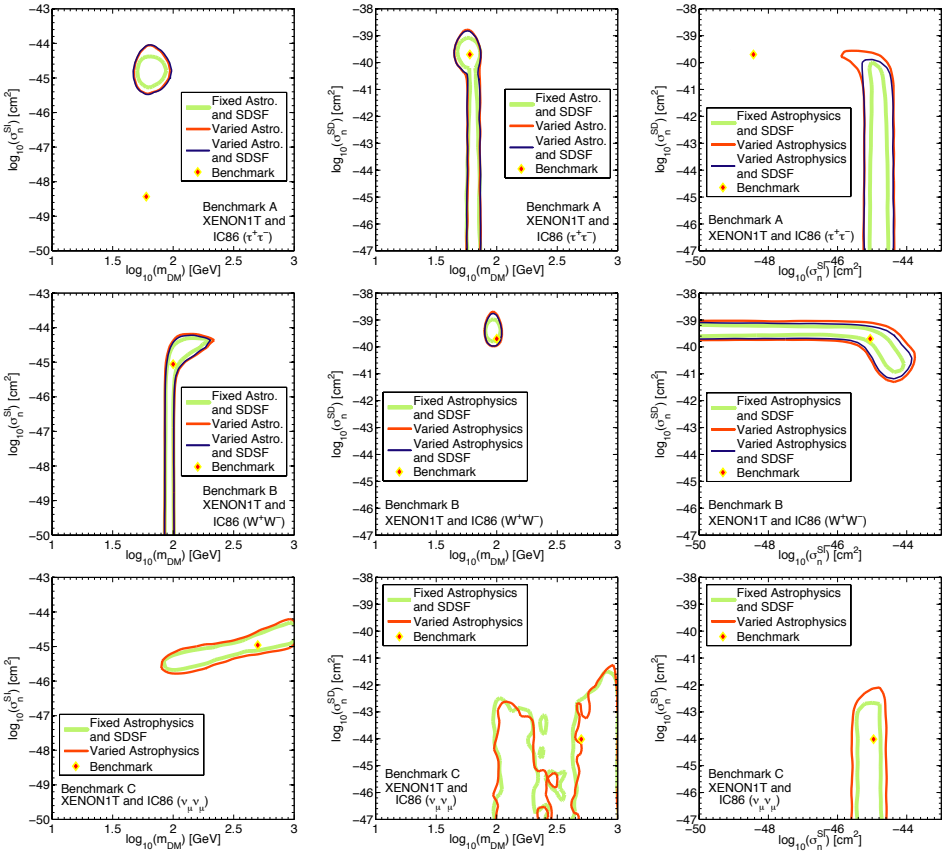

Figure 2.6: Reconstruction using XENON1T combined with IceCube (denoted IC86) for benchmark models A with annihilation channel $\tau^+\tau^-$ (top), B with annihilation channel W^+W^- (middle), and C with annihilation channel $\nu_\mu\bar{\nu}_\mu$ (bottom). The left, central and right plot shows the 2D marginal posterior pdf in the $\{m_{DM}, \sigma_n^{\rm SI}\}$-plane, $\{m_{\rm DM}, \sigma_n^{\rm SD}\}$-plane and $\{\sigma_n^{\rm SI}, \sigma_n^{\rm SD}\}$-plane respectively. The contours denote the 68% credible region as labeled: the green line (light thick solid) stands for fixed astrophysics and fixed SD structure function (SDSF), the red curve (darker solid) denotes marginalized astrophysics, while the dark blue outer line indicates that all nuisance parameters have been marginalized over. The diamond point shows the parameter values of the benchmark model.

additional uncertainties induced by the shape and parametrization of the velocity distribution.

2.7.1 Astrophysical uncertainties

A reconstruction of benchmark models fixing the astrophysical parameters to their observed value could hold for very well measured parameters, however, as mentioned in Section 2.3, these are known only up to various degrees of precision. We therefore introduce these uncertainties into our analysis, treating the Galactic parameters as nuisances $\psi_{\rm astro}$ and marginalizing over them. The astrophysical likelihood governing these parameters follows a Gaussian distribution centered on the observed value. The total likelihood is then

$$\mathcal{L} = \mathcal{L}(\psi_{\rm astro}) \times \mathcal{L}_{\rm XENON1T}(\Theta, \psi_{\rm astro}) \times \mathcal{L}_{\rm IC86}(\Theta, \psi_{\rm astro})\,. \tag{2.28}$$

The results of our analysis are illustrated in Fig. 2.6, which shows the 68% CL for marginalized astrophysics denoted by the medium thickness red line, for A (top), B (center) and C (bottom). The primary effect of marginalizing over the astrophysical parameters is to broaden the contour regions, which can be clearly seen by comparing the red contours to their fixed astrophysics counterparts given by the thick light green line.

As noted previously in Sections 1.5 and 1.6, departures from a spherically symmetric halo will introduce an additional uncertainty into the comparison of IceCube and XENON1T rates. The direct detection rate depends on $\rho_{\rm DM,\odot}$ at present time at the Sun's position, while the solar capture rate depends on the long term history of the Sun, which completes an orbit around the Galactic centre in $\sim 2 \times 10^8$ years. If we drop the assumption that the DM Galactic halo is isotropic and smooth, throughout its journey the Sun will cross over-dense or under-dense regions with respect to an averaged density ($\langle \rho_{\rm DM,\odot} \rangle$), to which the capture rate is sensitive. This difference has been evaluated for a triaxial DM halo arising from N-body simulations [373]. In case of simulation with baryons the difference is of the order of 30%, while it can reach a factor of 3 for pure DM simulations. The MSSM25 models which serve as the starting points for our benchmark models have small annihilation cross-section, close or below the thermal one, hence the equilibration time scales τ (see Section 2.2.2) ranges from 9×10^7 year for Benchmark B, up to $2 - 3 \times 10^9$ year for points A and C. These values imply that the capture process is fully sensitive to this averaged DM density (case B as well, since it spanned half of the solar period). Even if we do not know the initial position of the Sun we could assume the extreme scenario such that the local DM density is different from the average density and corresponds to an over-dense or under-dense region. In this case we would get a 30% or even a factor of

3 bias in the theoretical predictions. In other words the signal in one detector could be potentially boosted or suppressed by the same factor with respect to the signal in the other detector, as both rates scale linearly with the local DM density, affecting the complementarity in either a positive or negative way.

2.7.2 Nuclear uncertainties

The structure functions presented in Section 2.2.1 are important quantities to be computed. Regarding the xenon nuclei we are interested in, the variation of $S_{00}(q)$ leads to a different prediction of the events in the detector and hence, for example, to a huge uncertainty in the exclusion bound [252]. Considering our benchmark points, the difference in the counts for the two structure function is illustrated in Table 2.1. The NijmegenII structure function predicts fewer events in the detector with respect to the CEFT structure function: the variation is sizeable for A and B, where the events are affected by a factor of 3 of uncertainty while it is completely negligible for case C. The reconstruction in XENON1T of a benchmark model is therefore affected by the assumption of the structure function: if the reconstruction of $\sigma_n^{\rm SD}$ parameter is done assuming a different form factor with respect that used for the mock data a systematic offset is generated. If the reconstruction is done assuming CEFT and the mock data are generated with NijmegenII, this leads to an underestimation of the SD cross-section to account for the largest number of observed events; vice versa the SD cross-section will be overestimated.

To account for the nuclear uncertainties in our Bayesian framework we follow [323], which proposes a formula with three free parameters

$$S_{00}^{j}(u) = N_j \left((1-\beta_j)e^{-\alpha_j u} + \beta_j\right) , \tag{2.29}$$

where $j = 129$ or 131, depending on the xenon isotope, N_j is a overall normalization factor, α_j drives the slope in the low momentum regime, while β_j controls the height of a possible tail at large momentum. The variation of all parameters encompasses the whole region contained between the CEFT and NijmegenII parametrizations but it is not meant to be a proper fit of the nuclear structure functions. We take flat priors for all these additional nuisance parameters $\psi_{\rm nucl}$, over their allowed ranges, which are:

$$\begin{gathered} N_{129} = 0.045 \to 0.070 \ \text{ and } \ N_{131} = 0.025 \to 0.052\,, \\ \alpha_{129} = 3.8 \to 4.0 \ \text{ and } \ \alpha_{131} = 3.8. \to 4.0\,, \\ \beta_{129} = 0.013 \to 0.029 \ \text{ and } \ \beta_{131} = 0.10 \to 0.12\,. \end{gathered}$$

We therefore generate for each benchmark model new mock data based on the mean value of these parameters and, as before, we assess the impact on the reconstruction

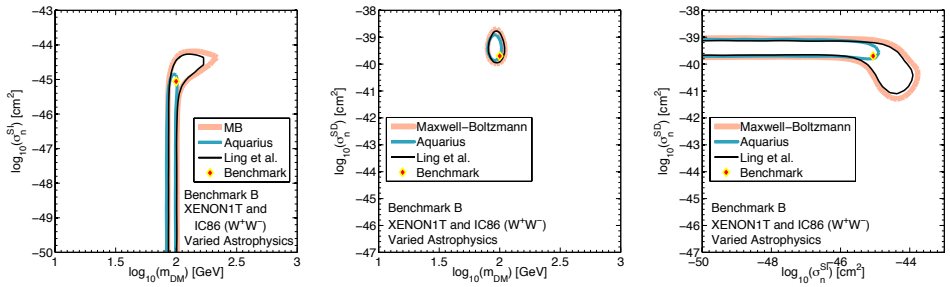

Figure 2.7: Bias due to parametrization of DM velocity distribution for Benchmark B with varied astrophysics. Each contour denotes the 68% CL for the benchmark point generated with an N-body simulation or with the MB distribution, as labeled, and reconstructed assuming a standard halo model.

of the benchmark points by letting them vary within their prior range, in combination with the astrophysical uncertainties. The new likelihood is given by

$$\mathcal{L} = \mathcal{L}(\psi_{\rm Tot}) \times \mathcal{L}_{\rm XENON1T}(\Theta, \psi_{\rm Tot}) \times \mathcal{L}_{\rm IC86}(\Theta, \psi_{\rm astro})\,, \tag{2.30}$$

where $\psi_{\rm Tot}$ accounts for both astrophysical and nuclear uncertainties. Notice that the latter do not affect the reconstruction in IceCube: in solar capture the dominant contribution for SD arises from the hydrogen atom, which does not need a coherence factor for describing its single proton. Thus IceCube potentially has the capability of resolving the nuclear uncertainties when combined with XENON1T.

In Fig. 2.6 the results for the 2D posterior pdf marginalized over all nuisance parameters are denoted by the dark blue solid line at 68% CL. This contour is not shown for Benchmark C as the nuclear uncertainties are not considered because of the negligible $\sigma_n^{\rm SD}$ cross-section. The main result is that the nuclear uncertainties are smaller or at most comparable with the astrophysical ones. This can be explained by the fact that we are considering the $S_{00}(q)$ nuclear structure function, which is known to be the better determined nuclear structure function, hence minimizing the role of nuclear uncertainties. Our findings are compatible with the analysis illustrated in [323, 326].

2.7.3 Effect of the shape of the velocity distribution

The shape of the DM velocity distribution affects the direct detection and IceCube signal rates in different ways. The nuclear recoil threshold for DM detection in XENON1T is in the range of 10 keV, which implies that only particles with the largest velocities have sufficient energy to produce a detectable nuclear recoil above the threshold, as given by the $v_{\rm min}$ definition in Eq. (2.2). For a 100 GeV WIMP, as

we have for Benchmark B, the typical $v_{\rm min}$ to produce a nuclear recoil is of the order of $v_{\rm min} \sim 300\,{\rm km\ s^{-1}}$. This means that it is crucial to accurately describe the high velocity tail of the DM velocity distribution in the Galactic halo. On the other hand, as explained in Section 2.2.2, the solar capture rate is sensitive to the low velocity tail of the DM velocity distribution, with the maximum velocity of a WIMP that can be captured being given by Eq. (2.14). For a 100 GeV WIMP the maximum velocity is of the order of $u_{\rm max} \sim 200\,{\rm km\ s^{-1}}$. Thus it is important to describe the low tail of the velocity distribution as well. This is another physical quantity, besides the DM density in our galaxy, biasing the direct detection and indirect detection rate in different ways.

Several N-body simulations of Milky Way-like galaxies suggest that the velocity distribution deviates from the standard MB halo. To deal with the discrepancy in the high velocity tail for direct detection experiments Ref. [374] has proposed a velocity distribution modelled as a function of one parameter k and based on the these simulations.

To assess if the shape of the velocity distribution is relevant for our analysis, we follow a different approach, which allows us to consider the effect of both tails of the velocity distribution. We consider the Aquarius N-body simulation [197] with only DM, and the simulation by Ling *et al.* [199], based on the RAMSES code, which includes baryons as well.

First, in order to quantify the degree of discrepancy, we fit the mean of the N-body simulation Aquarius with a MB distribution, keeping the escape velocity fixed to $565\,{\rm km\ s^{-1}}$ as given by the simulation but letting v_0 vary: the best fit point underestimates both tails of the velocity distribution. For Benchmark B the difference in the number of events is of the order of 17% in XENON1T and of 15% in IceCube. By allowing a similar procedure with $v_{\rm esc} = 520\,{\rm km\ s^{-1}}$ in the case of Ling *et al.* the velocity distribution is much closer to the MB shape, and the discrepancy in the number of predicted events is only of 4%.

Subsequently, the mean of these numerical velocity distributions is used to generate new mock data for our benchmarks in the case of XENON1T and rescaled for IceCube. These new benchmark models are then reconstructed assuming as usual a MB velocity distribution. We applied the procedure for Benchmark B, which is the point that takes full advantage of the combination of XENON1T and IceCube.

Figure 2.7 shows that our analysis is robust against variation of the shape of the velocity distribution, when both experiments are combined. From left to right the 2D marginalized posterior pdf for Benchmark B is shown, in the $\{m_{\rm DM}, \sigma_n^{\rm SI}\}$-plane, $\{m_{\rm DM}, \sigma_n^{\rm SD}\}$-plane and $\{\sigma_n^{\rm SI}, \sigma_n^{\rm SD}\}$-plane. The middle thickness blue curve is the 68% CL for a reconstruction of the DM physical parameters assuming that the true velocity

distribution is given by the Aquarius simulation: the discrepancy with the MB curve (thick light orange) is very limited and affects mostly the SI cross-section with a more stringent upper bound, closer to the true value. The discrepancy with the Ling *et al.* distribution is very small, as the 68% contour level (thin black line) follows closely the MB contour. In other words the shape of the DM velocity distribution will likely have a limited impact in the reconstruction of WIMP physical parameters, in case of a positive detection.

2.8 Conclusions

In the coming years experiments such as XENON1T, XENONnT, IceCube, and KM3NeT will probe ever larger regions of the $(m_{\rm DM}, \sigma_n^{\rm SD}, \sigma_n^{\rm SI})$ parameter space, potentially discovering a signal of WIMP DM. But even with such signals at hand, reconstructing the properties of the WIMP will be challenging due to degeneracies in the parameter space. In this chapter we have shown that combining data from direct detection and indirect detection via annihilation to neutrinos following solar capture can be used to break these degeneracies and give a better determination of the WIMP properties. Such complementarity exists between other direct and indirect experiments, and a full understanding of the nature of DM will also require the input of LHC searches, as discussed *e.g.* in [328, 375].

Specifically in this chapter we have discussed the reconstruction capabilities for the $m_{\rm DM}$, $\sigma_n^{\rm SD}$, and $\sigma_n^{\rm SI}$ parameters with a combination of data from XENON1T and IceCube. We have focused our attention on the degeneracy between the reconstruction of the SD and SI contributions, and we have shown the degeneracy between these two contributions arising from the analysis of the two experiments separately can be lifted from combining the two data sets.

To illustrate and quantify the degree of complementarity, we have focused on three benchmark models: Benchmark A, characterized by a light DM mass and large SD contribution; Benchmark B has intermediate mass and both sizable SI and SD cross-sections, and Benchmark C, with a large mass and dominant SI contribution.

The combined analysis for Benchmark A allows us to illustrate the fact that even in cases where the parameters are such that no signal can be observed with IceCube, taking this fact into account in the global likelihood does improve the reconstruction of the DM parameters, as can be seen from the top row of Fig. 2.3. The reconstruction of $\sigma_n^{\rm SI}$ and $\sigma_n^{\rm SD}$ in this case exhibits the same trend as the case of XENON1T only, except that now the 68% CL for SD cross-section in the right panel is upper bounded, because of the IceCube upper bound. The mass determination remains unchanged, demonstrating the good reconstruction capability of XENON1T and the

reduced sensitivity of IceCube.

Benchmark model B (second row of Fig. 2.5) fully exploits the properties of complementarity between DM search strategies and is the principal illustration of the main point of our analysis, as it can be detected by both experiments. Comparing with Figs. 2.3 and 2.4 we can see that the combination of the two experiments allows for the SD cross-section (middle panel) to be well determined at the 68% CL. The mass degeneracy is also significantly reduced and it is well determined at the 68% CL. The contours for the SI cross-section as a function of $m_{\rm DM}$ have been contracted sensibly with respect to the separate experiments, but at 68% CL the SI scattering cross-section is only upper bounded, as can be seen as well from the third panel: the SD is determined within one order of magnitude at most and contains the true value, while the SI cannot be larger than 10^{-44}cm^2. Therefore if a WIMP is detected by both experiments, meaning that it has sizeable cross-sections, the SD cross-section and the mass can be well reconstructed, while a precise reconstruction of SI interaction would require the use of a further experiment; in this case a direct detection experiment with different target material would be the optimal choice [326].

Benchmark C, finally, shows remarkably the constraining power of IceCube, even with only 8 expected events from high energy neutrinos. The most dramatic improvement is in the determination of $\sigma_n^{\rm SI}$: where previously the 68% and 95% CLs extended from the upper bound all the way down to the bottom of our prior range, they are now bounded from below as well. As expected, only an upper limit can be set on $\sigma_n^{\rm SD}$: the 95% CL is clearly bounded from above at values of $\sigma_n^{\rm SD} \approx 10^{-42}\text{cm}^2$. The effect of the SD upper bound is much more striking than for Benchmark A, signalling the fact the IceCube is more likely to be sensitive to high WIMP masses. In the absence of a publicly available energy response function for the 86-string configuration of IceCube our analysis could not utilize the energy information of the neutrinos observed by IceCube, limiting its mass determination capability. Including this spectral information would certainly improve the mass determination, one of the main limitations of the XENON1T-only reconstruction, and thus substantially reduce the degeneracy in the DM particle parameter space.

The inclusion of uncertainties on astrophysical parameters and nuclear structure functions only slightly affects the quality of the reconstruction of the 68% CLs, the degradation being worst in the case of less constrained scenarios, such as Benchmark C, while B appears to be fairly robust against variation of astrophysics and nuclear physics parameters. In other words the combination of XENON1T and IceCube in the case of a positive signal could also be a way of constraining the DM velocity distribution in the Galactic halo, once all the subtle effect of the astrophysical parameters entering into the capture and direct detection rates are consistently taken into account.

In the event of a WIMP detection in one or more experiment, reconstructing the properties of the particle will be of paramount importance. Degeneracies in the DM parameter space will make this a daunting task, yet as we have shown here, combining direct detection and indirect detection via neutrinos from the Sun, will further this endeavour.

***

3 Indirect Dark Matter Detection with CTA

3.1 Introduction

Having discussed the search for WIMPs passing through the Sun and Earth with direct detection and indirect detection via solar capture, we now turn our attention outwards to search for gamma-rays produced by WIMP DM annihilating throughout the MW. As discussed earlier in Section 1.7, the GC and dSphs are the best places to look for this signal due to their high concentration of DM compared to the wider Universe. Note that throughout this chapter we use DM and WIMP interchangeably.

Recent data from the Large Area Telescope (LAT) aboard the *Fermi* satellite set stringent and robust limits on the annihilation cross-section of WIMPs as a function of the DM particle mass, based on a lack of excess gamma-ray emission from dSphs [376]. As discussed earlier in Section 1.7, *Fermi* data have also shown excess emission of gamma-rays above predicted backgrounds towards the GC, though it is currently unclear whether this is a signal of DM annihilation or of an as-yet-unaccounted for background. Furthermore, the Imaging Air Cherenkov Telescopes (IACTs) HESS, VERITAS and MAGIC are searching for DM signals in dwarf spheroidal galaxies and the GC [377, 378, 379], with the current strongest limits on TeV-scale DM coming from HESS observations of the GC [123], as seen in earlier in Fig. 1.4.

One of the next major steps in high-energy gamma-ray astrophysics will be the construction of the Cherenkov Telescope Array (CTA), which is currently in the pre-construction phase and expected to start operations in 2019[1]. Several estimates of

[1] https://portal.cta-observatory.org/Pages/Preparatory-Phase.aspx

the sensitivity of CTA to gamma-rays from DM annihilation exist in the literature. All of these agree on the fact that CTA will improve existing constraints for values of the DM particle mass above $\mathcal{O}(100)$ GeV, but substantial differences exist, up to one order of magnitude or more in annihilation cross-section for a given mass, depending on the assumptions made about the telescope array configuration, analysis setup and observation time [380, 381, 382].

In this chapter we carry out a new estimation of the sensitivity of CTA to DM annihilation, and compare this to the sensitivity of *Fermi*. We improve on previous analyses in a number of ways. First, we present a detailed discussion of all backgrounds, including cosmic-ray protons and electrons, and also the effects of the diffuse astrophysical emission, which when this work was published as [2] was the first time this had been done in the context of CTA and DM. We estimate this from *Fermi*-LAT data, suitably extrapolated above 500 GeV in order to cover the range of energies relevant for CTA. Second, we study the impact of systematic errors. There are many sources of systematic uncertainty inherent in CTA measurements: event reconstruction, Monte Carlo determination of the effective area, and uncertainty in atmospheric conditions [383]. A detailed assessment can only realistically be performed by the CTA Collaboration itself after the instrument is built; here we instead present a simple but comprehensive statistical framework with which the impacts of these systematics on the sensitivity of CTA to DM annihilation can be illustrated and evaluated. Third, we show that performing the analysis over a series of suitably optimised regions of interest (RoIs) partially compensates for the degradation in sensitivity due to systematics and backgrounds. We carry out a multi-RoI 'morphological' analysis of the gamma-ray emission, and demonstrate how it improves the CTA sensitivity to DM compared to the so-called 'Ring' method previously discussed in the literature [380].

The chapter is organised as follows: in Section 3.2 we describe the CTA and *Fermi*-LAT experiments; in Section 3.3 we review the basics of indirect detection with gamma-rays; in Section 3.4 we discuss and quantify the cosmic-ray and diffuse gamma-ray background for CTA; in Section 3.5 we present our analysis strategy, in particular the implementation of systematic errors and the RoIs relevant for our analysis; we present our results in Section 3.6 and conclusions in Section 3.7.

3.2 The CTA and *Fermi*-LAT experiments

3.2.1 The CTA and other imaging air Cherenkov telescopes

Gamma-rays in the GeV to TeV regime initiate electromagnetic cascades in the atmosphere, which start at an altitude of 10–20 km and generate a focused cone of Cherenkov light that typically covers several hundred meters on the ground. Air Cherenkov telescopes detect gamma-rays by observing this dim Cherenkov light with optical telescopes. The overall light yield, the shape and the orientation of the air shower gives information about the energy and arrival direction of the gamma ray. Because observations can only be performed during (nearly) moonless nights, the observation time per year is limited to approximately 1000 hours.

Current active Imaging Air Cherenkov Telescopes (IACTs) are HESS II (Namibia; [318]), VERITAS (Arizona; [319]), and MAGIC (La Palma[2]). Although all three instruments have an active program to search for DM signals in various regions of the sky (see *e.g.* Refs. [384, 378, 379]), only HESS can observe the GC high above the horizon ($\theta_z \sim 6°$, compared to $\theta_z \gtrsim 57°$ for VERITAS and MAGIC). As a shorter transmission length through the atmosphere allows for a lower threshold energy, HESS is ideally situated to search for DM signals from the GC. Non-detection of a DM signal by HESS provides the strongest current limits on the DM self-annihilation cross-section for DM masses around the TeV scale [123], as seen in Fig. 1.4.

CTA will consist of several tens of telescopes of at least 3 different types, with sizes between about 5 and 24 meters, covering an area of several square kilometres. The sensitivity will be a factor ten better than current instruments, the field of view (FoV) will be up to 10° in diameter, and the energy threshold $\mathcal{O}(10\,\mathrm{GeV})$.

CTA is envisaged as a two-part observatory, with southern and northern sites. CTA South is the most relevant for DM searches towards the GC. The European Southern Observatory (ESO) Paranal location in Chile has been selected to host the southern site and La Palma, Spain, has been selected for the northern site [320]. Negotiations regarding the sites are ongoing, with the first telescopes being placed onsite in 2017 at the earliest.

At the time this work was first published [2] the final design had not yet been fixed. Apart from construction and maintenance questions, relevant remaining design choices were the relative emphasis on higher or lower energies, the angular and energy resolution, and the FoV. A first detailed Monte Carlo (MC) analysis was presented in Ref. [385], where 11 different configurations for the southern array were discussed.

[2] `http://magic.mpp.mpg.de/`

Depending on the array configuration and gamma-ray energy, the point source sensitivity varies within a factor of five[3], and can be further improved by about a factor of two with alternative analysis methods [385].

In this work we will concentrate on the proposed configuration known as 'Array I' [385],[4] which is a balanced configuration with three large (∼24 m aperture), 18 medium (∼12 m) and 56 small telescopes (∼4–7 m). This configuration provides a good compromise in sensitivity between low and high energies. One advantage of using Array I is that extensive information on the effective area, angular resolution, energy resolution and background rates is available. Furthermore, a very similar array has been used in previous DM sensitivity studies: Array E in Ref. [380], and the Paris-MVA version of Array I in Ref. [382]. The point-source sensitivities of Arrays E and I agree very well at energies $\lesssim 1$ TeV, whereas at higher energies Array I is more sensitive (but only by a factor of less than two).

For convenience, here we summarise some of the main performance aspects of Array I: it features an effective area of about $100\,\mathrm{m}^2$ at its threshold energy of 20 GeV, which then increases quickly with energy to about $4 \times 10^5\,\mathrm{m}^2$ at 1 TeV and $3 \times 10^6\,\mathrm{m}^2$ at 10 TeV. The angular resolution in terms of the 68% containment radius is about $r_{68} \simeq 0.3^\circ$ at threshold, and drops to below 0.06° at energies above 1 TeV. The energy resolution is relatively large at threshold, with $\sigma(E)/E \simeq 50\%$, but drops to below 10% at energies above 1 TeV.

As we will discuss below in more detail, the large effective area, irreducible background of cosmic-ray (CR) electrons, and the fact that electrons look identical to photons for an IACT, mean that the number of events passing analysis cuts will be extremely high, especially at low energies and for analyses of diffuse and extended sources. Statistical errors will therefore be small, making systematic uncertainties in the event identification particularly important. In fact, in the case of searches for DM particles with GeV to TeV masses, these systematics will turn out to be one of the limiting factors. Detailed instrumental uncertainties (*e.g.* the covariance matrix of reconstruction efficiencies in different regions of the FoV) will probably only become available once the instrument starts to operate, so in this work we resort to a few

[3]This is based on the adoption of a standard Hillas-based analysis. This is a classical analysis method, based on zeroth (amplitude), first (position) and second (width and orientation) momenta of the images [386].

[4]In particular, we adopt the version based on the Hillas-parameter analysis of the MPIK group. The choice of analysis method can impact the projected sensitivity; *e.g.* the Paris-MVA method produces an effective area that is at energies around 1 TeV about ~ 7 times that of the MPIK method [385], making Paris-MVA derived limits up to ~ 2.6 stronger than those using MPIK. However, this only holds for background limited observations. Observations of the diffuse emission are actually systematics limited in most of the parameter range of interest, which makes differences in the effective area much less relevant. For this reason, we concentrate here on the better documented MPIK method.

well-motivated benchmark scenarios.

The traditional observing strategy employed by IACTs in searching for DM annihilation (*e.g.* Ref. [123]) involves defining two regions on the sky expected to have approximately the same regular astrophysical emission, but different amounts of DM annihilation. The region with the larger expected annihilation is dubbed the 'ON' region, the other is called the 'OFF' region, and the analysis is performed using a test statistic defined as the difference in photon counts from the two regions. This is referred to as an 'ON-OFF' analysis, and obviously obtains the most power when the ON and OFF RoIs are chosen to differ as much as possible in their predicted annihilation rates.

The RoIs chosen for ON-OFF analyses may lie in the same or very different FoVs. Different FoVs allow a greater contrast in DM signal between ON and OFF regions, but have the potential to introduce differential systematics across the two FoVs. The 'Ring method' [380] is an ON-OFF analysis technique optimised for DM searches towards the GC with IACTs, which fits the ON and OFF regions into a single FoV, producing an approximately constant acceptance across the entire analysis region. Although both regions are expected to contain DM and background contributions, in the Ring method the ON and OFF regions are typically referred to as the 'signal' and 'background' regions. For simplicity, here we just call them ON and OFF.

A simple way to model the results of an ON-OFF analysis is to construct a Skellam likelihood [387, 388, 382], which is based on the expected difference between two Poisson counts (*i.e.* in the ON and OFF regions). However, once the assumption that astrophysical backgrounds are identical in the ON and OFF regions becomes questionable, a more straightforward method is simply to carry out a regular binned likelihood analysis. In this case, one predicts the photon counts in each RoI using detailed background and signal models, and compares them directly to the absolute number of photons observed in each RoI. This is the strategy that we investigate here for CTA, using both the original Ring method RoIs and a finer spatial binning. We show these two sets of RoIs in Fig. 3.1, and discuss their optimisation in Section 3.5. We still refer to the two-RoI analysis as the 'Ring method' even though we carry out a full likelihood analysis rather than an ON-OFF analysis. We refer to the multi-RoI analysis as a 'morphological analysis', as it uses the expected spatial distribution of the DM signal to improve limits.

3.2.2 The *Fermi* Large Area Telescope

The LAT aboard the *Fermi* satellite is a pair-conversion detector, with a large FoV and an energy range from 30 MeV to above 300 GeV. Since its launch in 2008 the

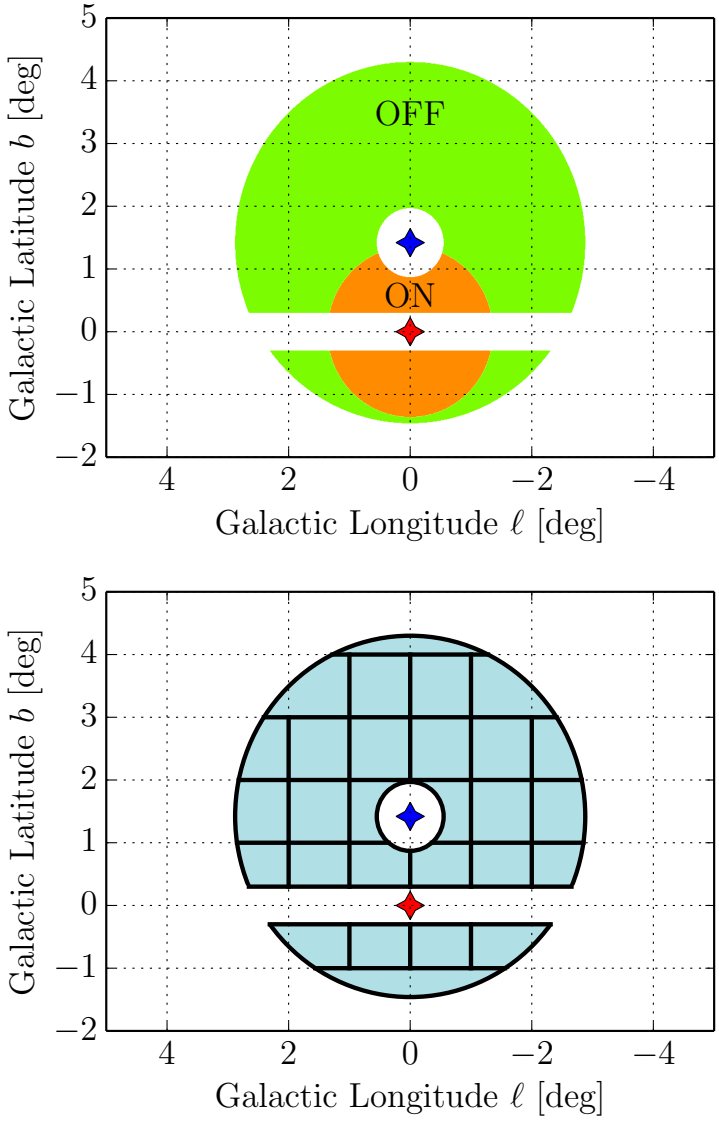

Figure 3.1: The different RoIs that we consider in this paper. The red star indicates the GC, while the blue star indicates the centre of the FoV. *Top:* RoIs used in the Ring method of Ref. [380] as 'signal' and 'background' regions; we refer to these as simply 'ON' and 'OFF' regions, respectively. A diagram detailing the construction of the annulus and the ON-OFF RoIs is given in Ref. [380], and the exact dimensions we use are given in Section 3.5.1. *Bottom:* Separation of the ON and OFF RoIs into 28 sub-RoIs, which we use in our morphological analysis.

dominant observation strategy has been a full-sky survey providing roughly equal exposure in all directions of the sky. The *Fermi*-LAT is a formidable tool in the search for signals of DM annihilation. It currently provides the strongest constraints on the DM self-annihilation cross-section, based on a combined observation of 15 dwarf spheroidal galaxies using 6 years of data [376].

The *Fermi*-LAT provides an accurate measurement of the Galactic diffuse emission (GDE) up to energies of about 100 GeV. Above 100 GeV the number of detected photons becomes very small, due to the LAT's comparatively small effective area ($\sim$ 8000 cm^2). This is about the energy where the acceptance of IACTs starts to become sizeable. Close to the Galactic disc and the GC, LAT measurements are actually dominated by GDE. This diffuse emission will be a critical foreground for any DM search, and—depending on the details of the search strategy—might mimic a DM signal.

Compared to IACTs, the LAT is an extremely clean gamma-ray telescope. Its plastic scintillator anti-coincidence detector, together with cuts on different event reconstruction quality estimators, allows proton and electron contamination in the gamma-ray sample to be suppressed to a level well below the very dim extragalactic gamma-ray background. The main uncertainties in the measured fluxes, especially at the high energies we are interested in, are hence of a statistical nature. The systematic uncertainty of the effective area is at the level of 10% [389], so we will neglect it throughout.

3.3 The dark matter signal

Assuming that the annihilation cross-section of DM does not depend on the relative velocity between particles, the calculation of the gamma-ray flux from DM annihilation can be divided into two parts.

The first part accounts for the DM distribution, and is commonly known as the 'J-factor', which we first encountered in Section 1.7. This is an integral of the DM density squared along the lines of sight (l.o.s.) within a cone $\Delta\Omega$ that covers a certain RoI:

$$J\left(\Delta\Omega\right) = \int_{\Delta\Omega} \mathrm{d}\Omega \int_{\mathrm{l.o.s}} \mathrm{d}l\, \rho_{\mathrm{DM}}(r)^2. \tag{3.1}$$

The DM density profiles seen in N-body simulations of Milky-Way type galaxies are best fit by the Einasto profile [390], also seen earlier in Section 1.7:

$$\rho_{\mathrm{DM}}(r) \propto \exp\left(-\frac{2}{\alpha}\left[\left(\frac{r}{r_s}\right)^{\alpha} - 1\right]\right), \tag{3.2}$$

which we assume for our calculation of the J-factors for the GC. We normalise to a local DM density of $\rho_{\rm DM}(r_\odot) = 0.4\,{\rm GeV\,cm^{-3}} = 10.54 \times 10^{-3} {\rm M_\odot\,pc^{-3}}$, choosing $\alpha = 0.17$, $r_s = 20\,{\rm kpc}$, and $r_\odot = 8.5\,{\rm kpc}$ [391].

We will also use a slightly contracted generalised NFW profile, to indicate how limits would improve with a more optimistic DM distribution. We parameterise this profile as

$$\rho_{\rm DM}(r) \propto \frac{1}{r^\gamma (r_s + r)^{3-\gamma}} \,, \tag{3.3}$$

where $\gamma = 1.3$ is the inner slope of the profile that we will adopt below, inspired by profiles fitted to the *Fermi* GeV excess (see Section 1.7). Also we take $r_s = 20\,{\rm kpc}$ as the scale radius, and the profile is normalised in the same way as the Einasto profile (Eq. 3.2).

The second part of the flux calculation covers the actual particle model for DM. Together with the J-factor, it yields the differential flux of DM signal photons,

$$\frac{{\rm d}\Phi}{{\rm d}E} = \frac{\langle \sigma v \rangle}{8\pi\, m_{\rm DM}^2} \frac{{\rm d}N_\gamma}{{\rm d}E}\, J\,(\Delta\Omega)\,. \tag{3.4}$$

Here $\langle \sigma v \rangle$ is the velocity-averaged DM self-annihilation cross-section, in the limit of zero relative velocity. The DM mass is given by $m_{\rm DM}$, and ${\rm d}N_\gamma/{\rm d}E$ is the annihilation spectrum, *i.e.* the average number of photons produced per annihilation per energy interval, which depends on the particular annihilation channel. For the gamma-ray yields, we will take the results from Ref. [392].

To calculate the expected number of signal events $\mu^{\rm DM}$ in a given observing time $T_{\rm obs}$, between energies E_0 and E_1, we weight Eq. (3.4) by the energy-dependent effective area $A_{\rm eff}$ and integrate over the energy range in question,

$$\mu^{\rm DM} = T_{\rm obs} \int_{E_0}^{E_1} {\rm d}E\, \frac{{\rm d}\Phi}{{\rm d}E} A_{\rm eff}(E). \tag{3.5}$$

Note that for simplicity, throughout this paper we neglect the effects of the finite angular and energy resolution of CTA, as well as variations of the effective area within the FoV. As discussed above, the 68% containment radius of the point spread function (PSF) is around $\theta_{68\%} \simeq 0.3^\circ$ at the lowest energies that we consider, and significantly better at high energies. This is significantly smaller than the RoIs that we adopt (*cf.* Fig. 3.1). The energy resolution at 20 GeV is however quite large ($\sigma(E)/E \simeq 50\%$), and should be taken into account when interpreting the differential sensitivities that we quote below (Section 3.6). We checked that smearing a $b\bar{b}$ spectrum with a log-normal distribution with a width of $\sigma(\ln E)/\ln E = 50\%$ increases the peak signal flux relative to an assumed E^{-2} background by a factor of about 1.5; for $\sigma(\ln E)/\ln E = 20\%$ this drops to a factor of 1.1. This is mostly due to event migration

from smaller to higher energies. Neglecting the finite energy resolution of CTA will hence affect our projected limits at most by a few tens of percent.[5]

3.4 Backgrounds

The dominant backgrounds for DM searches at the GC are the GDE and, in case of IACTs, the flux of cosmic rays that pass the photon cuts. Here we discuss the characteristics of these components, and describe how they enter our analysis.

3.4.1 Cosmic-ray background

CR electrons constitute an essentially irreducible background for gamma-ray observations with IACTs, because the electromagnetic cascades that they induce are practically indistinguishable from those caused by gamma-rays. A possible way to discriminate between the two is to use the detection of Cherenkov light from the primary particle as a veto. This is however beyond the reach of current and next-generation instruments [383]. Due to their relatively soft spectrum, CR electrons are especially relevant at low energies, were they are responsible for most of the measured flux of particles that are either gamma-rays or electrons. We parameterise the electron flux per unit energy and solid angle as

$$\frac{\mathrm{d}^2\phi}{\mathrm{d}E\mathrm{d}\Omega} = 1.17 \times 10^{-11} \left(\frac{E}{\mathrm{TeV}}\right)^{-\Gamma} (\mathrm{GeV\,cm^2\,s\,sr})^{-1} \,, \tag{3.6}$$

with $\Gamma = 3.0$ for $E < 1\,\mathrm{TeV}$, and $\Gamma = 3.9$ for $E > 1\,\mathrm{TeV}$ [393, 394].

Interactions between CR protons and the Earth's atmosphere initiate hadronic air showers, which are generally very different from electromagnetic showers. The initial hadronic interaction produces a large number of relatively slow pions. About 1/3 are neutral pions that decay into photon pairs and initiate electromagnetic sub-showers, whereas the other 2/3 are charged pions, which either decay and dump most of their energy into neutrinos, or interact again. The resulting shower is much more widely distributed than those initiated by gamma-rays, allowing the shower shape to be used as a means for discriminating between electromagnetic and hadronic showers. Hadronic CRs are however far more numerous than CR electrons and gamma-rays. The corresponding proton rejection factor (*i.e.* the fraction of incoming protons that are incorrectly identified as photons/electrons) is of the order $\epsilon_p \sim 10^{-2}$ to 10^{-1} for current instruments. The electrons produced in electromagnetic cascades from

[5] For an analysis including the effects of energy resolution see Ref. [382].

Figure 3.2: *(Opposite)* Background fluxes relevant for our analysis. Isotropic CR backgrounds are shown in black: protons with an assumed cut efficiency of $\epsilon_p = 10^{-2}$ (black dotted), electrons (black dashed), and total isotropic CR backgrounds (black solid). Galactic diffuse emission (GDE) is shown in red, and an example spectrum of DM annihilating to gamma-rays via $b\bar{b}$ is shown in green. We give the DM and GDE curves for the ON and OFF regions defined in the Ring Method, as described in Section 3.3. Beyond 500 GeV, we extrapolate the GDE spectrum using a simple power law.

neutral pion decay are the dominant contributors to the detectable Cherenkov light. This means that if a cosmic-ray proton with a given energy is mistakenly reconstructed as a gamma-ray, the gamma-ray is usually reconstructed to have roughly a third as much energy as the actual incoming proton.

Here we adopt the proton flux per unit energy and angle [395]

$$\frac{\mathrm{d}\phi}{\mathrm{d}E\mathrm{d}\Omega} = 8.73 \times 10^{-9} \left(\frac{E}{\mathrm{TeV}}\right)^{-2.71} (\mathrm{GeV\,cm^2\,s\,sr})^{-1} , \tag{3.7}$$

which we shift to lower energies by a factor of 3 to account for the reduced Cherenkov light emitted by hadronic showers [396]. We note that in principle heavier CR species are relevant, especially ^{4}He, but these can be effectively accounted for by increasing the proton cut efficiency factor ϵ_p.

Throughout the present analysis, we will adopt a proton cut efficiency of $\epsilon_p = 10^{-2}$ for definiteness. We note, however, that assuming that the proton rejection factor is constant across all energies is a simplification. At lower energies shower shape cuts are less effective at discriminating CR protons from gamma-rays. Thus our CR proton background is underestimated at low energy, yielding a slight over-estimation of sensitivity at low energies. However, even with this approximation we are still able to reproduce the background rates shown in Ref. [385] for Array I to within a factor of two, for energies of up to 10 TeV. We note that when switching off protons entirely (which corresponds to $\epsilon_p = 0$) the background rates remain practically unchanged at energies below 2 TeV, as in our setup they are dominated by electrons. We also checked that with our assumptions we can reproduce the point source sensitivity for Array I to within a factor of two below 100 GeV, and within a few tens of percent above.

While the flux of CRs is isotropic across the sky, their acceptance by CTA is not. The characterization of this variation in CR acceptance rates is a non-trivial task, and methods to deal with non-isotropic acceptance rates are discussed in [397]. For this analysis we make the simplification of assuming an isotropic CR acceptance, though

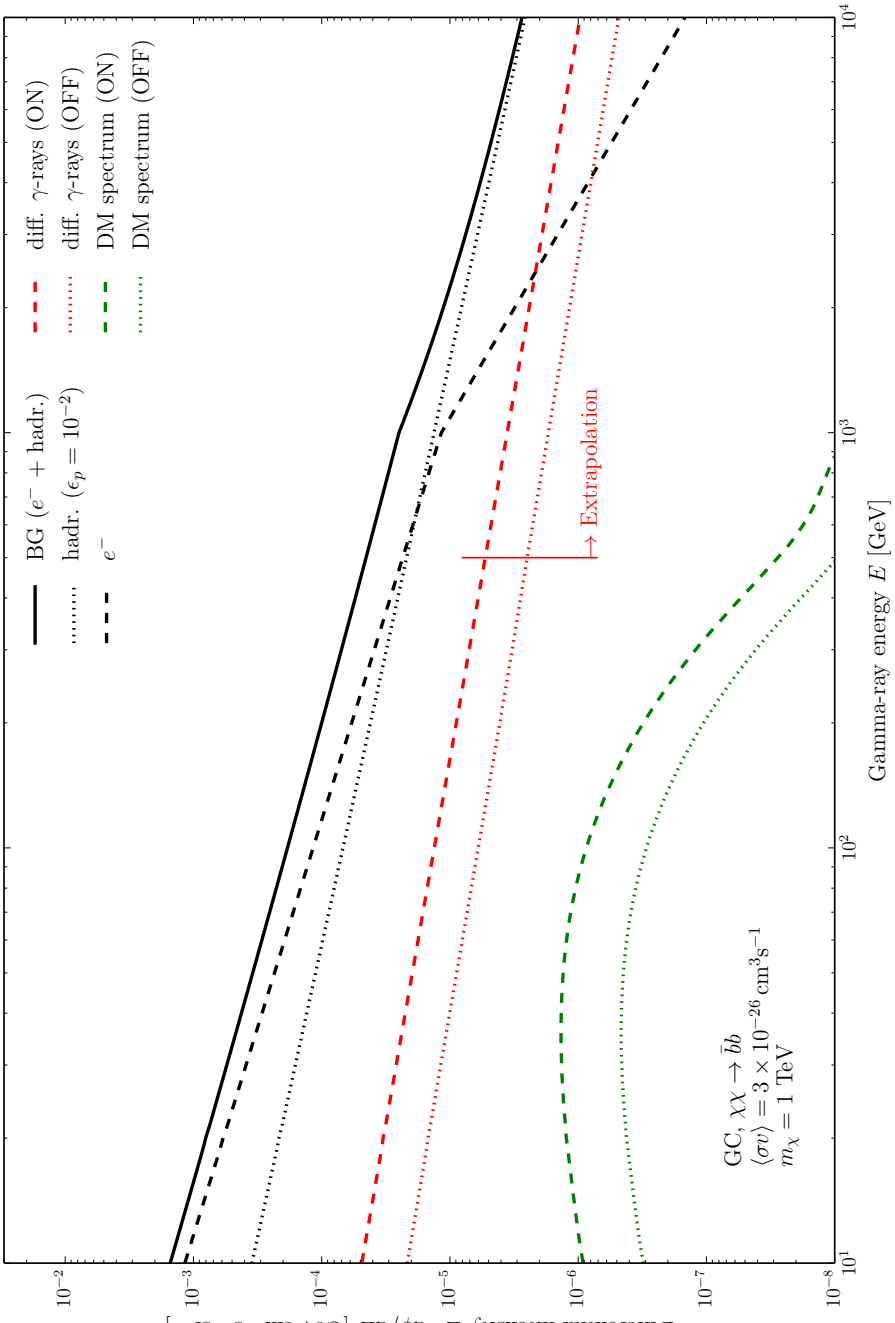
BG (e^- + hadr.)
hadr. ($\epsilon_p = 10^{-2}$)
e^-
diff. γ-rays (ON)
diff. γ-rays (OFF)
DM spectrum (ON)
DM spectrum (OFF)
→ Extrapolation
GC, $\chi\chi \to \bar{b}b$
$\langle\sigma v\rangle = 3 \times 10^{-26}$ cm^{3}s^{-1}
$m_\chi = 1$ TeV
Differential intensity E^2 dϕ/dE [GeV cm^{-2}s^{-1}sr^{-1}]
Gamma-ray energy E [GeV]

Figure 3.2

we note that our statistical framework can accommodate anisotropic uncertainties in the combined CR and gamma-ray acceptance, as discussed in Section 3.5.2.

As formal gamma-ray and CR electron efficiencies we adopt $\epsilon_\gamma = \epsilon_e = 1$, and note that these values (along with ϵ_p) are defined with respect to the effective area of Array I from Ref. [385].

In Fig. 3.2, we show the contributions from CR electrons and protons assuming $\epsilon_p = 10^{-2}$, and their sum. Note that in the highest energy range that we consider in this work, 6.7 to 10 TeV, 100 hr of CTA observations lead to approximately 7.0×10^3 or 1.5×10^3 CR background events in the OFF and ON regions, respectively. For comparison we also show the gamma-ray flux from a reference DM annihilation signal, based on a thermal annihilation cross-section and a DM mass of 1 TeV, within the ON and OFF regions employed in our version of the Ring method (*cf.* Section 3.3). The CR foreground is stronger than the DM signal by 2–3 orders of magnitude. Fig. 3.2 also shows a reference GDE gamma-ray background spectrum, which we discuss next.

3.4.2 Diffuse gamma-ray background

In 2006 HESS discovered diffuse gamma-ray emission from the GC at energies of 0.2–20 TeV [398]. The emission was found to be correlated with molecular clouds in the central 200 pc of the Milky Way, and is confined to Galactic latitudes $|b| < 0.3^\circ$ and longitudes $|\ell| < 0.8^\circ$. The spectrum suggests a hadronic origin. The absence of evidence for diffuse emission outside this window strongly influenced the choice of search regions for DM signals in previous analyses [123, 380].

Below 100 GeV, the GDE has been measured extremely well by the *Fermi*-LAT [399]. At these energies, it is expected to be dominated by π^0 decay from proton-proton interaction and bremsstrahlung. Diffuse gamma-rays below 100 GeV are an important background in searches for TeV-scale DM, particularly with CTA, which will have an energy threshold of tens of GeV.

To estimate the amount of GDE in different sky regions, and to study its impact on DM searches at the GC, we adopt the P7V6 GDE model by the LAT team. This model extends up to 500 GeV, above which we use a simple power-law extrapolation.[6] The P7V6 GDE model was fit using data between 50 MeV and 50 GeV, and structures with extensions of less than 2° were filtered out. As much of our analysis is done outside the bounds of the original data used to build the GDE model, *e.g.* at energies up to 1 TeV, and within 2° of the GC, the effects of GDE on our analysis should be considered

[6] This is not relevant to our discussion except at very high DM masses, close to 10 TeV. See `http://fermi.gsfc.nasa.gov/ssc/data/access/lat/BackgroundModels.html` for details on the BG model.

as approximate only. However we do not expect large changes in our results when using more realistic GDE models: even factor two changes in the background fluxes would affect our limits only at the $\sim$ 30–40% level. We leave a more detailed study of prospects for a combined CTA + *Fermi*-LAT diffuse analysis for future work.

In Fig. 3.2, we show the contribution that we inferred from this particular GDE model in the ON and OFF regions. For 100 hr of CTA observations, at energies of 6.7–10 TeV this corresponds to about 1.2×10^3 and 4.9×10^2 events respectively in the OFF and ON regions. This is a factor of ten higher than the reference DM signal at its peak value, and larger in the ON than in the OFF region. For these reasons, the GDE is a very important background that should not be neglected in DM searches at the GC.

3.5 Analysis

3.5.1 Analysis regions and J factors

For our version of the Ring method, we begin with the standard annulus of Ref. [380], with an inner radius r_1 and outer radius r_2. The centre of this annulus is offset from the GC ($b_0 = \ell_0 = 0^\circ$) by some Galactic latitude b. We then consider a circular region centred on the GC, with some radius $\Delta_{\rm cut}$. The area in which the annulus and this circular region intersect is what we refer to as the 'ON' region. The 'OFF' region consists of the remaining part of the annulus, outside the central disc. We adopt the parameters optimised for Array E in Ref. [380]: $b = 1.42^\circ$, $r_1 = 0.55^\circ$, $r_2 = 2.88^\circ$ and $\Delta_{\rm cut} = 1.36^\circ$. Further, we exclude the Galactic disc within $|b| \leq 0.3^\circ$ from both the ON and OFF regions, as per Ref. [380]. The resulting two RoIs can be seen in the top panel of Fig. 3.1. The corresponding solid angles and J factors are $\Delta\Omega_{\rm ON} = 1.2 \times 10^{-3}\,{\rm sr}$, $\Delta\Omega_{\rm OFF} = 5.6 \times 10^{-3}\,{\rm sr}$, $J_{\rm ON} = 7.4 \times 10^{21}\,{\rm GeV^2\,cm^{-5}}$ and $J_{\rm OFF} = 1.2 \times 10^{22}\,{\rm GeV^2\,cm^{-5}}$.

For our morphological analysis, we take the area covered by these two RoIs, and divide it into $1^\circ \times 1^\circ$ squares. We horizontally merge the various leftover regions resulting from this dissection into adjacent regions, yielding a total of 28 RoIs. These spatial bins are shown in the bottom panel of Fig. 3.1.

For comparison, we also consider DM annihilation in the Draco dwarf spheroidal galaxy, which, to a good approximation, is a point source to both CTA and *Fermi* at low energies (in the upper parts of their respective energy ranges, both would observe Draco as a somewhat extended source). For this analysis, we use the J-factor and solid angle from Table 1 of Ref. [400]: $\Delta\Omega_{\rm Draco} = 2.4 \times 10^{-4}\,{\rm sr}$, $J_{\rm Draco} = 6.31 \times 10^{18}\,{\rm GeV^2\,cm^{-5}}$.

3.5.2 Statistical framework

We use a binned Poisson likelihood function for comparing a DM model $\boldsymbol{\mu}$ to (mock) data $\boldsymbol{n}$

$$\mathcal{L}\left(\boldsymbol{\mu}|\boldsymbol{n}\right) = \prod_{i,j} \frac{{\mu_{ij}}^{n_{ij}}}{n_{ij}!} \exp(-\mu_{ij}). \tag{3.8}$$

Here the predictions of model $\boldsymbol{\mu}$ are the number of events μ_{ij} in the ith energy bin and the jth RoI, which are compared to the corresponding observed counts n_{ij}. We use 15 logarithmically-spaced energy bins, extending from 25 GeV to 10 TeV. Depending on the analysis (Ring or morphological), we use either two (Ring) or 28 (morphological) spatial bins (*i.e.* RoIs).

Each model prediction is composed of 3 parts: a gamma-ray signal resulting from DM annihilation (Eq. 3.5), an isotropic cosmic-ray background, and the GDE. In our statistical analysis each of these components can be rescaled via a parameter: $\langle\sigma v\rangle$ for the DM gamma-ray signal, and linear rescaling factors $R_{\rm CR}$ and $R_{\rm GDE}$ for the isotropic cosmic-ray background and the GDE respectively,

$$\mu_{ij} = {\mu_{ij}}^{\rm DM} + {\mu_{ij}}^{\rm CR} R_{{\rm CR},i} + {\mu_{ij}}^{\rm GDE} R_{{\rm GDE},i}. \tag{3.9}$$

Given that CR flux is isotropic to a good approximation and that we adopt the simplifying assumption that acceptance are isotropic, the $\mu_{ij}^{\rm CR}$s are trivially related by $\mu_{ij}^{\rm CR}/\mu_{ik}^{\rm CR} = \Omega_j/\Omega_k$, where Ω_j denotes the angular size of the jth RoI. Note that we do not vary the relative normalisations of the CR electron and proton spectra, only their sum. We also do not allow the GDE to be rescaled independently in each RoI, as this would simply allow the GDE to adjust to the data in its entirety in every bin, effectively non-parametrically.

Systematic uncertainties in the signal rates can be accounted for by multiplying the predicted signals μ_{ij} by scaling parameters α_{ij} and β_i, then profiling the likelihood over their values. We assume Gaussian nuisance likelihoods for all α and β, with respective variances σ_α^2 and σ_β^2 independent of i and j. Strictly, the distributions should be log-normal so that they go smoothly to zero as α and β go to zero, but for small σ this makes practically no difference; typical values of σ that we will consider in the following section are ≤ 0.03, well within the range where this is a good approximation. With these scaling parameters, the likelihood function becomes

$$\mathcal{L}\left(\boldsymbol{\mu},\boldsymbol{\alpha},\boldsymbol{\beta}|\boldsymbol{n}\right) = \prod_i \frac{1}{\sqrt{2\pi}\sigma_\beta} e^{-\frac{(1-\beta_j)^2}{2\sigma_\beta^2}} \prod_j \frac{\left(\mu_{ij}\alpha_{ij}\beta_i\right)^{n_{ij}}}{\sqrt{2\pi}\sigma_\alpha \cdot n_{ij}!} e^{-\mu_{ij}\alpha_{ij}\beta_i} e^{-\frac{(1-\alpha_{ij})^2}{2\sigma_\alpha^2}} \quad . \tag{3.10}$$

This formulation accounts for systematic uncertainty on any factor that enters linearly in the calculation of the total signal, such as effective area. The parameters α_{ij}, which

vary across both energy bins and RoIs, account for *e.g.* uncertainties related to non-uniformities in the acceptance of CTA within a FoV. We will refer to all uncertainties described by α_{ij} as *differential acceptance uncertainties*. Reasonable values for σ_α are of the order of a few percent [401, 402]. The parameters β_i, on the other hand, describes systematic uncertainties for a given energy that apply equally over the whole FoV.

Here we are most interested in the cross-RoI systematics, as systematics that apply equally across the whole FoV will essentially just degrade an entire $n\sigma$ confidence-level sensitivity curve by an offset of less than $n\sigma_\beta$ (although the rescaling could differ with energy, if σ_β were permitted to vary with energy). We therefore investigate the impacts of allowing each α_{ij} to vary independently, and simply set $\beta_i = 1$ for all i. The impacts of *e.g.* an energy-dependent systematic uncertainty on the *Fermi* or CTA effective areas could be easily accounted for by also profiling over each β_i.

Perhaps the largest source of uncertainties is the modelling of the CR acceptance. While in this analysis we assume an isotropic CR acceptance, this is a simplification, as noted above. This anisotropic acceptance could be incorporated in our analysis framework, but a detailed discussion is beyond the scope of this work.

Taking the likelihood function Eq. (3.10), we perform a maximum likelihood analysis across α_{ij}, $\langle\sigma v\rangle$, $R_{\rm CR}$, and in certain cases, $R_{\rm GDE}$. We can determine the maximum likelihood value of α_{ij} simply by solving

$$\frac{\mathrm{d}\mathcal{L}\left(\mu_{ij}, \alpha_{ij}, \beta_i | n_{ij}\right)}{\mathrm{d}\alpha_{ij}} = 0, \tag{3.11}$$

and demanding that α_{ij} be positive. This gives

$$\alpha_{ij} = \frac{1}{2}\left(1 - \sigma_\alpha^2 \mu_{ij}\beta_i + \sqrt{1 + 4\sigma_\alpha^2 n_{ij} - 2\sigma_\alpha^2 \mu_{ij}\beta_i + \sigma_\alpha^4 {\mu_{ij}}^2 {\beta_i}^2}\right). \tag{3.12}$$

In our morphological analysis we divide the FoV into bins of 1° squared, as laid out in Section 3.5.1 above. The systematic acceptance uncertainty in each bin is described by independent normal distributions in the likelihood function, which implies that the correlation scale of these uncertainties is of the order of $\sim 1^\circ$. Since the uncertainties are treated as statistically independent in the individual bins, they tend to average out. In fact, decreasing the solid angle of the bins by a factor of four would be roughly equivalent to reducing the differential acceptance uncertainty by a factor of two. Hence, when we quote these uncertainties for our morphological analysis, it is important to keep in mind that they refer to $\sim 1^\circ$ correlation scales, which we adopt here as reference value. A full exploration of the effect of different correlation scales would require more detailed knowledge of the detector performance, and is beyond the scope of this analysis.

The mock data $\boldsymbol{n}$ that we use for deriving sensitivities in the following section assume a fixed isotropic cosmic-ray background component with $R_{\mathrm{CR},i} = 1$ in all bins, and no contribution from DM annihilation. Depending on the analysis, we either include no GDE ($R_{\mathrm{GDE},i} = 0$ for all i) in the mock data, or a fixed GDE with $R_{\mathrm{GDE},i} = 1$. The mock data sets that we employ are not Poisson realisations of a model with these assumptions, but rather simply the expectation number of events given these assumptions; this has been referred to as the "Asimov data set" [403].

We calculate 95% confidence level (CL) upper limits by increasing the signal flux (or annihilation cross-section) from its best-fit value, whilst profiling over the remaining parameters, until $-2\ln\mathcal{L}$ changes by 2.71. In the case of the differential point-source sensitivity that we discuss in the next section, for a 95% CL upper limit we also require at least one energy bin to contain at least 3.09 events [404]. In this calculation, we determine background rates over the 80% containment region of the PSF, following *e.g.* Ref. [385]. Note that we neglect instrumental systematics when evalulating *Fermi*-LAT sensitivities (setting $\alpha_{ij} = \beta_i = 1$).

3.5.3 Background treatment

In both our Ring and morphological analyses, we allow the isotropic cosmic-ray background rescaling factor $R_{\mathrm{CR},i}$ to vary between 0.5 and 1.5 in our fits. We then profile the likelihood over this parameter in each energy bin.

Including the GDE in our analysis is more complicated, as in principle, the data-driven GDE model derived by *Fermi* could already contain some contribution from DM annihilation. Therefore, to gauge the impact of the diffuse emission upon current analysis methods, for our analysis with the Ring method we inject the GDE into our mock dataset $\boldsymbol{n}$, with $R_{\mathrm{GDE},i} = 1$ in all bins. We then carry out a full analysis with a model $\boldsymbol{\mu}$ where the GDE normalisation is left free to vary, *i.e.* $R_{\mathrm{GDE},i}$ is left free in the fits, but we require it to be non-negative. The idea in this exercise is to leave the analysis method as much as possible unaltered relative to previous analyses, but to make the mock data fed into the method more realistic. Leaving the GDE free to vary in each energy bin produces the most conservative constraints and avoids assumptions on the GDE energy spectrum. The results of this analysis are given in Section 3.6.2.

Our morphological analysis allows a more refined inclusion of GDE. Using more than two RoIs allows us to better exploit the shape differences between the GDE, which is concentrated along the Galactic plane, and the DM annihilation signal, which is spherically distributed around the GC. For this analysis we again include the GDE in the mock data with $R_{\mathrm{GDE}} = 1$ in all bins, and allow the individual $R_{\mathrm{GDE},i}$ values to vary in each energy bin. To implement this analysis we use lookup tables: for

each DM mass, and each energy bin and RoI, we consider a range of DM cross-sections. For each cross-section value, we calculate the maximum likelihood point when profiling numerically over $R_{\rm BG}$ and $R_{\rm GDE}$, and analytically over all α_{ij} using Eq. (3.12). Storing these values then gives us a partial likelihood as a function of cross-section in that bin, for each DM mass. For a given DM mass, we can then combine the partial likelihoods in different bins to determine cross-section limits at arbitrary confidence levels. The results of this analysis are given in Section 3.6.3 and 3.6.4.

3.6 Results

To keep the discussion as independent from specific DM scenarios as possible, in this section we will often quote the *differential sensitivity*, which is the sensitivity to a signal in an isolated energy bin. This measure is commonly used in the gamma-ray community (see *e.g.* Ref. [401]). Here we consider energy bins with a width of $\simeq 0.17$ dex (approximately six bins per decade), and quote sensitivities in terms of projected one-sided 95% CL upper limits.

We will start with a discussion of the point source sensitivity, which is relevant for DM searches in dwarf spheroidal galaxies. The remaining part of this section will then discuss DM searches at the GC. Finally, we will present projected upper limits on the DM annihilation cross-section for various annihilation channels and DM profiles.

3.6.1 Point source sensitivity

Some of the most powerful targets for indirect DM searches with gamma-rays are dwarf spheroidal galaxies. In order to compare the potential of CTA with the abilities of current instruments like *Fermi*-LAT, it is instructive to consider their differential point source sensitivity. In Fig. 3.3, we show the differential sensitivity of CTA, assuming an observation time of 100 hours, compared to the one of *Fermi*-LAT after ten years of observation (assuming 20% of the time is spend on the source). Due to its much larger effective area, CTA will outperform *Fermi*-LAT at energies above about 100 GeV, where *Fermi* becomes limited by photon statistics.

For comparison, we show the signal flux expected from the dwarf spheroidal galaxy Draco, in the case of a DM particle with $m_\chi = 1\,\text{TeV}$ mass, annihilating into $b\bar{b}$ final states with an annihilation cross-section of $\langle\sigma v\rangle = 3 \times 10^{-26}\,\text{cm}^3\,\text{s}^{-1}$. Draco is one of the most promising targets, and the envelope shows the uncertainty in the projected signal flux, which is primarily related to its overall mass (taken from Ref. [400]).

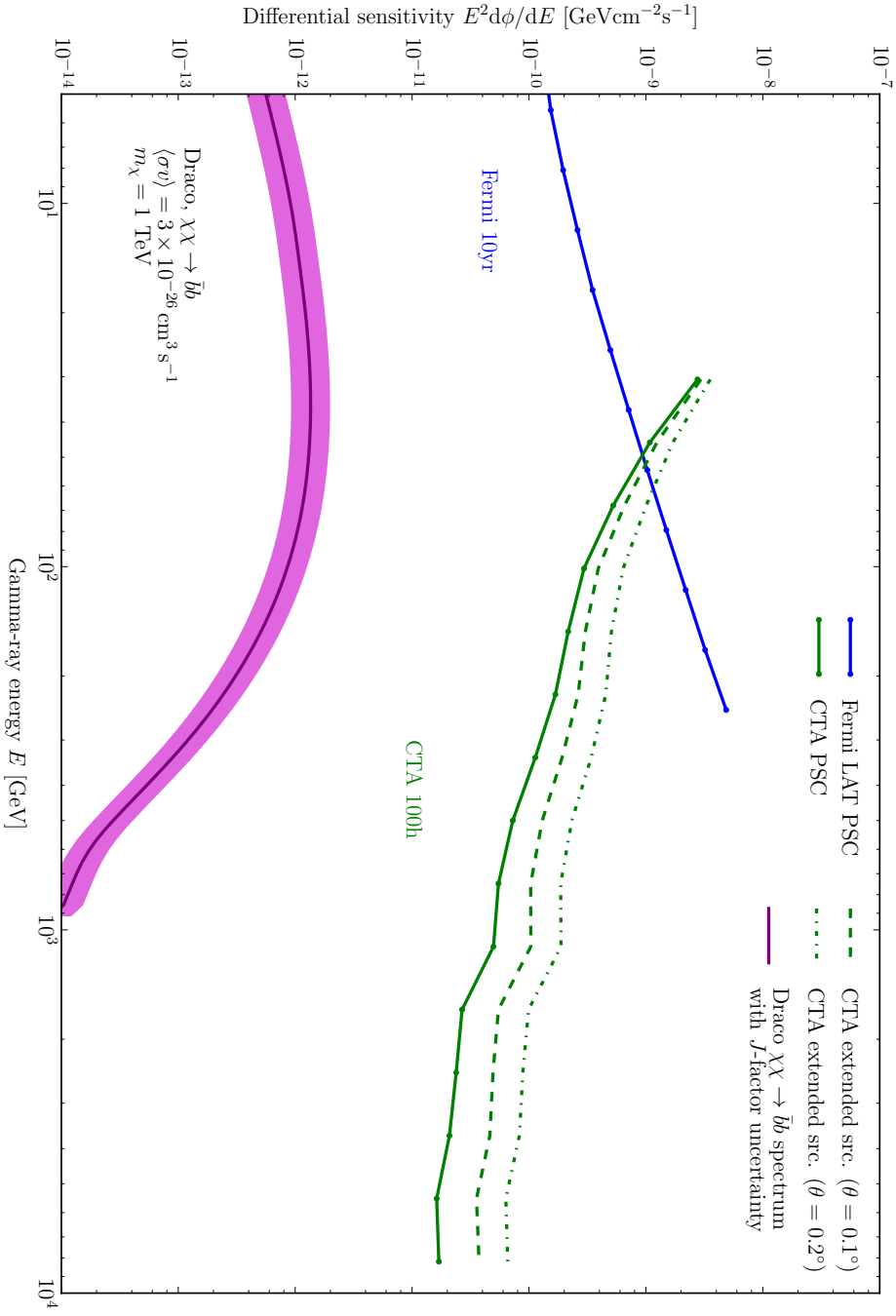
Differential sensitivity $E^2 \mathrm{d}\phi/\mathrm{d}E$ [GeVcm^{-2}s^{-1}]
Gamma-ray energy E [GeV]
Fermi LAT PSC
CTA PSC
CTA extended src. ($\theta = 0.1°$)
CTA extended src. ($\theta = 0.2°$)
Draco $\chi\chi \to \bar{b}b$ spectrum with J-factor uncertainty
Fermi 10yr
CTA 100h
Draco, $\chi\chi \to \bar{b}b$
$\langle\sigma v\rangle = 3 \times 10^{-26}$ cm^3 s^{-1}
$m_\chi = 1$ TeV

Figure 3.3

Figure 3.3: *(Opposite)* Differential sensitivity of *Fermi*-LAT (blue) and CTA (green) point source observations, in terms of 95% CL upper limits. The *Fermi*-LAT differential sensitivity assumes an observation time of 10 years, with energy bins of $\Delta \log_{10} E = 0.165$ size between $E = 5.0\,\mathrm{GeV}$ and $300\,\mathrm{GeV}$, and includes only statistical errors. The CTA sensitivities assume an observation time of 100 hours, include 1% differential acceptance uncertainty, with bins of $\Delta \log_{10} E = 0.173$ size between $E = 25\,\mathrm{GeV}$ and $10\,\mathrm{TeV}$. Sensitivities for extended sources of different sizes are also shown for CTA (green dashed and dot-dashed). The DM annihilation spectrum from the Draco dwarf galaxy uses a J-factor of $6.31^{+3.24}_{-1.94} \times 10^{18}\,\mathrm{GeV^2 cm^{-5}}$ from Table 1 of [400], with the band covering the uncertainty range.

Dwarf spheroidal galaxies have half-light radii of a few times 0.1° (see *e.g.* Ref. [405]), and at high energies will appear as extended sources for CTA. For comparison, we show the impact on the expected sensitivity in Fig. 3.3. We derive these sensitivity curves by assuming that a dwarf is observed by CTA to have an angular extent given by the sum in quadrature of the 68% PSF containment radius and the intrinsic angular extent indicated in the figures. This effect will degrade the sensitivity by a factor of a few at TeV energies. As can be seen in Fig. 3.3, for a gamma-ray spectrum from hadronic processes like annihilation into $b\bar{b}$, CTA will outperform *Fermi* for DM masses above about 1 TeV. However, the sensitivity of CTA will still fall about two orders of magnitude short of testing the canonical thermal cross-section.

In order to understand how the limits scale with observing time, it is helpful to realise that in this transition regime the limiting factor for CTA is the enormous background of CR electrons (and to a lesser degree unrejected protons and light nuclei; see Fig. 3.2). These CR electrons can easily swamp weak sources even if the number of events that are detected from the source is much larger than in case of *Fermi*-LAT. Indeed, apart from the difference in the effective area, the main difference between space-based and ground-based gamma-ray telescopes is their respective abilities to reject backgrounds. This is relatively simply realised by an anti-coincidence detector in the case of *Fermi*, but extremely challenging in the case of Cherenkov Telescopes like CTA. This means that even a larger observing time with CTA would not significantly affect the point-source sensitivity at the low energies relevant for TeV DM searches. In contrast, much longer observation times with space-based and practically background-free instruments like *Fermi* could (at least in principle) improve on existing limits by orders of magnitude.

Figure 3.4: *(Opposite)* Differential sensitivity of *Fermi*-LAT (blue) and CTA (green) for GC observations, using the Ring method as defined in Section 3.3. The two upper solid lines show our baseline estimate for the sensitivity, with galactic diffuse emission and a differential acceptance uncertainties of 1% included. For comparison, the dashed green line shows the differential sensitivity for CTA neglecting the GDE, but still including systematics of 1%; the dash-dotted lines in blue and green show the differential sensitivity for *Fermi*-LAT and CTA respectively, neglecting GDE and instrumental systematics. Observation times and energy binning are the same as in Fig. 3.3. The purple line shows the gamma-ray spectrum from the ON region assuming a DM mass of 1 TeV and an annihilation cross-section of $\langle \sigma v \rangle = 3 \times 10^{-26} \mathrm{cm}^3 \mathrm{s}^{-1}$ to $b\bar{b}$, using the Einasto profile from Eq. (3.2).

3.6.2 Galactic centre sensitivity with Ring method

The most intense signal from DM annihilation is expected to come from the GC. The large CR background will in that case be of lesser relevance than for observations of dwarf spheroidal galaxies, making the GC a particularly promising target for CTA. Previous analyses found that CTA will improve existing limits (with the strongest ones coming currently from HESS) by an order of magnitude or so [380, 381, 382]. However, all existing analyses have neglected the impact of the GDE, which is strongest in the direction of the Galactic center. We will demonstrate here that this in fact has a significant impact on DM searches with CTA.

In Fig. 3.4, we show the differential sensitivity for a DM signal in the GC that we obtain when using our version of the Ring method ([380], *cf.* Fig. 3.1), under various assumptions about the GDE and instrumental systematics. When creating mock data for our baseline analysis, we include individual estimates for the GDE in the different RoIs. The Ring method is only sensitive to integrated fluxes measured in the ON and OFF regions. In our likelihood fit to the mock data the normalisations of the DM and the GDE components are therefore degenerate, as these two components in general contribute a larger flux to the ON than the OFF region – whereas variations in the average intensity in both regions can be absorbed by slight changes in the CR background normalisation. An increased DM contribution can be compensated for by a smaller GDE contribution, and vice versa. This degeneracy breaks when the GDE contribution drops to zero, at which point the $-2 \ln \mathcal{L}$ increases with increasing DM annihilation cross-section, which then leads to a conservative upper limit on the DM flux.

The curves that we show in Fig. 3.4 where the GDE has not been included are based on neglecting GDE in the the mock data and the subsequent analysis (setting

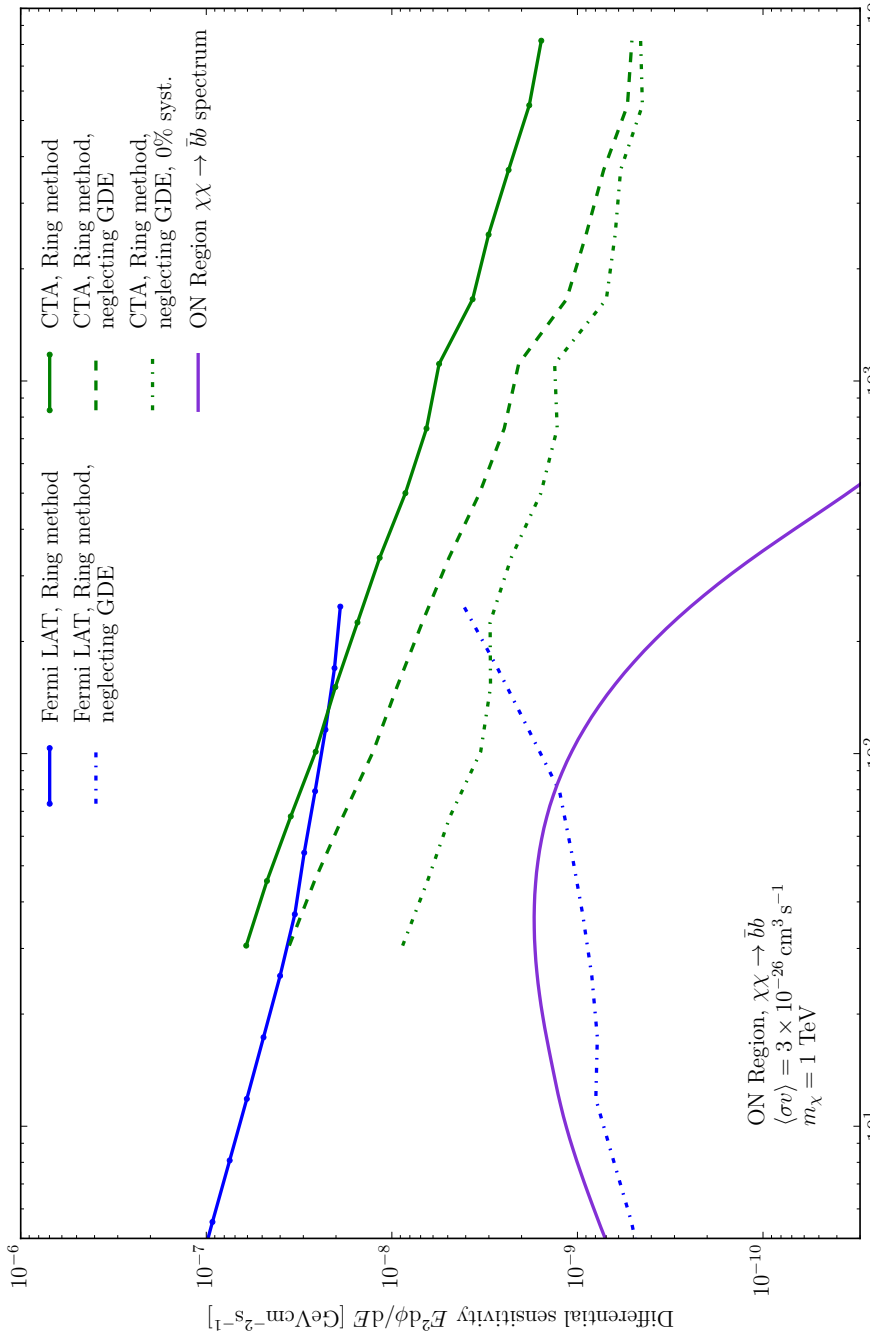
Fermi LAT, Ring method
Fermi LAT, Ring method, neglecting GDE
CTA, Ring method
CTA, Ring method, neglecting GDE
CTA, Ring method, neglecting GDE, 0% syst.
ON Region $\chi\chi \to \bar{b}b$ spectrum
ON Region, $\chi\chi \to \bar{b}b$
$\langle\sigma v\rangle = 3 \times 10^{-26}\,\mathrm{cm^3\,s^{-1}}$
$m_\chi = 1$ TeV
Differential sensitivity $E^2 \mathrm{d}\phi/\mathrm{d}E$ [GeVcm^{-2}s^{-1}]
Gamma-ray energy E [GeV]
10^{-6}
10^{-7}
10^{-8}
10^{-9}
10^{-10}
10^1
10^2
10^3
10^4

Figure 3.4

Figure 3.5: *(Opposite)* Same as Fig. 3.4, but comparing our previous Ring analysis (green) with our morphological analysis (red), again assuming 100 hr of observation. The solid lines show our baseline estimate for the sensitivity of the two analysis methods, with galactic diffuse emission included and differential acceptance uncertainties of 1%. The dotted orange line shows the same morphological analysis as our baseline estimate but neglecting the GDE and assuming 0% systematics. Also shown are sensitivities produced using the morphological analysis including GDE but using systematics of 3% (dashed) and 0.3% (dash-dotted) instead.

$R_{\rm GDE} = 0$ everywhere). We see here that in the case of the Ring method, neglecting the GDE artificially improves the projected sensitivity by a factor of up to about 3. Furthermore, neglecting instrumental systematics (as in Ref. [381]) increases the sensitivity again by another factor of a few. For comparison, we again show the flux expected from a DM particle with 1 TeV mass, annihilating into $b\bar{b}$ at the canonical thermal rate.

Since the GDE component is varying independently in each energy bin, our statistical framework is insensitive to spectral information that could help to discriminate between the GDE and the DM signal. Including this information could potentially increase the sensitivity of the Ring method, but would require precise assumptions on the poorly known spectrum of the GDE. By including spectral information, the authors of Ref. [378] were able to improve the limits derived from observations of Segue 1 by MAGIC by a factor of between 1.9 and 3.3, compared to a standard analysis using only spatial information. Applying similar analysis techniques to CTA could yield in the best case a comparable improvement in sensitivity. However, the uncertainty in the GDE spectra has to be carefully addressed in that case, which we leave to future work.

3.6.3 Galactic centre sensitivity with multi-bin morphological method

It is instructive to see the results that one would obtain by applying the Ring method to *Fermi*-LAT instead of CTA data. As shown in Fig. 3.4, the resulting sensitivity curve simply continues the curve from CTA to lower energies. This can be readily understood, as in both cases the actual limits are driven by the same GDE. We can see that the GDE is the factor holding back the Ring analysis. This motivates us to consider a procedure capable of taking into account morphological differences between

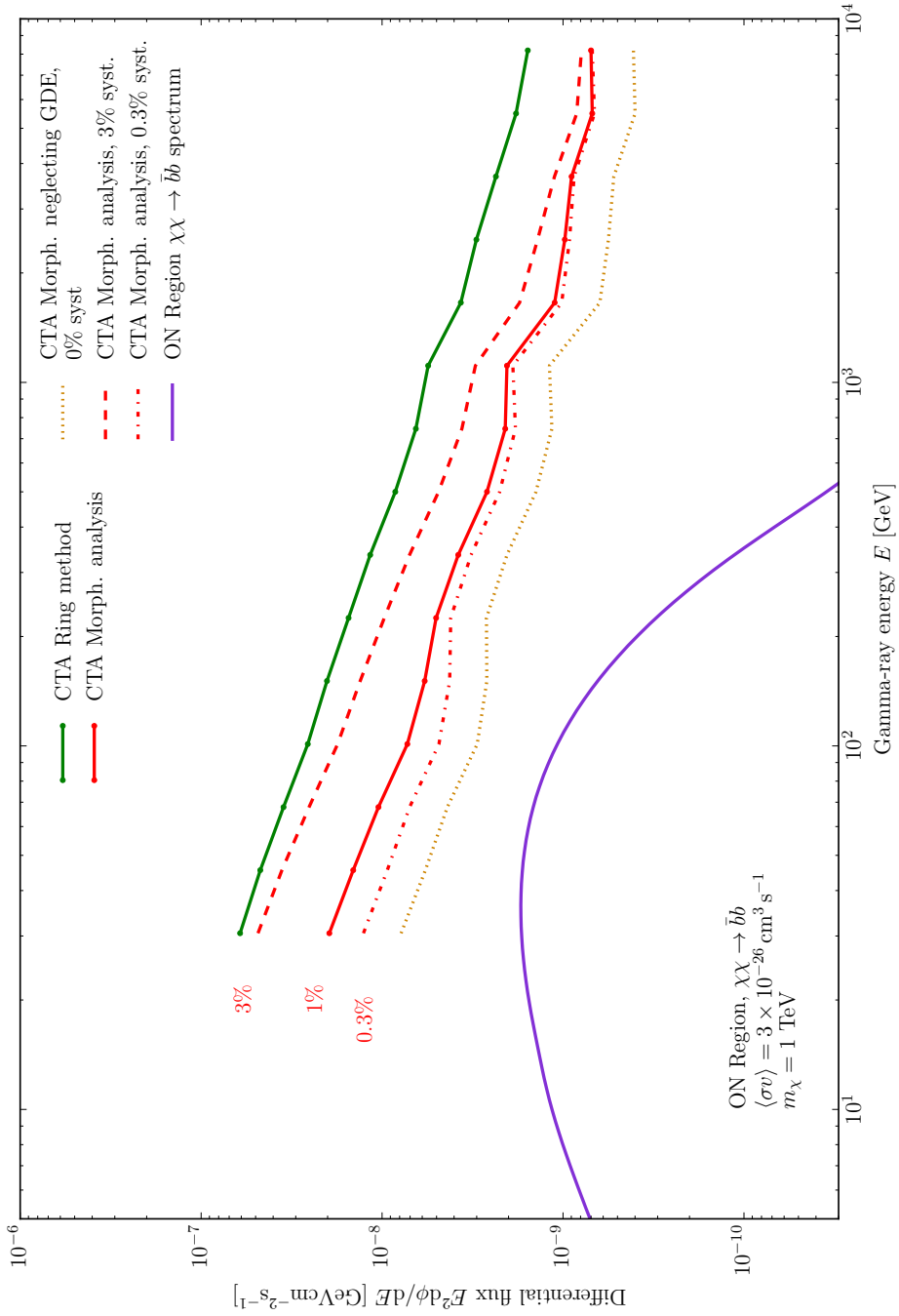
CTA Ring method
CTA Morph. analysis
CTA Morph. neglecting GDE, 0% syst
CTA Morph. analysis, 3% syst.
CTA Morph. analysis, 0.3% syst.
ON Region $\chi\chi \to \bar{b}b$ spectrum
3%
1%
0.3%
ON Region, $\chi\chi \to \bar{b}b$
$\langle\sigma v\rangle = 3 \times 10^{-26}$ cm^3 s^{-1}
$m_\chi = 1$ TeV
Differential flux $E^2 \mathrm{d}\phi/\mathrm{d}E$ [GeVcm^{-2}s^{-1}]
Gamma-ray energy E [GeV]
10^{-6}
10^{-7}
10^{-8}
10^{-9}
10^{-10}
10^1
10^2
10^3
10^4

Figure 3.5

the GDE and DM signal, which is what we discuss next.[7]

Here we take an important first step towards an improved DM search strategy for CTA by proposing a morphological analysis of the gamma-rays from the GC. We will estimate the *most optimistic* limits that one can obtain on DM annihilation in the presence of the known GDE, assuming that the morphology of the GDE is perfectly understood. To this end, we define the 28 subregions distributed as shown in the bottom panel of Fig. 3.1. They are all part of the original RoI from the Ring method. This has the advantage that the required observation strategy and results are directly comparable.

Fig. 3.5 shows that with our morphological analysis, the projected differential sensitivity is better by a factor of three than what can be obtained with the Ring method. Note that the limiting factor in our results, at least for sub-TeV energies, is now not the GDE but differential acceptance uncertainties, namely relative systematic uncertainties in the photon acceptance in different regions of the *same* FoV. For this uncertainty, we assume 1% throughout, which is a rather realistic value. This might however vary by a factor of a few up or down, depending on the experimental details (*cf.* Section 3.5.2). Indeed, varying the systematic uncertainty in a reasonable range has a significant impact on the actual projected constraints. Note that systematics of 0.3% give results extremely close to that of 0% systematics. Also shown for comparison in Fig. 3.5 is our morphological analysis assuming 0% systematics and neglecting the GDE, i.e. $\alpha_i = 1$ for all i, and $R_{\mathrm{GDE},i} = 0$ for all i in both mock data and model.[8]

3.6.4 Projected cross-section limits

We now present our results in terms of limits on DM annihilation, in the common $\langle\sigma v\rangle$-vs-mass plane, assuming DM annihilation into different final states with a branching ratio of 100%. First we provide some context by summarising the most relevant previous work, and later compare these to our own results.

In Fig. 3.6, we show existing experimental limits from the *Fermi*-LAT satellite [400] and HESS [123], on DM annihilation into $b\bar{b}$. In this figure, all limits from the GC are rescaled to our baseline Einasto DM profile. Projected limits correspond to 100 hr

[7] Considering the energy spectrum of the signal as we do here of course also improves CTA limits [382]; all our analyses are carried out including this information. Once a signal is detected however, if gamma-ray lines or virtual internal Bremsstrahlung seem relevant, a primarily spectral analysis would be preferable [406, 407].

[8] Although we introduced the morphological analysis method primarily to improve limits in the presence of the GDE, we also compared its performance to that of the Ring method in the case of no GDE and 0% systematics. In this case the morphological analysis produces limits that are marginally better than those of the Ring method. This is expected, as the smaller RoIs still provide an additional constraint on the spatial distribution of the signal.

observation time for CTA. The *Fermi*-LAT limits reach the thermal cross-section for DM masses below about 10 GeV. The HESS limits are strongest close to 1 TeV, where they reach $3 \times 10^{25}\,\mathrm{cm}^3\,\mathrm{s}^{-1}$.

Also shown are the projected limits for CTA from Refs. [380, 381, 382]. The analysis given in Ref. [381] assumes an observation time of 500 hr, and we have rescaled their limits to account for our baseline DM profile and observation time of 100 hr. In fact, even after this rescaling, the projected limits from Ref. [381] remain the most optimistic; they apparently do not account for systematic uncertainties or the effects of the GDE, and make use of an extended array with 61 mid-sized telescopes. This extended array is assumed to contain 36 extra mid-sized telescopes, as an additional, rather speculative, US contribution on top of the baseline array.

The limits presented in Ref. [380] include no GDE and no spectral analysis. They were built upon a profile derived from the Aquarius simulation, and therefore include an effective substructure boost compared to a regular NFW profile. We have removed this boost in order to allow direct comparison with our results, and those of others. The inclusion of substructure increases the J-factor and thus also the signal, which results in a stronger limit. As we use identical regions of interest to those of [380], we can estimate the substructure boost factor by comparing ON region J-factors: [380] give their result as $J_{\mathrm{ON,Aq.}} = 4.68 \times 10^{22}\mathrm{GeV}^2\mathrm{cm}^{-5}$, while our smooth Einasto profile (Section 3.3) gives $J_{\mathrm{ON,\,Ein.}} = 7.41 \times 10^{21}\mathrm{GeV}^2\,\mathrm{cm}^{-5}$. This yields a boost factor of 6.31; we hence multiply the limits of Ref. [380] by this factor for presentation in Fig. 3.6.

The limits presented in Ref. [382] are derived in a similar fashion to the Ring method ones in the present analysis, including spectral analysis, but neglect contributions from the GDE, systematics and proton CRs.

Our projected CTA upper limits on the annihilation cross-section using our version of the Ring method are shown in Fig. 3.6 by the thick green line. In contrast to Ref. [380], we *include* the expected GDE as discussed above (*cf.* Fig. 3.5). As a consequence, we find somewhat weaker limits at intermediate masses than in this previous work. From Fig. 3.4 one can see that neglecting GDE in the Ring method (in the mock data) falsely improves the sensitivity by a factor of $\sim 2-3$, which agrees with the factor ~ 3 difference between the results of Ref. [380] and our Ring method limit. The different shape of the limits as function of mass is due to our lower energy threshold, and the fact that we carry out a spectral analysis, whereas Ref. [380] used only one large energy bin. This consequence of including spectral information was noted previously in Ref. [382], whose limits have a very similar shape to our own.

The projected CTA upper limit produced by our morphological analysis is shown in Fig. 3.6 by the thick red line (while not shown on the figure, the limit neglecting

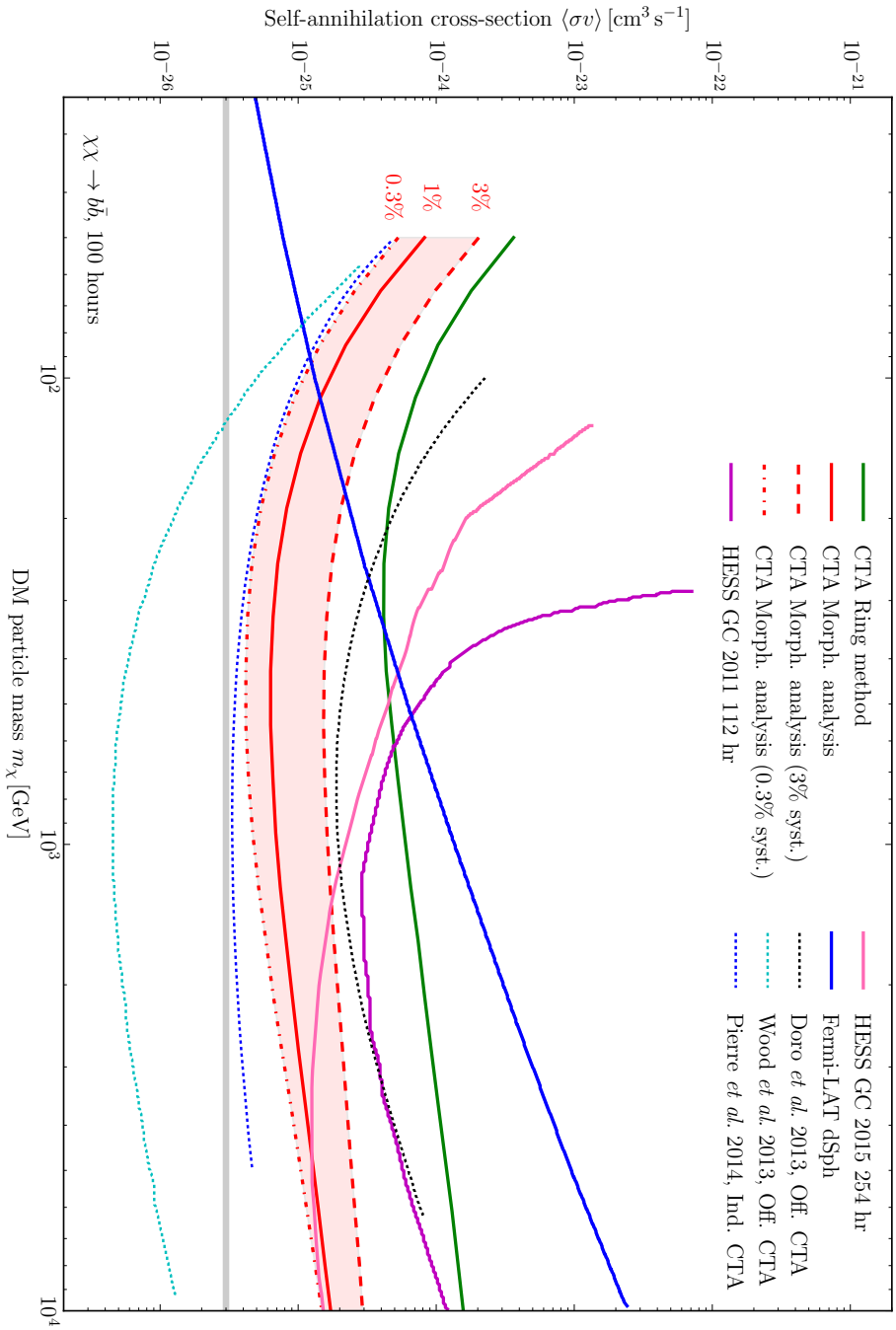
Self-annihilation cross-section $\langle\sigma v\rangle$ [cm^3 s^{-1}]
10^{-21}
10^{-22}
10^{-23}
10^{-24}
10^{-25}
10^{-26}
$\chi\chi \to b\bar{b}$, 100 hours
3%
1%
0.3%
10^2
10^3
10^4
DM particle mass m_χ [GeV]
CTA Ring method
CTA Morph. analysis
CTA Morph. analysis (3% syst.)
CTA Morph. analysis (0.3% syst.)
HESS GC 2011 112 hr
HESS GC 2015 254 hr
Fermi-LAT dSph
Doro *et al.* 2013, Off. CTA
Wood *et al.* 2013, Off. CTA
Pierre *et al.* 2014, Ind. CTA

Figure 3.6

Figure 3.6: *(Opposite)* Upper limits on the DM annihilation cross-section using the previous Ring method (green) and our morphological analysis (red), assuming 100 hr of observation of the GC. The thick solid green and red lines are our baseline estimates of the limits attainable using the two analysis methods, assuming differential acceptance uncertainties of 1% and including GDE. The red dashed and dot-dashed lines show the limits produced in the morphological analysis assuming 3% and 0.3% systematics, respectively. Also shown are current limits on the DM annihilation cross section (thin solid lines; *Fermi*-LAT dwarf analysis in blue [400], HESS GC 112 hour observations in magenta [123] and preliminary 254 hour observations in pink [408]), as well as various projected CTA limits, both official (thin dotted lines; Doro *et al.* 2013 in black [380], Wood *et al.* 2013 in cyan [381]), and independent (Pierre *et al.* 2014, thin dotted line in dark blue [382]). For the sake of comparison, the CTA projections are rescaled to 100 hr observation time and our adopted Einasto profile.

GDE is a factor of ~ 1.5 below this line). It is perhaps surprising that our limit including GDE is significantly better than that of Ref. [380], which neglects GDE both in the mock data as well as in the analysis. One reason is that using more bins allows for better shape discrimination of the signal over the isotropic background. Another reason might be differences in the adopted acceptance uncertainties (which are not quoted in Ref. [380]). However, the fact that our morphological analysis is an order of magnitude weaker than the scaled limits of Ref. [381] is primarily due to the unrealistic array considered in that paper and their complete neglect of systematics.

Interestingly, our projected constraints are actually also weaker than the existing limits from HESS, which are based on 112 hours of GC observations. This difference is likely due to two things. The first is simply that the RoIs adopted in the Ring method and in the HESS analysis are rather different. The second is that the HESS analysis is a true ON-OFF analysis, which neglects the GDE by definition; this was only possible to do in a valid way in the HESS analysis due to the instrument's high energy threshold and the fact that at such energies, the GDE intensity observed by *Fermi*-LAT happens (by chance?) to be very similar in the rather complicated ON and OFF regions chosen by HESS.

Most importantly, moving from the Ring method to our morphological analysis yields *a sensitivity improvement by up to an order of magnitude*. We show in Fig. 3.6 that morphological analysis improves the projected limits by up to a factor of ten for high DM masses compared to the Ring method.[9] This is mostly due to the fact that the

[9]This is not directly apparent from Fig. 3.5, where the difference is merely a factor of three. The reason is that a DM signal would appear in several energy bins simultaneously, which strengthens the limits in the case where the GDE is correctly modelled.

Figure 3.7: *(Opposite)* Comparison of $\langle\sigma v\rangle$ limits from CTA observations of the GC, assuming different annihilation channels and DM halo profiles. Einasto lines assume the main halo profile described in Section 3.3. The contracted NFW profile with an inner slope of $\gamma = 1.3$ can also be found in that section. All lines assume 1% systematics, 100 hr of observations and include GDE.

large number of subregions allows an efficient discrimination between the morphology of the GDE and a putative DM signal. Note that the projected limits again depend critically on instrumental systematics, and as indicated by the band in Fig. 3.6. This is due to the large number of measured events in the RoIs. For our baseline DM profile, we find that the thermal annihilation cross-section can be only reached if instrumental systematics (namely differential acceptance uncertainties as discussed above) are under control at the sub-percent level. At the same time, increasing the time over which the GC is observed by CTA will have a negligible effect on the projected limits.

Finally, we discuss how the projected limits depend on the adopted annihilation channel or DM halo profile. These results are shown in Fig. 3.7. Besides our baseline scenario, where we assumed an Einasto profile and annihilation into $b\bar{b}$ final states, we show limits for annihilation to $\tau^+\tau^-$, W^+W^-, $\mu^+\mu^-$, and $t\bar{t}$ with an Einasto profile, and to $b\bar{b}$ with an alternative density profile.[10] We find that in the case of annihilation via the $\tau^+\tau^-$ channel, CTA would be able to probe annihilation cross-sections well beyond the thermal value even for a standard Einasto profile. In the case of a contracted NFW profile with a inner slope of $\gamma = 1.3$, as described in Section 3.3, the J-factor increases by a factor of 2.9 (summed over all RoIs). If this profile is indeed realised in nature, it would bode well for future observations with CTA, as CTA could probe well beyond the canonical thermal cross-section for a large range of DM particle masses between 100 GeV and 10 TeV.

[10]Note that fluctuations of the limits, which are most visible in the cases of $\mu^+\mu^-$ and W^+W^- final states with strong final state radiation, come from variations in the adopted effective area.

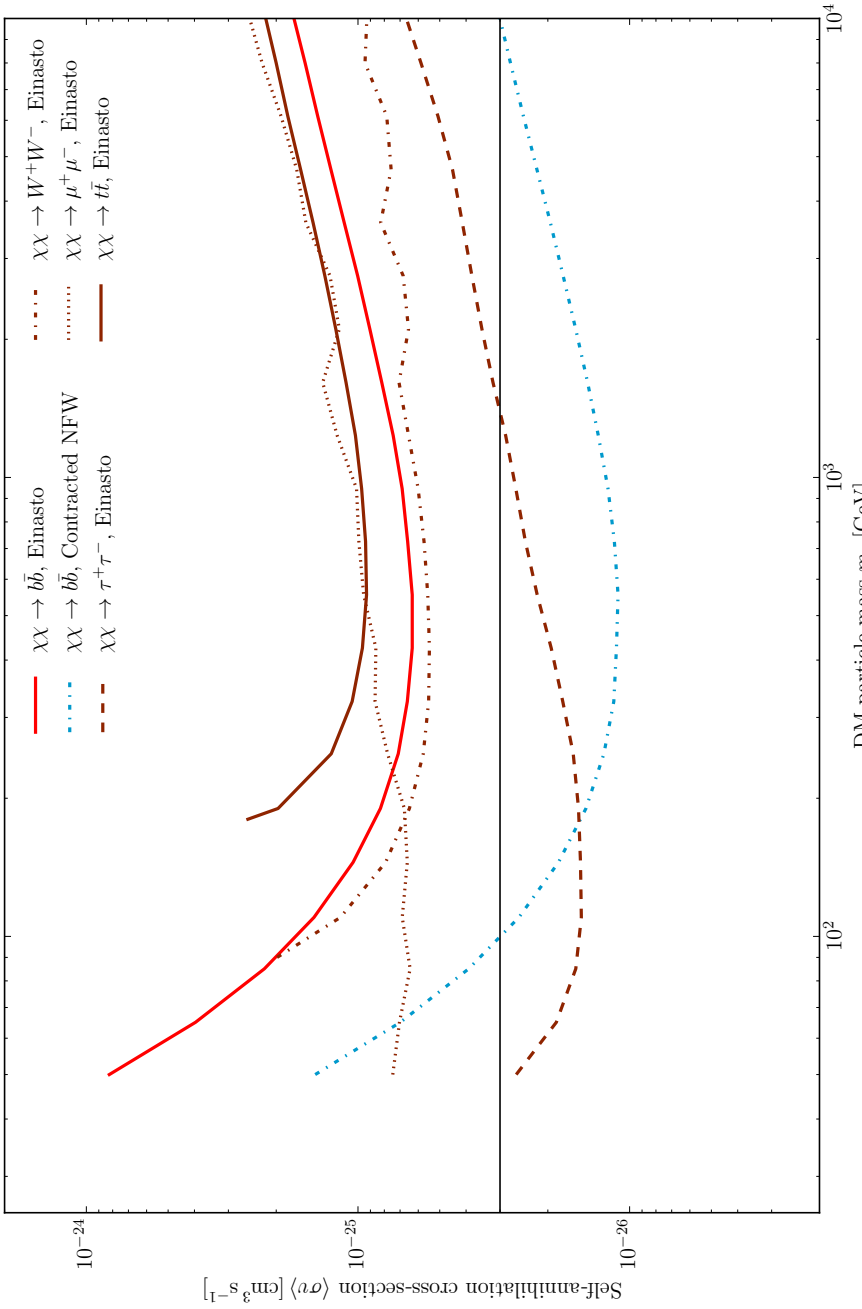
$\chi\chi \to b\bar{b}$, Einasto
$\chi\chi \to b\bar{b}$, Contracted NFW
$\chi\chi \to \tau^+\tau^-$, Einasto
$\chi\chi \to W^+W^-$, Einasto
$\chi\chi \to \mu^+\mu^-$, Einasto
$\chi\chi \to t\bar{t}$, Einasto
Self-annihilation cross-section $\langle\sigma v\rangle$ [cm^3 s^{-1}]
10^{-24}
10^{-25}
10^{-26}
10^2
10^3
10^4
DM particle mass m_χ [GeV]

Figure 3.7

3.7 Conclusion

In this chapter we have worked towards making a realistic assessment of the performance of CTA for detecting the gamma-rays produced by DM annihilating in the GC, including the effects of systematic uncertainties and the GDE.

We showed that the inclusion of the GDE substantially degrades the sensitivity of CTA when using a traditional two region analysis as previous official studies have done. We have assessed the impacts of all backgrounds, including protons and electrons in cosmic-rays hitting the atmosphere and, for the first time in this type of analysis, diffuse astrophysical emission. The impact of including the galactic diffuse emission can be observed in particular in Fig. 3.4, where the CTA differential sensitivity is found to be substantially degraded (solid line) with respect to the case where the GDE is neglected in the analysis (dashed green line). Although we only adopted one particular GDE scenario (which is an extrapolation of *Fermi*-LAT observations to higher energies), we do not expect these conclusions to change when adopting other realistic GDE models.

This reduction in sensitivity due to the GDE can, however, be mitigated by adopting a multi-region morphological analysis. Our morphological analysis allows a proper exploitation of the shape differences between the GDE, which is concentrated along the Galactic plane, and the DM annihilation signal, which is spherically distributed around the GC. The constraints derived under this approach are more stringent by a factor of a few compared to those obtained with the Ring analysis. This is best seen by comparing the red (morphological) and green (non-morphological) curves in Figs. 3.5 and 3.6.

The sensitivity degradation resulting from the inclusion of systematic errors cannot be escaped though, and must be taken into account. In this work we introduced a statistical framework that allowed us to account for the impact of differential acceptance uncertainties within a FoV on DM limits from CTA. This impact can be seen in Fig. 3.5, where the sensitivity of CTA to DM annihilation is shown for three different values of the magnitude of these systematics: 3% (dashed), 1% (solid) and 0.3% (dash-dotted).

From our analysis we can also estimate the prospects of detecting WIMPs with CTA. Our most realistic estimate of the upper limits on the DM annihilation cross-section possible with 100 hr of GC observation by CTA are shown as a red solid line in Fig. 3.6. These correspond to a morphological analysis assuming annihilation to $b\bar{b}$, systematics of 1%, and include diffuse emission. In order to reach canonical thermal cross-section, shown as a horizontal line, systematic errors should be reduced to less than 0.3%. If the DM profile is steeper than NFW or Einasto, the sensitivity curve drops below the

thermal cross-section for a broad range of masses, as we show in Fig. 3.7. Here, for the same annihilation channel and a contracted profile rising as $r^{-1.3}$, CTA is found to be able to probe WIMPs with a thermal cross-section between 100 GeV and 10 TeV.

When the work presented in this chapter was published in 2014 [2] it was the first study on the sensitivity to CTA to include the effects of systematic uncertainties and the GDE. A subsequent study, Ref. [409], was in broad agreement with our results, finding that the inclusion of systematics and GDE degraded CTA performance.

In closing, astrophysical gamma-rays are a powerful method to search for annihilating DM, and the upcoming CTA observatory will be a potent tool in observing these gamma-rays. However, certain realities must be taken into account when assessing the capability of CTA, not only to achieve a realistic estimate of its future performance, but also to develop new and better analysis tools.

***

4 The Local Dark Matter Density

4.1 Introduction

The last two chapters have been concerned with the detection of signals from WIMP DM, be they nuclear recoils, neutrinos from captured WIMPs annihilating in the Sun, or gamma-rays from WIMPs annihilating in the Galactic Centre. In all three cases the density of DM has been a crucial quantity in the search for these signals - the local density for direct detection (Eq. 2.1) and solar WIMP capture (Eq. 2.12), and the density towards the GC for the gamma-ray limits from CTA (Eq. 3.1). These densities are degenerate with certain particle physics properties of WIMP DM, such as the DM-nucleon scattering cross-sections $\sigma_{\rm SI}$ and $\sigma_{\rm SD}$, and the self annihilation cross-section $\langle\sigma v\rangle$. Thus a reliable determination of the DM density for each of these cases is crucial.

In this chapter we present a new method for determining the local DM density. First the scene is set by introducing the components of the Milky Way. Then we introduce the local DM density, the broad methods of determining it, and the data required to do so. From there we begin the derivation and testing of our method, including a brief outline of the Jeans equations (Section 4.5), which are fully derived in Appendix A. In this chapter we are largely agnostic as to the particular DM particle model considered, and these results could apply equally to axions, sterile neutrinos, or the WIMPs we have so far focused on.

4.2 The Milky Way

Structurally the Milky Way (MW) can be roughly split into three components: the DM halo, the disc, and the bulge/bar. At the centre of the MW is the bulge, which is thicker than the disc, and elongated such that it forms a bar as seen in Fig. 4.1. Outwards from the centre extends the flat, roughly axisymmetric Galactic disc, in which the Sun is located. Both the bulge and the disc are dominated by baryons, and rotate around the GC. These two elements are embedded within the much larger and roughly spherical DM halo, which was discussed earlier in Section 1.4.7. In Section 1.4.8 we also discussed a possible fourth component, the dark disc.

The baryonic disc itself contains many components such as gas, dust, and a panoply of types of stars with varying ages and metallicities[1]. As star formation and stellar evolution proceed throughout the galaxy the abundances of heavier elements increases, with subsequent generations of stars incorporating the higher metallicity debris of their antecessors. Thus a relationship between age and metallicity is formed, with older (younger) stars having lower (higher) metallicities.

Traditionally the stellar component is described by two components, a *thin disc* and a *thick disc*, modelled as exponentials with different scale heights z_d [410]:

$$\rho_*(R,z) = \rho_{\rm thin}(R,0)\exp\left(-\frac{|z|}{z_{d,\rm thin}(R)}\right) + \rho_{\rm thick}(R,0)\exp\left(-\frac{|z|}{z_{d,\rm thick}(R)}\right) \quad (4.1)$$

where R is the distance from the GC, z is the distance above or below the disc midplane in the galactocentric coordinate system of (R,ϕ,z) (see Fig. A.1), the z_d terms are the scale heights of the thin and thick discs, and $\rho(R,0)$ controls the radial profile, which can can be modelled in a similar way with scale length $R_{\rm d}$:

$$\rho(R,0) = \rho(0,0)\exp\left(-\frac{R}{R_{\rm d}}\right). \quad (4.2)$$

The canonical values for the parameters controlling the stellar disc are $z_{d,\rm thin} = 300$ kpc, $z_{d,\rm thick} = 1$ kpc, and $R_{\rm d} = 2.5$ kpc [410].

Stars populating the canonical thick disc tend to be older and have lower metallicity compared to those of the thin disc. Recent work however has found it more appropriate to describe the disc as a sum of many Mono-Abundance Populations (MAPs), each defined by a small range of metallicity parameters and with their own scale height [411]. While older, lower metallicity populations do have higher scale heights, there is no evidence for chemically distinct 'thick' and 'thin' discs [412]. Many mechanisms for how these MAPs acquired higher scale heights, *i.e.* how the 'thick disc' was formed, have been proposed, and this is an active field of research (see Introduction of [413]).

[1] In astronomy a *metal* is any element other than hydrogen or helium.

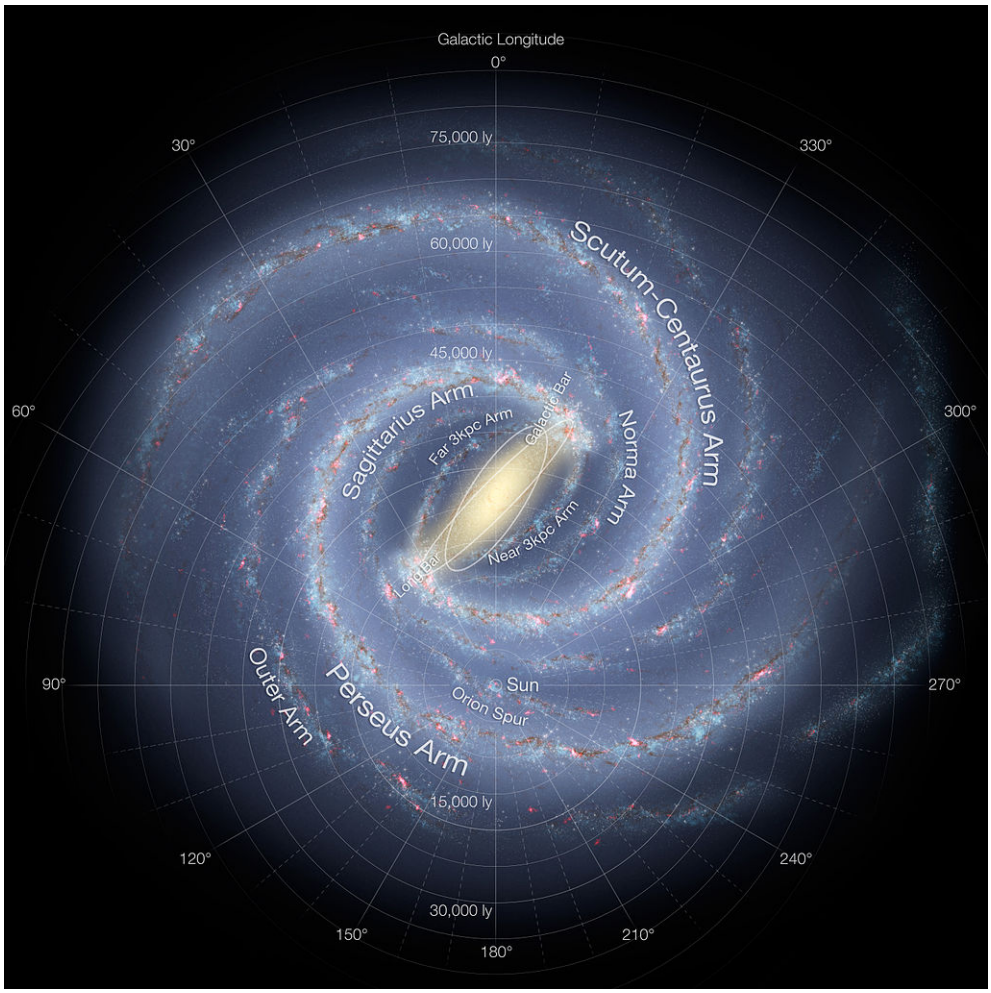

Figure 4.1: Artist's impression of the Milky Way, a barred spiral galaxy. Credit: NASA/JPL-Caltech/ESO/R. Hurt

Figure 4.2: *(Opposite) Top panel:* Comparison of a constant vertical DM density (navy) with the simplified K and D model used in this analysis (red), and a more complex model derived by Sofia Sivertsson based on observational data presented in [414]. DM density is equal to the baryon density at approximately $z = 0.5$ kpc, and is 10 times larger above approximately 1-1.5 kpc. *Bottom panel:* Comparison of the constant DM density (navy) to the vertical density profiles given by an Einasto profile (purple), and two classic NFW profiles with scale radii of $r_s = 20$ kpc (green) and $r_s = 40$ kpc (orange). The Einasto and NFW profiles only drop to below 90% of the constant DM density value above 3 kpc.

Along with its stellar component, the disc also contains significant amount of gas. These baryonic components significantly outweigh any DM contribution in the solar neighbourhood, as shown in Fig. 4.2: at the solar position the combined density of stars and gas is $\rho_{\mathrm{baryon},\odot} = 84 \pm 12 \times 10^{-3}\,\mathrm{M_\odot\,pc^{-3}} = 3.2 \pm 0.45\,\mathrm{GeV\,cm^{-3}}$ (pink line) [414], while in Chapters 2 and 3 we have taken the local DM density (solid black line) as $\rho_{\mathrm{DM},\odot} = 10.5 \times 10^{-3}\,\mathrm{M_\odot\,pc^{-3}} = 0.4\,\mathrm{GeV\,cm^{-3}}$, almost an order of magnitude less than the baryon density. With measurements only from within the solar neighbourhood, the uncertainty on the baryon distribution would swallow the putative DM density. These realities will thus dictate to us how we proceed in determining the local DM density.

4.3 Introduction to the Local Dark Matter Density and its Measurement

In Chapter 1 of this thesis we introduced the importance of the local DM density to direct detection (Section 1.5) and indirect detection via DM capture and annihilation in the Sun (Section 1.6), and in Chapter 2 we used a value of $\rho_{\mathrm{DM},\odot} = 0.4\,\mathrm{GeV/c^2} = 10.5 \times 10^{-3}\,\mathrm{M_\odot\,pc^{-3}}$ in analysing the complementarity of these two detection methods. The local DM density was also used to normalise the DM halo profiles used to calculate the gamma-ray limits from CTA in Chapter 3, where the same value of $\rho_{\mathrm{DM},\odot}$ was used.

There are two broad categories of local DM measurements: those that use measurements of stars in a small volume around the sun, and those which use a variety of dynamical tracers to constrain more global mass models of the MW, from which a local DM density is extrapolated. While previously we made no distinction between these methods, we now denote the local DM density derived from local measurements as $\rho_{\mathrm{DM},\odot}$ and that derived from global methods as $\rho_{\mathrm{DM},\odot,\mathrm{ext}}$. For a review of previous

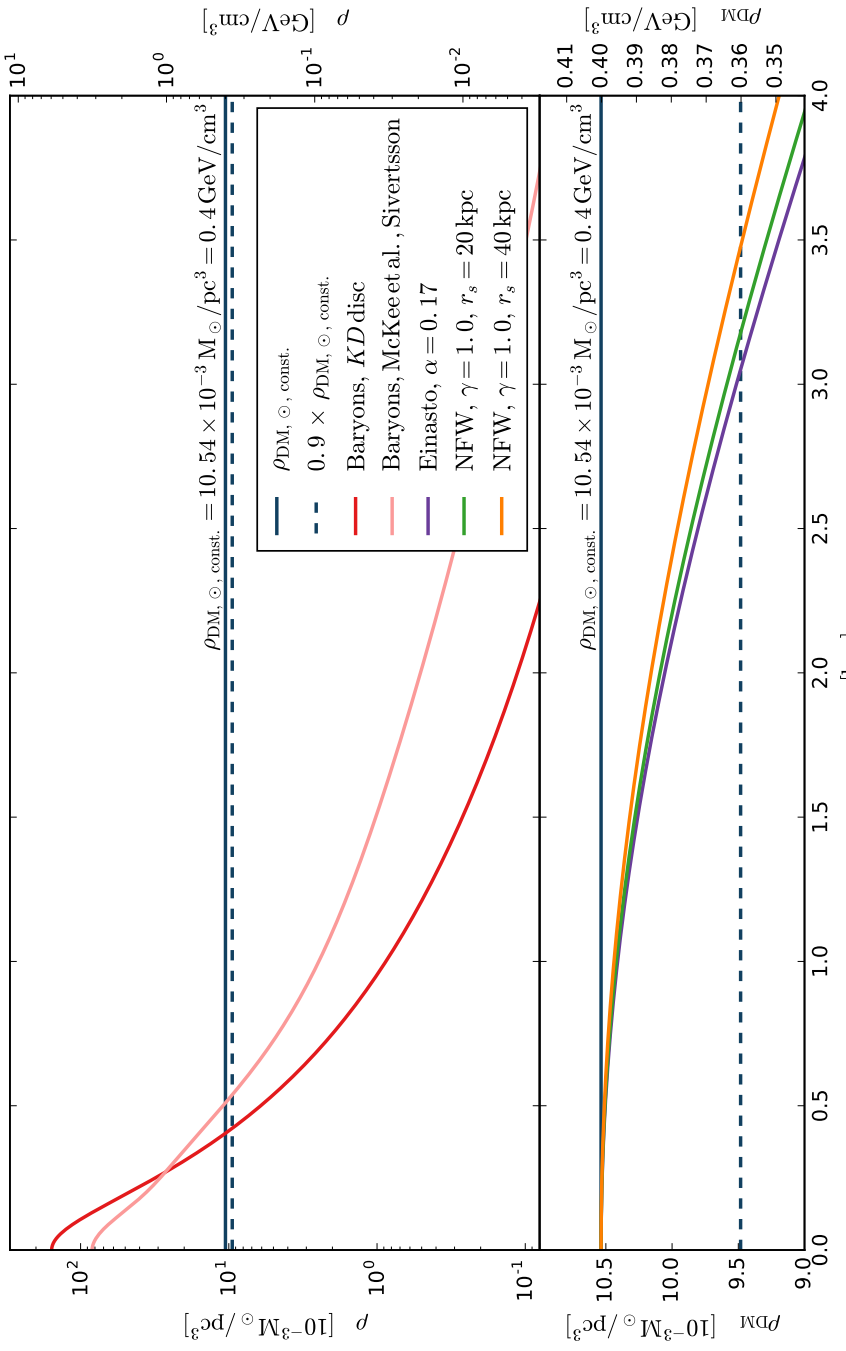
ρ [GeV/cm^3]
$\rho_{\rm DM}$ [GeV/cm^3]
ρ [10^{-3}M$_\odot$/pc^3]
$\rho_{\rm DM}$ [10^{-3}M$_\odot$/pc^3]
$\rho_{\rm DM,\,\odot,\,const.} = 10.54 \times 10^{-3}\,{\rm M}_\odot/{\rm pc}^3 = 0.4\,{\rm GeV/cm}^3$
$\rho_{\rm DM,\,\odot,\,const.}$
$0.9 \times \rho_{\rm DM,\,\odot,\,const.}$
Baryons, KD disc
Baryons, McKee et al., Sivertsson
Einasto, $\alpha = 0.17$
NFW, $\gamma = 1.0$, $r_s = 20$ kpc
NFW, $\gamma = 1.0$, $r_s = 40$ kpc
z [kpc]

Figure 4.2

local DM density measurements see [415].

We previously encountered the global measurements in Section 1.4.7, where we discussed the fitting of parameters to generalised NFW and Einasto DM halo profiles. There are a great many studies using this method, using a variety of data sets and modelling methods [*e.g.* 416, 417, 418, 419, 420, 421, 422, 166, 423, 167, 424, 425]. One unifying feature however is the assumption of a spherically symmetric DM halo, and so while these methods generally have smaller error bars on the local DM density, they have a greater systematic uncertainty due to this assumption. However, as discussed earlier in Section 1.4.8, the spherical halo can have a degree of triaxiality, and can change in shape due to the presence of baryonic disc. Reference [373] quantified the effect on $\rho_{\mathrm{DM},\odot}$ of differences between assumed spherical halos and more realistic halos found in numerical simulations containing both DM and baryons, finding deviations of up to 41% relative to the spherically averaged value.

The alternative is to focus on measurements of stars in a small volume around the sun [*e.g.* 7, 8, 426, 427, 428, 429, 430, 431, 432, 433, 434, 435, 436]. In general these methods give larger uncertainty on the local DM density but do not suffer the systematic uncertainty of assuming a global potential.

The primary local measurements used are the velocities and positions of tracer stars in the z-direction, *i.e.* vertically out of the disc plane. The stellar disc scale length is greater than the scale height (~ 2.5 kpc vs. ~ 1 kpc and ~ 300 pc for thick and thin discs respectively), and so for a first approximation one can neglect radial variation in the mass distribution, and the analysis can be reduced to a one-dimensional system. The z-direction is also advantageous as a faster decline in baryon density means that DM dominated regions are closer in that direction, when assuming a roughly spherical DM halo.

The assumption of a purely 1D vertical system becomes increasingly tenuous at higher z values, as will be discussed further in Section 4.6.6, and also would also require assuming a locally flat rotation curve to obviate the need for rotational data (see Eq. 4.22 and subsequent discussion). Many local measurement studies also assume that the DM density is constant with height - taking an NFW profile with scale radius of 20 kpc, the DM density at height z is within 10% of the midplane ($z = 0$) value up to a height of $z \sim 3$ kpc (see Fig. 4.2). The Einasto profile is similarly well fitted by a constant vertical DM density profile, and an NFW profile with a scale radius of 40 kpc even better.

For the bulk of this thesis we use galactocentric coordinate systems - either spherical $(r, \theta, \phi, v_r, v_\theta, v_\phi)$, (*e.g.* when we described the radial profiles of spherical DM halos in Section 1.4.7), or cylindrical $(R, \phi, z, v_R, v_\phi, v_z)$, which is used throughout this chapter. However astronomical observations will be inherently geocentric. The basic

observations are a star's position on the celestial sphere, given by *e.g.* right ascension α and declination δ; its distance from us d, derived from its parallax ω or from photometric measurements; its velocity across the celestial sphere, known as proper motions μ_α and μ_δ; and finally its velocity towards or away from us, referred to as the radial velocity $v_{r,\oplus}$ [437], where we have added the $\oplus$ subscript to avoid confusion with the galactocentric radial velocities v_r and v_R. Geocentric radial velocities $v_{r,\oplus}$ can be determined by measuring the redshifts or blueshifts of a star's spectral lines using a spectrometer, while proper motions across the sky are measured by comparing the positions of star at two different time points, and are generally less accurate than radial velocity measurements.

For stars directly above and below us in the disc plane, the paramount z-direction measurements correspond to distance d, measured through parallax or photometry, and radial velocity $v_{r,\oplus}$, measured with a spectrometer. However as we move away from the Sun in the (R, ϕ) plane the determination of v_z will become a function of radial velocities *and* less accurate proper motions. Thus most determinations of the local DM density select stars in a cone above and/or below us, such that v_z is dominated by radial velocity measurements and the impact of proper motions can be ignored (see *e.g.* Fig. 2 of [436]). This also limits the use of 1D vertical methods at other points in the disc plane, as they would be dependent on proper motion measurements.

There are several current astrometric surveys that have generated valuable data sets, and still better data lie in the future. The Sloan Digital Sky Survey (SDSS) at the Apache Point Obervatory (APO) has been running since 2000, collecting data on galaxy distribution (as seen earlier in Fig. 1.5), and also on stars and their distribution within the MW as part of the Sloan Extension for Galactic Understanding and Exploration (SEGUE) [438] and APO Galactic Evolution Experiment (APOGEE) [439] programmes. The complementary Radial Velocity Experiment (RAVE) at the Siding Spring Observatory in Australia is also collecting spectrometric data on MW stars, yielding observations from the Southern Hemisphere. Further data on the MW is being collected using the Large Sky Area Multi-Object Fibre Spectroscopic Telescope (LAMOST) at Xinglong Station in China. While proper motion information can be obtained from such survey data (for instance Ref. [440] combines SDSS-SEGUE data with historical data from the US Naval Observatory-B survey), their main strength lies in radial velocities.

The field of astrometrics is soon to be revolutionised by the advent of data from the Gaia satellite. Launched in 2013, the goal is to obtain 5D astrometric data (positions α and δ, proper motions μ_α and μ_δ, and parallax ω), for a billion stars down to an apparent magnitude[2] of ~ 20 (1% of the total number of stars in the MW), and radial

[2]Astronomers measure the brightness of stars in the *magnitude* scale, with higher (lower) numbers

velocities $v_{r,\oplus}$ for a subset of 150 million of the brightest stars. Gaia is a successor to the Hipparcos mission which operated from 1989 to 1993 and generated the Tycho-2 catalogue of 2.5 million stars [441]. The first data release of Gaia consisting of positions (α, δ) and magnitudes is expected at the end of the northern hemisphere summer of 2016. This data will be combined with data from the Tycho-2 catalogue to yield 5D astrometric data for 2.5 million stars of Tycho-2, giving us an early look into the Gaia-era [442, 443]. The final data release is scheduled for 2022.

Several surveys are underway or are planned that will complement the Gaia data, gathering radial velocity and elemental abundances for stars that are too dim for Gaia's spectrometer to measure. These include the Gaia-ESO survey, which began collecting data at the end of 2011 using the Very Large Telescope at the ESO site in Paranal, Chile [444]; the WEAVE spectrometer planned for the William Herschel Telescope on La Palma in the Canary Islands, which should begin data taking in 2018 [445]; and the 4-metre Multi-Object Spectroscopic Telescope (4MOST) planned for the VISTA telescope, also at the ESO Paranal site, which is scheduled to begin science operations in 2021 [446]. In 2023 the Large Synoptic Survey Telescope (LSST) will begin its 10 year survey programme, imaging the entire sky visible from its site in Cerro Pachón, Chile, every few nights. The LSST will serve as a deep complement to Gaia, giving 5D astrometric data for approximately 20 billion stars down to a magnitude of ~ 27 [447]. Given the coming Gaia data, its current and future spectrometric complements, and LSST, the future is indeed promising for astrometrics.

With the advent of large survey data such as those described above, local and global methods to determine the local DM density are beginning to converge [424, 422]. However robust differences between $\rho_{\rm DM}$ to $\rho_{\rm DM,ext}$ can provide insight into the shape of the Milky Way's DM halo, and thus into the formation of the galaxy [415]. First note that a local measurement gives $\rho_{\rm DM}$ in a small volume around the sun, while a global measurement gives the value for $\rho_{\rm DM}$ averaged over a spherical shell with radius equal to the Sun's galactocentric radius. If $\rho_{\rm DM}$ from local measurements is smaller than that extrapolated from global measurements, $\rho_{\rm DM,ext}$, then this implies a prolate halo, while the opposite would imply a squashed, oblate halo. The latter possibility could also result from the presence of an dark disc formed via accretion or by PIDM, or from some modified theories of gravity [*e.g.* 448, 449].

With sufficiently high quality data on tracer stars distributed vertically in the plane, and a robust map of the baryon distribution, it could be possible to probe non-constant vertical DM density profiles, moving from $\rho_{\rm DM}$ to $\rho_{\rm DM}(z)$. This could provide another

meaning fainter (brighter) stars. Absolute magnitude is a measure of how intrinsically bright an object is, while apparent magnitudes are how bright it appears to us in the sky, taking into account distance, dust absorption and the like. Differences in apparent magnitude m_i are linked to differences flux f_i via $m_1 - m_2 = -2.5 \log_{10}(f_1/f_2)$. The Sun has an apparent magnitude of -26.74, while Sirius, the brightest star in the sky has an apparent magnitude of -1.45 [437].

avenue to investigate the presence of an oblate halo or a dark disc.

Measurements of the local DM density date back almost 100 years [7]. The history of this measurement is one of both increasingly precise data and decreasingly strong assumptions. As such, the error bars on $\rho_{\rm DM}$ have not always shrunk with time, as better data often allows one to discard previous assumptions. With the advent of Gaia data from 2016 onwards we will have access to high precision data on individual stars, and the primary uncertainty in the determination of $\rho_{\rm DM}$ will be systematic model uncertainties. Recent results for the local DM density include [435], who used RAVE data to derive a value of $\rho_{\rm DM} = 0.0143 \pm 0.0011 {\rm M}_\odot {\rm pc}^{-3} = 0.542 \pm 0.042\,{\rm GeV cm}^{-3}$, and [434] who used SDSS/SEGUE data to find $\rho_{\rm DM} = 0.0065 \pm 0.0023 {\rm M}_\odot {\rm pc}^{-3} = 0.25 \pm 0.09\,{\rm GeV cm}^{-3}$. Note that these two results do not overlap within their stated uncertainties. The significance of this discrepancy is hard to interpret though, as they each use different data sets and analysis techniques, and both methodologies rely on rather different assumptions. To make progress we should endeavour to minimise the number of assumptions made, and apply the same analysis techniques to both data sets. More recently data from the LAMOST survey was used to find a local DM density of $\rho_{\rm DM} = 0.0159^{+0.0047}_{-0.0057} {\rm M}_\odot\,{\rm pc}^{-3} = 0.603^{+0.178}_{-0.216} {\rm GeV\,cm}^{-3}$ [436], compatible with the RAVE result, but not with that from SDSS/SEGUE.

4.4 Towards a New Local DM Density Method

The goal of this project is to limit the number of assumptions to a bare minimum, and hence reduce the systematic uncertainty on the local DM density. To achieve this we introduce a one-dimensional Jeans analysis method to probe the local DM density using the vertical motions of tracer stars. We construct a representation of the tracer density ν, and also allow for a DM density profile that is more complex than simply constant with height as previous local studies have assumed. Additionally, we deal with the so-called tilt term, which links radial and vertical motions of the tracer stars. This term is crucial to understand stellar motions at high-z, where the baryonic contribution falls off and DM becomes increasingly important. Using the vertical Jeans equation we calculate the velocity dispersion $\sigma_z(z)$ for each mass model, and then fit to data in ν, σ_z, and σ^2_{Rz} using MultiNest [356, 357, 450]. We test this method on mock data sets, and explore the impact of tracer star sample size, the tilt term, and non-constant DM profiles. The mock data for this work are 'as good as it gets' – we assume the population to have no observational biases and there to be no measurement error on individual stars – allowing us to isolate the effects of sampling error and model uncertainties. This is similar to what we will have with Gaia data, where the measurement errors on stars will be small compared to sampling error. We will explore the effect of adding realistic Gaia uncertainties to our method in future work.

We reiterate that this method is one dimensional, allowing us to keep assumptions to a minimum. However, we show that we are still able to deal with tilt and high-z data, which usually requires a 2-dimensional method. The key disadvantages of our method are that we bin data and thus lose information, a problem of Jeans analysis methods in general, and that our strictly local method cannot take advantage of the 'long lever arm' of a global model that would ensure, for example, that the DM density in radial slices close to the 'local volume' is continuous and smooth. However the effect of these disadvantages is to overestimate the errors on $\rho_{\rm DM}$, which is acceptable as we aim for a conservative and robust estimate of $\rho_{\rm DM}$. The alternative to binning and Jeans analysis is distribution function modelling, which fits a parameterised form of the distribution function $f(\mathbf{x}, \mathbf{v})$ directly to data (see [415] and references therein). This has the advantage of using all available data, but at the cost of assuming a functional form for $f(\mathbf{x}, \mathbf{v})$, however general it may be.

The remainder of this chapter is organised as follows: in Section 4.5 we outline the formalism of the Jeans equations on which our method is built. In Section 4.6 we introduce our particular method, covering our treatment of the rotation curve and tilt term, our our descriptions of the elements of our mass and tracer density models. We then outline our statistical analysis, introducing the framework for Bayesian parameter estimation and the MultiNest nested sampling code. In Section 4.7 we describe the array of mock data sets we use to test out methods. In Section 4.8 we present and discuss the results of our analyses, before finally drawing conclusions in Section 4.9.

4.5 Jeans equations

One of the fundamental sets of tools of galactic dynamics is the Jeans equations. The optimal piece of data to map the mass distribution of a system is the acceleration of particles, which determines the potential via

$$\mathbf{a} = -\nabla\Phi \tag{4.3}$$

However astrometric data only yields the positions and velocities of stars, and so we must find a method of linking these two quantities with the gravitational potential Φ. We do this by modelling the bulk motions of populations of stars as a collisionless fluid. This fluid is described by the collisionless Boltzmann equation,

$$\frac{\mathrm{d}f}{\mathrm{d}t} = \frac{\partial f}{\partial t} + \{f, H\} = 0, \tag{4.4}$$

where $f = f(\mathbf{x}, \mathbf{v}, t)$ is the phase space distribution function, defined such that $f(\mathbf{x}, \mathbf{v}, t)\mathrm{d}^3\mathbf{x}\mathrm{d}^3\mathbf{v}$ is the probability that at time t a given star has position and velocity in the ranges $\mathrm{d}^3\mathbf{x}$ and $\mathrm{d}^3\mathbf{v}$. The brackets $\{a, b\}$ are the Poisson brackets,

$$\{a, b\} \equiv \sum_i \left(\frac{\partial a}{\partial q_i}\frac{\partial b}{\partial p_i} - \frac{\partial a}{\partial p_i}\frac{\partial b}{\partial q_i} \right), \tag{4.5}$$

and the Hamiltonian of the system in cylindrical coordinates is given by

$$H(R, \phi, z, v_R, v_\phi, v_z, t) = \frac{1}{2}\left(v_R^2 + v_\phi^2 + v_z^2\right) + \Phi(R, \phi, z) \tag{4.6}$$

where $v_R = \dot{R}$, $v_\phi = R\dot{\phi}$, and $v_z = \dot{z}$, and Φ is the gravitational potential.

From Eq. 4.4 the set of three Jeans equations can be derived, as given in Appendix A. In full these are:

$$R: \quad 0 = \frac{\partial(\nu\,\overline{v_R})}{\partial t} + \frac{\partial(\nu\,\overline{v_R^2})}{\partial R} + \frac{1}{R}\frac{\partial(\nu\,\overline{v_R v_\phi})}{\partial \phi} + \frac{\partial(\nu\,\overline{v_R v_z})}{\partial z} + \frac{\nu}{R}\left(\overline{v_R^2} - \overline{v_\phi^2}\right) + \nu\frac{\partial \Phi}{\partial R}, \tag{4.7}$$

$$\phi: \quad 0 = \frac{\partial(\nu\,\overline{v_\phi})}{\partial t} + \frac{\partial(\nu\,\overline{v_R v_\phi})}{\partial R} + \frac{1}{R}\frac{\partial(\nu\,\overline{v_\phi^2})}{\partial \phi} + \frac{\partial(\nu\,\overline{v_\phi v_z})}{\partial z} + \frac{2\nu}{R}\overline{v_R v_\phi} + \frac{\nu}{R}\frac{\partial \Phi}{\partial \phi}, \tag{4.8}$$

$$z: \quad 0 = \frac{\partial(\nu\,\overline{v_z})}{\partial t} + \frac{\partial(\nu\,\overline{v_R v_z})}{\partial R} + \frac{1}{R}\frac{\partial(\nu\,\overline{v_\phi v_z})}{\partial \phi} + \frac{\partial(\nu\,\overline{v_z^2})}{\partial z} + \frac{\nu}{R}\overline{v_R v_z} + \nu\frac{\partial \Phi}{\partial z}. \tag{4.9}$$

where ν is the *tracer density* $\nu = \nu(\mathbf{x})$, the probability to find a star of any velocity at $\mathbf{x}$:

$$\nu(\mathbf{x}) \equiv \int \mathrm{d}^3\mathbf{v}\, f(\mathbf{x}, \mathbf{v}). \tag{4.10}$$

The *mean velocity* in direction i, also known as the first velocity moment, is

$$\overline{v_i}(\mathbf{x}) = \frac{1}{\nu(\mathbf{x})}\int \mathrm{d}^3\mathbf{v}\; v_i f(\mathbf{x}, \mathbf{v}), \tag{4.11}$$

while the second velocity moment is

$$\overline{v_i v_j}(\mathbf{x}) = \frac{1}{\nu(\mathbf{x})}\int \mathrm{d}^3\mathbf{v}\; v_i v_j f(\mathbf{x}, \mathbf{v}). \tag{4.12}$$

A useful quantity to introduce at this point is the *velocity-dispersion tensor* [410]:

$$\begin{aligned}\sigma_{ij}^2(\mathbf{x}) &\equiv \frac{1}{\nu(\mathbf{x})}\int \mathrm{d}^3\mathbf{v}(v_i - \overline{v_i})(v_j - \overline{v_j})f(\mathbf{x}, \mathbf{v}) \\ &= \overline{v_i v_j} - \overline{v_i}\,\overline{v_j}.\end{aligned} \tag{4.13}$$

This tensor is symmetric, and so it is possible to find a set of orthogonal axes $\hat{\mathbf{e}}_i(\mathbf{x})$ for which σ^2 is diagonal. These three axes $\hat{\mathbf{e}}_i(\mathbf{x})$ can be used to define the orientation of the *velocity ellipsoid*, and the eigenvalues of the tensor determine the length of the ellipsoid's semi-principal axes. The velocity ellipsoid will be discussed in greater depth in Section 4.6.5.

We now assume that the system is static, which means that partial time derivatives are zero, and that $\overline{v_R} = \overline{v_z} = 0$ *i.e.* the average velocity of stars in R- and z-directions is zero as there are an equal number of stars moving outwards and inwards radially, and moving upwards and downwards vertically. Under this assumption some elements of the velocity-dispersion tensor simplify to

$$\sigma_R^2 = \overline{v_R^2}, \quad \sigma_z^2 = \overline{v_z^2}, \quad \sigma_{R\phi}^2 = \overline{v_R v_\phi}, \quad \sigma_{Rz}^2 = \overline{v_R v_z}, \quad \text{and} \quad \sigma_{\phi z}^2 = \overline{v_\phi v_z}, \tag{4.14}$$

allowing Eqs. 4.7-4.9 to be rewritten as:

$$R: \quad 0 = \frac{1}{R}\frac{\partial(R\nu\,\sigma_R^2)}{\partial R} + \frac{1}{R}\frac{\partial(\nu\,\sigma_{R\phi}^2)}{\partial \phi} + \frac{\partial(\nu\,\sigma_{Rz}^2)}{\partial z} - \frac{\nu}{R}\overline{v_\phi^2} + \nu\frac{\partial \Phi}{\partial R}, \tag{4.15}$$

$$\phi: \quad 0 = \frac{1}{R^2}\frac{\partial(R^2\nu\,\sigma_{R\phi}^2)}{\partial R} + \frac{1}{R}\frac{\partial(\nu\,\overline{v_\phi^2})}{\partial \phi} + \frac{\partial(\nu\,\sigma_{\phi z}^2)}{\partial z} + \frac{\nu}{R}\frac{\partial \Phi}{\partial \phi}, \tag{4.16}$$

$$z: \quad 0 = \frac{1}{R}\frac{\partial(R\nu\,\sigma_{Rz}^2)}{\partial R} + \frac{1}{R}\frac{\partial(\nu\,\sigma_{\phi z}^2)}{\partial \phi} + \frac{\partial(\nu\,\sigma_z^2)}{\partial z} + \nu\frac{\partial \Phi}{\partial z}. \tag{4.17}$$

Note that in this work we follow the convention of [410] in labelling velocitiy dispersions; *i.e.* we write $\sigma_{Rz}^2 = \overline{v_R v_z} - \overline{v_R}\,\overline{v_z}$, as opposed to $\sigma_{Rz} = \overline{v_R v_z} - \overline{v_R}\,\overline{v_z}$, (*i.e.* without the square on σ_{Rz}). Thus σ_{ij}^2 has the units of $[\mathrm{km}^2\,\mathrm{s}^{-2}]$, which is appropriate for a covariance ($i \neq j$) or standard deviation ($i = j$) quantity. The latter convention was used in some previous works, such as [433] and the paper in which the bulk of this chapter first appeared [3].

4.6 Method

The broad picture of our problem is this: we have quantities derived from the motions of the tracer stars, namely ν, the tracer density, σ_z, the vertical velocity dispersion, and $\sigma_{R,z}^2$, the (R, z) velocity dispersion. Then we have elements of the mass profile, one of which is unknown – the DM density ρ_{DM}, and the other which is known within a band of uncertainty – the baryon density ρ_{baryon}. In this section we first derive the equations to link these quantities, and then describe how each is modelled.

4.6.1 Deriving a general 1D Jeans method

The starting point of our method is the static, z-direction Jeans equation (Eq. 4.17), which is moulded into

$$\underbrace{\frac{1}{R\nu}\frac{\partial}{\partial R}\left(R\nu\sigma_{Rz}^2\right)}_{\text{'tilt' term: } \mathcal{T}} + \underbrace{\frac{1}{R\nu}\frac{\partial}{\partial \phi}\left(\nu\sigma_{\phi z}^2\right)}_{\text{'axial' term: } \mathcal{A}} + \frac{1}{\nu}\frac{d}{dz}\left(\nu\sigma_z^2\right) = \underbrace{-\frac{d\Phi}{dz}}_{K_z}. \tag{4.18}$$

To reiterate, ν and σ_z are the density and vertical velocity dispersion profile of a tracer population as a function of height z above the disc plane, σ_{Rz}^2 is the cross term in the velocity dispersion tensor that couples radial and vertical motions, and $\sigma_{\phi z}^2$ is the cross term coupling vertical and axial motions.

Integrating both sides of equation Eq. 4.18, we derive our key equation for this work,

$$\sigma_z^2(z) = \frac{1}{\nu(z)}\int_0^z \nu(z')\left[K_z(z') - \mathcal{T}(z') - \mathcal{A}(z')\right]dz' + \frac{C}{\nu(z)} \tag{4.19}$$

where C is a normalisation parameter. For $z = 0$, we have that

$$\sigma_z^2(0)\nu(0) = C, \tag{4.20}$$

and so C simply sets the vertical velocity dispersion at $z = 0$. (Note that a similar but less general equation was derived recently in [433], Eq. 10.) We implement the constant C as a parameter in our model that we will ultimately marginalize over. The alternative would be to calculate C directly from Eq. 4.19, utilising the fact that as $z \to \infty$, $\nu(z) \to 0$, which gives us

$$C = -\int_0^\infty \nu(z')\left[K_z(z') - \mathcal{T}(z') - \mathcal{A}(z')\right]dz'. \tag{4.21}$$

However this would mean that the derived value for $\sigma_z(z)$ at some finite z would depend on the properties of our mass model, tilt and axial terms not just in the range $[0, z]$ but also for the range $[0, \infty)$.

Equation (4.19) is numerically appealing to solve since, unlike many previous methods [*e.g.* 451, 431], it does not require any numerical differentiation and is therefore rather robust to noise in the data. Furthermore, Eq. 4.19 is valid for *any gravity theory* and can therefore be used as a constraint on alternative gravity models. In this sense, we follow the early pioneering work of [452] who attempted to also measure K_z directly without reference to the Poisson equation.

To connect the vertical acceleration K_z to the surface mass density of the disc, however, we must specify a gravitational model. For standard Newtonian weak field

Source	Stellar Type	A	B
		$[\mathrm{km\,s^{-1}kpc^{-1}}]$	
[453]	K-M giants	14.5 ± 1.0	-11.5 ± 1.0
[454]	F giants	14.85 ± 7.47	-10.85 ± 6.83
[455]	G giants	14.05 ± 3.28	-9.30 ± 2.87

Table 4.1: Values of Oort constants. We include the F giants even though the errors for them are substantially larger to show that, within current uncertainties, the Oort constants A and B do not depend on stellar type.

gravity, this is given by the Poisson equation,

$$\nabla^2\Phi = \frac{\partial^2\Phi}{\partial z^2} + \underbrace{\frac{1}{R}\frac{\partial V_c^2(R)}{\partial R}}_{\text{'rotation curve' term: } \mathcal{R}} = 4\pi G\rho, \tag{4.22}$$

where $V_c(R)$ is the circular speed (rotation) curve at radius R, and ρ is the total matter density. Notice that for a flat rotation curve, $V_c = \text{const.}$, and the 'rotation curve' term $\mathcal{R}$ vanishes. If $\mathcal{R}$ does not vanish, then it appears as a shift (potentially as a function of height z) to the recovered $\rho_{\rm DM}$ that can be corrected for at the end of the calculation [431]. Equation (4.22) can be rewritten as

$$\frac{\partial^2\Phi}{\partial z^2} = 4\pi G\rho(z)_{\rm eff} \tag{4.23}$$

where

$$\rho(z)_{\rm eff} = \rho(z) - \frac{1}{4\pi GR}\frac{\partial V_c^2(R)}{\partial R}. \tag{4.24}$$

The contribution of this term to the mass density profile can be quantified via the Oort constants A and B [410]:

$$\frac{1}{4\pi GR}\frac{\partial V_c^2(R)}{\partial R} = \frac{B^2 - A^2}{2\pi G}. \tag{4.25}$$

Note that $|B| < |A|$, meaning that the terms in Eq. 4.25 are negative. Thus the effective density $\rho(z)_{\rm eff}$ will be higher with the inclusion of a non-zero rotation curve term. If the rotation curve term is erroneously neglected it will be absorbed into the density profile, yielding an over-estimate of the DM density, assuming the baryonic contribution is well constrained. Taking the most precise values for A and B from Table 4.1 [453] yields a value for Eq. 4.25 of $\sim 0.1\,\mathrm{GeV}/c^2$, which is roughly a third of the expected local DM density [*e.g.* 415]. For any accurate measure of the local DM density derived from real data we will need to incorporate this correction, but we leave this for future work.

Neglecting $\mathcal{R}$ and integrating both sides of Eq. 4.22, we derive the familiar result of

$$\Sigma_z(z) = \frac{|K_z|}{2\pi G}, \tag{4.26}$$

where $\Sigma_z(z)$ is the surface mass density of the disc.

The overall flow of our method is now apparent. We model i. the tracer density $\nu(z)$; ii. the mass density distribution $\rho(z) = \rho_{\rm DM}(z) + \rho_{\rm baryon}(z)$ (which gives us the K_z term); iii. the tilt term $\mathcal{T}(z)$; and iv. the axial term $\mathcal{A}(z)$. These elements each have a number of parameters, and so in total each model will have an N-dimensional parameter space. After picking a point in this parameter space we can calculate the values for the elements i. to iv. across the range of z-values, which for this study are the bin centres. Elements i. to iv. can then be inserted into Eq. 4.19 to derive $\sigma_z^2(z)$ for that parameter space point. We then compare $\nu(z)$ and $\sigma_z^2(z)$ (and $\sigma_{Rz}^2(z)$ and $\sigma_{\phi z}^2(z)$ as part of the tilt term and axial term models) to data via a χ^2 test, and then update our parameter space point.

Note that the only assumptions that go into Eq. 4.19 are that the motions of stars obey the collisionless Boltzmann equation, and that the galaxy is in dynamic equilibrium. The assumption of dynamic equilibrium can be negated somewhat by the presence of disequilibria ('wobbling') in the disc caused by *e.g.* the Sagittarius merger [456, 457] or in part by the presence of spiral arms [458]. However the impact of these effects on the measurement of the local DM density is estimated to be approximately 10% [459, 415], less than the corrections arising from the tilt and rotation curve terms.

In practice further assumptions are necessary to model the individual components on the RHS of Eq. 4.19. However this method can accommodate almost any model for each of these elements – the only strict requirement is that each element can be defined at the z-values corresponding to the centres of the bins used to calculate the tracer density and velocity dispersion. Hence we call this method 'non-parametric' – we can in principle have many more parameters for each model than there are data points. In the following sections we describe how we model each element for this particular study. In Section 4.6.7 we discuss model selection using the Bayesian evidence, which could potentially allow us to compare alternate models.

As the galaxy is close to being axisymmetric in both the thin disc [460, 461, 462, 463, 464, 465] and the thick disc [466, 467], the axial term $\mathcal{A}(z)$ is expected to be small. For this study we assume complete axisymmetry, and thus take $\mathcal{A}(z) = 0$. If the data shows significant non-axisymmetry in the Milky Way, the axial term could be modelled in a similar way to the tilt term as described below.

In the context of the Milky Way non-negligible axial terms at the solar position would arise from non-axisymmetric features such as spiral arms, perturbations driven by the bar, or a warping of the disc. Such features are time dependent, implying that

if $\mathcal{A}(z) \neq 0$, we should also worry about the time dependence of the gravitational potential $\Phi(t)$ and, therefore, also the partial time derivative of the distribution function $\partial f/\partial t$ [*e.g.* 468]. It is not clear if there can exist a regime in which $\mathcal{A}(z) \neq 0$ and such time dependence can be ignored. Here, we simply note that since empirically $\mathcal{A}(z) \ll \mathcal{T}(z)\,\forall z$ [*e.g.* 466, 464], to leading order we can also safely neglect the time dependence of the distribution function, as we have already done.

4.6.2 Tracer density model

To apply the Jeans equations we bin data in z to obtain the tracer density ν and the velocity dispersions σ_z and σ^2_{Rz}. Thus at a bare minimum we only have to define ν and σ^2_{Rz}, and derive σ_z via Eq. 4.19, at the bin centers, *i.e.* at a discrete set of z values.

For this work we model the tracer density as a sum of N exponential discs:

$$\nu(z) = \sum_i \nu(0)_i \exp\left(-\frac{z}{h_i}\right), \tag{4.27}$$

where for the i^{th} disc $\nu(0)_i$ is the tracer density at $z = 0$ and h_i is the scale height. The number of exponential discs can be increased until the Bayesian evidence shows no improvement (see Section 4.6.7). This method avoids overfitting as each disc is smooth, while still giving freedom to describe more complex data. If we were working with multiple populations each with distinct velocity dispersion profiles, for instance 'thick' and 'thin' disc samples, or multiple MAPs as discussed earlier, we would apply one copy of 4.27 per population, *i.e.* each population would be described by its own sum of exponentials. From this point onwards we consider only $z \geq 0$.

4.6.3 Baryon parameterisation

For this study we use a simple 2-parameter model to describe the baryon distribution[3]:

$$\rho_{\text{baryon}}(z) = \frac{1}{4\pi G}\left|\frac{K_{\text{bn}} D^2_{\text{bn}}}{(D^2_{\text{bn}} + z^2)^{1.5}}\right|. \tag{4.28}$$

The K_{bn} parameter sets the mass of the disc, and has dimensions of acceleration, while D_{bn} controls the scale height of the disc, and has dimensions of length. Expressed in terms of the K_z parameter of Eq. 4.19, the baryon profile becomes

$$K_{z,\text{baryon}} = -\left[\frac{K_{\text{bn}} z}{\sqrt{z^2 + D^2_{\text{bn}}}}\right]. \tag{4.29}$$

[3] In the context of the values of the prior ranges given in Table 4.4 below the gravitational constant equals $G = 4.229 \times 10^{-6} \text{km}^2\,\text{kpc}\,\text{M}_\odot^{-1}\text{s}^{-2}$.

While this model is not likely realistic for the Milky Way [469, 414], it has been applied to observational data by [470, 428], and also more recently by [434]. When applying our method to real data we will consider more sophisticated baryon models, but for this initial study where we are primarily interested in testing our methodology, Eq. 4.29 will suffice.

The stellar populations we take as kinematical tracers would be a subset of the total baryon profile of the MW. Ongoing and future surveys such as Gaia, WEAVE, 4MOST, and LSST will not only give us better kinematic data, helping constrain the total mass distribution, but also improve the stellar component of baryonic mass models, helping constrain the DM mass.

4.6.4 Dark Matter parameterisation

The simplest way to parameterise the DM density profile $\rho_{\rm DM}$ is to assume it is constant with z, as done in previous work [*e.g.* 427, 470, 428, 430, 451, 431]. This assumption works well at low z: as mentioned earlier, for a spherical NFW halo with a scale radius of 20 kpc the midplane value is correct within 10% up to a height of $z \sim 3$ kpc. For some analyses we also make this assumption, and set $\rho_{\rm DM}(z) = \rho_{\rm DM,const.}$.

However, this assumption does not allow for the exploration of several interesting effects such as a flattened, oblate halo or a dark disc. To accommodate such phenomena we add a dark disc (DD) on top of the constant DM. The dark disc is described using the same disc model as we use for the baryons, yielding a total DM profile:

$$\rho_{\rm DM}(z) = \rho_{\rm DM,const.} + \frac{1}{4\pi G}\left|\frac{K_{\rm DD} D_{\rm DD}^2}{(D_{\rm DD}^2 + z^2)^{1.5}}\right|. \tag{4.30}$$

To ensure this disc does not simply become degenerate with the baryonic disc we give the scale height $D_{\rm DD}$ a higher prior range than that for $D_{\rm bn}$. In terms of the K_z parameter of Eq. 4.19, the DM profile is

$$K_{z,\rm DM} = -\left[2Fz + \frac{K_{\rm DD} z}{\sqrt{z^2 + D_{\rm DD}^2}}\right] \tag{4.31}$$

where $F = 2\pi G \rho_{\rm DM,const}$. This disc parameterisation of the non-constant DM profile can describe both the accreted dark disc and a flattened DM halo, and so henceforth we refer only to a 'dark disc'.

Additional dark disc terms could in principle be added to $\rho_{\rm DM}(z)$ with parameters $K_{{\rm DD},n}$ and $D_{{\rm DD},n}$, giving a total density profile of

$$\rho_{\rm DM}(z) = \rho_{\rm DM,const.} + \frac{1}{4\pi G}\sum_n \left|\frac{K_{{\rm DD},n} D_{{\rm DD},n}^2}{(D_{{\rm DD},n}^2 + z^2)^{1.5}}\right|. \tag{4.32}$$

The prior ranges on the n^{th} dark disc parameters $K_{\text{DD},n}$ and $D_{\text{DD},n}$ can be set in relation to those of the $(n-1)^{\text{th}}$ dark disc, *e.g.* requiring $K_{\text{DD},n} < K_{\text{DD},n-1}$, meaning each dark disc is less massive than the previous one. The number of dark discs to add could be determined from the data via the Bayesian evidence, with dark disc terms being added up until this degrades significantly. For this study however we limit ourselves to one dark disc term.

4.6.5 The Velocity Ellipsoid and the Tilt Term

Previously in Section 4.5 we introduced the velocity dispersion tensor, and also the velocity ellipsoid, whose orientation is defined by the axes $\hat{\mathbf{e}}_i(\mathbf{x})$ which diagonalise the velocity dispersion tensor $\sigma^2_{ij}(\mathbf{x})$. The velocity dispersion tensor appears in the tilt term of Eq. 4.18, and is a crucial element of the analysis presented here.

The orientation of the velocity ellipsoid at points above the disc plane lies somewhere between the extreme cases of having its principal axes aligned with the cylindrical coordinates (R, ϕ, z), or aligned with the spherical coordinates (r, θ, ϕ) [410, Section 4.8.2]. The orientation can be parameterised by the tilt angle α_{Rz} and vertex deviation angle $\alpha_{R\phi}$, calculated from the velocity dispersion tensor as

$$\alpha_{ij}(\mathbf{x}) = 0.5 \arctan\left(\frac{2\sigma^2_{ij}(\mathbf{x})}{\sigma^2_i(\mathbf{x}) - \sigma^2_j(\mathbf{x})}\right), \tag{4.33}$$

where $\mathbf{x} = (R, \phi, z)$. As we assume axisymmetry for this analysis, the vertex deviation angle is ignored here. If there is no radial-vertical coupling, we have $\sigma^2_{Rz} = 0$, and thus $\alpha_{Rz} = 0$.

There have been a number of previous measurements of the tilt angle and the velocity dispersion for a variety of stellar types, the results of which are listed in Table 4.2. Several of the measurements (Refs. [471, 472, 440]) combine measurements from both positive and negative z (eg above and below the plane) and quote results for $|z|$. There is also an apparent inconsistency in the sign of the tilt angle α_{Rz} and velocity dispersion σ^2_{Rz} in regards to the sign of z. For instance [472] quotes positive values for the α_{Rz} for both positive and negative z, and both [433] and [440] give negative values for α_{Rz} but quote negative and positive values for z respectively. Given that the sign of the tilt term $\mathcal{T}$ is dependent on the sign of σ^2_{Rz}, as is the sign of the tilt angle via the antisymmetric arctan function, a rigorous exploration of this topic is in order.

First we establish the details of our velocity ellipsoid. Following the convention of [474] we define the longest axis in the (R, z) plane as $\sigma^2_1(R, z)$ in the direction of $\hat{\mathbf{e}}_1$, and the shorter axis as $\sigma^2_3(R, z)$ in the perpendicular direction of $\hat{\mathbf{e}}_1$, as shown in

Source	Sample	z [kpc]	$\alpha_{Rz}[^\circ]$	$\pm$ cor.	$\sigma^2_{Rz}\,[\mathrm{km^2\,s^{-2}}]$	$\pm$ cor.
[473]		$z \in [-0.5, -1.5]$	7.3 ± 1.8	$(-)$		
[471]	$[\mathrm{Fe/H}] \in [-0.8, -0.6]$	$\lvert z\rvert \in [1, 2]$	7.1 ± 1.5			
		$\lvert z\rvert \in [2, 4]$	5.2 ± 1.2			
	$[\mathrm{Fe/H}] \in [-1.5, -0.8]$	$\lvert z\rvert \in [1, 2]$	10.3 ± 0.4			
		$\lvert z\rvert \in [2, 4]$	15.1 ± 0.3			
	$[\mathrm{Fe/H}] < -1.5$	$\lvert z\rvert \in [1, 2]$	8.6 ± 0.5			
		$\lvert z\rvert \in [2, 4]$	13.1 ± 0.4			
[472]		$z \in [0.7, 2]$	6.3 ± 4.9			
		$z \in [-2, -0.7]$	8.8 ± 1.9	$(-)$		
		$\lvert z\rvert \in [0.7, 2]$	$8.6 \pm 1.8^\dagger$			
[433]	$[\mathrm{Fe/H}] \in [-0.5, 0.2]$	$z = -0.59$	$-5.6^{+2.1}_{-2.1}$		$-99.5^{+36.8}_{-36.8}$	
		$z = -0.86$	$-14.6^{+2.9}_{-2.8}$		$-322.5^{+66.6}_{-66.7}$	
		$z = -1.11$	$-12.0^{+4.1}_{-4.1}$		$-242.3^{+85.6}_{-86.5}$	
		$z = -1.53$	$-12.4^{+3.5}_{-3.5}$		$-362.9^{+104.2}_{-106.0}$	
	$[\mathrm{Fe/H}] \in [-0.8, -0.5]$	$z = -0.59$	$-12.7^{+4.6}_{-4.6}$		$-193.6^{+71.9}_{-70.9}$	
		$z = -0.96$	$-10.2^{+8.3}_{-8.4}$		$-154.0^{+127.6}_{-127.8}$	
		$z = -1.26$	$-8.7^{+6.3}_{-6.4}$		$-181.0^{+133.7}_{-135.0}$	
		$z = -1.69$	$-9.7^{+5.6}_{-5.5}$		$-311.3^{+179.3}_{-179.8}$	
[440, V1]	$[\mathrm{Fe/H}] = -0.07$	$z = 449 \pm 124$	-3.0 ± 2.9	$(+)$	-40 ± 40	$(+)$
	$\&\,[\alpha/\mathrm{Fe}] = 0.11$	$z = 565 \pm 89$	-4.1 ± 2.8	$(+)$	-61 ± 42	$(+)$
		$z = 667 \pm 83$	-4.8 ± 2.6	$(+)$	-84 ± 45	$(+)$
		$z = 766 \pm 97$	-5.1 ± 2.5	$(+)$	-92 ± 46	$(+)$
		$z = 966 \pm 357$	-6.3 ± 2.9	$(+)$	-110 ± 45	$(+)$
	$[\mathrm{Fe/H}] = -0.89$	$z = 817 \pm 272$	-10.6 ± 4.3	$(+)$	-407 ± 179	$(+)$
	$\&\,[\alpha/\mathrm{Fe}] = 0.34$	$z = 1093 \pm 230$	-8.5 ± 4.2	$(+)$	-344 ± 179	$(+)$
		$z = 1378 \pm 242$	-12.0 ± 4.7	$(+)$	-468 ± 202	$(+)$
		$z = 1675 \pm 251$	-6.4 ± 3.4	$(+)$	-337 ± 186	$(+)$
		$z = 2113 \pm 583$	-15.3 ± 1.4	$(+)$	-927 ± 68	$(+)$

Table 4.2: Data regarding the tilt angle α_{Rz} and velocity dispersion σ^2_{Rz}. †: velocity error bias correction applied.

z	$\hat{\mathbf{e}}_i$	v_R	v_z	$v_R v_z$
+	$\hat{\mathbf{e}}_1$	+	+	+
		−	−	+
	$\hat{\mathbf{e}}_3$	−	+	−
		+	−	−
−	$\hat{\mathbf{e}}_1$	+	−	−
		−	+	−
	$\hat{\mathbf{e}}_3$	+	+	+
		−	−	+

Table 4.3: Sign of Tilt Term

Fig. 4.3. The roughly radial alignment of the long axis $\hat{\mathbf{e}}_1$ is both seen in data [474], but is also a natural expectation for a disc galaxy. A larger velocity dispersion in the radial direction makes sense in a disc galaxy, because if the opposite were true the disc would puff-up and tear itself apart.

Taking the orientation of the velocity ellipsoid alone we can perform a consistency check on what sign σ^2_{Rz} should have. The velocity ellipsoid is a representation of a statistical quantity, and extension in one particular direction means the population tends in that direction. Taking the top ellipsoid of Fig. 4.3 we can see that direction $\hat{\mathbf{e}}_1$ corresponds to stars with either positive v_R and positive v_Z, or negative v_R and negative v_Z, always yielding positive $v_R v_z$. Direction $\hat{\mathbf{e}}_3$ corresponds to negative v_R and positive v_z, or positive v_R and negative v_z, always yielding negative $v_R v_z$. These options are laid out in Table 4.3. Given that $\sigma_1^2 > \sigma_3^2$ the average value $\overline{v_R v_z}$ should be positive, and assuming negligible values for $\overline{v_R}$ and $\overline{v_z}$ (*i.e.* the MW is close to static), σ^2_{Rz} should also be positive.

For negative z the outcomes are reversed. The direction $\hat{\mathbf{e}}_1$ corresponds now to positive v_R and negative v_Z, or negative v_R and positive v_Z, while $\hat{\mathbf{e}}_3$ corresponds to v_R and v_z that are either both positive or both negative. Again these options are shown in Table 4.3. With $\sigma_1^2 > \sigma_3^2$ still the case, the average value of $\overline{v_R v_z}$, and thus the static of σ^2_{Rz}, should be negative in the case of negative z.

The tilt angle is defined as the angle between $\hat{\mathbf{e}}_1$ and the horizontal, as shown in Fig. 4.3. As noted previously, the R-direction velocity dispersion σ_R^2 is larger than that in the z-direction σ_z^2, and so the denominator on the RHS of Eq. 4.33 is always positive. As arctan is antisymmetric, α_{Rz} will have the same sign as σ_{Rz}, and thus should also be positive for positive z and negative for negative z.

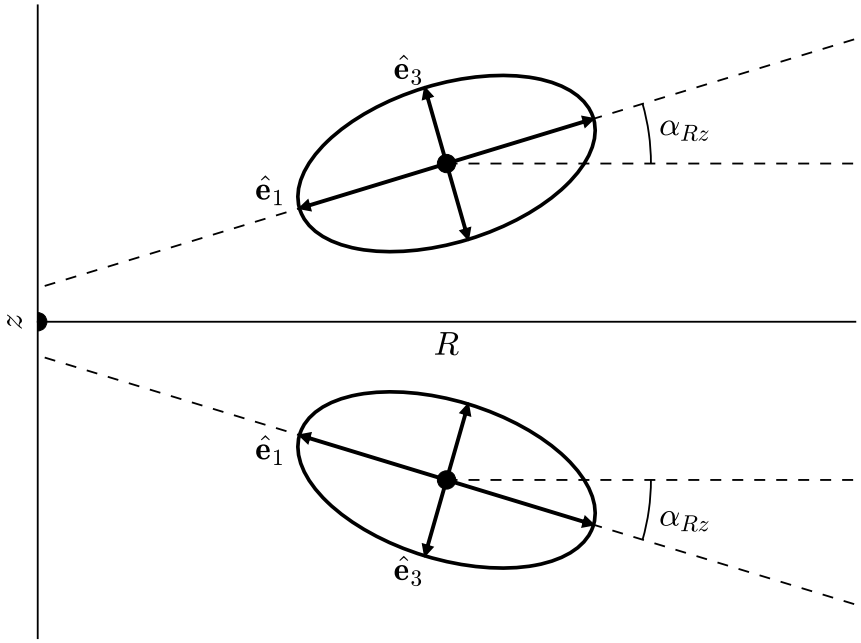

Figure 4.3: Sign of the Tilt Term

This consistency check reveals that the some of the data presented in Table 4.2 requires sign corrections, which are applied in the table in the columns labeled "± cor.". The tilt angle presented in [473] should technically be $\alpha_{Rz} = -7.3° \pm 1.8°$, as it is measured at negative z. Similarly the negative z measurement of [472] should also be negative. Reference [440] combines data from both above and below the disc, and so for a positive z (as the values of $|z|$ are taken) the tilt angle α_{Rz} and velocity dispersion σ^2_{Rz} should be positive.

4.6.6 Modelling the Tilt term

The importance of the tilt term has been noted previously, *e.g.* [470, 475, 440]. Here we demonstrate that it is possible to deal with this term while remaining within our vertical, one-dimensional framework. Given the data quality currently available for the Milky Way we are required to make a well-motivated assumption about the radial form of $\mathcal{T}$, but in the Gaia-era we will be able to directly measure this from the data.

Figure 4.4: *(Opposite) Top:* σ^2_{Rz} for two populations of G-type dwarf stars in the solar neighbourhood from the SDSS/*SEGUE* survey [440, V1]. The blue data points are from a younger, high metallicity population, with $\overline{[\mathrm{Fe/H}]} = -0.07$ and $\overline{[\alpha/\mathrm{H}]} = 0.11$, while the data points in red are from an older, low metallicity population with $\overline{[\mathrm{Fe/H}]} = -0.89$ and $\overline{[\alpha/\mathrm{H}]} = 0.34$. The blue and red lines are power laws in the form of Eq. 4.38 fitted to the blue and red data points respectively. The older, lower metallicity stars probe further above the disc plane. Dashed lines indicate extrapolation from data. *Bottom:* The importance of tilt, as quantified by Eq. 4.41. The blue and red lines correspond to tilt terms derived from the high and low metalicity population fits of (a). The deviation arising from the tilt term increases more rapidly with height for the low metallicity population (red line), which probes the high-z region most useful for determining the DM profile. Dashed lines indicate extrapolation from data. For this case $R_0 = R_1 = 2.5$ kpc., and $F = 267.65\,\mathrm{km^2\,kpc^{-2}\,s^{-2}}$.

We first assume that the radial profiles of the tracer density and the (R, z)-velocity dispersion are exponentials with scale radii of R_0 and R_1, respectively:

$$\nu(R,z) = \nu(z)|_{R_\odot} \exp\left(-\frac{R-R_\odot}{R_0}\right), \tag{4.34}$$

$$\sigma^2_{Rz}(R,z) = \sigma^2_{Rz}(z)\big|_{R_\odot} \exp\left(-\frac{R-R_\odot}{R_1}\right). \tag{4.35}$$

With this assumption the tilt term becomes

$$\mathcal{T}(R,z) = \sigma^2_{Rz}(z)\big|_{R_\odot} \exp\left(-\frac{R-R_\odot}{R_1}\right)\left[\frac{1}{R}-\frac{1}{R_0}-\frac{1}{R_1}\right] \tag{4.36}$$

$$= \sigma^2_{Rz}(R,z)\left[\frac{1}{R}-\frac{1}{R_0}-\frac{1}{R_1}\right]. \tag{4.37}$$

If the disc were observed not to be an exponential then an alternative model could be easily applied at this stage. Indeed, similar but more complex models have featured previously in the literature, *e.g.* [474].

We then model the (z)-velocity dispersion as a power law at a given galactocentric radius R:

$$\sigma^2_{Rz}(z)\big|_R = A\left(\frac{z}{\mathrm{kpc}}\right)^n\Bigg|_R. \tag{4.38}$$

The tilt term thus becomes

$$\mathcal{T}(R,z) = A\left(\frac{z}{\mathrm{kpc}}\right)^n\Bigg|_R \exp\left(-\frac{R-R_\odot}{R_1}\right)\left[\frac{1}{R_\odot}-\frac{1}{R_0}-\frac{1}{R_1}\right]. \tag{4.39}$$

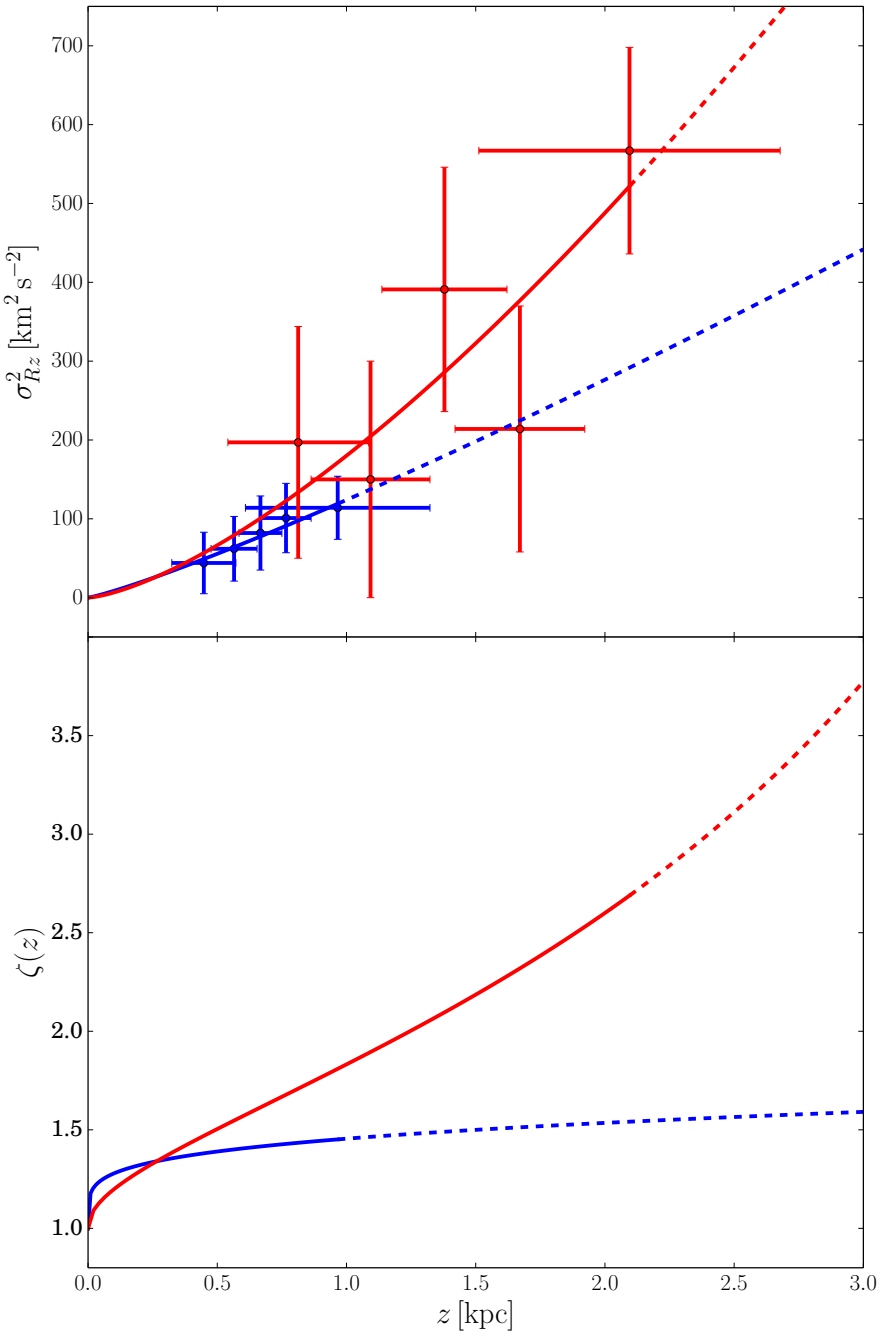
700
600
500
400
300
200
100
0
σ^2_{Rz} [km^2 s^{-2}]
3.5
3.0
2.5
2.0
1.5
1.0
$\zeta(z)$
0.0
0.5
1.0
1.5
2.0
2.5
3.0
z [kpc]

Figure 4.4

To model the tilt term at the solar position we take $R = R_\odot$, and also $R_0 = R_1$, simplifying the tilt term to a model described by the parameters A, n, and R_0:

$$\mathcal{T}(R_\odot, z) = A \left(\frac{z}{\mathrm{kpc}} \right)^n \Big|_{R_\odot} \left[\frac{1}{R_\odot} - \frac{2}{R_0} \right]. \tag{4.40}$$

Note that we are not affected by the assumption $R_0 = R_1$ since these two parameters are trivially degenerate in Eq. 4.40. It remains the case that any observational constraints on R_0 and/or R_1 can be used as priors on Eq. 4.40, where these would constrain the term $2/R_0$. The description of $\sigma^2_{Rz}(z)$ of Eq. 4.38 fulfils $\sigma^2_{Rz}(z = 0) = 0$ by construction and fits remarkably well to different populations, as shown in the top panel of Fig. 4.4. This figure presents (z, σ^2_{Rz}) data points for high and low metallicity populations (blue and red points respectively) from the SDSS/*SEGUE* survey as analysed and presented in [440, V1], and listed in Table 4.2. We also apply the sign correction discussed above in Section 4.6.5[4]. The high metallicity sample has $\overline{[\mathrm{Fe/H}]} = -0.07$ and $\overline{[\alpha/\mathrm{H}]} = 0.11$, while the low metallicity sample has $\overline{[\mathrm{Fe/H}]} = -0.89$ and $\overline{[\alpha/\mathrm{H}]} = 0.34$. Metallicity can be used as a proxy for age, with the high metallicity sample being younger than the older, low metallicity population [*e.g.* 476].

Taking these data points we fit power laws models as per Eq. 4.38, with parameters $A = 123.99\,\mathrm{km^2\ s^{-2}}$, $n = 1.16$ for the high metallicity population (blue) and $A = 180.08\,\mathrm{km^2\ s^{-2}}$, $n = 1.44$ for the low metallicity population (red). The low metallicity population samples further above the disc plane and populates the canonical thick disc of the Milky Way. Populations such as this are more interesting for local DM searches as they allow us to probe higher z regions where the baryon mass contribution begins to drop away leaving behind the DM halo. However as we go higher in the disc the tilt term becomes increasingly important, as illustrated by the bottom panel of Fig. 4.4, which shows the variable $\zeta(z)$, defined as

$$\zeta(z) = \frac{K_{z,\mathrm{DM}}}{K_{z,\mathrm{DM}} - \mathcal{T}}, \tag{4.41}$$

where $K_{z,\mathrm{DM}} = -2Fz$, the constant DM density term, with $F = 267.65\,\mathrm{km^2\,kpc^{-2}\,s^{-2}}$ and $R_0 = R_1 = 2.5$ kpc, the same values as are used to later generate our mock data in Section 4.7. Compared to the thin disc population (blue line), the effects of the tilt term become important at much lower z values. In short, to probe local DM we want to use thick disc stars probing higher-z ranges, but the cost is that we must include the tilt term in our analyses.

Ignoring the tilt term will always cause an underestimation of the local DM density, if all other components of the model such as baryons are held steady. Looking at

[4]Confirmed by private communication with authors of [440].

Eq. 4.40, we note that $R_0 < R_\odot$ and $A > 0$, meaning the tilt term $\mathcal{T}(R_\odot, z)$ is always negative. Then considering Eq. 4.19 we see that to fit to $\sigma_z^2(z)$ in the absence of the tilt term $\mathcal{T}(z')$, the $K_z(z')$ term, a negative term, is forced to become less negative in order to compensate. This requires a lower mass density, which if the baryon density profile is held constant, manifests itself as a decrease in the DM mass density.

Here we also see the importance of the consistency check on the tilt angle and (R, z) velocity dispersion performed above. A change in sign on σ_{Rz}^2 would cause a similar change in sign for the tilt term $\mathcal{T}(R, z)$. The reasoning just given would be reversed, and a neglected tilt term contribution would cause an increase in the reconstructed DM density.

4.6.7 Statistical analysis and MultiNest

The model outlined above gives us an N-dimensional parameter space. To explore this parameter space and derive limits on the various observables we adopt nested sampling [477] as implemented in the publicly available MultiNest code [356, 357, 450]. MultiNest is a tool for Bayesian inference and parameter estimation. Bayes Theorem is

$$P(\theta|D, \mathcal{M}) = \frac{P(D|\theta, \mathcal{M})P(\theta|\mathcal{M})}{P(D|\mathcal{M})} \tag{4.42}$$

where $\mathcal{M}$ is the given model, θ is the set of parameters for that model, and D is the data. The left hand side, $P(\theta|D, \mathcal{M})$ is known as the *posterior*, while the three terms on the right are the *likelihood* $P(D|\theta, \mathcal{M}) = \mathcal{L}(\theta)$, the *prior* $P(\theta|\mathcal{M})$, and the *Bayesian evidence* $P(D|\mathcal{M})$.

The Bayesian evidence, a.k.a. the marginal or model likelihood, is a measure of how well the model performs given the data, and can be expressed as

$$\mathcal{Z} = P(D|\mathcal{M}) = \int P(D|\theta, \mathcal{M})P(\theta|\mathcal{M})d\theta. \tag{4.43}$$

The performance of two different models given the same data can be compared using the *Bayes factor*:

$$B_{01} = \frac{P(D|\mathcal{M}_0)}{P(D|\mathcal{M}_1)}. \tag{4.44}$$

Assuming Gaussian errors it is possible to derive an empirical scale relating the Bayes factor to the strength of evidence for one model over another, as done in [478]. There, a $|\ln B_{01}|$ value of less than 1 is considered inconclusive, while values of 1.0, 2.5 and 5.0 are considered to give weak, moderate and strong evidence, respectively.

MultiNest takes a given prior probability distribution and likelihood function and calculates the posterior distribution and Bayesian evidence. Our likelihood function

is based on the χ^2 distribution:

$$\mathcal{L}(\theta) = \exp\left(\frac{-\chi^2}{2}\right). \tag{4.45}$$

The value of χ^2 is simply

$$\chi^2 = \chi^2_\nu + \chi^2_{\sigma_z^2} + \chi^2_{\sigma^2_{Rz}}, \tag{4.46}$$

where

$$\chi^2_\nu = \sum_j \frac{(\nu_{\mathrm{data},j} - \nu_{\mathrm{model},j})^2}{SD^2_{\nu,j}}, \tag{4.47}$$

$$\chi^2_{\sigma_z^2} = \sum_j \frac{(\sigma^2_{z,\mathrm{data},j} - \sigma^2_{z,\mathrm{model},j})^2}{SD^2_{\sigma_z^2,j}}, \tag{4.48}$$

$$\chi^2_{\sigma^2_{Rz}} = \sum_j \frac{(\sigma^2_{Rz,\mathrm{data},j} - \sigma^2_{Rz,\mathrm{model},j})^2}{SD^2_{\sigma^2_{Rz},j}}. \tag{4.49}$$

Note that if the reconstruction model does not contain a tilt term (*e.g.* $\mathcal{T} = 0$) then $\chi^2_{\sigma_{Rz}}$ is set to zero.

Table 4.4 shows the prior ranges used for our analyses. The kinematics of stars is driven by the total potential, and is agnostic to whether it is generated by baryons or DM. For a study using kinematic data alone, as we do here, the baryon distribution is accounted for as a prior over which we marginalize. For our simplified baryon model we use a Gaussian prior, resembling an observational model with a ∼10% error. The other priors are set to be flat with generous ranges around the mock data values, except for the stellar disc scale length R_0. As will be discussed further in Section 4.8.3, we are able to fit for the tilt parameters A and n using G-type dwarf data from [440], but R_0, which controls the radial profile of σ^2_{Rz} in our model, remains unconstrained. Hence we use a canonical value from [410] as a prior, but with future Gaia data the radial profile of σ^2_{Rz} will be directly measurable. We also set a lower limit on the dark disc scale height, as it has the same functional form as the baryonic disc, and thus with no lower bound would become completely degenerate with it.

We derive credible regions (CRs) for the DM density parameters by taking its posterior distribution and marginalising over the remaining parameters. As outlined above our model has several components that can be turned on or off, such as the dark disc. Using the Bayesian evidence as calculated by MultiNest it is potentially possible to perform model comparison to determine which reconstruction model best fits the data. This idea will be explored in greater depth in subsequent studies.

Model Parameter		Range *or* Gaussian μ & SD	Type
Baryons	$K_{\rm bn}$	$\mu = 1500$, $SD = 150$	Gaussian
	$D_{\rm bn}$	$\mu = 0.18$ kpc, $SD = 0.02$ kpc	Gaussian
Constant DM	$\rho_{\rm DM}$	$[2, 20] \times 10^{-3}\,{\rm M}_\odot\,{\rm pc}^{-3}$ $[0.076, 0.796]\,{\rm GeV\,cm}^{-3}$	Linear
Dark Disc	$K_{\rm DD}$	[0, 1500]	Linear
	$D_{\rm DD}$	[1.5, 3.5] kpc	Linear
Tilt term	A	[0, 200] ${\rm km}^2\,{\rm s}^{-1}$	Linear
	n	[1.0, 1.9]	Linear
	R_0	$\mu = 2.5$ kpc, $SD = 0.5$ kpc	Gaussian [410]
Tracer density	$\nu(0)$	$[0,\ \nu_0 + 2 \times SD_{\nu,0}]$	Linear
	h	[0.4, 1.4] kpc	Linear
Velocity disp.	$\sigma_z(0)$	$[\sigma_{z,0} - 2 \times SD_{\sigma_z,0},$ $\sigma_{z,0} + 2 \times SD_{\sigma_z,0}]$ km s^{-1}	Linear

Table 4.4: Prior ranges for parameters. Gaussian priors are described by a median μ and a standard deviation SD. Note that $\nu(0)$ and $\sigma_z(0)$ are the tracer density and velocity dispersion at $z = 0$, while quantities subscripted with 0, such as ν_0 and $SD_{\nu,0}$, are the values derived from data in the $0^{\rm th}$ bin, whose bin centre $z_0 > 0$. Tracer density $\nu(0)$ has units of [stars kpc^{-3}]. $K_{\rm bn}$ and $K_{\rm DD}$ terms have units [km^2 kpc^{-1} s^{-2}].

4.7 Mock data sets

In this work we apply our method only to mock data in order to hone and verify it. This mock data is 'as good as it gets', in the sense that it has no measurement errors, nor observational biases added to it, and is drawn from relatively simple, known distribution functions. While dynamically realistic 'N-body' mocks are preferred, it has already been shown that 1D Jeans analyses are robust to the presence of local non-axisymmetric structure in the disc [451]. Furthermore, N-body mocks are expensive; even state-of-the-art simulations do not approach the local sampling expected from Gaia. Finally, the expense of building well sampled N-body mocks makes it challenging to explore a large parameter space of models, including models with and without tilt, or with and without a dark disc. For these reasons, we focus here on simpler mock data, similarly to the Read (2014) review [415]. We will consider more dynamically realistic mocks, and mocks that give a faithful representation of the expected Gaia

data uncertainties in future work.

We generate here a variety of mock data sets as outlined in Table 4.5, with different samplings (10^4, 10^5, and 10^6 tracer stars), with and without a tilt term, and also with either no dark disc, a dark disc (`dd`), or a more massive 'big dark disc' (`bdd`). We assume the axial term $\mathcal{A}$ and the rotation curve term $\mathcal{R}$ are zero. Our simple baryonic disc model is set up to mimic the real Milky Way, with a scale height parameter of $D_{\rm bn} = 0.18\,\mathrm{kpc}$ and a surface density of $\Sigma_{\rm bn} = 55.53\,\mathrm{M}_\odot\,\mathrm{pc}^{-2}$, similar to those measured near the solar position [469, 415, 414]. The value of the F parameter (see Eq. 4.31) corresponds to a DM density of $\rho_{\rm DM,const} = 10 \times 10^{-3}\,\mathrm{M}_\odot\,\mathrm{pc}^{-3} = 0.38\,\mathrm{GeV\,cm}^{-3}$. For each scenario we generate 20 mock data sets, allowing us to explore the effects of poisson noise over a range of realisations.

The mock data consist of a list of stars each with three pieces of data: the position z, the vertical velocity v_z, and the product of the vertical and radial velocities, $v_R v_Z$. The first element, z, is generated by drawing randomly from an exponential tracer distribution with scale height h:

$$\nu(z) = \exp\left(-\frac{z}{h}\right). \tag{4.50}$$

This gives us our list of stellar positions. For a given level of sampling X the model tracer density would be

$$\nu(z)_X = \nu(0)_X \exp\left(-\frac{z}{h}\right), \tag{4.51}$$

with $\nu(0)_X = X/z_h$ such that $\int_0^\infty \nu(z)_X \mathrm{d}z = X$. The tracer density at $z = 0$ is thus a quantity derived from the choice of scale height and sampling level.

To derive the velocities for the mock catalogue we first must define a mass model and tilt. Taking the same parameterisations as described in Sections 4.6.3, 4.6.4, and 4.6.6 for baryons, DM, and tilt, respectively, we set their parameters as per Table 4.5. This allows us to calculate K_z and $\mathcal{T}(z)$. Using Eq. 4.21 and its associated assumptions we can calculate C. We then use Eq. 4.19 to derive $\sigma_z(z)$. For each star we take its position z', find the value of $\sigma_z(z')$, and then draw a velocity from a Gaussian centred on $v_z = 0$ and with variance $\sigma_z^2(z')$.

To generate $v_R v_Z$ mock data, when necessary, we take the A, n, and R_0 parameters listed in Table 4.5 and calculate the $\sigma^2_{Rz}(z)$ profile via Eq. 4.38. Taking each star's position z', we calculate $\sigma^2_{Rz}(z')$, and draw a value of $v_R v_z$ from a Gaussian centered on $v_R v_z = 0$ and with variance of $\sigma^4_{Rz}(z')$.

		thick_X_M	thick_dd_X_M	thick_bdd_X_M	thick_tilt_X_M	thick_bdd_tilt_X_M
Tracer density	h [kpc]		0.9			
Potential	$K_{\rm bn}$		1500			
	$D_{\rm bn}$ [kpc]		0.18			
	F		267.65			
Dark Disc	$K_{\rm DM}$	×	300	900	×	900
	$D_{\rm DD}$ [kpc]	×	2.5	2.5	×	2.5
Tilt Term	A [km^2 s^{-2}]	×	×	×	180.08	180.08
	n	×	×	×	1.44	1.44
	R_0 [kpc]	×	×	×	2.5	2.5

Table 4.5: Mock data parameters. _X is the number of stars sampled, *e.g.* 10^4, 10^5, 10^6, and _M is the mock number, ranging from 0 to 19. A cross mark × indicate that a certain mock data set does not include that element. The baryon model corresponds to a baryonic surface density of $\Sigma_{\rm bn} = 55.53\,{\rm M}_\odot\,{\rm pc}^{-2}$, while the F parameter corresponds to a constant DM density of $\rho_{\rm DM,const} = 10\times10^{-3}\,{\rm M}_\odot\,{\rm pc}^{-3} = 0.38\,{\rm GeV\,cm}^{-3}$. $K_{\rm bn}$ and $K_{\rm DD}$ terms have units [km^2 kpc^{-1} s^{-2}], while F has units [km^2 kpc^{-2} s^{-2}].

4.8 Results

Here we present the results of our scans. We first investigate how the precision of the reconstruction varies with different numbers of tracer stars. We then look at the effects of the tilt term and the dark disc. For certain parts of these analyses the model used to generate the mock data and the model used to reconstruct the mock data are not the same – this is done to investigate the effects of ignoring terms (as in the case of the tilt term) or using incorrect models.

In the following coloured band plots (*e.g.* Fig. 4.5) and DM profile plots (*e.g.* Fig. 4.16) we plot the marginalized posterior for the DM density $\rho_{\rm DM}(z)$, showing 68%, 95%, and 99.7% CRs in dark, medium and light shading, respectively. The mock data profile is shown by the solid black line, while the median of the posterior distribution is shown by a solid line in the same colour as the CR. Binning of stars to calculate $\nu(z)$, $\sigma_z(z)$, and $\sigma^2_{Rz}(z)$ is performed such that each bin contains an equal number of stars. The bin centre is defined as the median position of the stars in that bin, so there are equal numbers of stars above and below the bin centre. For this study we use 20 bins up to a height of 2.4 kpc, and in Section 4.8.2 we briefly explore the effects of changing the number of bins used. For plots with constant DM density in both mock data set and reconstruction model we plot all 20 mock data sets together, while for non-constant DM density in either mock or reconstruction we show one representative figure in this section, and show the full set of figures in Appendix C.

We also show marginalized 1D posterior histograms and 2D posterior heat maps for the full set of parameters (*e.g.* Fig. 4.6). Contours showing the 68%, 95%, and 99.7% CRs are plotted over the heat map, and the values of the mock data points are shown by a blue circle. The marginalization and plotting of the 1D posterior histograms and 2D posterior plots is performed using the BARRETT software package [479].

Our method and code is set up to describe the tracer density as a sum of exponentials. To determine the necessary number of exponentials required to describe the data we can use the Bayes factor as described earlier in Section 4.6.7. Test reconstructions give a Bayes factor of 1.5 when comparing one exponential to two, and 3.3 when comparing one exponential to three, with one exponential favoured in both cases. This is to be expected given that the mock data is generated using a single exponential. Given this result we use a single exponential for all subsequent reconstructions.

4.8.1 Sampling

Fig. 4.5 shows reconstructions of the local DM density for using varying numbers of tracer stars. The mock data sets used here are the most simple case, `thick_X_M` as

described in Table 4.5, and has no dark disc or tilt added. As expected the credible regions shrink as the number of tracer stars is increased from 10^4 stars up to 10^6 stars. The SDSS survey has sampling on the order of 10^4 stars [434, 440] while data from Gaia will give upwards of 10^6 tracer stars.

The 2D marginalized posteriors for the first three reconstructions of 10^6 sampling are shown in Figs. 4.6, 4.7, and 4.8. These three posterior grids correspond to the first three constant DM density bands of the right-hand set in Fig. 4.5, coloured purple, green, and purple. The underestimation and overestimation in the first (`thick_1E6_0`) and third (`thick_1E6_2`) mock sets can be seen in the 1D and 2D ρ_{DM} posterior distributions in Figs. 4.6 and 4.8. Also visible in these posterior plots is the tripartite degeneracy between the local DM density $\rho_{\mathrm{DM,\,const}}$ and the baryon parameters K_{baryon} and D_{baryon}, illustrated by the tilted ellipsoids in the 2D posterior diagrams comparing the three parameters with each other. Also, looking at the 1D histograms of the extreme cases of Fig. 4.6 and 4.8 we see that when the DM is underestimated the K_{baryon} parameter is overestimated, and vice versa. This variation is the result of poisson binning noise.

There is also a slight bias on the reconstructed tracer density scale height ν_h. This is a systematic effect seen in all reconstructions. The root cause of this is the fact that the binned value for the tracer density is an average over an entire bin, but the underlying tracer density function differs across the range of the bin. The bias induced by this effect was quantified by Sofia Sivertsson assuming an underlying tracer density model given by an single exponential, as we model our tracer density (eg Eq. 4.27 with $i = 1$), and is given by the formula:

$$\frac{\nu_{\mathrm{B}}(\tilde{z})}{\nu_{\mathrm{mod}}(\tilde{z})} = \frac{2h}{d}\frac{\exp(d/h) - 1}{\exp(d/h) + 1} \tag{4.52}$$

where $\tilde{z}$ is the bin center, defined as the median star position, $\nu_{\mathrm{B}}(\tilde{z})$ is the binned value of the tracer density, $\nu_{\mathrm{mod}}(\tilde{z})$ is the value of the underlying exponential tracer density model, d is the width of the bin, and h is the scale height. The derivation of this result is reproduced with permission in Appendix B. As we use an exponential model for this study we can apply Eq. 4.52 to Eq. 4.27 to find the appropriate binned value $\nu_{\mathrm{B}}(\tilde{z})$. A run with this correction applied is shown in Fig. 4.9, showing that the mock value for ν_h is reconstructed within the 68% CR of the marginalized posterior. With 20 bins between 0 and 2.4 kpc this correction factor is at most 2%, and as this is smaller than other uncertainties we neglect it in all other runs.

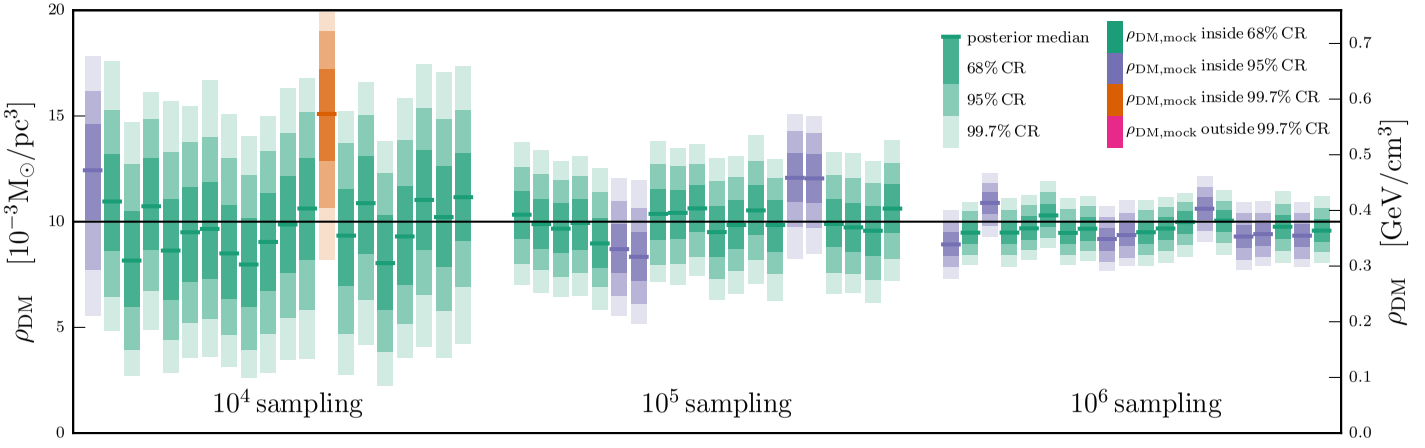

Figure 4.5: Determination of the DM density profile for varying numbers of tracer stars. These plots show marginalized posteriors for $\rho_{\mathrm{DM}}(z) = \rho_{\mathrm{DM,const}}$ for the 20 mock data sets generated for each sampling level. Dark, medium, and light shading show the 68%, 95%, and 99.7% credible regions (CRs), respectively. Green, purple, and orange colouring indicates that the 68%, 95%, or 99.7% CR respectively contains the correct answer. The median value of each posterior is shown by a solid line in green, purple, or orange, while the DM density value used to generate the mock data is shown as a solid black line across the entire plot. The mock data and reconstruction models used contain no tilt term or dark disc terms. As the number of tracer stars is increased from 10^4 to 10^6 the credible regions for $\rho_{\mathrm{DM,const}}$ naturally shrink around the mock data value.

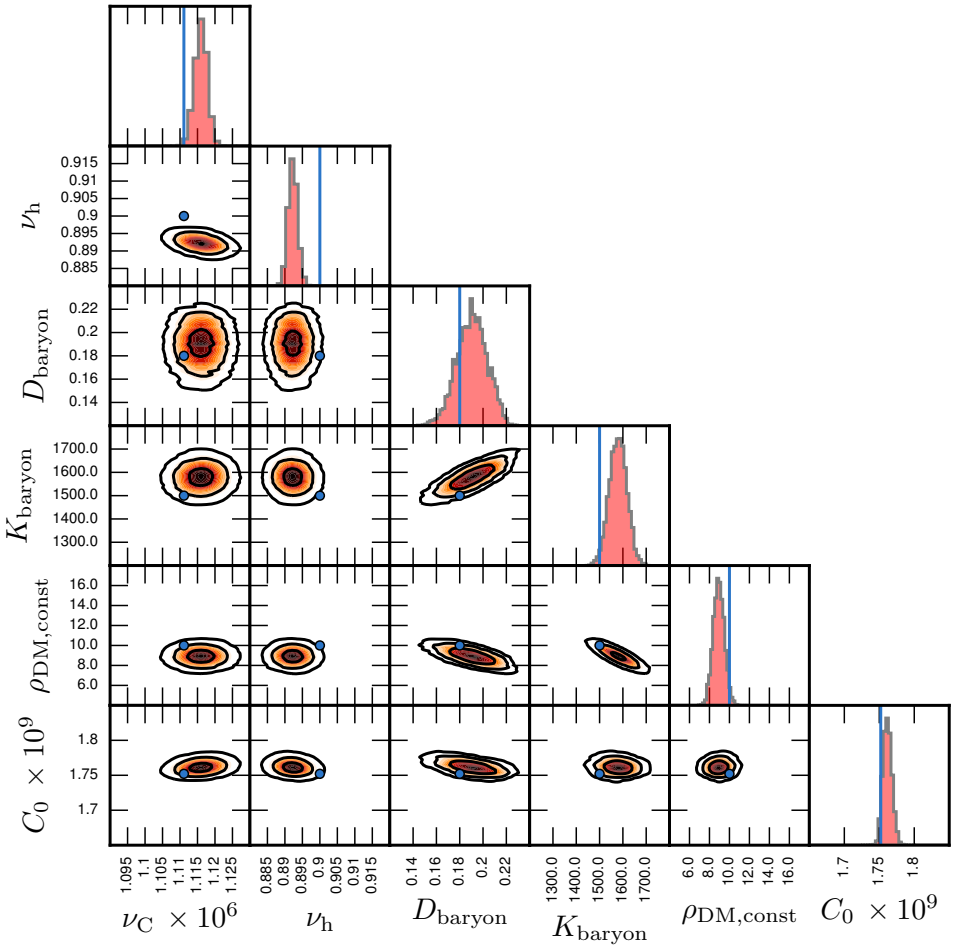

Figure 4.6: Marginalized posterior distributions for mock data set `thick_1E6_0` (10^6 sampling, no tilt term, no dark disc), reconstructed with a model featuring no tilt term and no dark disc. This mock data set and reconstruction corresponds to the first DM density range of the 10^6 sampling set of Fig. 4.5, which had $\rho_{\rm DM,mock}$ inside the 95% CR. The blue points and lines indicate the parameter values used to generate the mock data set, or the values derived directly from those parameters for $\nu(0)$ and C_0. Contours indicate the 68%, 95%, and 99.7% CRs.

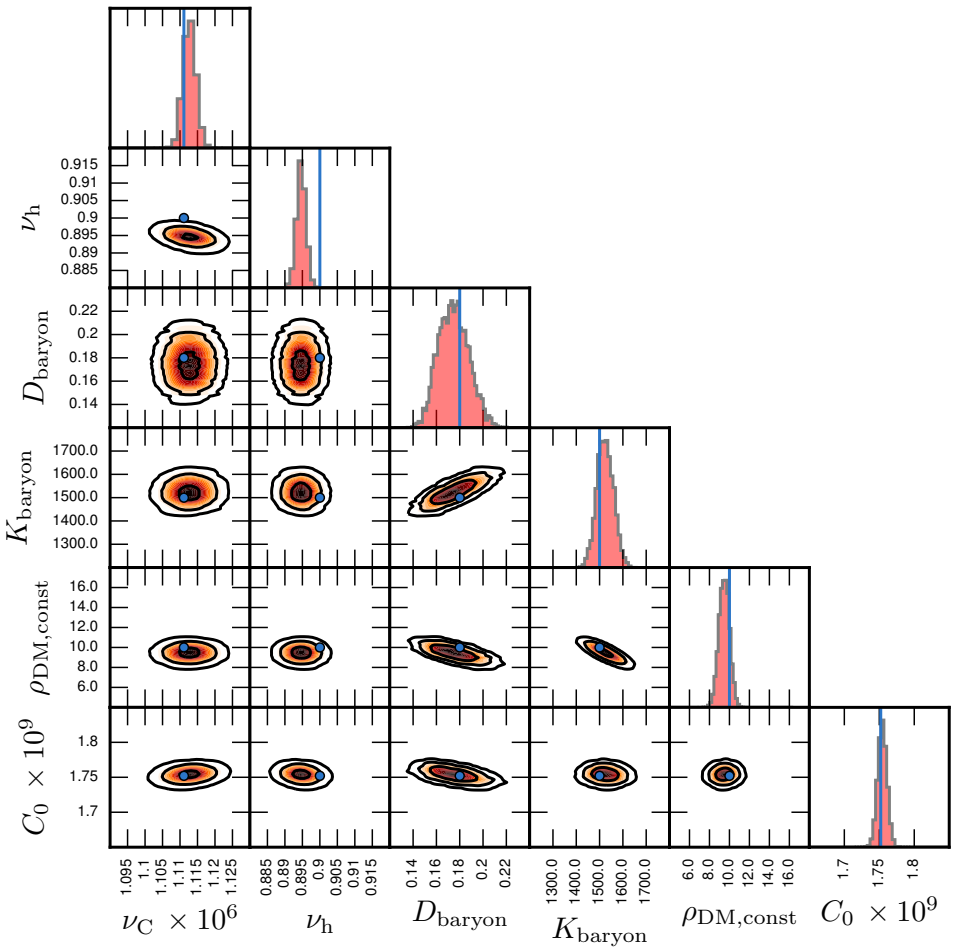

Figure 4.7: Marginalized posterior distributions for mock data set `thick_1E6_1` (10^6 sampling, no tilt term, no dark disc), reconstructed with a model featuring no tilt term and no dark disc. This mock data set and reconstruction corresponds to the second DM density range of the 10^6 sampling set of Fig. 4.5, which had $\rho_{\rm DM,mock}$ inside the 68% CR. The blue points and lines indicate the parameter values used to generate the mock data set, or the values derived directly from those parameters for $\nu(0)$ and C_0. Contours indicate the 68%, 95%, and 99.7% CRs.

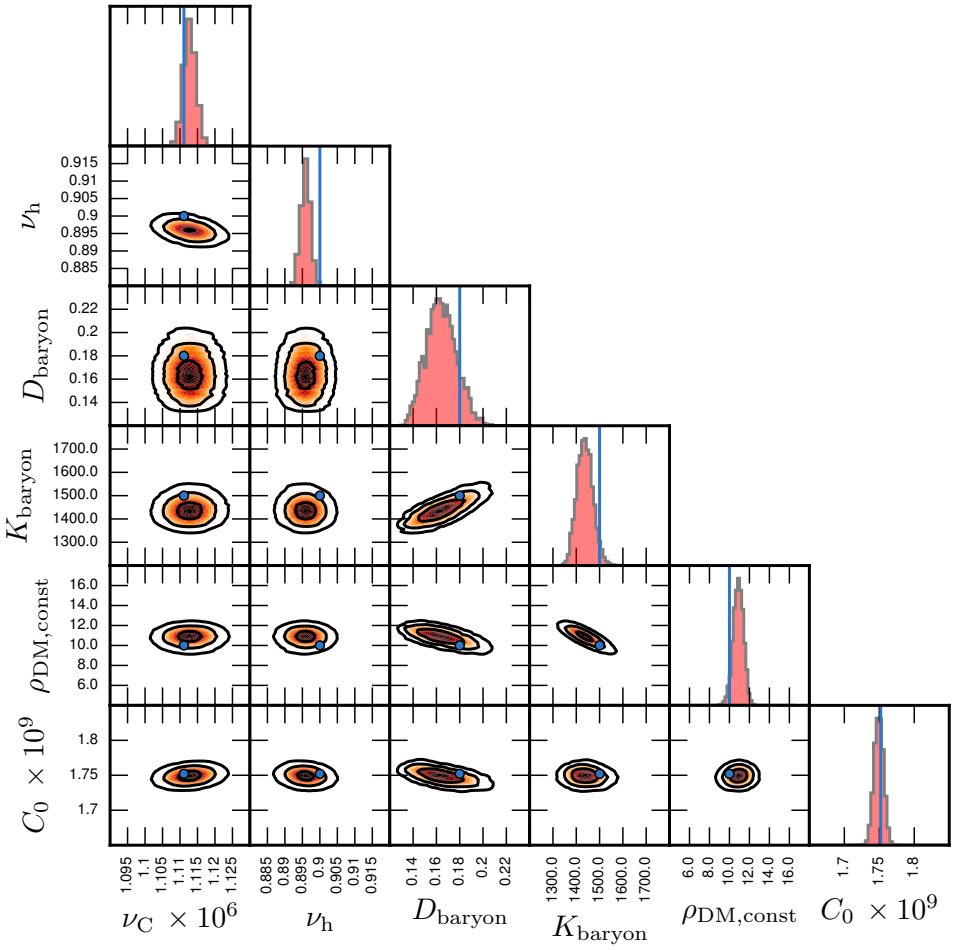

Figure 4.8: Marginalized posterior distributions for mock data set `thick_1E6_2` (10^6 sampling, no tilt term, no dark disc), reconstructed with a model featuring no tilt term and no dark disc. This mock data set and reconstruction corresponds to the third DM density range of the 10^6 sampling set of Fig. 4.5, which had $\rho_{\mathrm{DM,mock}}$ inside the 95% CR. The blue points and lines indicate the parameter values used to generate the mock data set, or the values derived directly from those parameters for $\nu(0)$ and C_0. Contours indicate the 68%, 95%, and 99.7% CRs.

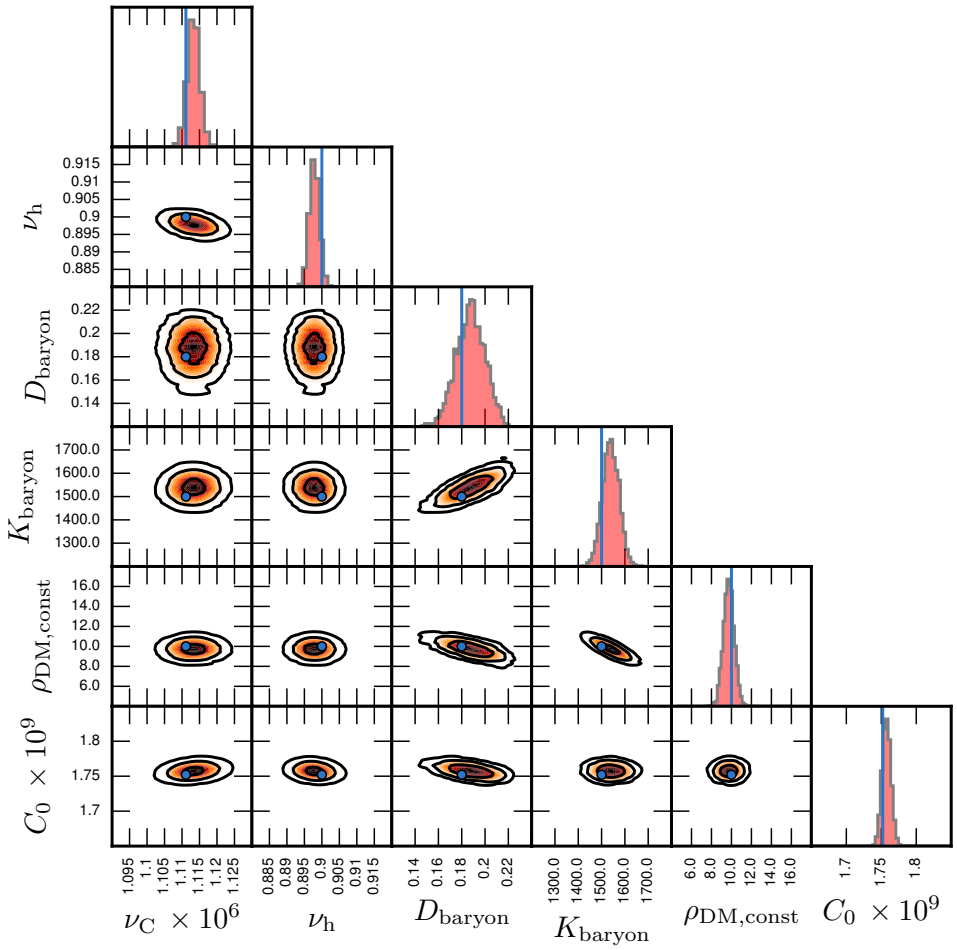

Figure 4.9: Marginalized posterior distributions for mock data set `thick_1E6_0` (10^6 sampling, no tilt term, no dark disc), reconstructed with a model featuring no tilt term and no dark disc, and including the tracer density bias correction given in Eq. 4.52. This mock data set and reconstruction corresponds to the first DM density range of the 10^6 sampling set of Fig. 4.5, which had $\rho_{\rm DM,mock}$ inside the 95% CR. The blue points and lines indicate the parameter values used to generate the mock data set, or the values derived directly from those parameters for $\nu(0)$ and C_0. Contours indicate the 68%, 95%, and 99.7% CRs. Applying the tracer density bias correction moves the posterior such that the mock data value is contained within the 68% CR.

4.8.2 Variation due to the number of bins

Figure 4.10 illustrates the effects of changing the number of bins in z used for this analysis. There we plot the 68%, 95%, or 99.7% CRs for 20 mock data sets (`thick_1E6_0-19`, no tilt and no DD), and vary the number of bins from five to 30, in increments of five. For only five bins (top left set), the true answer for $\rho_{\rm DM,const}$ is outside the 99.7% CR for all but two of the mocks, for which the true answer is within only the 99.7% CR. The systematic underestimation is due to an over estimation of the baryonic disc. The fifth bin in this scheme covers a range from 1.2 kpc to 2.4 kpc and has its bin centre at $z = 1.6$ kpc, so it is unsurprising that such a low number of bins fails to correctly reconstruct the DM profile, which is a subdominant component only becomes apparent at higher z. Increasing the number of bins to 10, 15, and then to 20 improves the results. The gain from increasing from 20 to 25 and 30 bins is very slight.

4.8.3 Tilt

In Fig. 4.11 we explore the effects of the tilt term. The left hand set of CRs in Fig. 4.11 are the same as the right hand set of CRs from Fig. 4.5, with no tilt term in the mock data or reconstruction. In the centre set of Fig. 4.11 however, the mock data `thick_tilt_1e6_M` has the tilt term turned on, but the analyses are performed with the tilt term set to zero. This illustrates the danger of ignoring tilt as discussed earlier in Section 4.6.6: the reconstructions return narrow credible regions, but as expected they systematically underestimate the value of $\rho_{\rm DM}$, with the true $\rho_{\rm DM}$ lying outside even the 99.7% CRs. The 1D and 2D marginalized posteriors for the reconstruction of one mock data set, `thick_tilt_1E6_0`, are shown in Fig. 4.12, again showing the systematic underestimation in the reconstructed DM density.

This underestimation however is remedied by turning on the tilt term in the model, as shown in the right hand set CRs in Fig. 4.11, where the correct DM density always at least within the 95% credible region. The inclusion of extra parameters to describe the tilt term does however increase the size of the CRs. Fig. 4.13 shows the 1D and 2D marginalized posteriors for the reconstruction of mock data set `thick_tilt_1E6_0` with the inclusion of the tilt term.

Just as our determination of $\rho_{\rm DM}(z)$ is dependent on the tilt term, the tilt term is in turn dependent on its input parameters, A, n, and $R_0 = R_1$. While we have been able to fit for A and n using G-type dwarf data (Section 4.6.6), for R_0 we have taken the canonical value of $R_0 = 2.5 \pm 0.5$ kpc from [410], and further made the assumption that $\sigma^2_{Rz}(R, z)$ has the same radial profile as $\nu(R, z)$ (*i.e.* $R_0 = R_1$). When using only a single population, determination of R_0 and R_1 will be important, as illustrated in

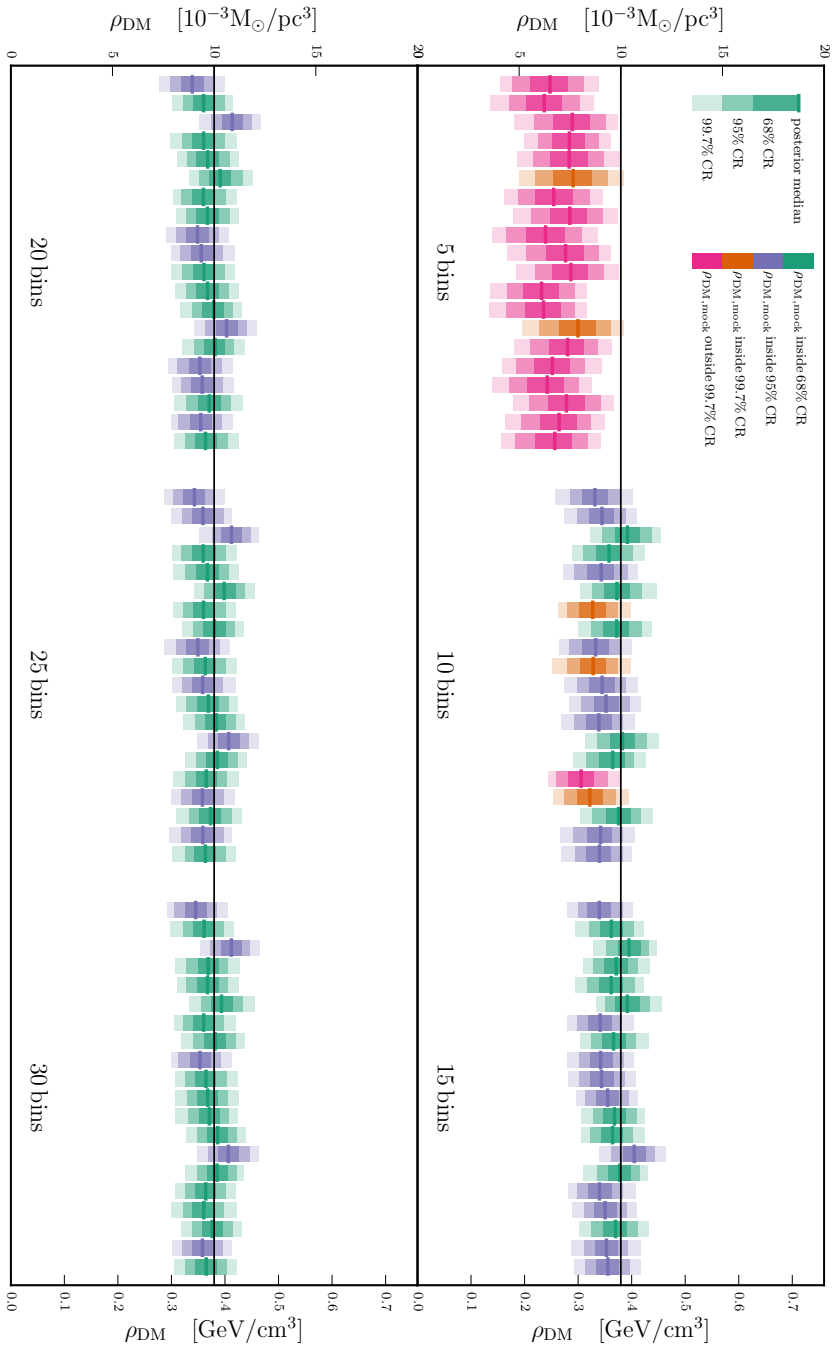
ρ_{DM} $[10^{-3}\mathrm{M}_\odot/\mathrm{pc}^3]$
posterior median
68% CR
95% CR
99.7% CR
$\rho_{\mathrm{DM,mock}}$ inside 68% CR
$\rho_{\mathrm{DM,mock}}$ inside 95% CR
$\rho_{\mathrm{DM,mock}}$ inside 99.7% CR
$\rho_{\mathrm{DM,mock}}$ outside 99.7% CR
5 bins
10 bins
15 bins
20 bins
25 bins
30 bins
ρ_{DM} [GeV/cm^3]

Figure 4.10

Figure 4.10: *(Opposite)* Exploring the effects of binning on the determination of $\rho_{\rm DM}$. These plots show marginalized posteriors for $\rho_{\rm DM}(z) = \rho_{\rm DM,const}$ for the 20 mock data sets `thick_1E6_0-19`, reconstructed using 5, 10, 15, 20, 25, and 30 bins. Dark, medium, and light shading show the 68%, 95%, and 99.7% credible regions (CRs) respectively. Green, purple, and orange colouring indicates that the 68%, 95%, or 99.7% CR respectively contains the correct answer, while pink colouring indicated that the correct answer lies outside even the 99.7% CR.. The median value of each posterior is shown by a solid line in green, purple, or orange, while the DM density value used to generate the mock data is shown as a solid black line across the entire plot.

---

the ($R_{0,\,\rm tilt}$ - $\rho_{\rm DM,\,const}$) 2D marginalized posterior given in Fig. 4.13 (bottom row, fifth plot from the left). This posterior is for a reconstruction of mock data set `thick_tilt_1e6_0` with a model including tilt, and demonstrates the degeneracy that exists between $\rho_{\rm DM,const}$ and $R_0 = R_1$. If using multiple tracer population, each will have different R_0 and/or R_1, but will all have their motions dictated by the same potential. This will help us break the degeneracy between R_0, R_1, and $\rho_{\rm DM}$. Further, with the advent of Gaia data we will be able to directly measure the radial profile of σ^2_{Rz} and $\nu(R, z)$ for a given set of tracer stars.

While Fig. 4.13 shows an excellent reconstruction of the local DM density, the $n_{0,\,\rm tilt}$ parameter marginalized posterior (see Eq. 4.40) is far from its mock data value of 1.44. So too is the A_0 value, though to a lesser extent. The cause of this bias traces back to how we calculate σ^2_{Rz} from the data. In Fig. 4.14 (a), the first two values of σ^2_{Rz} derived from our normal analysis of the `thick_tilt_1e6_0` mock data set are shown as green points, along with the bin centres and bin edges that are calculated. The value of σ^2_{Rz} generated from mock data is plotted as the blue line, with its values at the bin centres given as blue points. The values derived from binning the mock data (green) are systematically higher than what the mock data model calculates (blue). This is consistent across the other mock data sets.

This bias is caused by the fact that the binned σ^2_{Rz} value is an average over the entire bin, and the binned value is assigned the z value of the bin center. This can be clearly seen from the straight red lines, which connect the values of σ^2_{Rz} on the bin edges as calculated from the mock model. The binned values (green points) match very closely with the straight red lines.

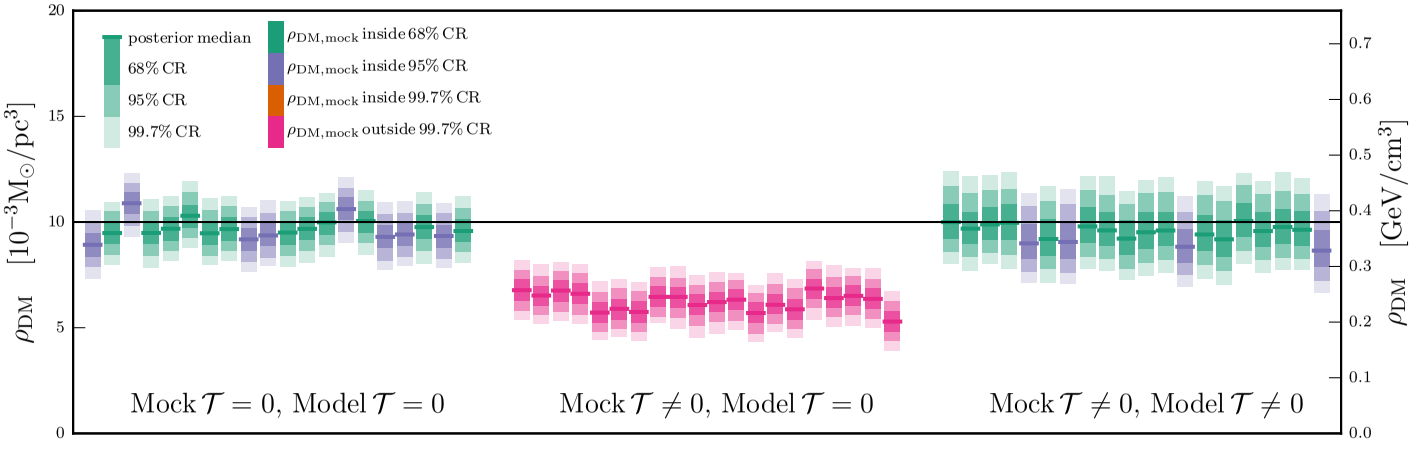

Figure 4.11: Determination of the DM density profile using 10^6 tracer stars and exploring the effects of including or neglecting the tilt term in the mock data sets and reconstruction models. These plots show marginalized posteriors for $\rho_{\mathrm{DM}}(z) = \rho_{\mathrm{DM,const}}$ for the 20 mock data sets generated for each tilt scenario. Dark, medium, and light shading show the 68%, 95%, and 99.7% credible regions (CRs) respectively. Green, purple, and orange colouring indicates that the 68%, 95%, or 99.7% CR respectively contains the correct answer, while pink colouring indicated that the correct answer lies outside even the 99.7% CR. The median value of each posterior is shown by a solid line in green, purple, or orange, while the DM density value used to generate the mock data is shown as a solid black line across the entire plot. The left set of mocks shows the same result as the right set of Fig. 4.5, with no tilt term in mock data or reconstruction model. The centre set has a tilt term in the mock data but not in the reconstruction model, yielding a systemic underestimation of ρ_{DM}. The right set has a tilt term in both mock data and reconstruction model, demonstrating that our method can successfully deal with the tilt term.

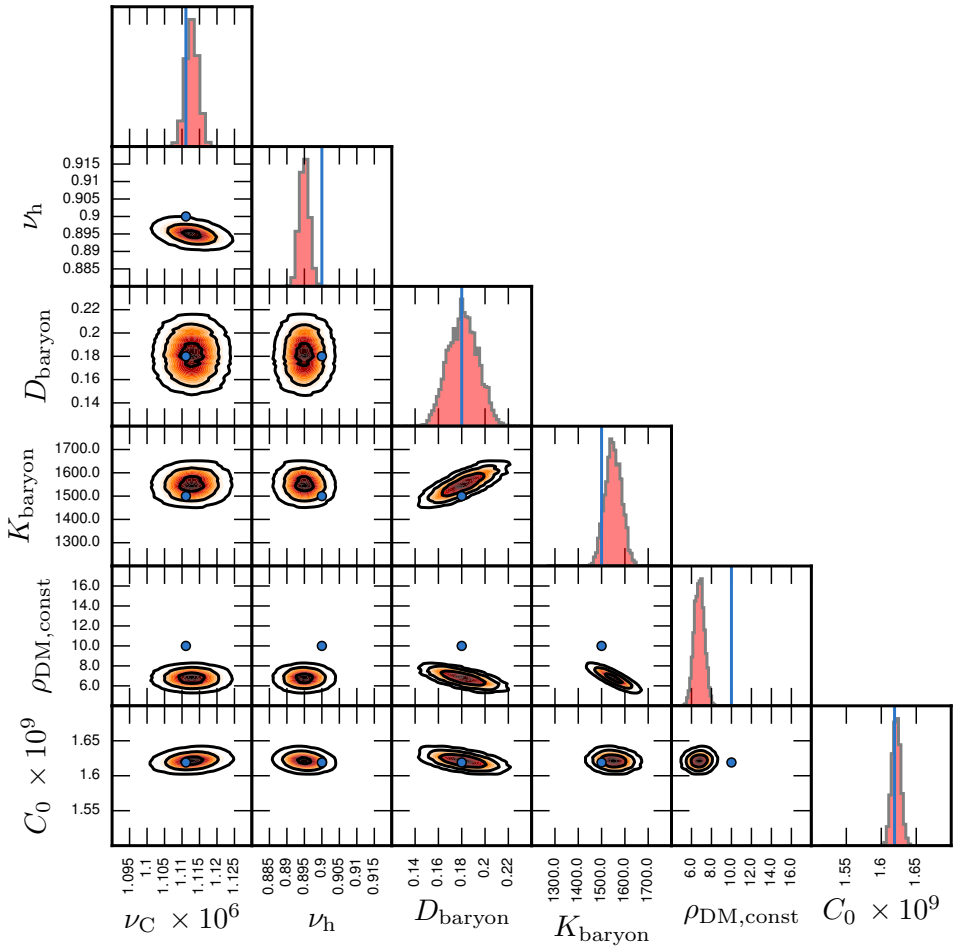

Figure 4.12: Marginalized posterior distributions for mock data set `thick_tilt_1E6_0` (10^6 sampling, tilt term, no dark disc), reconstructed with a model featuring no tilt term and no dark disc. This mock data set and reconstruction corresponds to the first DM density range of the middle sampling set of Fig. 4.11, which shows $\rho_{\mathrm{DM,mock}}$ outside the 99.7% CR. The blue points and lines indicate the parameter values used to generate the mock data set, or the values derived directly from those parameters for $\nu(0)$ and C_0. Contours indicate the 68%, 95%, and 99.7% CRs. This figure illustrates the bias in reconstructed DM density due to the omission of the tilt term.

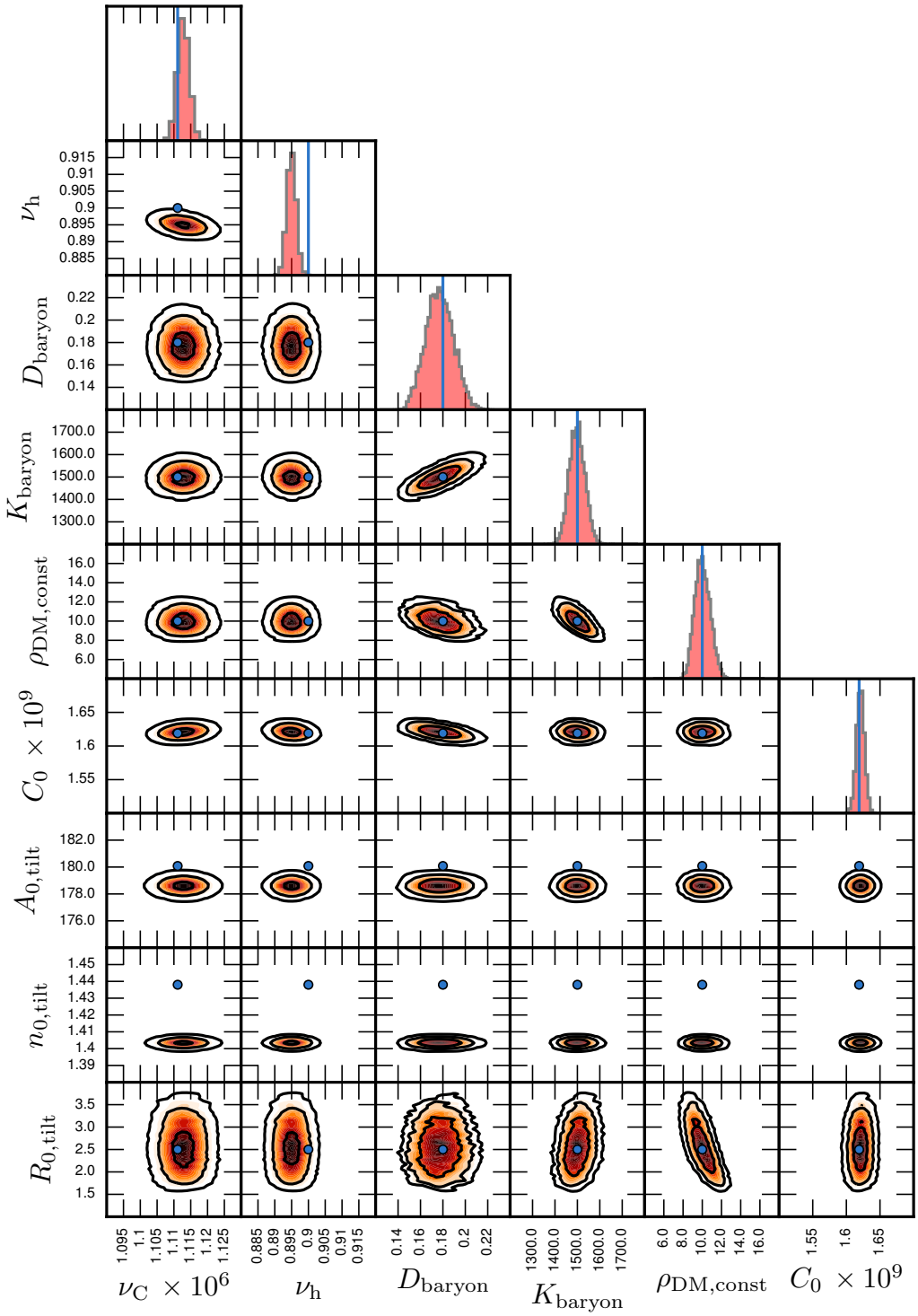
$\nu_{\rm C} \times 10^6$
$\nu_{\rm h}$
$D_{\rm baryon}$
$K_{\rm baryon}$
$\rho_{\rm DM,const}$
$C_0 \times 10^9$
$A_{0,\rm tilt}$
$n_{0,\rm tilt}$
$R_{0,\rm tilt}$

Figure 4.13: Marginalized posterior distributions for mock data set `thick_tilt_1E6_0` (10^6 sampling, tilt term, no dark disc), reconstructed with a model featuring a tilt term and no dark disc. This mock data set and reconstruction corresponds to the first DM density range of the right-hand sampling set of Fig. 4.11, which shows $\rho_{\mathrm{DM,mock}}$ inside the 68% CR. This shows the ability of our method to deal with the tilt term and successfully reconstruct the local DM density. The blue points and lines indicate the parameter values used to generate the mock data set, or the values derived directly from those parameters for $\nu(0)$ and C_0. Contours indicate the 68%, 95%, and 99.7% CRs. The offset in $n_{0,\,\mathrm{tilt}}$ is due to a binning issue that will be discussed in Fig. 4.15 and associated text.

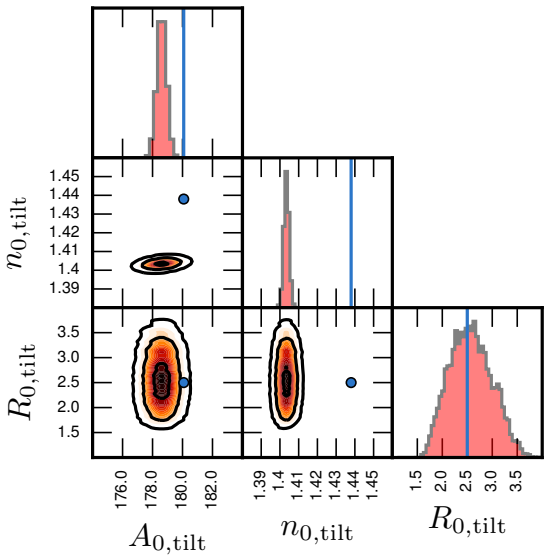

The reason this bias changes the reconstructed n_0 and A_0 values is illustrated in Fig. 4.14(b). First note that there is a degeneracy between A_0 and n_0; to a certain extent a reduction (increase) in n_0 can be compensated for by a reduction (increase) in A_0 to keep σ^2_{Rz} fixed. For the forthcoming discussion we focus on n_0 as it has the larger deviation, but a similar argument could be made using A_0. As in Fig. 4.14(a) we plot the binned σ^2_{Rz} values in green, and the mock data values as the blue line and points. In magenta we plot the σ^2_{Rz} lines generated by the mock model but with different n_0 values, ranging from $n_0 = 1.42$ to $n_0 = 1.38$. The upwards bias from the binned data points favours σ^2_{Rz} profiles with lower n_0, and so pulls the posterior value downwards. Artificially setting the two lowest binned σ^2_{Rz} values downwards to the perfect mock model values remedies this problem, as shown in Fig. 4.15, where the n_0 marginalized posterior is exactly on top of the mock data value.

But what is the importance of the lower bins? First, notice in Fig. 4.14 that the blue and magenta lines, each showing a σ^2_{Rz} profile for different n_0, are diverging with increasing z. A constant difference in n_0 corresponds with a larger σ^2_{Rz} difference at higher z. Essentially, at high z a σ^2_{Rz} has to be more biased to pull the n_0 value away from the true value, compared to at low z. Additionally the biases due to the bin averaging effect discussed above will be strongest at low z, as illustrated in Fig. 4.14 (c). There we plot the curvature k, defined as

$$k = \frac{f''}{(1 + f'^2)^{3/2}} \qquad \text{for function } f(x). \tag{4.53}$$

The curvature quantifies how much the true curve in blue will bend away from the the straight line approximation in red, and thus how much bias there will be. This peaks towards $z = 0$, and thus the bias will be strongest at low z, the same region where it can affect the n_0 parameter most strongly. Thus the initial few bins have greater importance in fitting the σ^2_{Rz} under our model.

The bias on the n_0 parameter has very little effect on the reconstruction of the local DM density $\rho_{\rm DM}$, as can be seen by comparing Fig. 4.13 with Fig. 4.15, where the first two σ^2_{Rz} values have been set to values directly from the mock model. When we alter the σ^2_{Rz} values to correct the n_0 bias the A_0 marginalized posterior moves upwards as expected. The degeneracy between A_0 and n_0 allows for the overall σ^2_{Rz} profile be well fitted, which in turn gives the proper tilt term $\mathcal{T}(R, z)$. Further investigation found that the exact size of the bias was slightly prior dependent, but the DM posterior remained unchanged and the bias still disappeared upon the application of the correction described above.

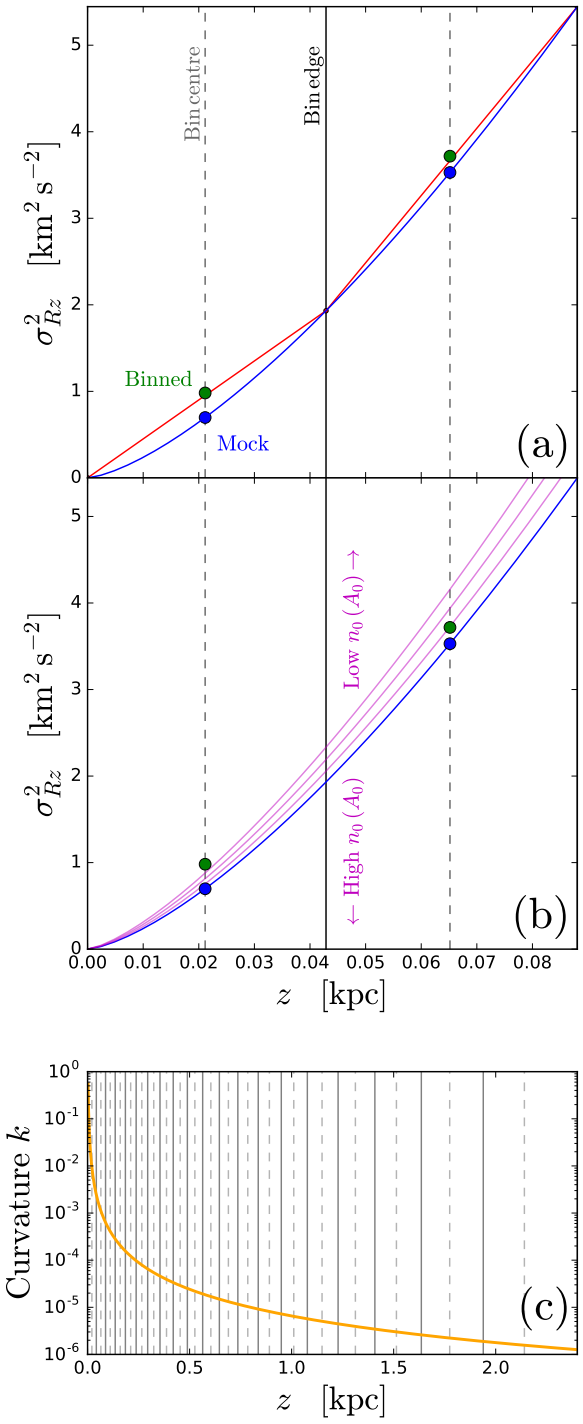

Figure 4.14: Exploration of the cause of the reconstruction bias in tilt parameters n_0 and A_0. (a): Comparison of σ^2_{Rz} values directly from the mock model (Eq. 4.40, blue line and points), and those from the binning of the mock data generated by sampling the mock model. The red lines join the model values of σ^2_{Rz} between their values at the bin edges. (b): Illustration of how upwards bias in σ^2_{Rz} values leads to profiles with lower n_0 values (or equivalently lower A_0 values) being fitted. (c): Plot of the curvature k (Eq. 4.53) of the σ^2_{Rz} model, showing that the binned value, which follow the red straight lines of (a), will be greatest at low z, where the model line curves away from the straight line the most.

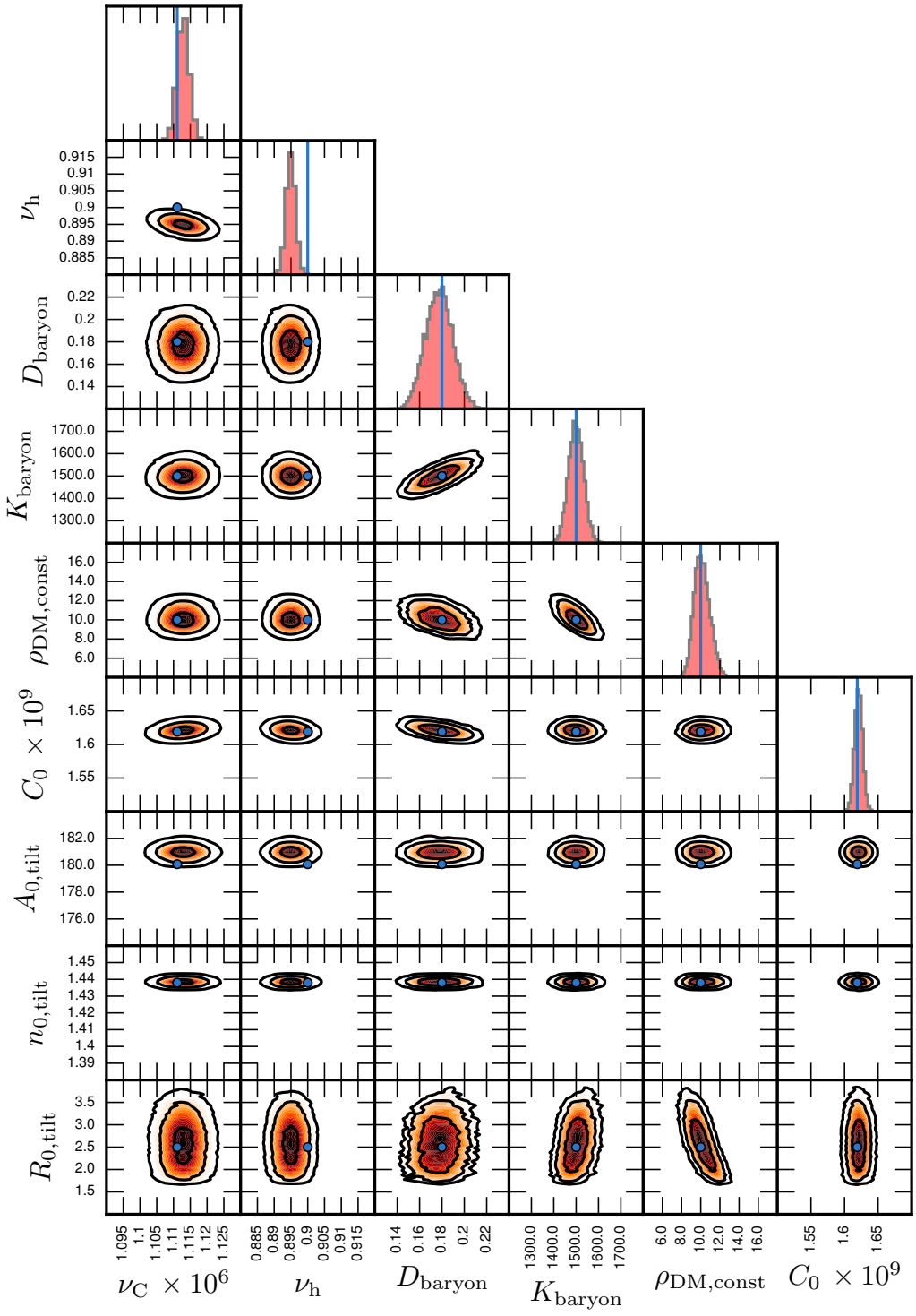
$\nu_{\rm C} \times 10^6$
$\nu_{\rm h}$
$D_{\rm baryon}$
$K_{\rm baryon}$
$\rho_{\rm DM,const}$
$C_0 \times 10^9$
$A_{0,\rm tilt}$
$n_{0,\rm tilt}$
$R_{0,\rm tilt}$

Figure 4.15: Marginalized posterior distributions for mock data set `thick_tilt_1E6_0` (10^6 sampling, tilt term, no dark disc), reconstructed with a model featuring a tilt term and no dark disc, and with the first two values of σ^2_{Rz} set to the values given by the mock model, *i.e.* the green points of Figure 4.14(a) are replaced by the blue points. The blue points and lines indicate the parameter values used to generate the mock data set, or the values derived directly from those parameters for $\nu(0)$ and C_0. Contours indicate the 68%, 95%, and 99.7% CRs. Substituting for the first two σ^2_{Rz} points results in the posterior 95% CRs containing the mock data parameter values for A_0 and n_0.

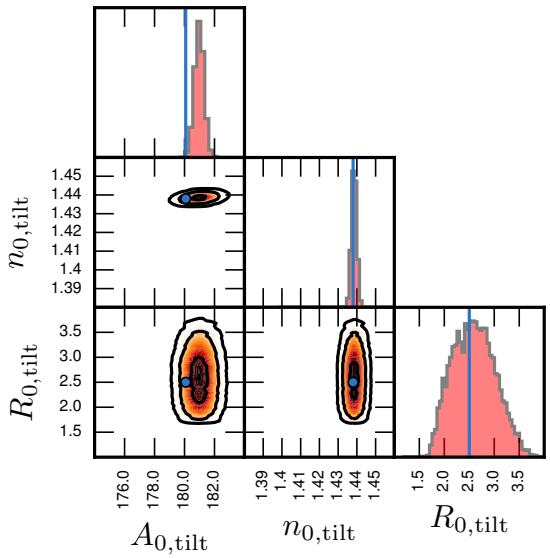

Figure 4.16: *(Opposite)* Determination of the DM density profile using 10^6 tracer stars and exploring the effects of including or neglecting a dark disc in the mock data sets and reconstruction models. For comparison the top left panel shows the same reconstructions as the right hand set from Fig. 4.5, *i.e.* basic mock data sets with no DD, reconstructed with a constant DM density. The remaining panels each show one representative mock and reconstruction, with the full set of mocks and reconstructions given in Appendix C. These panels show marginalized posteriors for $\rho_{\rm DM}(z)$, with dark, medium, and light shading indicating the 68%, 95%, and 99.7% CRs respectively. The median value of the posterior is shown by the solid blue line, while the DM density profile used to generate the mock data is shown as a solid black line. From left to right the columns show reconstructions of mock data sets containing no dark disc ($\rho_{\rm DM,const}$ only), a dark disc (DD), or a 'big' dark disc (BDD). The top centre and top right panels show the determination of a constant DM density from the DD and BDD mock data sets respectively. The bottom row shows the reconstruction of each of the mock data sets using a model with a constant DM term and a dark disc term. Light grey vertical lines indicate the bin centres.

4.8.4 Dark Disc

Here we present initial explorations into the detection of dark discs through astrometric measurements. As mentioned in Section 1.4.8, a dark disc is degenerate with an highly oblate halo, and so it can be difficult to distinguish the two. Here we consider two cases that can be dealt with within our framework. The first is an optimal scenario where we are confident in the overall shape of the halo, perhaps from observations of tidal streams produced by the infall and destruction of dSphs or globular clusters [*e.g.* 480], and/or the results of simulations. In this case we endeavour to extract the dark disc as a separate component, *i.e.* constraining the individual parameters $\rho_{\rm DM,const.}$, $K_{\rm DD}$, and $D_{\rm DD}$, working here with the simplifying assumption that the halo is spherical and so the constant vertical DM density approximation is valid. Second, we take the more conservative approach that knowledge about the overall halo profile is uncertain, and any departure from the constant vertical DM profile can be from either a dark disc or an oblate halo. All we can hope to constrain is the total vertical profile, and we do not attempt to separate the halo from the dark disc. In this case we use the same parametrization as before, but look only at the total DM profile, and not the separate $\rho_{\rm DM,const.}$, $K_{\rm DD}$, and $D_{\rm DD}$ parameters.

In the first case, constraining the constant DM density profile and the dark disc as separate elements is a challenging task, as they are to a certain degree degenerate with each other, and also with the baryon disc. Previously in Section 4.8.1 we saw

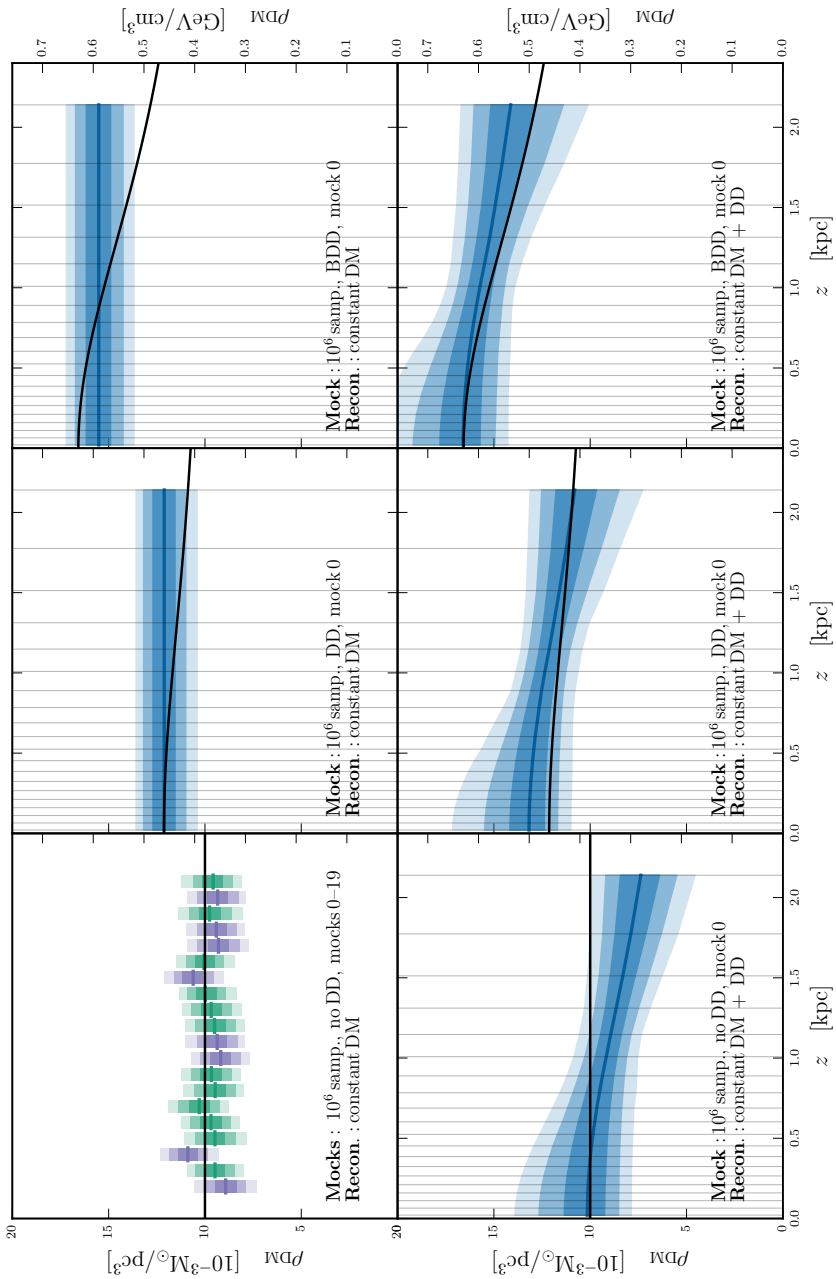
Mocks : 10^6 samp., no DD, mocks 0–19
Recon. : constant DM
Mock : 10^6 samp., no DD, mock 0
Recon. : constant DM + DD
Mock : 10^6 samp., DD, mock 0
Recon. : constant DM
Mock : 10^6 samp., DD, mock 0
Recon. : constant DM + DD
Mock : 10^6 samp., BDD, mock 0
Recon. : constant DM
Mock : 10^6 samp., BDD, mock 0
Recon. : constant DM + DD
$\rho_{\rm DM}$ [10^{-3}M$_\odot$/pc^3]
$\rho_{\rm DM}$ [GeV/cm^3]
z [kpc]

Figure 4.16

that a degree of degeneracy persisted between the baryonic disc and the constant DM density profile, even given their differing vertical profiles. Adding a dark disc complicates matters still further, as depending on the scale height of the disc it can mimic either the baryonic disc on the constant DM density component. In this chapter we also investigate the impact of a dark disc component on the case where we assume there is none, which is pertinent to the comparison of direct and indirect detection experiments (see Sections 1.5 and 1.6).

Fig. 4.16 shows mock data set `thick_1e6_0-19`, `thick_dd_1e6_0`, and `thick_bdd_1e6_0` reconstructed using models with and without a dark disc component. The top left panel shows the same CRs as seen in the left hand set of Fig. 4.11 and the right hand set of Fig. 4.5. The left column of Fig. 4.16 shows the reconstruction of mock data sets with a constant DM density profile; mocks 0-19 in top left and mock 0 in bottom left. The reconstruction in the top panel uses a model with a constant DM density, while the bottom panel uses a model with an additional dark disc component, the prior ranges for which are listed in Table 4.4. The dark disc reconstruction exhibits a disc structure even though the correct answer is constant $\rho_{\rm DM}$. This is likely due to a bias in the hyper-volume set by the priors – the prior range on the dark disc parameters goes between no dark disc ($K_{\rm DD} = 0$) and a maximal dark disc ($K_{\rm DD} = 1500$), and thus the bulk of the parameter space features at least some dark disc. There is no 'negative dark disc' to counteract this effect and push the mean of the prior range back to no dark disc.

In the centre and right columns of Fig. 4.16 we reconstruct mock data sets with a dark discs of different masses: `thick_dd_1e6_0` and `thick_bdd_1e6_0` (the 'big dark disc'). A constant DM density reconstruction (top row) is able to contain the `thick_dd_1e6` dark disc within the 95% credible region almost to the last bin, but fails to contain the big dark disc beyond $z = 1.3$ kpc. Adding a dark disc term allows the reconstruction to accommodate the mock data DM profile, as shown in the bottom centre and bottom right panels of Fig. 4.16. However, as we will see now, these profiles are somewhat dependent on the prior ranges we choose.

In Fig. 4.17 we show the 1D and 2D marginalized posteriors for a reconstruction of `thick_bdd_1E6_0` using a model including a dark disc component (but no tilt). This reconstruction corresponds to the bottom right panel of Fig. 4.16, with prior ranges listed in Table 4.4. The biases in both the scale height ν_h the tilt parameter n_0 are present here, which were discussed and resolved earlier. These posteriors show that the dark disc parameters $K_{\rm DD}$ and $D_{\rm DD}$ are not well constrained, filling their entire prior range. There is a clear degeneracy between $\rho_{\rm DM,const}$ and the $K_{\rm DD}$, which quantifies the mass of the dark disc. This illustrates the difficulty of disentangling a baryonic disc, a dark disc, and a constant DM density term.

Furthermore, if we increase the prior range on $K_{\rm DD}$ and $D_{\rm DD}$ the marginalized posterior expands also, as shown in Fig. 4.18. There we show the $K_{\rm DD} - D_{\rm DD}$ posterior for three prior ranges: in (a) we repeat the posterior shown in Fig. 4.17, with the standard prior range of $K_{\rm DD} \in [0, 1500]$ and $D_{\rm DD} \in [1.5, 3.5]$; in (b) we double the upper limits, so $K_{\rm DD} \in [0, 3000]$ and $D_{\rm DD} \in [1.5, 7.0]$; and in (c) we triple them, giving $K_{\rm DD} \in [0, 4500]$ and $D_{\rm DD} \in [1.5, 10.5]$. In each case the posterior distribution simply expands upwards to fill the prior range. The total DM profiles (constant plus dark disc) are shown in Fig. 4.19 (a), (b), and (c). We have also tried moving to a linear binning scheme, with 20 bins and 30 bins, in order to increase the number of bins at hight-z, but the degeneracy persists.

The presence of this degeneracy is to expected. We are using a general profile for the dark disc that has the functional form as the baryonic disc, and we previously noted in Section 4.6.7 the need for a lower bound on the dark disc scale height to avoid a complete degeneracy between the two. As the dark disc scale height increases it becomes flatter in the our region of analysis, and can increasingly resemble the constant DM density component. We have three degenerate elements, and the data used here is not informative enough to break this degeneracy.

There are several potential routes out of this degeneracy. The first is simply adding more stars, both in absolute numbers to drive down the poisson error, and through the use of multiple populations with varying scale heights to place multiple intersecting constraints on the underlying mass model. Another would be to adopt a different profile for the dark disc motivated by a particular DM model, for instance the dark disc formed by Double Disc Dark Matter suggested by Ref. [178], which could potentially be constrained due to its $\rho(z) \propto \mathrm{sech}^2(z/2h)$ profile.

We now consider the second case, where we attempt only to constrain the total DM profile be it from a dark disc or an oblate halo. In this case the results of the reconstructions shown in Figs. 4.18 and 4.19 can be seen in a different light. Despite expanding the dark disc priors to preposterous levels in panel (c), the total density at $z = 0$ remains within the 95% CR. This illustrates that our method is able to reconstruct the total local DM density arising from non-constant DM vertical density profiles well.

Finally, the analysis of the dark disc given in this section can also guide us in comparing direct and indirect detection rates between the spherical halo-only scenario, and the halo plus co-rotating dark disc scenario. The top centre and top right panels of Fig. 4.16 illustrate the fact that if a dark disc is indeed present in the MW then its effect has already been felt in previous measurements of the local DM density. This point is crucial to the earlier discussion in Sections 1.5 and 1.6 of the impact of a dark disc on direct detection and indirect detection via solar capture. If a constant vertical

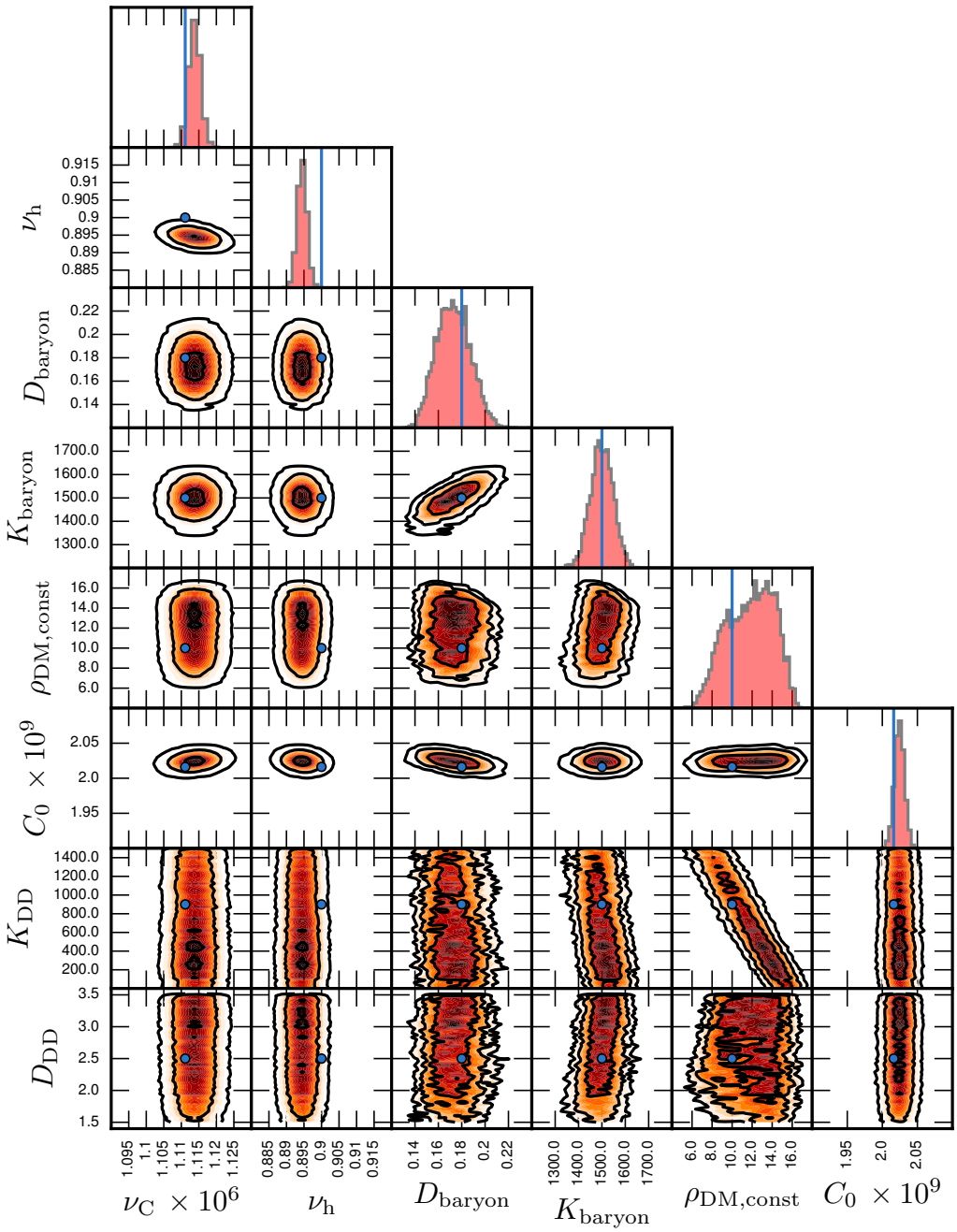
$\nu_{\rm C} \times 10^6$
$\nu_{\rm h}$
$D_{\rm baryon}$
$K_{\rm baryon}$
$\rho_{\rm DM,const}$
$C_0 \times 10^9$
$K_{\rm DD}$
$D_{\rm DD}$

Figure 4.17: Posterior distributions for mock data set `thick_bdd_1E6_0` (10^6 sampling, no tilt term, big dark disc), reconstructed with a model featuring a dark disc but not DD. The blue points and lines indicate the parameter values used to generate the mock data set, or the values derived directly from those parameters for $\nu(0)$ and C_0. Contours indicate the 68%, 95%, and 99.7% CRs.

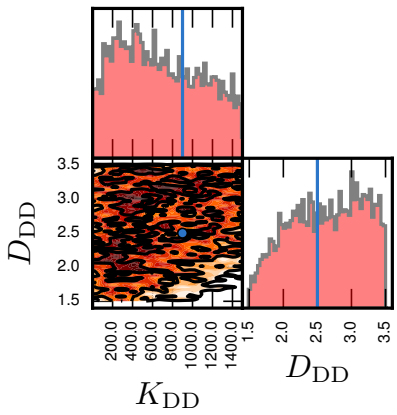

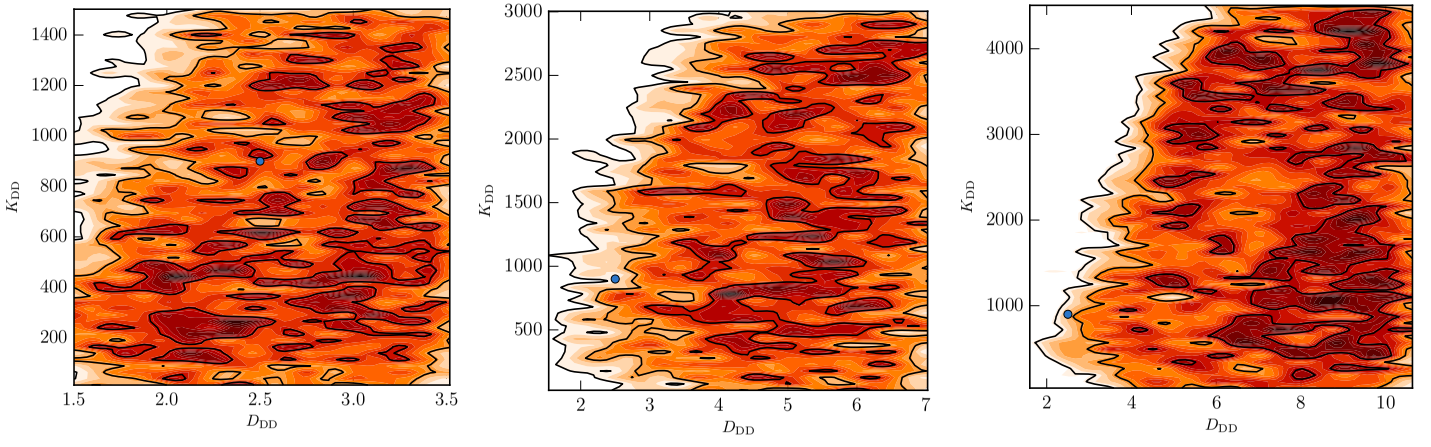

Figure 4.18: 2D marginalized posteriors of dark disc parameters $K_{\rm DD}$ and $D_{\rm DD}$, for the mock data set `thick_bdd_1E6_0`. Here the prior ranges for these parameters are increased from left to right: (a) has the standard priors as listed in Table 4.4, and corresponds to the reconstruction shown in the bottom right panel of Fig. 4.17 and Fig. 4.17; (b) has $K_{\rm DD} \in [0, 3000]$ and $D_{\rm DD} \in [1.5, 7.0]$; and (c) has $K_{\rm DD} \in [0, 4500]$ and $D_{\rm DD} \in [1.5, 10.5]$. The mock data value is plotted in blue. Expanding the priors from (a) to (b) shifts the posterior upwards further away from the mock data value (blue point).

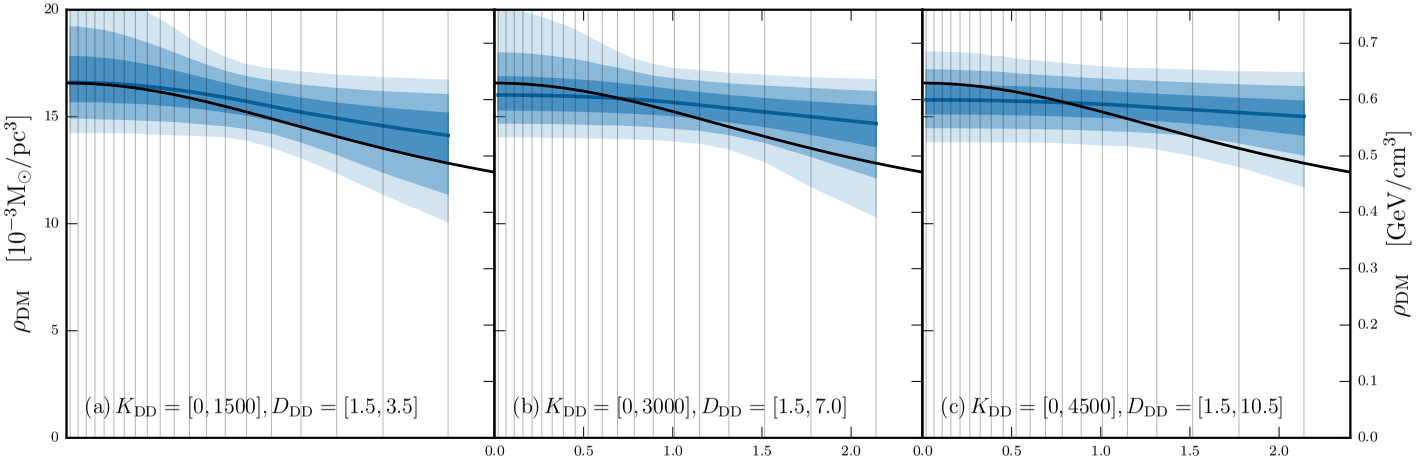

Figure 4.19: Total DM $\rho_{\rm DM}(z)$ marginalized posterior profiles corresponding to the posteriors shown in Fig. 4.18(a), (b), and (c) with dark, medium, and light shading indicating the 68%, 95%, and 99.7% CRs respectively. The median value of the posterior is shown by the solid blue line, while the DM density profile used to generate the mock data is shown as a solid black line. Panel (a) has the standard priors as listed in Table 4.4, and corresponds to the reconstruction shown in the bottom right panel of Fig. 4.17 and Fig. 4.17; (b) has $K_{\rm DD} \in [0, 3000]$ and $D_{\rm DD} \in [1.5, 7.0]$; and (c) has $K_{\rm DD} \in [0, 4500]$ and $D_{\rm DD} \in [1.5, 10.5]$.

DM density profile is assumed, as many previous studies have done, then a dark disc has the effect of raising the measured local DM density. Thus the appropriate way to compare the spherical halo only scenario to the halo plus dark disc scenario is in the first case to set the local spherical halo density to the measured value, and in the second case, to reduce the local spherical halo density to a fraction of the measured value to account for the portion of the dark disc component that has already been included in the local measured value.

4.8.5 Tilt and Dark Disc

Here we combine the two elements discussed in previous sections, the tilt term and the dark disc. Fig. 4.20 shows reconstructions of the mock data set `thick_bdd_tilt_1e6_0`. In the top panel the reconstruction model contains neither dark disc nor tilt term. Again we see the same effects as we did previously. The missing tilt term yields a consistent underestimation of the DM density, and the constant DM density envelope is too narrow to encompass the density range of the dark disc. The consistent underestimation can remedied by adding a tilt term to the reconstruction model, as shown in the middle panel, where the reconstruction model has a tilt term included. Both problems can be resolved in tandem by using a reconstruction model with both tilt and dark disc terms, as shown in the bottom panel of Fig. 4.20.

Figure 4.21 shows the 1D and 2D marginalized posteriors for the reconstruction of `thick_bdd_tilt_1E6_0` using a model featuring both tilt and dark disc. This corresponds to the bottom profile of Fig. 4.20. Again we see the biases in the tracer density scale height ν_h, and the n_0 tilt parameter, which were discussed and remedied in Sections 4.8.1 and 4.8.3. The degeneracies associated with the dark disc that were discussed in the previous section are also present, and the same solutions given there will apply to this case.

4.9 Conclusions

In this chapter we have presented a new method of determining the vertical DM density profile, and thus the local DM density. The key equation of this method, Eq. 4.19, depends only on the assumption of dynamical equilibrium. In practice further assumptions are made to describe the components going into Eq. 4.19, however the scope of possible models is wide, and in principle model selection using the Bayesian evidence can be used to determine the best model. We leave exploration of this last aspect to future work.

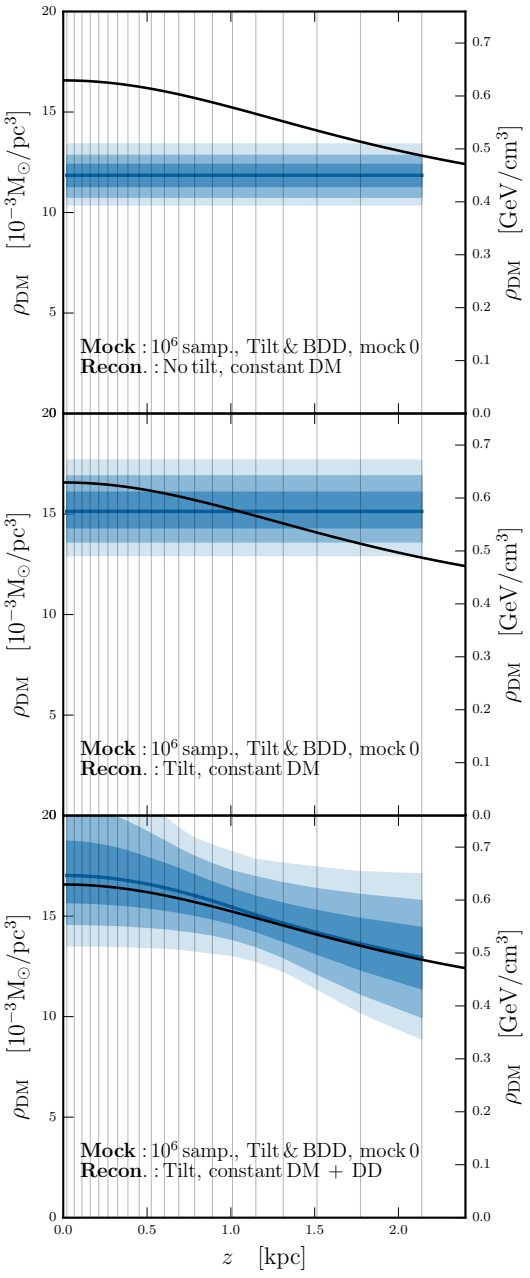

Figure 4.20: Determination of the DM density profile using 10^6 tracer stars with a combination of a tilt term and a dark disc in the mock data (`thick_bdd_tilt_1e6_0`) and using a variety of reconstruction models. These plots show marginalized posteriors for $\rho_{\mathrm{DM}}(z)$, with dark, medium, and light shading indicating the 68%, 95%, and 99.7% CRs respectively. The median value of the posterior is shown as the solid blue line, while the DM density profile used to generate the mock data is shown as a solid black line.

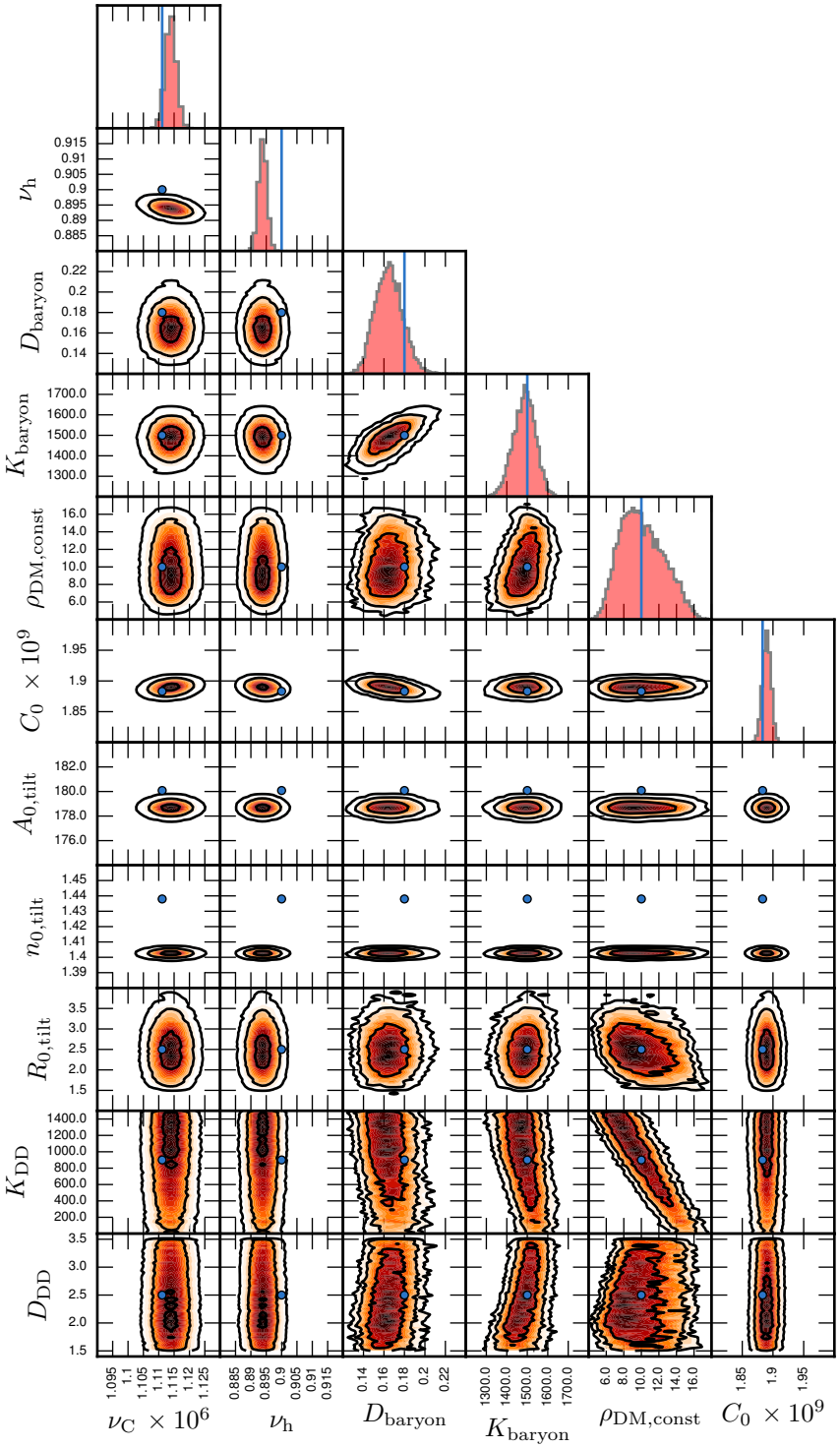
$\nu_{\rm h}$
$D_{\rm baryon}$
$K_{\rm baryon}$
$\rho_{\rm DM,const}$
$C_0 \times 10^9$
$A_{0,\rm tilt}$
$n_{0,\rm tilt}$
$R_{0,\rm tilt}$
$K_{\rm DD}$
$D_{\rm DD}$
$\nu_{\rm C} \times 10^6$

Figure 4.21: Marginalized posterior distributions for mock data set `thick_bdd_tilt_1E6_0` (10^6 sampling, tilt term, big dark disc), reconstructed with a model featuring a tilt term and a dark disc. The blue points and lines indicate the parameter values used to generate the mock data set, or the values derived directly from those parameters for $\nu(0)$ and C_0. Contours indicate the 68%, 95%, and 99.7% CRs.

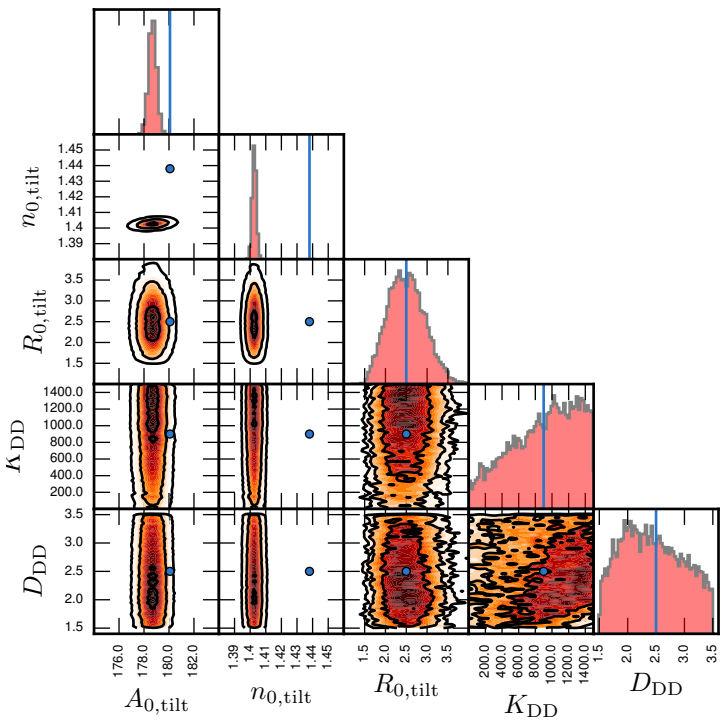

The importance of the tilt term has been previously noted [470, 475, 440], and to derive an accurate value for the local DM density it is vital that our method be able to deal with this term. The baryonic contribution to the galactic density profile drops rapidly as z increases, leaving DM as the dominant component, as seen in Fig. 4.2. Thus to probe the DM density profile sampling thick disc stars that travel higher above the plane is preferable. For these populations the tilt term is more important, as illustrated in the bottom panel of Fig. 4.4. Failure to include the tilt term in the analysis leads to a systematic underestimation of the local DM density, as explained in Section 4.6.6 and demonstrated in Section 4.8.3.

One of the novel aspects of our method is that it can deal with the tilt term while remaining within the confines of the one-dimensional z-direction Jeans equation, which can be seen in Fig. 4.11. With only the data currently available for the Milky Way, this requires several well motivated assumptions, as described in Section 4.6.6. However, with data from Gaia we will be able to directly measure the radial profile of the tilt and tracer density, removing the need for such assumptions. While for this work we have disregarded the rotation curve term (Eq. 4.22), we note that an accurate determination of this will be necessary for the implementation of this or other z-direction methods to real data.

Non-spherical DM density profiles, such as oblate halos or accreted dark discs, can also be accommodated within our method by incorporating an additional dark disc term into the reconstruction model as shown in Fig. 4.16, and Fig. 4.20 which includes a tilt term also. However while the value of the total DM profile at $z = 0$ can be constrained relatively well by the data (Fig. 4.19), the parameters constraining the constant DM component and the dark disc component, cannot be constrained with the mock data used here, and are dependent on the chosen prior range (Fig. 4.18). In the case of a co-rotating accreted dark disc, constraining each element is crucial to direct detection of DM, and indirect detection via solar capture and annihilation into neutrinos, as these rates are velocity dependent.

The work presented in this Chapter is a first step on a path that will extend many years into the future, incorporating data from Gaia as it is released, and also eventually from WEAVE, 4MOST, and LSST. Larger samples and multiple populations will be incorporated, potentially allowing a dark disc to be constrained as a separate element. The current method is one-dimensional in the z direction, with information from the radial direction R being incorporated via the tilt term correction. In future the method could instead be expanded to be inherently two dimensional, using both z- and R-direction Jeans equations, and even three dimensional, using the ϕ-direction Jeans equation also.

The problem of DM brings together particle physics and astronomy, and the distribution of DM exemplifies the necessity of this union. Astronomical observations are required to determine the densities of DM locally and throughout the Galaxy, which in turn govern the signals expected in direct and indirect detection, and the limits on theoretical parameter space which are then derived. The dark shapes the light we see around us in the Galaxy and the Universe, but it is by this light that we will discover the true nature of the dark.

***

A Appendix: Jeans Equations

Here we present a full derivation of the Jeans equations, as used previously in Chapter 4.

A.1 Motion in Cylindrical Coordinates

Galactic dynamics generally uses cylindrical coordinates (R, ϕ, z), with the origin placed on the Galactic Centre, and the $z = 0$ plane aligned with the galactic disc. Thus z is the distance above or below the galactic disc, R is the horizontal distance from the galactic centre, and ϕ is the angle around the disc from some arbitrary reference point. The cylindrical coordinates and their time derivatives are linked to the Cartesian coordinates as:

$$x = R\cos\phi \qquad \dot{x} = \dot{R}\cos\phi - R\sin\phi\dot{\phi} \tag{A.1}$$

$$y = R\sin\phi \qquad \dot{y} = \dot{R}\sin\phi + R\cos\phi\dot{\phi} \tag{A.2}$$

with z unchanged from Cartesian coordinates.

To describe motion in these coordinates we begin with the Lagrangian $\mathcal{L} = K - U$ in simple Cartesian coordinates:

$$\mathcal{L} = \frac{1}{2}\left(\dot{x}^2 + \dot{y}^2 + \dot{z}^2\right) - \Phi(R, \phi, z) \tag{A.3}$$

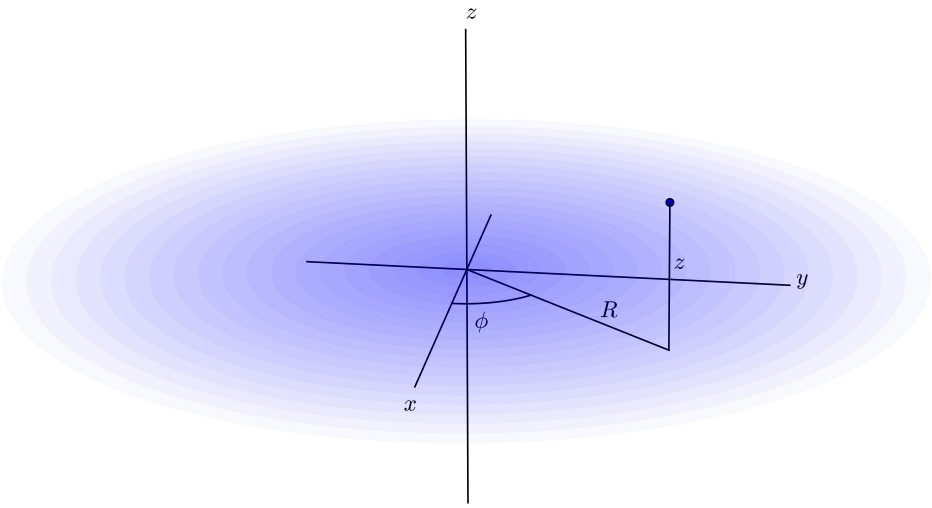

Figure A.1: Cylindrical coordinates (R, ϕ, z) in relation to the Milky Way disc (blue).

Moving to cylindrical coordinates using equations A.1 and A.2 yields

$$\mathcal{L} = \frac{1}{2}\left(\dot{R}^2 + R^2\dot{\phi}^2 + \dot{z}^2\right) - \Phi(R, \phi, z) \tag{A.4}$$

Now we move to a Hamiltonian description of the system, with canonical coordinates $\mathbf{q} = (R, \phi, z)$, and $\mathbf{p} = (p_R, p_\phi, p_z)$ given by:

$$p_i = \frac{\partial \mathcal{L}}{\partial \dot{q}_i} \quad \Rightarrow \quad p_R = \dot{R}, \quad p_\phi = R^2\dot{\phi}, \quad p_z = \dot{z}. \tag{A.5}$$

The Hamiltonian is given by the Legendre transformation (equation A.6), and in cylindrical coordinates is given by equation A.7:

$$H(\mathbf{q}, \mathbf{p}, \mathbf{t}) = \dot{q}_i p_i - \mathcal{L}(\mathbf{q}, \dot{\mathbf{q}}, \mathbf{t}) \tag{A.6}$$

$$= \frac{1}{2}\left(p_R^2 + \frac{p_\phi^2}{R^2} + p_z^2\right) + \Phi(R, \phi, z) \tag{A.7}$$

Applying Hamilton's equations to this Hamiltonian gives us the equations of motion:

$$\dot{p}_R = \ddot{R} = \frac{p_\phi^2}{R^3} - \frac{\partial \Phi}{\partial R} \tag{A.8}$$

$$\dot{p}_\phi = 2R\dot{R}\dot{\phi} + R^2\ddot{\phi} = -\frac{\partial \Phi}{\partial \phi} \tag{A.9}$$

$$\dot{p}_z = \ddot{z} = -\frac{\partial \Phi}{\partial z} \tag{A.10}$$

However simple and attractive these equations are in describing the motions of individual stars, we cannot apply them to galactic dynamics because they involve accelerations, quantities which are virtually impossible to measure. We must instead move to describing whole populations stars and their motions as something akin to a fluid, flowing *en masse* around the galaxy. This is done via the Collisionless Boltzmann Equation, introduced in the next section.

A.2 Collisionless Boltzmann Equation

Within the galaxy stars move as a collisionless system, with each particle moving under the influence of a smooth gravitational potential generated by the sum of all the other particles. We can describe these motions as a collisionless fluid, and thus apply the Collisionless Boltzmann Equation is [410]:

$$\frac{\mathrm{d}f}{\mathrm{d}t} = \frac{\partial f}{\partial t} + \{f, H\} = 0 \tag{A.11}$$

where $f = f(\mathbf{x}, \mathbf{v}, t)$ is the phase space distribution function, defined such that $f(\mathbf{x}, \mathbf{v}, t)\mathrm{d}^3\mathbf{x}\mathrm{d}^3\mathbf{v}$ is the probability that at time t a given star has position and velocity in the ranges $\mathrm{d}^3\mathbf{x}$ and $\mathrm{d}^3\mathbf{v}$. The brackets $\{a, b\}$ are the Poisson brackets:

$$\{a, b\} \equiv \sum_i \left(\frac{\partial a}{\partial q_i}\frac{\partial b}{\partial p_i} - \frac{\partial a}{\partial p_i}\frac{\partial b}{\partial q_i} \right) \tag{A.12}$$

Combining the Hamiltonian from equation A.7 with the CBE from equation A.11 gives us the CBE in cylindrical coordinates:

$$\begin{aligned} 0 \quad &= \frac{\partial f}{\partial t} + \frac{\partial f}{\partial R}\frac{\partial H}{\partial p_R} - \frac{\partial f}{\partial p_R}\frac{\partial H}{\partial R} \\ &\quad + \frac{\partial f}{\partial \phi}\frac{\partial H}{\partial p_\phi} - \frac{\partial f}{\partial p_\phi}\frac{\partial H}{\partial \phi} + \frac{\partial f}{\partial z}\frac{\partial H}{\partial p_z} - \frac{\partial f}{\partial p_z}\frac{\partial H}{\partial z} \end{aligned} \tag{A.13}$$

$$\begin{aligned} &= \frac{\partial f}{\partial t} + \frac{\partial f}{\partial R}p_R - \frac{\partial f}{\partial p_R}\left[-\frac{p_\phi^2}{R^3} + \frac{\partial \Phi}{\partial R} \right] \\ &\quad + \frac{\partial f}{\partial \phi}\frac{p_\phi}{R^2} - \frac{\partial f}{\partial p_\phi}\frac{\partial \Phi}{\partial \phi} + \frac{\partial f}{\partial z}p_z - \frac{\partial f}{\partial p_z}\frac{\partial \Phi}{\partial z} \end{aligned} \tag{A.14}$$

If the system is in dynamic equilibrium (steady state), then we may neglect the partial time derivative of f. Thus for equilibrium tracers, if we know their phase space distribution function f, then we can directly measure the gravitational force from equation (A.14). In practice, however, this is hard because f is six-dimensional (even a million stars gives only 10 sample points per dimension) and we need to estimate the partial derivatives of f to solve equation (A.14). For this reason, it is common to integrate equation (A.14) over velocity to obtain a set of moment equations: the Jeans equations [410].

A.3 General Jeans Equations

We now want to express the CBE in terms of physical quantities that we can derive from populations of stars, such as densities and average velocities. This was first done in the context of stellar motions by James Jeans in 1922 [8].

The first step is to rewrite equation A.14 in terms of radial velocity v_R, tangential velocity v_ϕ, and v_z:

$$p_R = v_R = \dot{R} \qquad \mathrm{d}p_R = \mathrm{d}v_R \tag{A.15}$$

$$p_\phi = Rv_\phi = R^2\dot{\phi} \qquad \mathrm{d}p_\phi = R\mathrm{d}v_\phi \tag{A.16}$$

$$p_z = v_z = \dot{z} \qquad \mathrm{d}p_z = \mathrm{d}v_z \tag{A.17}$$

$$\begin{aligned} 0 = \frac{\partial f}{\partial t} \quad &+ \quad v_R\frac{\partial f}{\partial R} + \frac{v_\phi}{R}\frac{\partial f}{\partial \phi} + v_z\frac{\partial f}{\partial z} \quad + \quad \frac{v_\phi^2}{R}\frac{\partial f}{\partial v_R} - \frac{\partial \Phi}{\partial R}\frac{\partial f}{\partial v_R} \\ &- \quad \frac{v_R v_\phi}{R}\frac{\partial f}{\partial v_\phi} - \frac{1}{R}\frac{\partial \Phi}{\partial \phi}\frac{\partial f}{\partial v_\phi} \quad - \quad \frac{\partial \Phi}{\partial z}\frac{\partial f}{\partial v_z} \end{aligned} \tag{A.18}$$

The first term of the second line of equation A.18 is a result of the v_ϕ has a dependence on R during the change of variables.

Here we are changing variables from $(z, \phi, R, p_R, p_\phi, p_z)$ to $(z', \phi', R', v_R, v_\phi, v_z)$. Due to the dependence of v_ϕ on R we get

$$\frac{\partial f}{\partial R} = \frac{\partial R'}{\partial R}\frac{\partial f}{\partial R'} + \frac{\partial \phi'}{\partial R}\frac{\partial f}{\partial \phi'} + \frac{\partial z'}{\partial R}\frac{\partial f}{\partial z'} + \frac{\partial v_R}{\partial R}\frac{\partial f}{\partial v_R} + \frac{\partial v_\phi}{\partial R}\frac{\partial f}{\partial v_\phi} + \frac{\partial v_z}{\partial R}\frac{\partial f}{\partial v_z} \tag{A.19}$$

$$= \frac{\partial f}{\partial R'} - \frac{p_\phi}{R^2}\frac{\partial f}{\partial v_\phi} \tag{A.20}$$

$$= \frac{\partial f}{\partial R'} - \frac{v_\phi}{R}\frac{\partial f}{\partial v_\phi} \tag{A.21}$$

Following the change of variables we drop the prime superscript.

There are three Jeans equations, one for each spatial dimension. To derive each of them, we multiply equation A.18 by v_R, v_ϕ, or v_z, and then integrate over the velocities $\mathbf{v}$. We now perform this derivation for R, ϕ, and finally z directions.

A.3.1 R-direction Jeans Equation

Taking equation A.18, we multiply by v_R and apply the $\int \mathrm{d}^3\mathbf{v}$ integral:

$$\begin{aligned} 0 = \int \mathrm{d}^3\mathbf{v}\, v_R \frac{\partial f}{\partial t} \quad &+ \quad \int \mathrm{d}^3\mathbf{v}\, v_R^2 \frac{\partial f}{\partial R} + \int \mathrm{d}^3\mathbf{v}\, \frac{v_R v_\phi}{R} \frac{\partial f}{\partial \phi} + \int \mathrm{d}^3\mathbf{v}\, v_R v_z \frac{\partial f}{\partial z} \\ &+ \quad \int \mathrm{d}^3\mathbf{v}\, \frac{v_R v_\phi^2}{R} \frac{\partial f}{\partial v_R} - \int \mathrm{d}^3\mathbf{v}\, v_R \frac{\partial \Phi}{\partial R} \frac{\partial f}{\partial v_R} \\ &- \quad \int \mathrm{d}^3\mathbf{v}\, \frac{v_R^2 v_\phi}{R} \frac{\partial f}{\partial v_\phi} - \int \mathrm{d}^3\mathbf{v}\, \frac{v_R}{R} \frac{\partial \Phi}{\partial \phi} \frac{\partial f}{\partial v_\phi} \\ &- \quad \int \mathrm{d}^3\mathbf{v}\, v_R \frac{\partial \Phi}{\partial z} \frac{\partial f}{\partial v_z} \end{aligned} \tag{A.22}$$

With a wide variety of terms in equation A.22 to evaluate, we first step back, define some new quantities, and examine general forms of the integrals involved.

Recall the distribution function $f(\mathbf{x}, \mathbf{v})$, which gives the probability of a given star having position in range $\mathrm{d}^3\mathbf{x}$ and velocity in range $\mathrm{d}^3\mathbf{v}$ at time t. We can integrate out the velocity component to give the *tracer density* $\nu(\mathbf{x})$, which is the probability to find a star of any velocity at $\mathbf{x}$:

$$\nu(\mathbf{x}) \equiv \int \mathrm{d}^3\mathbf{v}\, f(\mathbf{x}, \mathbf{v}) \tag{A.23}$$

Multiplying the distribution function by the velocity and then integrating with $\int \mathrm{d}^3\mathbf{v}$ will give the *mean velocity*:

$$\overline{\mathbf{v}}(\mathbf{x}) = \frac{1}{\nu(\mathbf{x})} \int \mathrm{d}^3\mathbf{v}\, \mathbf{v} f(\mathbf{x}, \mathbf{v}) \tag{A.24}$$

This definition gives us the first two useful formulas for taking equation A.22 forward:

$$\int \mathrm{d}^3\mathbf{v}\, v_i f = \nu\, \overline{v_i} \tag{A.25}$$

$$\int \mathrm{d}^3\mathbf{v}\, v_i v_j f = \nu\, \overline{v_i v_j} \tag{A.26}$$

where we now take as given the $(\mathbf{x}, \mathbf{v})$ and $\mathbf{x}$ dependencies for f and ν respectively. To deal with terms involving velocity derivatives, we turn to the divergence theorem, which gives

$$\int \mathrm{d}^3\mathbf{v} \left(v_i \frac{\partial f}{\partial v_\ell} + f \frac{\partial v_i}{\partial v_\ell} \right) = \oint d\mathbf{S} f v_i. \tag{A.27}$$

The right hand side of equation A.27 disappears due to $f(\mathbf{x}, \mathbf{v}, t) \to 0$ as $\mathbf{v} \to \infty$.

$$\int \mathrm{d}^3\mathbf{v}\; v_i \frac{\partial f}{\partial v_\ell} = -\int \mathrm{d}^3\mathbf{v}\; f \frac{\partial v_i}{\partial v_\ell} \tag{A.28}$$

$$= -\int \mathrm{d}^3\mathbf{v} f \delta_{i\ell} \tag{A.29}$$

$$= -\delta_{i\ell}\nu. \tag{A.30}$$

Similar use of the divergence theorem gives us expressions for terms with two and three velocity terms, which are known as *velocity moments*:

$$\int \mathrm{d}^3\mathbf{v}\; v_i v_j \frac{\partial f}{\partial v_\ell} = -\nu\,\overline{v_i}\,\delta_{j\ell} - \nu\,\overline{v_j}\,\delta_{i\ell} \tag{A.31}$$

$$\int \mathrm{d}^3\mathbf{v}\; v_i v_j v_k \frac{\partial f}{\partial v_\ell} = -\nu\,\overline{v_j v_k}\,\delta i\ell\; - \nu\,\overline{v_i v_k}\,\delta_{j\ell} - \nu\,\overline{v_i v_j}\,\delta_{k\ell}. \tag{A.32}$$

With these in hand equation A.22 simplifies to the ***R*-Jeans equation**:

$$0 = \frac{\partial(\nu\,\overline{v_R})}{\partial t} + \frac{\partial(\nu\,\overline{v_R^2})}{\partial R} + \frac{1}{R}\frac{\partial(\nu\,\overline{v_R v_\phi})}{\partial \phi} + \frac{\partial(\nu\,\overline{v_R v_z})}{\partial z} + \frac{\nu}{R}\left(\overline{v_R^2} - \overline{v_\phi^2}\right) + \nu\frac{\partial \Phi}{\partial R}. \tag{A.33}$$

A.3.2 ϕ-direction Jeans Equation

To find the ϕ-direction we perform the same procedure, taking equation A.18 but instead multiplying by v_ϕ before applying the $\int \mathrm{d}^3\mathbf{v}$ integral. This gives:

$$\begin{aligned} 0 = \int \mathrm{d}^3\mathbf{v}\, v_\phi \frac{\partial f}{\partial t} \quad &+ \quad \int \mathrm{d}^3\mathbf{v}\, v_R v_\phi \frac{\partial f}{\partial R} + \int \mathrm{d}^3\mathbf{v}\, \frac{v_\phi^2}{R}\frac{\partial f}{\partial \phi} + \int \mathrm{d}^3\mathbf{v}\, v_\phi v_z \frac{\partial f}{\partial z} \\ &+ \quad \int \mathrm{d}^3\mathbf{v}\, \frac{v_\phi^3}{R}\frac{\partial f}{\partial v_R} - \int \mathrm{d}^3\mathbf{v}\, v_\phi \frac{\partial \Phi}{\partial R}\frac{\partial f}{\partial v_R} \\ &- \quad \int \mathrm{d}^3\mathbf{v}\, \frac{v_R v_\phi^2}{R}\frac{\partial f}{\partial v_\phi} - \int \mathrm{d}^3\mathbf{v}\, \frac{v_\phi}{R}\frac{\partial \Phi}{\partial \phi}\frac{\partial f}{\partial v_\phi} \\ &- \quad \int \mathrm{d}^3\mathbf{v}\, v_\phi \frac{\partial \Phi}{\partial z}\frac{\partial f}{\partial v_z}. \end{aligned} \tag{A.34}$$

Applying the general integrals derived above gives us the **ϕ-Jeans equation**:

$$0 = \frac{\partial(\nu\,\overline{v_\phi})}{\partial t} + \frac{\partial(\nu\,\overline{v_R v_\phi})}{\partial R} + \frac{1}{R}\frac{\partial(\nu\,\overline{v_\phi^2})}{\partial \phi} + \frac{\partial(\nu\,\overline{v_\phi v_z})}{\partial z} + \frac{2\nu}{R}\,\overline{v_R v_\phi} + \frac{\nu}{R}\frac{\partial \Phi}{\partial \phi}. \tag{A.35}$$

A.3.3 z-direction Jeans Equation

Finally we repeat the process with v_z as the multiplier:

$$\begin{aligned} 0 = \int \mathrm{d}^3\mathbf{v}\, v_z \frac{\partial f}{\partial t} \quad &+ \quad \int \mathrm{d}^3\mathbf{v}\, v_R v_z \frac{\partial f}{\partial R} + \int \mathrm{d}^3\mathbf{v}\, \frac{v_\phi v_z}{R} \frac{\partial f}{\partial \phi} + \int \mathrm{d}^3\mathbf{v}\, v_z^2 \frac{\partial f}{\partial z} \\ &+ \quad \int \mathrm{d}^3\mathbf{v}\, \frac{v_\phi^2 v_z}{R} \frac{\partial f}{\partial v_R} - \int \mathrm{d}^3\mathbf{v}\, v_z \frac{\partial \Phi}{\partial R} \frac{\partial f}{\partial v_R} \\ &- \quad \int \mathrm{d}^3\mathbf{v}\, \frac{v_R v_\phi v_z}{R} \frac{\partial f}{\partial v_\phi} - \int \mathrm{d}^3\mathbf{v}\, \frac{v_z}{R} \frac{\partial \Phi}{\partial \phi} \frac{\partial f}{\partial v_\phi} \\ &- \quad \int \mathrm{d}^3\mathbf{v}\, v_z \frac{\partial \Phi}{\partial z} \frac{\partial f}{\partial v_z}, \end{aligned} \tag{A.36}$$

which simplifies to the z**-Jeans Equation**

$$0 = \frac{\partial(\nu\,\overline{v_z})}{\partial t} + \frac{\partial(\nu\,\overline{v_R v_z})}{\partial R} + \frac{1}{R}\frac{\partial(\nu\,\overline{v_\phi v_z})}{\partial \phi} + \frac{\partial(\nu\,\overline{v_z^2})}{\partial z} + \frac{\nu}{R}\,\overline{v_R v_z} + \nu\frac{\partial \Phi}{\partial z} \tag{A.37}$$

To summarize, we now have three general Jeans equations in cylindrical coordinates:

$$R: \quad 0 = \frac{\partial(\nu\,\overline{v_R})}{\partial t} + \frac{\partial(\nu\,\overline{v_R^2})}{\partial R} + \frac{1}{R}\frac{\partial(\nu\,\overline{v_R v_\phi})}{\partial \phi} + \frac{\partial(\nu\,\overline{v_R v_z})}{\partial z} + \frac{\nu}{R}\left(\overline{v_R^2} - \overline{v_\phi^2}\right) + \nu\frac{\partial \Phi}{\partial R}, \tag{A.38}$$

$$\phi: \quad 0 = \frac{\partial(\nu\,\overline{v_\phi})}{\partial t} + \frac{\partial(\nu\,\overline{v_R v_\phi})}{\partial R} + \frac{1}{R}\frac{\partial(\nu\,\overline{v_\phi^2})}{\partial \phi} + \frac{\partial(\nu\,\overline{v_\phi v_z})}{\partial z} + \frac{2\nu}{R}\,\overline{v_R v_\phi} + \frac{\nu}{R}\frac{\partial \Phi}{\partial \phi}, \tag{A.39}$$

$$z: \quad 0 = \frac{\partial(\nu\,\overline{v_z})}{\partial t} + \frac{\partial(\nu\,\overline{v_R v_z})}{\partial R} + \frac{1}{R}\frac{\partial(\nu\,\overline{v_\phi v_z})}{\partial \phi} + \frac{\partial(\nu\,\overline{v_z^2})}{\partial z} + \frac{\nu}{R}\,\overline{v_R v_z} + \nu\frac{\partial \Phi}{\partial z}. \tag{A.40}$$

At this point we introduce the *velocity-dispersion tensor* [410]:

$$\begin{aligned} \sigma_{ij}^2(\mathbf{x}) &\equiv \frac{1}{\nu(\mathbf{x})} \int \mathrm{d}^3\mathbf{v} (v_i - \overline{v_i})(v_j - \overline{v_j}) f(\mathbf{x}, \mathbf{v}) \\ &= \overline{v_i v_j} - \overline{v_i}\,\overline{v_j} \end{aligned} \tag{A.41}$$

As the tensor is symmetric it is possible to find a set of orthogonal axes $\hat{\mathbf{e}}_i(\mathbf{x})$ for which σ^2 is diagonal. As discussed earlier in Chapter 4, these three axes $\hat{\mathbf{e}}_i(\mathbf{x})$ can be used to define the orientation of the *velocity ellipsoid*, and the eigenvalues of the tensor determine the length of the ellipsoid's semi-principal axes. The velocity ellipsoid is discussed in Section 4.6.5.

A.4 Simplified Jeans Equations

We can now make several simplifying assumptions to further reduce equations A.38, A.39, and A.40. As shown in Chapter 4 assuming the system is static yields

$$R: \quad 0 = \frac{1}{R}\frac{\partial(R\nu\,\sigma_R^2)}{\partial R} + \frac{1}{R}\frac{\partial(\nu\,\sigma_{R\phi}^2)}{\partial \phi} + \frac{\partial(\nu\,\sigma_{Rz}^2)}{\partial z} - \frac{\nu}{R}\overline{v_\phi^2} + \nu\frac{\partial \Phi}{\partial R}, \tag{A.42}$$

$$\phi: \quad 0 = \frac{1}{R^2}\frac{\partial(R^2\nu\,\sigma_{R\phi}^2)}{\partial R} + \frac{1}{R}\frac{\partial(\nu\,\overline{v_\phi^2})}{\partial \phi} + \frac{\partial(\nu\,\sigma_{\phi z}^2)}{\partial z} + \frac{\nu}{R}\frac{\partial \Phi}{\partial \phi}, \tag{A.43}$$

$$z: \quad 0 = \frac{1}{R}\frac{\partial(R\nu\,\sigma_{Rz}^2)}{\partial R} + \frac{1}{R}\frac{\partial(\nu\,\sigma_{\phi z}^2)}{\partial \phi} + \frac{\partial(\nu\,\sigma_z^2)}{\partial z} + \nu\frac{\partial \Phi}{\partial z}. \tag{A.44}$$

A further assumption of axisymmetry eliminates all partial ϕ derivatives, giving:

$$R: \quad 0 = \frac{1}{R}\frac{\partial(R\nu\,\sigma_R^2)}{\partial R} + \frac{\partial(\nu\,\sigma_{Rz}^2)}{\partial z} - \frac{\nu}{R}\overline{v_\phi^2} + \nu\frac{\partial \Phi}{\partial R}, \tag{A.45}$$

$$\phi: \quad 0 = \frac{1}{R^2}\frac{\partial(R^2\nu\,\sigma_{R\phi}^2)}{\partial R} + \frac{\partial(\nu\,\sigma_{\phi z}^2)}{\partial z} \tag{A.46}$$

$$z: \quad 0 = \frac{1}{R}\frac{\partial(R\nu\,\sigma_{Rz}^2)}{\partial R} + \frac{\partial(\nu\,\sigma_z^2)}{\partial z} + \nu\frac{\partial \Phi}{\partial z}. \tag{A.47}$$

***

B Appendix: Binned ν Bias Calculation

Here we present the derivation Eq. 4.52, which describes the bias induced by the binning of an changing tracer density model. This calculation was derived by Sofia Sivertsson, and is presented here with permission.

We first assume that the tracer density model profile is given by

$$\nu_{\rm mod}(z) = \exp\left(-\frac{z}{h}\right) \tag{B.1}$$

where h is the scale height of the tracer population. We then consider a bin with center $\tilde{z}$ defined as the median star position, a lower limit $\tilde{z} - d_0$, an upper limit $\tilde{z} + d_1$, and a total width of $d = d_1 + d_0$. The binned tracer density is denoted as $\nu_{\rm B}(\tilde{z})$, and to quantify the bias induced by binning we compare $\nu_{\rm B}(\tilde{z})$ to $\nu_{\rm mod}(\tilde{z})$.

The binned tracer density averages over the entire bin width, and is given by:

$$\nu_{\rm B}(\tilde{z}) = \frac{1}{d}\int_{\tilde{z}-d_0}^{\tilde{z}+d_1} \exp\left(-\frac{z}{h}\right) {\rm d}z \tag{B.2}$$

$$= \exp\left(-\frac{\tilde{z}}{h}\right)\frac{h}{d}\left[\exp\left(-\frac{d_0}{h}\right) - \exp\left(-\frac{d_1}{h}\right)\right] \tag{B.3}$$

The bin centre $\tilde{z}$ is given defined as the position of the median star in the bin, and

so:

$$\int_{\tilde{z}-d_0}^{\tilde{z}} \exp\left(-\frac{z}{h}\right) \mathrm{d}z = \int_{\tilde{z}}^{\tilde{z}+d_1} \exp\left(-\frac{z}{h}\right) \mathrm{d}z \tag{B.4}$$

$$\Rightarrow \exp\left(\frac{d_0}{h}\right) + \exp\left(-\frac{d_1}{h}\right) = 2. \tag{B.5}$$

Reformulating this we get expressions for d_0 and d_1 in terms of d:

$$\exp\left(-d_0/h\right) = \frac{\exp(-d/h)+1}{2} \quad \text{and} \quad \exp\left(-d_1/h\right) = \frac{\exp(d/h)+1}{2}. \tag{B.6}$$

We then substitute these into Eq. B.3 to get

$$\nu_B(\tilde{z}) = \exp\left(-\frac{\tilde{z}}{h}\right) \frac{h}{d} \left[\frac{1}{\exp(-d/h)+1} - \frac{1}{\exp(d/h)+1}\right] \tag{B.7}$$

$$= \exp\left(-\frac{\tilde{z}}{h}\right) \frac{2h}{d} \frac{\exp(d/h)-1}{\exp(d/h)+1}. \tag{B.8}$$

The first exponential on the RHS of B.8 is the model tracer density profile evaluated at the bin center $\tilde{z}$, and so we arrive at

$$\frac{\nu_{\mathrm{B}}(\tilde{z})}{\nu_{\mathrm{mod}}(\tilde{z})} = \frac{2h}{d} \frac{\exp(d/h)-1}{\exp(d/h)+1}. \tag{B.9}$$

Thus the bias is dependent on the bin size. Due to our binning scheme, where we set bin the bin boundaries such that each bin has an equal number of stars, the last bin is the largest, and thus the bias is greatest there. For a scale height of $h = 0.9$ kpc, and 20 bins between 0 kpc and 2.4 kpc, the bias in the last bin is approximately 2%.

***

C Appendix: Dark Disc Reconstructions with Multiple Mocks

Here we show the results of reconstructing all mocks data sets generated using a constant DM density only (`thick_X_M`), constant DM and a regular dark disc (`thick_dd_X_M`), or constant DM and a 'big' dark disc (`thick_bdd_X_M`); see Table 4.5 for details. The reconstruction models either have a constant DM density only, or a constant DM density plus a dark disc.

***

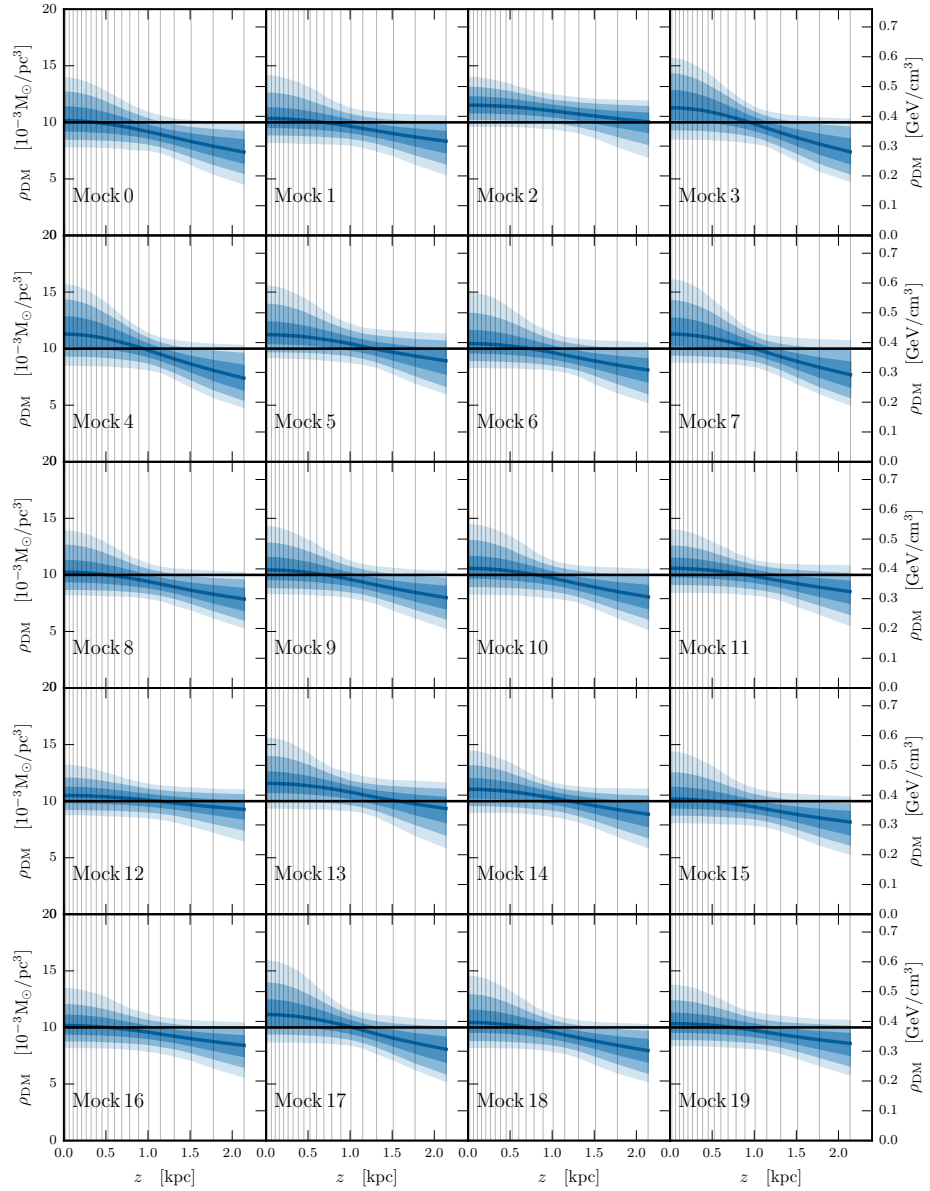

Figure C.1: Marginalized posteriors of $\rho_{\rm DM}(z)$ for mock data sets `thick_1E6_0-19` with $\rho_{\rm DM,const}$ only (no DD component) reconstructed using a model with $\rho_{\rm DM,const}$ plus a DD. Dark, medium, and light shading indicate the 68%, 95%, and 99.7% CRs respectively. The median value of the posterior is shown as the solid blue line, while the DM density profile used to generate the mock data is shown as a solid black line.

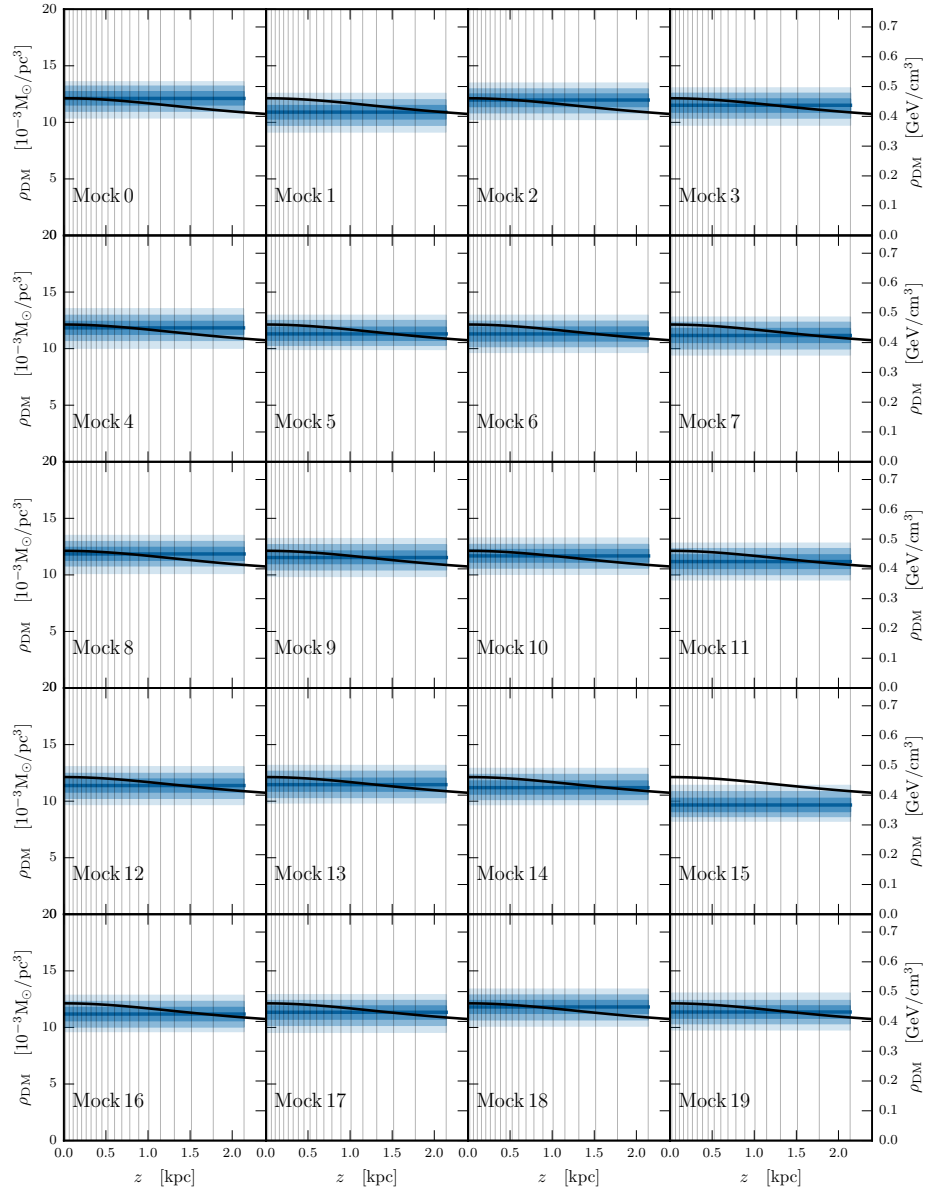

Figure C.2: Marginalized posteriors of $\rho_{\rm DM}(z)$ for mock data sets `thick_dd_1E6_0-19` with $\rho_{\rm DM,const}$ plus a DD component, reconstructed using a model with $\rho_{\rm DM,const}$ only. Dark, medium, and light shading indicate the 68%, 95%, and 99.7% CRs respectively. The median value of the posterior is shown as the solid blue line, while the DM density profile used to generate the mock data is shown as a solid black line.

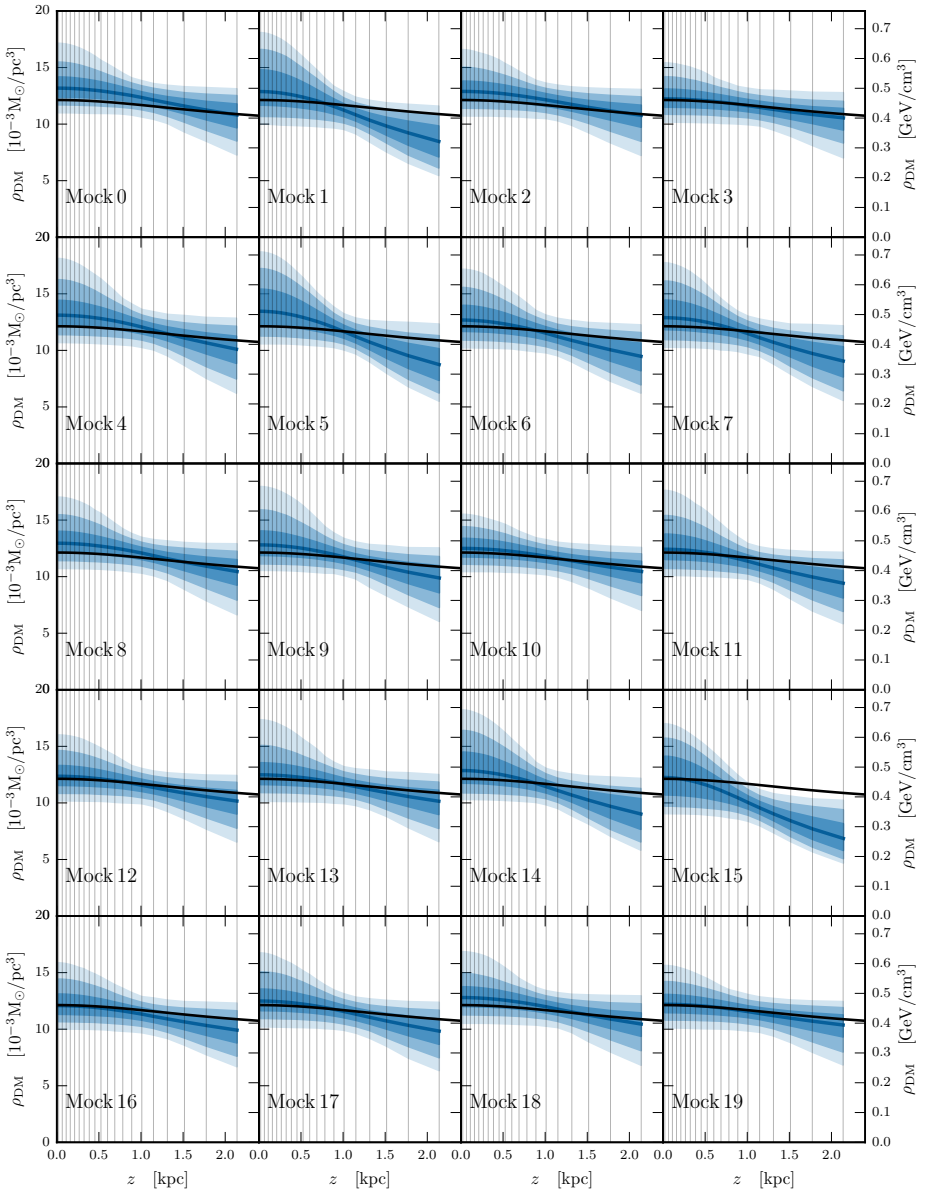

Figure C.3: Marginalized posteriors of $\rho_{\rm DM}(z)$ for mock data sets `thick_dd_1E6_0-19` with $\rho_{\rm DM,const}$ plus a DD component, reconstructed using a model with $\rho_{\rm DM,const}$ and a DD component. Dark, medium, and light shading indicate the 68%, 95%, and 99.7% CRs respectively. The median value of the posterior is shown as the solid blue line, while the DM density profile used to generate the mock data is shown as a solid black line.

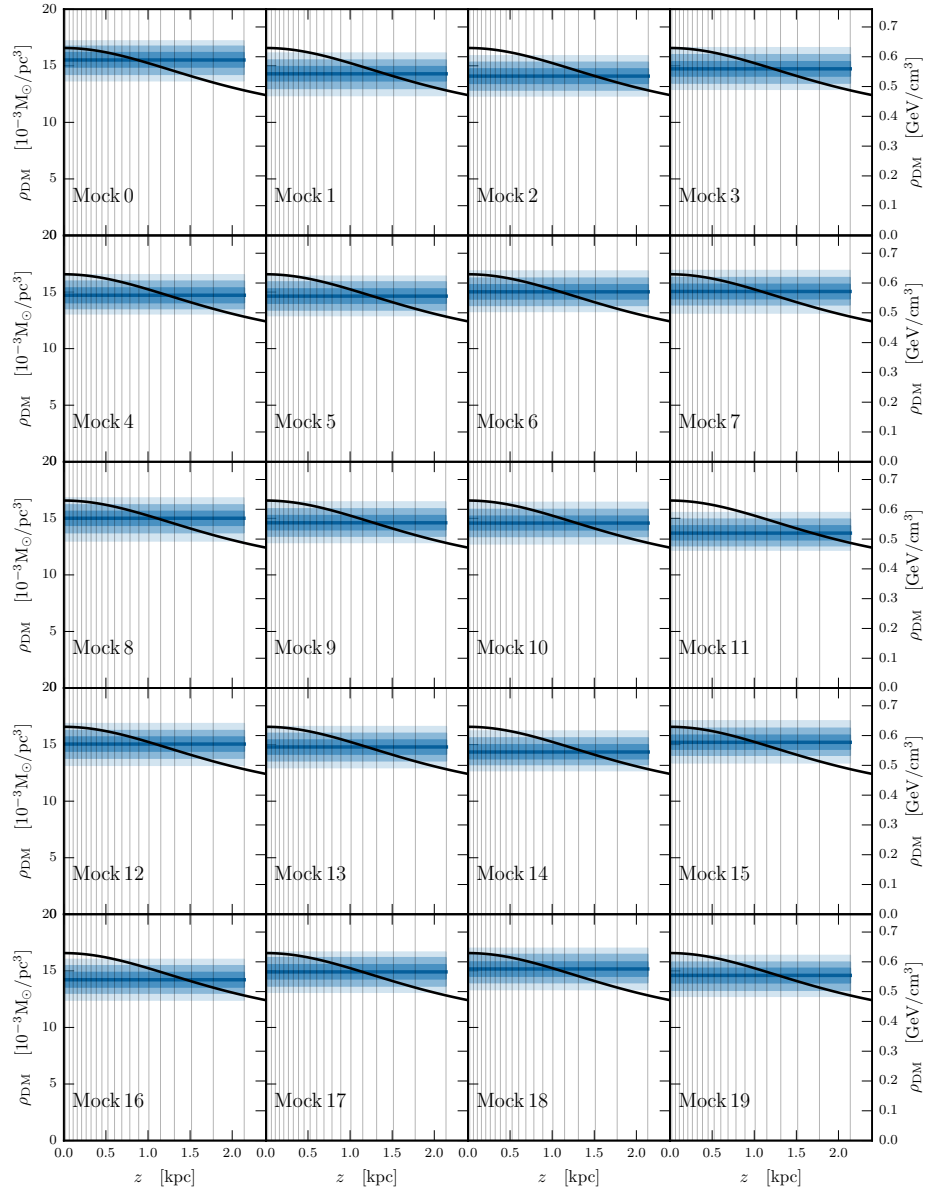

Figure C.4: Marginalized posteriors of $\rho_{\rm DM}(z)$ for mock data sets `thick_bdd_1E6_0-19` with $\rho_{\rm DM,const}$ plus a DD component, reconstructed using a model with $\rho_{\rm DM,const}$ only. Dark, medium, and light shading indicate the 68%, 95%, and 99.7% CRs respectively. The median value of the posterior is shown as the solid blue line, while the DM density profile used to generate the mock data is shown as a solid black line.

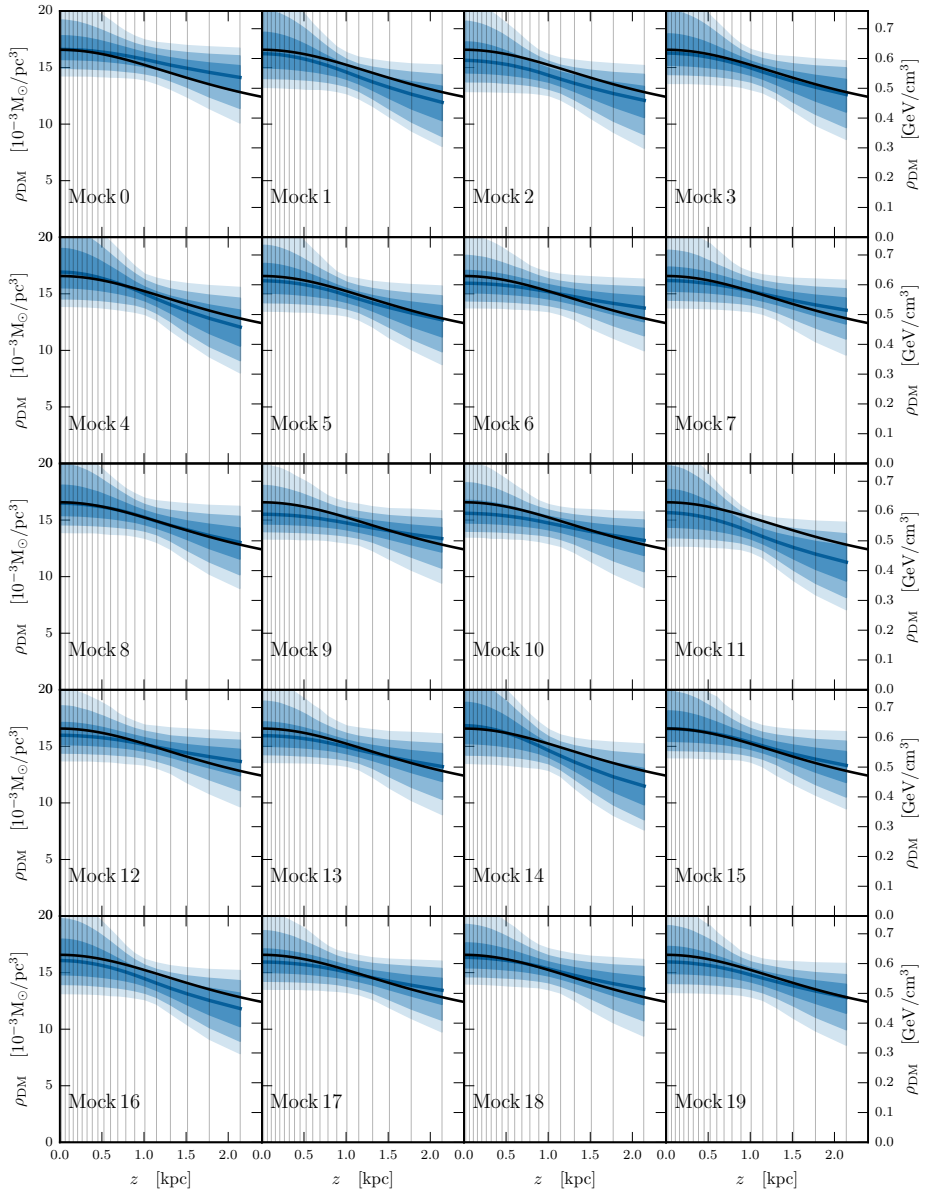

Figure C.5: Marginalized posteriors of $\rho_{\rm DM}(z)$ for mock data sets `thick_bdd_1E6_0-19` with $\rho_{\rm DM,const}$ plus a 'big' DD component, reconstructed using a model with $\rho_{\rm DM,const}$ and a DD component. Dark, medium, and light shading indicate the 68%, 95%, and 99.7% CRs respectively. The median value of the posterior is shown as the solid blue line, while the DM density profile used to generate the mock data is shown as a solid black line.

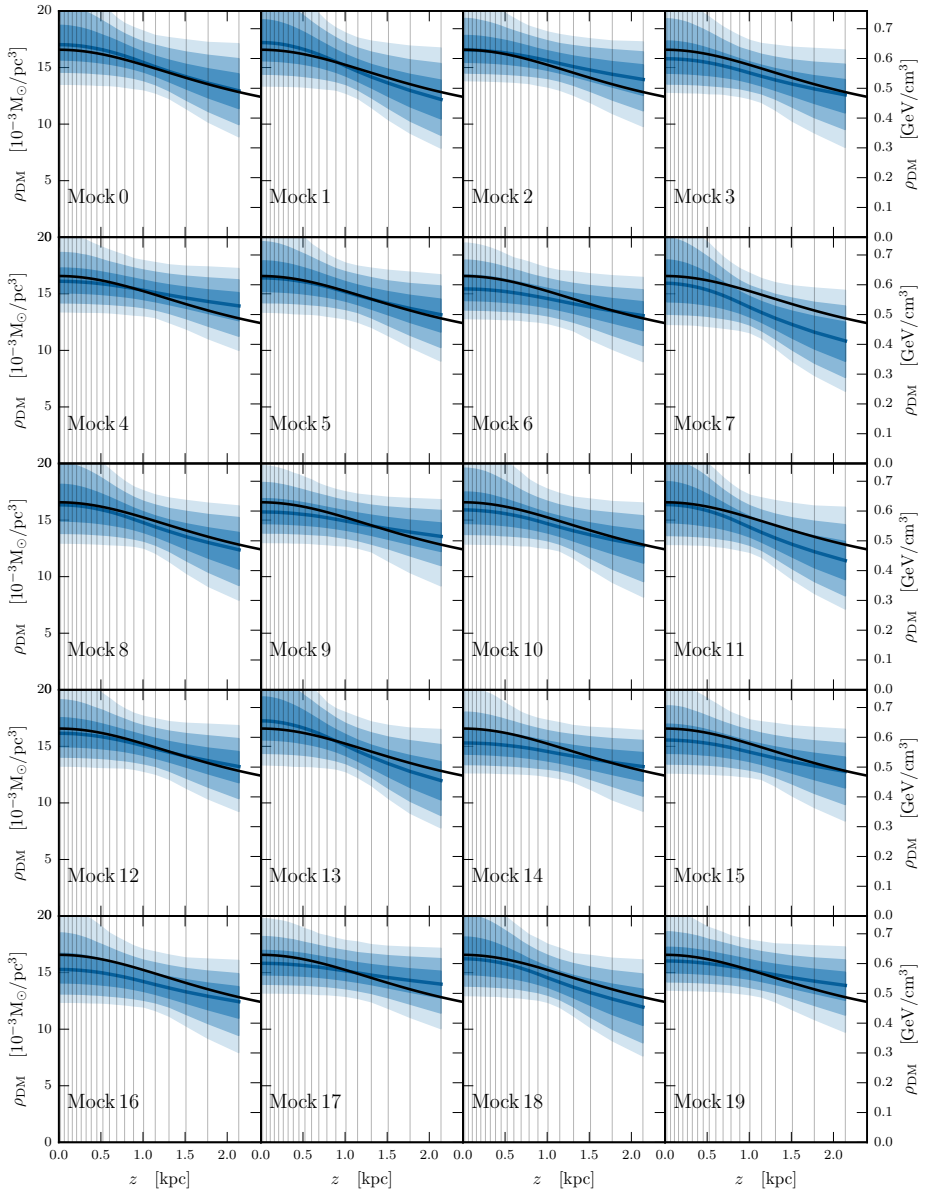

Figure C.6: Marginalized posteriors of $\rho_{\rm DM}(z)$ for mock data sets `thick_bdd_tilt_X_0-19` with $\rho_{\rm DM,const}$ plus a 'big' DD component and including the effects of tilt, reconstructed using a model with $\rho_{\rm DM,const}$, a DD component, and incorporating tilt. Dark, medium, and light shading indicate the 68%, 95%, and 99.7% CRs respectively. The median value of the posterior is shown as the solid blue line, while the DM density profile used to generate the mock data is shown as a solid black line.

Bibliography

[1] C. Arina, G. Bertone and H. Silverwood, *Complementarity of direct and indirect dark matter detection experiments*, *Phys. Rev. D* **88** (July, 2013) 013002, [1304.5119].

[2] H. Silverwood, C. Weniger, P. Scott and G. Bertone, *A realistic assessment of the CTA sensitivity to dark matter annihilation*, *JCAP* **3** (Mar., 2015) 055, [1408.4131].

[3] H. Silverwood, S. Sivertsson, P. Steger, J. I. Read and G. Bertone, *A non-parametric method for measuring the local dark matter density*, *MNRAS* **459** (Apr., 2016) 4191–4208, [1507.08581].

[4] M. G. Aartsen, K. Abraham, M. Ackermann, J. Adams, J. A. Aguilar, M. Ahlers et al., *Improved limits on dark matter annihilation in the Sun with the 79-string IceCube detector and implications for supersymmetry*, *JCAP* **4** (Apr., 2016) 022, [1601.00653].

[5] S. Horiuchi, O. Macias, D. Restrepo, A. Rivera, O. Zapata and H. Silverwood, *The Fermi-LAT gamma-ray excess at the Galactic Center in the singlet-doublet fermion dark matter model*, *JCAP* **3** (Mar., 2016) 048, [1602.04788].

[6] E. Öpik*Bull. de la Soc. Astr. de Russie* **21** (1915) .

[7] J. Kapteyn, *First Attempt at a Theory of the Arrangement and Motion of the Sidereal System*, *Astrophys.J.* **55** (1922) 302–328.

[8] J. H. Jeans, *The motions of stars in a Kapteyn universe*, *MNRAS* **82** (Jan., 1922) 122–132.

[9] F. Zwicky, *Die Rotverschiebung von extragalaktischen Nebeln*, *Helvetica Physica Acta* **6** (1933) 110–127.

[10] F. Zwicky, *On the Masses of Nebulae and of Clusters of Nebulae*, *ApJ* **86** (Oct., 1937) 217.

[11] V. C. Rubin and W. K. Ford, Jr., *Rotation of the Andromeda Nebula from a Spectroscopic Survey of Emission Regions*, *ApJ* **159** (Feb., 1970) 379.

[12] V. C. Rubin, N. Thonnard and W. K. Ford, Jr., *Extended rotation curves of high-luminosity spiral galaxies. IV - Systematic dynamical properties, SA through SC*, *ApJ* **225** (Nov., 1978) L107–L111.

[13] V. Rubin, N. Thonnard and J. Ford, W.K., *Rotational properties of 21 SC galaxies with a large range of luminosities and radii, from NGC 4605 /R = 4kpc/ to UGC 2885 /R = 122 kpc/*, *Astrophys.J.* **238** (1980) 471.

[14] G. S. Shostak and D. H. Rogstad, *Aperture synthesis study of neutral hydrogen in NGC 2403 and NGC 4236. I. Observations.*, *A&A* **24** (May, 1973) 405–410.

[15] D. H. Rogstad, G. S. Shostak and A. H. Rots, *Aperture synthesis study of neutral hydrogen in the galaxies NGC 6946 and IC 342.*, *A&A* **22** (Jan., 1973) 111–119.

[16] D. H. Rogstad, I. A. Lockhart and M. C. H. Wright, *Aperture-synthesis observations of H I in the galaxy M83.*, *ApJ* **193** (Oct., 1974) 309–319.

[17] G. A. Seielstad and M. C. H. Wright, *Neutral-hydrogen aperture-synthesis maps of IC 2574 and NGC 7640.*, *ApJ* **184** (Sept., 1973) 343–351.

[18] M. S. Roberts, *The rotation curves of galaxies*, *Symposium - International Astronomical Union* **69** (1, 1975) 331–340.

[19] M. S. Roberts and R. N. Whitehurst, *The rotation curve and geometry of M31 at large galactocentric distances.*, *ApJ* **201** (Oct., 1975) 327–346.

[20] W. K. Huchtmeier, *Rotation-curves of galaxies from 21 cm-line observations*, *A&A* **45** (Dec., 1975) 259–268.

[21] A. Bosma, *The distribution and kinematics of neutral hydrogen in spiral galaxies of various morphological types.* PhD thesis, PhD Thesis, Groningen Univ., (1978), 1978.

[22] J. Einasto, A. Kaasik and E. Saar, *Dynamic evidence on massive coronas of galaxies*, *Nature* **250** (July, 1974) 309–310.

[23] J. P. Ostriker, P. J. E. Peebles and A. Yahil, *The size and mass of galaxies, and the mass of the universe*, *Astrophys. J.* **193** (1974) L1–L4.

[24] P. J. E. Peebles, *Primeval adiabatic perturbations - Constraints from the mass distribution*, *ApJ* **248** (Sept., 1981) 885–897.

[25] P. J. E. Peebles, *Primeval adiabatic perturbations - Effect of massive neutrinos*, *ApJ* **258** (July, 1982) 415–424.

[26] S. D. M. White, C. S. Frenk and M. Davis, *Clustering in a neutrino-dominated universe*, *ApJ* **274** (Nov., 1983) L1–L5.

[27] C. Alcock, R. A. Allsman, D. R. Alves, T. S. Axelrod, A. C. Becker, D. P. Bennett et al., *The MACHO Project: Microlensing Results from 5.7 Years of Large Magellanic Cloud Observations*, *ApJ* **542** (Oct., 2000) 281–307, [astro-ph/0001272].

[28] EROS Collaboration collaboration, T. Lasserre, C. Afonso, J. N. Albert, J. Andersen, R. Ansari, É. Aubourg et al., *Not enough stellar mass Machos in the Galactic halo*, *A&A* **355** (Mar., 2000) L39–L42, [astro-ph/0002253].

[29] EROS-2 Collaboration collaboration, P. Tisserand, L. Le Guillou, C. Afonso, J. N. Albert, J. Andersen, R. Ansari et al., *Limits on the Macho content of the Galactic Halo from the EROS-2 Survey of the Magellanic Clouds*, *A&A* **469** (July, 2007) 387–404, [astro-ph/0607207].

[30] N. W. Boggess, J. C. Mather, R. Weiss, C. L. Bennett, E. S. Cheng, E. Dwek et al., *The COBE mission - Its design and performance two years after launch*, *ApJ* **397** (Oct., 1992) 420–429.

[31] D. Larson, J. Dunkley, G. Hinshaw, E. Komatsu, M. R. Nolta, C. L. Bennett et al., *Seven-Year Wilkinson Microwave Anisotropy Probe (WMAP) Observations: Power Spectra and WMAP-Derived Parameters*, arXiv:1001.4635.

[32] E. Komatsu, K. M. Smith, J. Dunkley, C. L. Bennett, B. Gold, G. Hinshaw et al., *Seven-year Wilkinson Microwave Anisotropy Probe (WMAP) Observations: Cosmological Interpretation*, *ApJS* **192** (Feb., 2011) 18, [1001.4538].

[33] Planck collaboration, P. Ade et al., *Planck 2015 results. XIII. Cosmological parameters*, 1502.01589.

[34] D. Clowe, A. Gonzalez and M. Markevitch, *Weak-Lensing Mass Reconstruction of the Interacting Cluster 1E 0657-558: Direct Evidence for the Existence of Dark Matter*, *ApJ* **604** (Apr., 2004) 596–603, [astro-ph/0312273].

[35] D. Clowe, M. Bradač, A. H. Gonzalez, M. Markevitch, S. W. Randall, C. Jones et al., *A Direct Empirical Proof of the Existence of Dark Matter*, *ApJ* **648** (Sept., 2006) L109–L113, [astro-ph/0608407].

[36] M. Markevitch, A. H. Gonzalez, D. Clowe, A. Vikhlinin, W. Forman, C. Jones et al., *Direct Constraints on the Dark Matter Self-Interaction Cross Section from the Merging Galaxy Cluster 1E 0657-56*, *ApJ* **606** (May, 2004) 819–824, [astro-ph/0309303].

[37] M. Markevitch, *Chandra Observation of the Most Interesting Cluster in the Universe*, in *Proceedings of The X-ray Universe 2005* (A. Wilson, ed.), vol. 604 of *ESA Special Publication*, p. 723, Jan., 2006. astro-ph/0511345.

[38] M. Taoso, G. Bertone and A. Masiero, *Dark matter candidates: a ten-point test*, *JCAP* **3** (Mar., 2008) 22, [0711.4996].

[39] M. Kobayashi and T. Maskawa, *CP-Violation in the Renormalizable Theory of Weak Interaction*, *Progress of Theoretical Physics* **49** (Feb., 1973) 652–657.

[40] F. Abe, H. Akimoto, A. Akopian, M. G. Albrow, S. R. Amendolia, D. Amidei et al., *Observation of Top Quark Production in $\bar{p}p$ Collisions with the Collider Detector at Fermilab*, *Physical Review Letters* **74** (Apr., 1995) 2626–2631, [hep-ex/9503002].

[41] S. Abachi, B. Abbott, M. Abolins, B. S. Acharya, I. Adam, D. L. Adams et al., *Search for High Mass Top Quark Production in $p\bar{p}$ Collisions at $s = 1.8$ TeV*, *Physical Review Letters* **74** (Mar., 1995) 2422–2426, [hep-ex/9411001].

[42] M. L. Perl, G. S. Abrams, A. M. Boyarski, M. Breidenbach, D. D. Briggs, F. Bulos et al., *Evidence for anomalous lepton production in e^+e^- annihilation*, *Physical Review Letters* **35** (Dec., 1975) 1489–1492.

[43] DONUT Collaboration, K. Kodama, N. Ushida, C. Andreopoulos, N. Saoulidou, G. Tzanakos et al., *Observation of tau neutrino interactions*, *Physics Letters B* **504** (Apr., 2001) 218–224, [hep-ex/0012035].

[44] F. Englert and R. Brout, *Broken Symmetry and the Mass of Gauge Vector Mesons*, *Physical Review Letters* **13** (Aug., 1964) 321–323.

[45] P. W. Higgs, *Broken Symmetries and the Masses of Gauge Bosons*, *Physical Review Letters* **13** (Oct., 1964) 508–509.

[46] G. S. Guralnik, C. R. Hagen and T. W. Kibble, *Global Conservation Laws and Massless Particles*, *Physical Review Letters* **13** (Nov., 1964) 585–587.

[47] S. Chatrchyan, V. Khachatryan, A. M. Sirunyan, A. Tumasyan, W. Adam, E. Aguilo et al., *Observation of a new boson at a mass of 125 GeV with the CMS experiment at the LHC*, *Physics Letters B* **716** (Sept., 2012) 30–61, [1207.7235].

[48] G. Aad, T. Abajyan, B. Abbott, J. Abdallah, S. Abdel Khalek, A. A. Abdelalim et al., *Observation of a new particle in the search for the Standard Model Higgs boson with the ATLAS detector at the LHC*, *Physics Letters B* **716** (Sept., 2012) 1–29, [1207.7214].

[49] D. J. E. Marsh, *Axion Cosmology*, 1510.07633.

[50] R. J. Crewther, P. Di Vecchia, G. Veneziano and E. Witten, *Chiral Estimate of the Electric Dipole Moment of the Neutron in Quantum Chromodynamics*, *Phys. Lett.* **B88** (1979) 123.

[51] C. A. Baker et al., *An Improved experimental limit on the electric dipole moment of the neutron*, *Phys. Rev. Lett.* **97** (2006) 131801, [hep-ex/0602020].

[52] R. D. Peccei and H. R. Quinn, *CP Conservation in the Presence of Instantons*, *Phys. Rev. Lett.* **38** (1977) 1440–1443.

[53] S. Weinberg, *A New Light Boson?*, *Phys. Rev. Lett.* **40** (1978) 223–226.

[54] F. Wilczek, *Problem of Strong p and t Invariance in the Presence of Instantons*, *Phys. Rev. Lett.* **40** (1978) 279–282.

[55] J. Preskill, M. B. Wise and F. Wilczek, *Cosmology of the Invisible Axion*, *Phys. Lett.* **B120** (1983) 127–132.

[56] L. F. Abbott and P. Sikivie, *A Cosmological Bound on the Invisible Axion*, *Phys. Lett.* **B120** (1983) 133–136.

[57] M. Dine and W. Fischler, *The Not So Harmless Axion*, *Phys. Lett.* **B120** (1983) 137–141.

[58] J. E. Kim, *Light Pseudoscalars, Particle Physics and Cosmology*, *Phys. Rept.* **150** (1987) 1–177.

[59] S. Dodelson and L. M. Widrow, *Sterile neutrinos as dark matter*, *Physical Review Letters* **72** (Jan., 1994) 17–20, [hep-ph/9303287].

[60] M. Drewes, *The Phenomenology of Right Handed Neutrinos*, *International Journal of Modern Physics E* **22** (Aug., 2013) 1330019, [1303.6912].

[61] R. Adhikari, M. Agostini, N. A. Ky, T. Araki, M. Archidiacono, M. Bahr et al., *A White Paper on keV Sterile Neutrino Dark Matter*, *ArXiv e-prints* (Feb., 2016) , [1602.04816].

[62] P. Minkowski, $\mu \to e\gamma$ *at a rate of one out of 10* ^{9} *muon decays?*, *Physics Letters B* **67** (Apr., 1977) 421–428.

[63] R. N. Mohapatra and G. Senjanovic, *Neutrino mass and spontaneous parity nonconservation*, *Physical Review Letters* **44** (Apr., 1980) 912–915.

[64] T. Yanagida, *Horizontal Symmetry and Masses of Neutrinos*, *Progress of Theoretical Physics* **64** (Sept., 1980) 1103–1105.

[65] E. Bulbul, M. Markevitch, A. Foster, R. K. Smith, M. Loewenstein and S. W. Randall, *Detection of an Unidentified Emission Line in the Stacked X-Ray Spectrum of Galaxy Clusters*, *ApJ* **789** (July, 2014) 13, [1402.2301].

[66] A. Boyarsky, O. Ruchayskiy, D. Iakubovskyi and J. Franse, *Unidentified Line in X-Ray Spectra of the Andromeda Galaxy and Perseus Galaxy Cluster*, *Physical Review Letters* **113** (Dec., 2014) 251301, [1402.4119].

[67] O. Ruchayskiy, A. Boyarsky, D. Iakubovskyi, E. Bulbul, D. Eckert, J. Franse et al., *Searching for decaying dark matter in deep XMM-Newton observation of the Draco dwarf spheroidal*, *MNRAS* **460** (Aug., 2016) 1390–1398, [1512.07217].

[68] ATLAS collaboration, G. Aad et al., *Observation of a new particle in the search for the Standard Model Higgs boson with the ATLAS detector at the LHC*, *Phys. Lett.* **B716** (2012) 1–29, [1207.7214].

[69] CMS collaboration, S. Chatrchyan et al., *Observation of a new boson at a mass of 125 GeV with the CMS experiment at the LHC*, *Phys. Lett.* **B716** (2012) 30–61, [1207.7235].

[70] M. Drees, R. Godbole and P. Roy, *Theory and phenomenology of sparticles: An account of four-dimensional N=1 supersymmetry in high energy physics*. Hackensack, USA: World Scientific (2004) 555 p, 2004.

[71] S. P. Martin, *A Supersymmetry primer*, hep-ph/9709356.

[72] M. Ibe, S. Matsumoto and T. T. Yanagida, *Flat Higgs Potential from Planck Scale Supersymmetry Breaking*, *Phys. Lett.* **B732** (2014) 214–217, [1312.7108].

[73] S. Dimopoulos and H. Georgi, *Softly broken supersymmetry and SU(5)*, *Nuclear Physics B* **193** (Dec., 1981) 150–162.

[74] M. E. Peskin and D. V. Schroeder, *An Introduction to Quantum Field Theory*. Westview Press, 1995.

[75] G. Jungman, M. Kamionkowski and K. Griest, *Supersymmetric dark matter*, *Phys. Rep.* **267** (1996) 195–373, [hep-ph/9506380].

[76] L. Bergstrom and P. Ullio, *Full one loop calculation of neutralino annihilation into two photons*, *Nucl. Phys.* **B504** (1997) 27–44, [hep-ph/9706232].

[77] Z. Bern, P. Gondolo and M. Perelstein, *Neutralino annihilation into two photons*, *Phys. Lett.* **B411** (1997) 86–96, [hep-ph/9706538].

[78] Particle Data Group collaboration, K. A. Olive et al., *Review of Particle Physics*, *Chin. Phys.* **C38** (2014) 090001.

[79] G. Bertone, D. Hooper and J. Silk, *Particle dark matter: evidence, candidates and constraints*, *Phys. Rep.* **405** (2005) 279–390, [hep-ph/0404175].

[80] A. H. Guth, *Inflationary universe: A possible solution to the horizon and flatness problems*, *Phys. Rev. D* **23** (Jan., 1981) 347–356.

[81] A. A. Starobinsky, *A new type of isotropic cosmological models without singularity*, *Physics Letters B* **91** (Mar., 1980) 99–102.

[82] D. Kazanas, *Dynamics of the universe and spontaneous symmetry breaking*, *ApJ* **241** (Oct., 1980) L59–L63.

[83] K. Sato, *Cosmological baryon-number domain structure and the first order phase transition of a vacuum*, *Physics Letters B* **99** (Feb., 1981) 66–70.

[84] M. B. Einhorn and K. Sato, *Monopole production in the very early universe in a first-order phase transition*, *Nuclear Physics B* **180** (May, 1981) 385–404.

[85] A. D. Linde, *A new inflationary universe scenario: A possible solution of the horizon, flatness, homogeneity, isotropy and primordial monopole problems*, *Physics Letters B* **108** (Feb., 1982) 389–393.

[86] A. Albrecht and P. J. Steinhardt, *Cosmology for grand unified theories with radiatively induced symmetry breaking*, *Physical Review Letters* **48** (Apr., 1982) 1220–1223.

[87] S. Dodelson, *Modern Cosmology*. Academic Press, Amsterdam, 2003.

[88] D. Baumann, "Cosmology - Part III Mathematical Tripos." `http://www.damtp.cam.ac.uk/user/db275/Cosmology/Lectures.pdf`, 2013.

[89] G. Steigman, B. Dasgupta and J. F. Beacom, *Precise Relic WIMP Abundance and its Impact on Searches for Dark Matter Annihilation*, *Phys. Rev.* **D86** (2012) 023506, [`1204.3622`].

[90] K. Griest and M. Kamionkowski, *Unitarity limits on the mass and radius of dark-matter particles*, *Physical Review Letters* **64** (Feb., 1990) 615–618.

[91] B. W. Lee and S. Weinberg, *Cosmological lower bound on heavy-neutrino masses*, *Physical Review Letters* **39** (July, 1977) 165–168.

[92] D. J. Schwarz and S. Hofmann, *Small-scale structure of cold dark matter*, *Nuclear Physics B Proceedings Supplements* **87** (June, 2000) 93–95, [`astro-ph/9912343`].

[93] S. Hofmann, D. J. Schwarz and H. Stöcker, *Damping scales of neutralino cold dark matter*, *Phys. Rev. D* **64** (Oct., 2001) 083507, [`astro-ph/0104173`].

[94] C. Bœhm, P. Fayet and R. Schaeffer, *Constraining dark matter candidates from structure formation*, *Physics Letters B* **518** (Oct., 2001) 8–14, [`astro-ph/0012504`].

[95] X. Chen, M. Kamionkowski and X. Zhang, *Kinetic decoupling of neutralino dark matter*, *Phys. Rev. D* **64** (July, 2001) 021302, [astro-ph/0103452].

[96] S. Profumo, K. Sigurdson and M. Kamionkowski, *What mass are the smallest protohalos?*, *Phys. Rev. Lett.* **97** (2006) 031301, [astro-ph/0603373].

[97] T. Bringmann, *Particle Models and the Small-Scale Structure of Dark Matter*, *New J. Phys.* **11** (2009) 105027, [0903.0189].

[98] Z. Maki, M. Nakagawa and S. Sakata, *Remarks on the Unified Model of Elementary Particles*, *Progress of Theoretical Physics* **28** (Nov., 1962) 870–880.

[99] B. Pontecorvo, *Neutrino Experiments and the Problem of Conservation of Leptonic Charge*, *Soviet Journal of Experimental and Theoretical Physics* **26** (May, 1968) 984.

[100] V. Gribov and B. Pontecorvo, *Neutrino astronomy and lepton charge*, *Physics Letters B* **28** (Jan., 1969) 493–496.

[101] J. Schechter and J. W. F. Valle, *Neutrino masses in SU(2) $\otimes$ U(1) theories*, *Phys. Rev. D* **22** (Nov., 1980) 2227–2235.

[102] R. Davis, D. S. Harmer and K. C. Hoffman, *Search for Neutrinos from the Sun*, *Physical Review Letters* **20** (May, 1968) 1205–1209.

[103] Q. R. Ahmad, R. C. Allen, T. C. Andersen, J. D. Anglin, G. Bühler, J. C. Barton et al., *Measurement of the Rate of $\nu_e + d$ –¿ $p + p + e^-$ Interactions Produced by ^8B Solar Neutrinos at the Sudbury Neutrino Observatory*, *Physical Review Letters* **87** (Aug., 2001) 071301, [nucl-ex/0106015].

[104] Y. Fukuda, T. Hayakawa, E. Ichihara, K. Inoue, K. Ishihara, H. Ishino et al., *Evidence for Oscillation of Atmospheric Neutrinos*, *Physical Review Letters* **81** (Aug., 1998) 1562–1567, [hep-ex/9807003].

[105] F. P. An, J. Z. Bai, A. B. Balantekin, H. R. Band, D. Beavis, W. Beriguete et al., *Observation of Electron-Antineutrino Disappearance at Daya Bay*, *Physical Review Letters* **108** (Apr., 2012) 171803, [1203.1669].

[106] K. Abe, N. Abgrall, H. Aihara, T. Akiri, J. B. Albert, C. Andreopoulos et al., *Evidence of electron neutrino appearance in a muon neutrino beam*, *Phys. Rev. D* **88** (Aug., 2013) 032002, [1304.0841].

[107] G. Bertone, ed., *Particle Dark Matter: Observations, Models and Searches*. Cambridge University Press, 2010.

[108] S. A. Balashev, E. O. Zavarygin, A. V. Ivanchik, K. N. Telikova and D. A. Varshalovich, *The primordial deuterium abundance: subDLA system at $z_{\rm abs} = 2.437$ towards the QSO J1444+2919*, 1511.01797.

[109] K. Jedamzik, *Neutralinos and Big Bang nucleosynthesis*, *Phys. Rev.* **D70** (2004) 083510, [astro-ph/0405583].

[110] W. Hu, *Lecture Notes on CMB Theory: From Nucleosynthesis to Recombination*, *ArXiv e-prints* (Feb., 2008) , [0802.3688].

[111] Planck collaboration, P. A. R. Ade et al., *Planck 2013 results. XVI. Cosmological parameters*, *Astron. Astrophys.* **571** (2014) A16, [1303.5076].

[112] R. K. Sachs and A. M. Wolfe, *Perturbations of a cosmological model and angular variations of the microwave background*, *Astrophys. J.* **147** (1967) 73–90.

[113] J. Kovac, E. M. Leitch, C. Pryke, J. E. Carlstrom, N. W. Halverson and W. L. Holzapfel, *Detection of polarization in the cosmic microwave background using DASI*, *Nature* **420** (2002) 772–787, [astro-ph/0209478].

[114] SPTpol collaboration, D. Hanson et al., *Detection of B-mode Polarization in the Cosmic Microwave Background with Data from the South Pole Telescope*, *Phys. Rev. Lett.* **111** (2013) 141301, [1307.5830].

[115] Planck collaboration, P. A. R. Ade et al., *Planck 2015 results. XV. Gravitational lensing*, 1502.01591.

[116] BICEP2 collaboration, P. A. R. Ade et al., *Detection of B-Mode Polarization at Degree Angular Scales by BICEP2*, *Phys. Rev. Lett.* **112** (2014) 241101, [1403.3985].

[117] BICEP2/Keck and Planck Collaborations, P. A. R. Ade, N. Aghanim, Z. Ahmed, R. W. Aikin, K. D. Alexander et al., *Joint Analysis of BICEP2/Keck Array and Planck Data*, *Physical Review Letters* **114** (Mar., 2015) 101301, [1502.00612].

[118] N. Padmanabhan and D. P. Finkbeiner, *Detecting dark matter annihilation with CMB polarization: Signatures and experimental prospects*, *Phys. Rev. D* **72** (July, 2005) 023508, [astro-ph/0503486].

[119] S. Galli, F. Iocco, G. Bertone and A. Melchiorri, *CMB constraints on dark matter models with large annihilation cross section*, *Phys. Rev. D* **80** (July, 2009) 023505, [0905.0003].

[120] T. R. Slatyer, N. Padmanabhan and D. P. Finkbeiner, *CMB constraints on WIMP annihilation: Energy absorption during the recombination epoch*, *Phys. Rev. D* **80** (Aug., 2009) 043526, [0906.1197].

[121] D. P. Finkbeiner, S. Galli, T. Lin and T. R. Slatyer, *Searching for dark matter*

in the CMB: A compact parametrization of energy injection from new physics, *Phys. Rev. D* **85** (Feb., 2012) 043522, [1109.6322].

[122] Fermi-LAT, MAGIC collaboration, M. L. Ahnen et al., *Limits to dark matter annihilation cross-section from a combined analysis of MAGIC and Fermi-LAT observations of dwarf satellite galaxies*, *JCAP* **1602** (2016) 039, [1601.06590].

[123] H.E.S.S. Collaboration collaboration, A. Abramowski et al., *Search for a Dark Matter annihilation signal from the Galactic Center halo with H.E.S.S*, *Phys. Rev. Lett.* **106** (2011) 161301, [1103.3266].

[124] D. J. Eisenstein, I. Zehavi, D. W. Hogg, R. Scoccimarro, M. R. Blanton, R. C. Nichol et al., *Detection of the Baryon Acoustic Peak in the Large-Scale Correlation Function of SDSS Luminous Red Galaxies*, *ApJ* **633** (Nov., 2005) 560–574, [astro-ph/0501171].

[125] S. Cole, W. J. Percival, J. A. Peacock, P. Norberg, C. M. Baugh, C. S. Frenk et al., *The 2dF Galaxy Redshift Survey: power-spectrum analysis of the final data set and cosmological implications*, *MNRAS* **362** (Sept., 2005) 505–534, [astro-ph/0501174].

[126] F. Beutler, C. Blake, M. Colless, D. H. Jones, L. Staveley-Smith, L. Campbell et al., *The 6dF Galaxy Survey: baryon acoustic oscillations and the local Hubble constant*, *MNRAS* **416** (Oct., 2011) 3017–3032, [1106.3366].

[127] C. Blake, E. A. Kazin, F. Beutler, T. M. Davis, D. Parkinson, S. Brough et al., *The WiggleZ Dark Energy Survey: mapping the distance-redshift relation with baryon acoustic oscillations*, *MNRAS* **418** (Dec., 2011) 1707–1724, [1108.2635].

[128] L. Anderson, E. Aubourg, S. Bailey, D. Bizyaev, M. Blanton, A. S. Bolton et al., *The clustering of galaxies in the SDSS-III Baryon Oscillation Spectroscopic Survey: baryon acoustic oscillations in the Data Release 9 spectroscopic galaxy sample*, *MNRAS* **427** (Dec., 2012) 3435–3467, [1203.6594].

[129] V. Springel et al., *Simulating the joint evolution of quasars, galaxies and their large-scale distribution*, *Nature* **435** (2005) 629–636, [astro-ph/0504097].

[130] M. J. Geller and J. P. Huchra, *Mapping the universe*, *Science* **246** (1989) 897–903.

[131] 2DFGRS collaboration, M. Colless et al., *The 2dF Galaxy Redshift Survey: Spectra and redshifts*, *Mon. Not. Roy. Astron. Soc.* **328** (2001) 1039, [astro-ph/0106498].

[132] J. R. Gott, III, M. Juric, D. Schlegel, F. Hoyle, M. Vogeley, M. Tegmark et al., *A map of the universe*, *Astrophys. J.* **624** (2005) 463, [astro-ph/0310571].

[133] V. Springel, C. S. Frenk and S. D. M. White, *The large-scale structure of the Universe*, *Nature* **440** (2006) 1137, [astro-ph/0604561].

[134] M. Davis, J. Huchra, D. W. Latham and J. Tonry, *A survey of galaxy redshifts. II - The large scale space distribution*, *ApJ* **253** (Feb., 1982) 423–445.

[135] C. S. Frenk and S. D. M. White, *Dark matter and cosmic structure*, *Annalen der Physik* **524** (Oct., 2012) 507–534, [1210.0544].

[136] S. Tremaine and J. E. Gunn, *Dynamical role of light neutral leptons in cosmology*, *Physical Review Letters* **42** (Feb., 1979) 407–410.

[137] J. Madsen and R. I. Epstein, *Firm bounds on the neutrino mass from the distribution of dark matter in galaxies*, *ApJ* **282** (July, 1984) 11–18.

[138] J. J. Dalcanton and C. J. Hogan, *Halo Cores and Phase-Space Densities: Observational Constraints on Dark Matter Physics and Structure Formation*, *ApJ* **561** (Nov., 2001) 35–45, [astro-ph/0004381].

[139] D. Gorbunov, A. Khmelnitsky and V. Rubakov, *Constraining sterile neutrino dark matter with phase space density observations*, *JCAP* **10** (Oct., 2008) 041, [0808.3910].

[140] A. Boyarsky, O. Ruchayskiy and D. Iakubovskyi, *A lower bound on the mass of dark matter particles*, *JCAP* **3** (Mar., 2009) 005, [0808.3902].

[141] B. Moore, S. Ghigna, F. Governato, G. Lake, T. R. Quinn, J. Stadel et al., *Dark matter substructure within galactic halos*, *Astrophys. J.* **524** (1999) L19–L22, [astro-ph/9907411].

[142] A. A. Klypin, A. V. Kravtsov, O. Valenzuela and F. Prada, *Where are the missing Galactic satellites?*, *Astrophys. J.* **522** (1999) 82–92, [astro-ph/9901240].

[143] J. I. Read, M. I. Wilkinson, N. W. Evans, G. Gilmore and J. T. Kleyna, *The importance of tides for the local group dwarf spheroidals*, *Mon. Not. Roy. Astron. Soc.* **367** (2006) 387–399, [astro-ph/0511759].

[144] M. Boylan-Kolchin, J. S. Bullock and M. Kaplinghat, *Too big to fail? The puzzling darkness of massive Milky Way subhaloes*, *Mon. Not. Roy. Astron. Soc.* **415** (2011) L40, [1103.0007].

[145] E. J. Tollerud et al., *The SPLASH Survey: Spectroscopy of 15 M31 Dwarf Spheroidal Satellite Galaxies*, *Astrophys. J.* **752** (2012) 45, [1112.1067].

[146] M. L. M. Collins et al., *The masses of Local Group dwarf spheroidal galaxies: The death of the universal mass profile*, *Astrophys. J.* **783** (2014) 7, [1309.3053].

[147] A. M. Brooks, M. Kuhlen, A. Zolotov and D. Hooper, *A Baryonic Solution to the Missing Satellites Problem*, *Astrophys. J.* **765** (2013) 22, [1209.5394].

[148] J. F. Navarro, C. S. Frenk and S. D. M. White, *The Structure of cold dark matter halos*, *Astrophys. J.* **462** (1996) 563–575, [astro-ph/9508025].

[149] J. F. Navarro, C. S. Frenk and S. D. M. White, *A Universal density profile from hierarchical clustering*, *Astrophys. J.* **490** (1997) 493–508, [astro-ph/9611107].

[150] O. Y. Gnedin, A. V. Kravtsov, A. A. Klypin and D. Nagai, *Response of dark matter halos to condensation of baryons: Cosmological simulations and improved adiabatic contraction model*, *Astrophys. J.* **616** (2004) 16–26, [astro-ph/0406247].

[151] O. Y. Gnedin, D. Ceverino, N. Y. Gnedin, A. A. Klypin, A. V. Kravtsov, R. Levine et al., *Halo Contraction Effect in Hydrodynamic Simulations of Galaxy Formation*, 1108.5736.

[152] S. Mashchenko, J. Wadsley and H. M. P. Couchman, *Stellar Feedback in Dwarf Galaxy Formation*, *Science* **319** (2008) 174, [0711.4803].

[153] A. Pontzen and F. Governato, *How supernova feedback turns dark matter cusps into cores*, *Mon. Not. Roy. Astron. Soc.* **421** (2012) 3464, [1106.0499].

[154] A. V. Maccio', G. Stinson, C. B. Brook, J. Wadsley, H. M. P. Couchman, S. Shen et al., *Halo expansion in cosmological hydro simulations: towards a baryonic solution of the cusp/core problem in massive spirals*, *Astrophys. J.* **744** (2012) L9, [1111.5620].

[155] F. Governato, A. Zolotov, A. Pontzen, C. Christensen, S. H. Oh, A. M. Brooks et al., *Cuspy No More: How Outflows Affect the Central Dark Matter and Baryon Distribution in Lambda CDM Galaxies*, *Mon. Not. Roy. Astron. Soc.* **422** (2012) 1231–1240, [1202.0554].

[156] J. I. Read, O. Agertz and M. L. M. Collins, *Dark matter cores all the way down*, 1508.04143.

[157] J. F. Navarro, E. Hayashi, C. Power, A. Jenkins, C. S. Frenk, S. D. M. White et al., *The Inner structure of Lambda-CDM halos 3: Universality and asymptotic slopes*, *Mon. Not. Roy. Astron. Soc.* **349** (2004) 1039, [astro-ph/0311231].

[158] J. Einasto, *On the Construction of a Composite Model for the Galaxy and on the Determination of the System of Galactic Parameters*, *Trudy Astrofizicheskogo Instituta Alma-Ata* **5** (1965) 87–100.

[159] J. Einasto, *On constructing models of stellar systems. V. The binomial model.*, *Publications of the Tartu Astrofizica Observatory* **36** (1968) 414–441.

[160] J. Einasto and U. Haud, *Galactic models with massive corona. I - Method. II - Galaxy*, *A&A* **223** (Oct., 1989) 89–106.

[161] J. Schaye, R. A. Crain, R. G. Bower, M. Furlong, M. Schaller, T. Theuns et al., *The EAGLE project: simulating the evolution and assembly of galaxies and their environments*, *MNRAS* **446** (Jan., 2015) 521–554, [1407.7040].

[162] R. A. Crain, J. Schaye, R. G. Bower, M. Furlong, M. Schaller, T. Theuns et al., *The EAGLE simulations of galaxy formation: calibration of subgrid physics and model variations*, *MNRAS* **450** (June, 2015) 1937–1961, [1501.01311].

[163] A. Fattahi, J. F. Navarro, T. Sawala, C. S. Frenk, K. A. Oman, R. A. Crain et al., *The APOSTLE project: Local Group kinematic mass constraints and simulation candidate selection*, *MNRAS* **457** (Mar., 2016) 844–856, [1507.03643].

[164] T. Sawala, C. S. Frenk, A. Fattahi, J. F. Navarro, R. G. Bower, R. A. Crain et al., *The APOSTLE simulations: solutions to the Local Group's cosmic puzzles*, *MNRAS* **457** (Apr., 2016) 1931–1943, [1511.01098].

[165] F. Calore, N. Bozorgnia, M. Lovell, G. Bertone, M. Schaller, C. S. Frenk et al., *Simulated Milky Way analogues: implications for dark matter indirect searches*, *JCAP* **12** (Dec., 2015) 053, [1509.02164].

[166] F. Iocco, M. Pato and G. Bertone, *Evidence for dark matter in the inner Milky Way*, *Nature Physics* **11** (Mar., 2015) 245–248, [1502.03821].

[167] M. Pato, F. Iocco and G. Bertone, *Dynamical constraints on the dark matter distribution in the Milky Way*, *JCAP* **12** (Dec., 2015) 001, [1504.06324].

[168] C. S. Frenk, S. D. M. White, M. Davis and G. Efstathiou, *The formation of dark halos in a universe dominated by cold dark matter*, *ApJ* **327** (Apr., 1988) 507–525.

[169] J. Dubinski and R. G. Carlberg, *The structure of cold dark matter halos*, *ApJ* **378** (Sept., 1991) 496–503.

[170] M. S. Warren, P. J. Quinn, J. K. Salmon and W. H. Zurek, *Dark halos formed via dissipationless collapse. I - Shapes and alignment of angular momentum*, *ApJ* **399** (Nov., 1992) 405–425.

[171] S. Cole and C. Lacey, *The structure of dark matter haloes in hierarchical clustering models*, *MNRAS* **281** (July, 1996) 716, [astro-ph/9510147].

[172] N. Katz and J. E. Gunn, *Dissipational galaxy formation. I - Effects of gasdynamics*, *ApJ* **377** (Aug., 1991) 365–381.

[173] J. Dubinski, *The effect of dissipation on the shapes of dark halos*, *ApJ* **431** (Aug., 1994) 617–624, [astro-ph/9309001].

[174] S. Kazantzidis, A. V. Kravtsov, A. R. Zentner, B. Allgood, D. Nagai and B. Moore, *The Effect of Gas Cooling on the Shapes of Dark Matter Halos*, *ApJ* **611** (Aug., 2004) L73–L76, [astro-ph/0405189].

[175] V. P. Debattista, B. Moore, T. Quinn, S. Kazantzidis, R. Maas, L. Mayer et al., *The Causes of Halo Shape Changes Induced by Cooling Baryons: Disks versus Substructures*, *ApJ* **681** (July, 2008) 1076–1088, [0707.0737].

[176] J. I. Read, L. Mayer, A. M. Brooks, F. Governato and G. Lake, *A dark matter disc in three cosmological simulations of Milky Way mass galaxies*, *MNRAS* **397** (July, 2009) 44–51, [0902.0009].

[177] J. Fan, A. Katz, L. Randall and M. Reece, *Dark-Disk Universe*, *Physical Review Letters* **110** (May, 2013) 211302, [1303.3271].

[178] J. Fan, A. Katz, L. Randall and M. Reece, *Double-Disk Dark Matter*, *Physics of the Dark Universe* **2** (Sept., 2013) 139–156, [1303.1521].

[179] L. Randall and M. Reece, *Dark Matter as a Trigger for Periodic Comet Impacts*, *Physical Review Letters* **112** (Apr., 2014) 161301, [1403.0576].

[180] P. J. Quinn and J. Goodman, *Sinking satellites of spiral systems*, *ApJ* **309** (Oct., 1986) 472–495.

[181] P. J. Quinn, L. Hernquist and D. P. Fullagar, *Heating of galactic disks by mergers*, *ApJ* **403** (Jan., 1993) 74–93.

[182] G. Lake, *Must the disk and halo dark matter be different?*, *AJ* **98** (Nov., 1989) 1554–1556.

[183] J. Read, G. Lake, O. Agertz and V. P. Debattista, *Thin, thick and dark discs in LCDM*, *Mon.Not.Roy.Astron.Soc.* **389** (2008) 1041–1057, [0803.2714].

[184] J. Read, L. Mayer, A. Brooks, F. Governato and G. Lake, *A dark matter disc in three cosmological simulations of Milky Way mass galaxies*, *Mon.Not.Roy.Astron.Soc.* **397** (2009) 44, [0902.0009].

[185] S. Chandrasekhar, *Dynamical Friction. I. General Considerations: the Coefficient of Dynamical Friction.*, *ApJ* **97** (Mar., 1943) 255.

[186] G. R. Ruchti, J. I. Read, S. Feltzing, A. Pipino and T. Bensby, *The hunt for the Milky Way's accreted disc*, *MNRAS* **444** (Oct., 2014) 515–526, [1407.4464].

[187] G. Ruchti, J. Read, S. Feltzing, A. Serenelli, P. McMillan et al., *The Gaia-ESO Survey: a quiescent Milky Way with no significant dark/stellar accreted disc*, *Mon.Not.Roy.Astron.Soc.* **450** (2015) 2874, [1504.02481].

[188] K. Freese, J. Frieman and A. Gould, *Signal modulation in cold-dark-matter detection*, *Phys. Rev. D* **37** (June, 1988) 3388–3405.

[189] LUX collaboration, D. S. Akerib et al., *Improved Limits on Scattering of Weakly Interacting Massive Particles from Reanalysis of 2013 LUX Data*, *Phys. Rev. Lett.* **116** (2016) 161301, [1512.03506].

[190] XENON100 Collaboration collaboration, E. Aprile, M. Alfonsi, K. Arisaka, F. Arneodo, C. Balan, L. Baudis et al., *Dark Matter Results from 225 Live Days of XENON100 Data*, *Phys. Rev. Lett.* **109** (Nov., 2012) 181301, [1207.5988].

[191] A. S. Eddington, *The distribution of stars in globular clusters*, *MNRAS* **76** (May, 1916) 572–585.

[192] J. D. Vergados and D. Owen, *New Velocity Distribution for Cold Dark Matter in the Context of the Eddington Theory*, *ApJ* **589** (May, 2003) 17–28, [astro-ph/0203293].

[193] P. Ullio and M. Kamionkowski, *Velocity distributions and annual-modulation signatures of weakly-interacting massive particles*, *Journal of High Energy Physics* **3** (Mar., 2001) 049, [hep-ph/0006183].

[194] N. W. Evans, C. M. Carollo and P. T. de Zeeuw, *Triaxial haloes and particle dark matter detection*, *MNRAS* **318** (Nov., 2000) 1131–1143, [astro-ph/0008156].

[195] L. P. Osipkov, *Spherical systems of gravitating bodies with an ellipsoidal velocity distribution*, *Pisma v Astronomicheskii Zhurnal* **5** (Feb., 1979) 77–80.

[196] D. Merritt, *Spherical stellar systems with spheroidal velocity distributions*, *AJ* **90** (June, 1985) 1027–1037.

[197] M. Vogelsberger, A. Helmi, V. Springel, S. D. White, J. Wang, C. S. Frenk et al., *Phase-space structure in the local dark matter distribution and its signature in direct detection experiments*, *Mon.Not.Roy.Astron.Soc.* **395** (2009) 797–811, [0812.0362].

[198] M. Kuhlen, N. Weiner, J. Diemand, P. Madau, B. Moore, D. Potter et al., *Dark Matter Direct Detection with Non-Maxwellian Velocity Structure*, *JCAP* **1002** (2010) 030, [0912.2358].

[199] F. Ling, E. Nezri, E. Athanassoula and R. Teyssier, *Dark Matter Direct Detection Signals inferred from a Cosmological N-body Simulation with Baryons*, *JCAP* **1002** (2010) 012, [0909.2028].

[200] N. Bozorgnia, F. Calore, M. Schaller, M. Lovell, G. Bertone, C. S. Frenk et al., *Simulated Milky Way analogues: implications for dark matter direct searches*, *JCAP* **5** (May, 2016) 024, [1601.04707].

[201] M. C. Smith, G. Ruchti, A. Helmi, R. Wyse, J. Fulbright et al., *The RAVE Survey: Constraining the Local Galactic Escape Speed*, *Mon.Not.Roy.Astron.Soc.* **379** (2007) 755–772, [astro-ph/0611671].

[202] T. Piffl, C. Scannapieco, J. Binney, M. Steinmetz, R.-D. Scholz, M. E. K. Williams et al., *The RAVE survey: the Galactic escape speed and the mass of the Milky Way*, *A&A* **562** (Feb., 2014) A91, [1309.4293].

[203] P. Sikivie, *Experimental tests of the 'invisible' axion*, *Physical Review Letters* **51** (Oct., 1983) 1415–1417.

[204] P. Sikivie, *Detection rates for "invisible"-axion searches*, *Phys. Rev. D* **32** (Dec., 1985) 2988–2991.

[205] L. Krauss, J. Moody, F. Wilczek and D. E. Morris, *Calculations for cosmic axion detection*, *Physical Review Letters* **55** (Oct., 1985) 1797–1800.

[206] M. W. Goodman and E. Witten, *Detectability of certain dark-matter candidates*, *Phys. Rev. D* **31** (June, 1985) 3059–3063.

[207] T. Marrodán Undagoitia and L. Rauch, *Dark matter direct-detection experiments*, *Journal of Physics G Nuclear Physics* **43** (Jan., 2016) 013001, [1509.08767].

[208] C. Arina, *Chasing a consistent picture for dark matter direct searches*, *Phys. Rev. D* **86** (Dec., 2012) 123527, [1210.4011].

[209] C. Savage, G. Gelmini, P. Gondolo and K. Freese, *Compatibility of DAMA/LIBRA dark matter detection with other searches*, *JCAP* **4** (Apr., 2009) 10, [0808.3607].

[210] C. McCabe, *The Astrophysical Uncertainties Of Dark Matter Direct Detection Experiments*, *Phys.Rev.* **D82** (2010) 023530, [1005.0579].

[211] A. M. Green, *Dependence of direct detection signals on the WIMP velocity distribution*, *JCAP* **1010** (2010) 034, [1009.0916].

[212] A. M. Green, *Astrophysical Uncertainties on Direct Detection Experiments*, *Modern Physics Letters A* **27** (2012) 1230004–1–1230004–20, [1112.0524].

[213] M. Fairbairn, T. Douce and J. Swift, *Quantifying astrophysical uncertainties on dark matter direct detection results*, *Astroparticle Physics* **47** (July, 2013) 45–53, [1206.2693].

[214] N. Bozorgnia, R. Catena and T. Schwetz, *Anisotropic dark matter distribution functions and impact on WIMP direct detection*, *JCAP* **12** (Dec., 2013) 050, [1310.0468].

[215] M. Pato, L. E. Strigari, R. Trotta and G. Bertone, *Taming astrophysical bias in direct dark matter searches*, *JCAP* **1302** (2013) 041, [1211.7063].

[216] L. E. Strigari and R. Trotta, *Reconstructing WIMP Properties in Direct Detection Experiments Including Galactic Dark Matter Distribution Uncertainties*, *JCAP* **0911** (2009) 019, [0906.5361].

[217] M. Pato, L. Baudis, G. Bertone, R. Ruiz de Austri, L. E. Strigari and R. Trotta, *Complementarity of Dark Matter Direct Detection Targets*, *Phys.Rev.* **D83** (2011) 083505, [1012.3458].

[218] P. J. Fox, J. Liu and N. Weiner, *Integrating Out Astrophysical Uncertainties*, *Phys.Rev.* **D83** (2011) 103514, [1011.1915].

[219] E. Del Nobile, G. B. Gelmini, P. Gondolo and J.-H. Huh, *Update on the Halo-independent Comparison of Direct Dark Matter Detection Data*, *Physics Procedia* **61** (2015) 45–54, [1405.5582].

[220] A. K. Drukier, K. Freese and D. N. Spergel, *Detecting Cold Dark Matter Candidates*, *Phys. Rev.* **D33** (1986) 3495–3508.

[221] K. Freese, M. Lisanti and C. Savage, *Annual Modulation of Dark Matter: A Review*, *Rev. Mod. Phys.* **85** (2013) 1561–1581, [1209.3339].

[222] B. C. Allanach and C. G. Lester, *Multidimensional mSUGRA likelihood maps*, *Phys. Rev. D* **73** (Jan., 2006) 015013, [hep-ph/0507283].

[223] O. Buchmueller et al., *The CMSSM and NUHM1 after LHC Run 1*, *Eur. Phys. J.* **C74** (2014) 2922, [1312.5250].

[224] C. Strege, G. Bertone, G. J. Besjes, S. Caron, R. Ruiz de Austri, A. Strubig et al., *Profile likelihood maps of a 15-dimensional MSSM*, *JHEP* **09** (2014) 081, [1405.0622].

[225] L. Roszkowski, E. M. Sessolo and A. J. Williams, *Prospects for dark matter searches in the pMSSM*, *JHEP* **02** (2015) 014, [1411.5214].

[226] G. Bertone, F. Calore, S. Caron, R. Ruiz, J. S. Kim, R. Trotta et al., *Global analysis of the pMSSM in light of the Fermi GeV excess: prospects for the LHC Run-II and astroparticle experiments*, *JCAP* **4** (Apr., 2016) 037, [1507.07008].

[227] T. Bruch, J. Read, L. Baudis and G. Lake, *Detecting the Milky Way's Dark Disk*, *ApJ* **696** (May, 2009) 920–923, [0804.2896].

[228] T. Bruch, A. H. G. Peter, J. Read, L. Baudis and G. Lake, *Dark matter disc enhanced neutrino fluxes from the Sun and Earth*, *Physics Letters B* **674** (Apr., 2009) 250–256, [0902.4001].

[229] K. Choi, C. Rott and Y. Itow, *Impact of the dark matter velocity distribution on capture rates in the Sun*, *JCAP* **5** (May, 2014) 049, [1312.0273].

[230] XENON collaboration, E. Aprile et al., *Physics reach of the XENON1T dark matter experiment*, *Submitted to: JCAP* (2015) , [1512.07501].

[231] CRESST collaboration, G. Angloher et al., *Results on light dark matter particles with a low-threshold CRESST-II detector*, *Eur. Phys. J.* **C76** (2016) 25, [1509.01515].

[232] H. Silverwood, P. Scott, M. Danninger, C. Savage, J. Edsjö, J. Adams et al., *Sensitivity of IceCube-DeepCore to neutralino dark matter in the MSSM-25*, *JCAP* **1303** (2013) 027, [1210.0844].

[233] SuperCDMS collaboration, R. Agnese et al., *New Results from the Search for Low-Mass Weakly Interacting Massive Particles with the CDMS Low Ionization Threshold Experiment*, *Phys. Rev. Lett.* **116** (2016) 071301, [1509.02448].

[234] J. Billard, L. Strigari and E. Figueroa-Feliciano, *Implication of neutrino backgrounds on the reach of next generation dark matter direct detection experiments*, *Phys. Rev.* **D89** (2014) 023524, [1307.5458].

[235] K. Freese, M. Lisanti and C. Savage, *Colloquium: Annual modulation of dark matter*, *Rev. Mod. Phys.* **85** (2013) 1561–1581, [1209.3339].

[236] J. H. Davis, *Dark matter vs. neutrinos: the effect of astrophysical uncertainties and timing information on the neutrino floor*, *JCAP* **3** (Mar., 2015) 012, [1412.1475].

[237] F. Ruppin, J. Billard, E. Figueroa-Feliciano and L. Strigari, *Complementarity of dark matter detectors in light of the neutrino background*, *Phys. Rev. D* **90** (Oct., 2014) 083510, [1408.3581].

[238] J. B. Dent, B. Dutta, J. L. Newstead and L. E. Strigari, *Effective field theory*

treatment of the neutrino background in direct dark matter detection experiments, *Phys. Rev. D* **93** (Apr., 2016) 075018, [1602.05300].

[239] T. Franarin and M. Fairbairn, *Reducing the Solar Neutrino Background Using Polarised Helium-3*, *ArXiv e-prints* (May, 2016) , [1605.08727].

[240] S. Ahlen et al., *The case for a directional dark matter detector and the status of current experimental efforts*, *Int. J. Mod. Phys.* **A25** (2010) 1–51, [0911.0323].

[241] J. Billard, F. Mayet, J. F. Macias-Perez and D. Santos, *Directional detection as a strategy to discover galactic Dark Matter*, *Phys. Lett.* **B691** (2010) 156–162, [0911.4086].

[242] J. Billard, F. Mayet and D. Santos, *Markov Chain Monte Carlo analysis to constrain Dark Matter properties with directional detection*, *Phys. Rev.* **D83** (2011) 075002, [1012.3960].

[243] P. Grothaus, M. Fairbairn and J. Monroe, *Directional dark matter detection beyond the neutrino bound*, *Phys. Rev. D* **90** (Sept., 2014) 055018, [1406.5047].

[244] C. A. J. O'Hare, A. M. Green, J. Billard, E. Figueroa-Feliciano and L. E. Strigari, *Readout strategies for directional dark matter detection beyond the neutrino background*, *Phys. Rev. D* **92** (Sept., 2015) 063518, [1505.08061].

[245] D. G. Cerdeno, M. Fairbairn, T. Jubb, P. A. N. Machado, A. C. Vincent and C. Boehm, *Physics from solar neutrinos in dark matter direct detection experiments*, *ArXiv e-prints* (Apr., 2016) , [1604.01025].

[246] PICO Collaboration, C. Amole, M. Ardid, D. M. Asner, D. Baxter, E. Behnke et al., *Dark matter search results from the PICO-60 CF_3 I bubble chamber*, *Phys. Rev. D* **93** (Mar., 2016) 052014, [1510.07754].

[247] PICO Collaboration, C. Amole, M. Ardid, I. J. Arnquist, D. M. Asner, D. Baxter et al., *Improved dark matter search results from PICO-2L Run 2*, *Phys. Rev. D* **93** (Mar., 2016) 061101, [1601.03729].

[248] E. Aprile, F. Agostini, M. Alfonsi, K. Arisaka, F. Arneodo, M. Auger et al., *Conceptual design and simulation of a water Cherenkov muon veto for the XENON1T experiment*, *Journal of Instrumentation* **9** (Nov., 2014) P11006, [1406.2374].

[249] The LZ Collaboration, D. S. Akerib, C. W. Akerlof, D. Y. Akimov, S. K. Alsum, H. M. Araújo et al., *LUX-ZEPLIN (LZ) Conceptual Design Report*, *ArXiv e-prints* (Sept., 2015) , [1509.02910].

[250] L. Baudis and DARWIN Consortium, *DARWIN dark matter WIMP search with noble liquids*, *Journal of Physics Conference Series* **375** (July, 2012) 012028, [1201.2402].

[251] LUX Collaboration collaboration, LUX Collaboration, D. S. Akerib, H. M. Araújo, X. Bai, A. J. Bailey, J. Balajthy et al., *Results on the Spin-Dependent Scattering of Weakly Interacting Massive Particles on Nucleons from the Run 3 Data of the LUX Experiment*, *Physical Review Letters* **116** (Apr., 2016) 161302, [1602.03489].

[252] XENON100 collaboration, E. Aprile et al., *Limits on spin-dependent WIMP-nucleon cross sections from 225 live days of XENON100 data*, *Phys. Rev. Lett.* **111** (2013) 021301, [1301.6620].

[253] W. H. Press and D. N. Spergel, *Capture by the sun of a galactic population of weakly interacting, massive particles*, *ApJ* **296** (1985) 679–684.

[254] A. Gould, *Resonant enhancements in weakly interacting massive particle capture by the earth*, *ApJ* **321** (1987) 571–585.

[255] A. Gould, *Direct and indirect capture of weakly interacting massive particles by the earth*, *ApJ* **328** (1988) 919–939.

[256] A. Gould, *Cosmological density of WIMPs from solar and terrestrial annihilations*, *ApJ* **388** (1992) 338–344.

[257] G. Wikström and J. Edsjö, *Limits on the WIMP-nucleon scattering cross-section from neutrino telescopes*, *JCAP* **4** (Apr., 2009) 9, [0903.2986].

[258] L. Wolfenstein, *Neutrino Oscillations in Matter*, *Phys. Rev.* **D17** (1978) 2369–2374.

[259] L. Wolfenstein, *Neutrino Oscillations and Stellar Collapse*, *Phys. Rev.* **D20** (1979) 2634–2635.

[260] S. P. Mikheev and A. Yu. Smirnov, *Resonance Amplification of Oscillations in Matter and Spectroscopy of Solar Neutrinos*, *Sov. J. Nucl. Phys.* **42** (1985) 913–917.

[261] M. Blennow, J. Edsjo and T. Ohlsson, *Neutrinos from WIMP annihilations using a full three-flavor Monte Carlo*, *JCAP* **0801** (2008) 021, [0709.3898].

[262] M. Cirelli, N. Fornengo, T. Montaruli, I. A. Sokalski, A. Strumia and F. Vissani, *Spectra of neutrinos from dark matter annihilations*, *Nucl. Phys.* **B727** (2005) 99–138, [hep-ph/0506298].

[263] ANTARES Collaboration, *First results on dark matter annihilation in the Sun*

using the ANTARES neutrino telescope, *JCAP* **11** (Nov., 2013) 032, [1302.6516].

[264] IceCube collaboration collaboration, M. Aartsen et al., *Search for dark matter annihilations in the Sun with the 79-string IceCube detector*, *Phys.Rev.Lett.* **110** (2013) 131302, [1212.4097].

[265] Super-Kamiokande collaboration, K. Frankiewicz, *Searching for Dark Matter Annihilation into Neutrinos with Super-Kamiokande*, in *Proceedings, Meeting of the APS Division of Particles and Fields (DPF 2015)*, 2015. 1510.07999.

[266] Super-Kamiokande collaboration, S. Desai et al., *Search for dark matter WIMPs using upward through-going muons in Super-Kamiokande*, *Phys. Rev.* **D70** (2004) 083523, [hep-ex/0404025].

[267] IceCube collaboration, M. G. Aartsen et al., *Multipole analysis of IceCube data to search for dark matter accumulated in the Galactic halo*, *Eur. Phys. J.* **C75** (2015) 20, [1406.6868].

[268] IceCube collaboration, M. G. Aartsen et al., *Search for Dark Matter Annihilation in the Galactic Center with IceCube-79*, *Eur. Phys. J.* **C75** (2015) 492, [1505.07259].

[269] ANTARES collaboration, S. Adrian-Martinez et al., *Search of Dark Matter Annihilation in the Galactic Centre using the ANTARES Neutrino Telescope*, *JCAP* **1510** (2015) 068, [1505.04866].

[270] BAIKAL collaboration, A. D. Avrorin et al., *A search for neutrino signal from dark matter annihilation in the center of the Milky Way with Baikal NT200*, 1512.01198.

[271] IceCube collaboration, M. G. Aartsen, K. Abraham, M. Ackermann, J. Adams, J. A. Aguilar et al., *All-flavour Search for Neutrinos from Dark Matter Annihilations in the Milky Way with IceCube/DeepCore*, *ArXiv e-prints* (June, 2016) , [1606.00209].

[272] IceCube collaboration, M. G. Aartsen et al., *First observation of PeV-energy neutrinos with IceCube*, *Phys. Rev. Lett.* **111** (2013) 021103, [1304.5356].

[273] IceCube collaboration, M. G. Aartsen et al., *Observation of High-Energy Astrophysical Neutrinos in Three Years of IceCube Data*, *Phys. Rev. Lett.* **113** (2014) 101101, [1405.5303].

[274] J. Zavala, *Galactic PeV neutrinos from dark matter annihilation*, *Phys. Rev.* **D89** (2014) 123516, [1404.2932].

[275] C. Rott, K. Kohri and S. C. Park, *Superheavy dark matter and IceCube neutrino signals: Bounds on decaying dark matter*, *Phys. Rev.* **D92** (2015) 023529, [1408.4575].

[276] A. Esmaili, S. K. Kang and P. D. Serpico, *IceCube events and decaying dark matter: hints and constraints*, *JCAP* **1412** (2014) 054, [1410.5979].

[277] K. Murase, R. Laha, S. Ando and M. Ahlers, *Testing the Dark Matter Scenario for PeV Neutrinos Observed in IceCube*, *Phys. Rev. Lett.* **115** (2015) 071301, [1503.04663].

[278] A. Esmaili and P. D. Serpico, *Gamma-ray bounds from EAS detectors and heavy decaying dark matter constraints*, *JCAP* **1510** (2015) 014, [1505.06486].

[279] C. El Aisati, M. Gustafsson and T. Hambye, *New Search for Monochromatic Neutrinos from Dark Matter Decay*, *Phys. Rev.* **D92** (2015) 123515, [1506.02657].

[280] M. D. Kistler, *On TeV Gamma Rays and the Search for Galactic Neutrinos*, 1511.05199.

[281] J. Silk and M. Srednicki, *Cosmic-ray antiprotons as a probe of a photino-dominated universe*, *Physical Review Letters* **53** (Aug., 1984) 624–627.

[282] F. W. Stecker, S. Rudaz and T. F. Walsh, *Galactic antiprotons from photinos*, *Physical Review Letters* **55** (Dec., 1985) 2622–2625.

[283] J. Ellis, R. A. Flores, K. Freese, S. Ritz, D. Seckel and J. Silk, *Cosmic ray constraints on the annihilations of relic particles in the galactic halo*, *Physics Letters B* **214** (Nov., 1988) 403–412.

[284] M. Kamionkowski and M. S. Turner, *Distinctive positron feature from particle dark-matter annihilations in the galactic halo*, *Phys. Rev. D* **43** (Mar., 1991) 1774–1780.

[285] PAMELA collaboration, O. Adriani et al., *An anomalous positron abundance in cosmic rays with energies 1.5-100 GeV*, *Nature* **458** (2009) 607–609, [0810.4995].

[286] Fermi-LAT collaboration, M. Ackermann et al., *Measurement of separate cosmic-ray electron and positron spectra with the Fermi Large Area Telescope*, *Phys. Rev. Lett.* **108** (2012) 011103, [1109.0521].

[287] AMS collaboration, M. Aguilar et al., *First Result from the Alpha Magnetic Spectrometer on the International Space Station: Precision Measurement of the Positron Fraction in Primary Cosmic Rays of 0.5âĂŞ350 GeV*, *Phys. Rev. Lett.* **110** (2013) 141102.

[288] S. Profumo, *Dissecting cosmic-ray electron-positron data with Occam's Razor: the role of known Pulsars*, *Central Eur. J. Phys.* **10** (2011) 1–31, [0812.4457].

[289] D. Hooper, P. Blasi and P. Dario Serpico, *Pulsars as the sources of high energy cosmic ray positrons*, *JCAP* **1** (Jan., 2009) 25, [0810.1527].

[290] Q. Yuan, X.-J. Bi, G.-M. Chen, Y.-Q. Guo, S.-J. Lin and X. Zhang, *Implications of the AMS-02 positron fraction in cosmic rays*, *Astropart. Phys.* **60** (2015) 1–12, [1304.1482].

[291] J. E. Gunn, B. W. Lee, I. Lerche, D. N. Schramm and G. Steigman, *Some astrophysical consequences of the existence of a heavy stable neutral lepton*, *ApJ* **223** (Aug., 1978) 1015–1031.

[292] F. W. Stecker, *The cosmic gamma-ray background from the annihilation of primordial stable neutral heavy leptons*, *ApJ* **223** (Aug., 1978) 1032–1036.

[293] G. Lake, *Detectability of gamma-rays from clumps of dark matter*, *Nature* **346** (July, 1990) 39.

[294] P. Ullio and M. Valli, *A critical reassessment of particle Dark Matter limits from dwarf satellites*, *ArXiv e-prints* (Mar., 2016) , [1603.07721].

[295] W. B. Atwood, A. A. Abdo, M. Ackermann, W. Althouse, B. Anderson, M. Axelsson et al., *The Large Area Telescope on the Fermi Gamma-Ray Space Telescope Mission*, *ApJ* **697** (June, 2009) 1071–1102, [0902.1089].

[296] L. Goodenough and D. Hooper, *Possible Evidence For Dark Matter Annihilation In The Inner Milky Way From The Fermi Gamma Ray Space Telescope*, 0910.2998.

[297] V. Vitale, A. Morselli and The *Fermi*-LAT Collaboration, *Indirect Search for Dark Matter from the center of the Milky Way with the Fermi-Large Area Telescope*, in *Proceedings of the 2009 Fermi Symposium, eConf Proceedings*, vol. C091122, Dec., 2009. 0912.3828.

[298] D. Hooper and L. Goodenough, *Dark matter annihilation in the Galactic Center as seen by the Fermi Gamma Ray Space Telescope*, *Phys. Lett. B* **697** (Mar., 2011) 412–428, [1010.2752].

[299] D. Hooper and T. Linden, *Origin of the gamma rays from the Galactic Center*, *Phys. Rev. D* **84** (Dec., 2011) 123005, [1110.0006].

[300] K. N. Abazajian and M. Kaplinghat, *Detection of a gamma-ray source in the Galactic Center consistent with extended emission from dark matter annihilation and concentrated astrophysical emission*, *Phys. Rev. D* **86** (Oct., 2012) 083511, [1207.6047].

[301] C. Gordon and O. Macías, *Dark matter and pulsar model constraints from Galactic Center Fermi-LAT gamma-ray observations*, *Phys. Rev. D* **88** (Oct., 2013) 083521, [1306.5725].

[302] O. Macias and C. Gordon, *Contribution of cosmic rays interacting with molecular clouds to the Galactic Center gamma-ray excess*, *Phys. Rev. D* **89** (Mar., 2014) 063515, [1312.6671].

[303] K. N. Abazajian, N. Canac, S. Horiuchi and M. Kaplinghat, *Astrophysical and dark matter interpretations of extended gamma-ray emission from the Galactic Center*, *Phys. Rev. D* **90** (July, 2014) 023526, [1402.4090].

[304] B. Zhou, Y.-F. Liang, X. Huang, X. Li, Y.-Z. Fan, L. Feng et al., *GeV excess in the Milky Way: The role of diffuse galactic gamma-ray emission templates*, *Phys. Rev. D* **91** (June, 2015) 123010, [1406.6948].

[305] F. Calore, I. Cholis and C. Weniger, *Background model systematics for the Fermi GeV excess*, *JCAP* **3** (Mar., 2015) 038, [1409.0042].

[306] F. Calore, I. Cholis, C. McCabe and C. Weniger, *A tale of tails: Dark matter interpretations of the Fermi GeV excess in light of background model systematics*, *Phys. Rev. D* **91** (Mar., 2015) 063003, [1411.4647].

[307] Fermi-LAT collaboration, M. Ajello et al., *Fermi-LAT Observations of High-Energy γ-Ray Emission Toward the Galactic Center*, *Astrophys. J.* **819** (2016) 44, [1511.02938].

[308] T. Daylan, D. P. Finkbeiner, D. Hooper, T. Linden, S. K. N. Portillo, N. L. Rodd et al., *The characterization of the gamma-ray signal from the central Milky Way: A case for annihilating dark matter*, *Physics of the Dark Universe* **12** (June, 2016) 1–23, [1402.6703].

[309] J. M. Siegal-Gaskins, *Separating astrophysical sources from indirect dark matter signals*, 1308.2228.

[310] E. Carlson and S. Profumo, *Cosmic ray protons in the inner Galaxy and the Galactic Center gamma-ray excess*, *Phys. Rev. D* **90** (July, 2014) 023015, [1405.7685].

[311] D. Gaggero, M. Taoso, A. Urbano, M. Valli and P. Ullio, *Towards a realistic astrophysical interpretation of the gamma-ray Galactic center excess*, *JCAP* **12** (Dec., 2015) 056, [1507.06129].

[312] J. Petrović, P. Dario Serpico and G. Zaharijaš, *Galactic Center gamma-ray "excess" from an active past of the Galactic Centre?*, *JCAP* **10** (Oct., 2014) 052, [1405.7928].

[313] K. N. Abazajian, *The consistency of Fermi-LAT observations of the galactic center with a millisecond pulsar population in the central stellar cluster*, *JCAP* **3** (Mar., 2011) 010, [1011.4275].

[314] R. Bartels, S. Krishnamurthy and C. Weniger, *Strong Support for the Millisecond Pulsar Origin of the Galactic Center GeV Excess*, *Physical Review Letters* **116** (Feb., 2016) 051102, [1506.05104].

[315] S. K. Lee, M. Lisanti, B. R. Safdi, T. R. Slatyer and W. Xue, *Evidence for Unresolved γ -Ray Point Sources in the Inner Galaxy*, *Physical Review Letters* **116** (Feb., 2016) 051103, [1506.05124].

[316] T. C. Weekes, G. G. Fazio, H. F. Helmken, E. O'Mongain and G. H. Rieke, *A Search for Discrete Sources of Cosmic Gamma Rays of Energy 10^{11}-10^{12} eV*, *ApJ* **174** (May, 1972) 165.

[317] T. C. Weekes et al., *Observation of TeV gamma rays from the Crab nebula using the atmospheric Cerenkov imaging technique*, *Astrophys. J.* **342** (1989) 379–395.

[318] H.E.S.S. Collaboration collaboration, F. Aharonian et al., *Observations of the Crab Nebula with H.E.S.S*, *A&A* **457** (2006) 899–915, [astro-ph/0607333].

[319] VERITAS Collaboration collaboration, J. Holder et al., *The first VERITAS telescope*, *Astropart. Phys.* **25** (2006) 391–401, [astro-ph/0604119].

[320] CTA Consortium, *Paranal and la palma sites chosen for final negotiations to host world's largest array of gamma-ray telescopes*, 2015.

[321] C. Strege, R. Trotta, G. Bertone, A. H. Peter and P. Scott, *Fundamental statistical limitations of future dark matter direct detection experiments*, *Phys.Rev.* **D86** (2012) 023507, [1201.3631].

[322] B. J. Kavanagh and A. M. Green, *Improved determination of the WIMP mass from direct detection data*, 1207.2039.

[323] D. Cerdeno, M. Fornasa, J. Huh and M. Peiro, *Nuclear uncertainties in the spin-dependent structure functions for direct dark matter detection*, *Phys.Rev.* **D87** (2013) 023512, [1208.6426].

[324] G. Bertone, D. G. Cerdeno, J. Collar and B. C. Odom, *WIMP identification through a combined measurement of axial and scalar couplings*, *Phys.Rev.Lett.* **99** (2007) 151301, [0705.2502].

[325] M. Pato, *What can(not) be measured with ton-scale dark matter direct detection experiments*, *JCAP* **1110** (2011) 035, [1106.0743].

[326] D. G. Cerdeño et al., *Complementarity of dark matter direct detection: the role of bolometric targets*, *JCAP* **1307** (2013) 028, [1304.1758].

[327] R. Catena and P. Gondolo, *Global fits of the dark matter-nucleon effective interactions*, *JCAP* **9** (Sept., 2014) 045, [1405.2637].

[328] G. Bertone, D. G. Cerdeno, M. Fornasa, R. R. de Austri and R. Trotta, *Identification of Dark Matter particles with LHC and direct detection data*, *Phys.Rev.* **D82** (2010) 055008, [1005.4280].

[329] N. Bernal, A. Goudelis, Y. Mambrini and C. Munoz, *Determining the WIMP mass using the complementarity between direct and indirect searches and the ILC*, *JCAP* **0901** (2009) 046, [0804.1976].

[330] B. J. Kavanagh, M. Fornasa and A. M. Green, *Probing WIMP particle physics and astrophysics with direct detection and neutrino telescope data*, *Phys. Rev. D* **91** (May, 2015) 103533, [1410.8051].

[331] L. Roszkowski, E. M. Sessolo, S. Trojanowski and A. J. Williams, *Reconstructing WIMP properties through an interplay of signal measurements in direct detection, Fermi-LAT, and CTA searches for dark matter*, *ArXiv e-prints* (Mar., 2016) , [1603.06519].

[332] S. Liem, G. Bertone, F. Calore, R. Ruiz de Austri, T. M. P. Tait, R. Trotta et al., *Effective Field Theory of Dark Matter: a Global Analysis*, *ArXiv e-prints* (Mar., 2016) , [1603.05994].

[333] D. Hooper and A. M. Taylor, *Determining Supersymmetric Parameters With Dark Matter Experiments*, *JCAP* **0703** (2007) 017, [hep-ph/0607086].

[334] V. Niro, A. Bottino, N. Fornengo and S. Scopel, *Investigating light neutralinos at neutrino telescopes*, *Phys. Rev. D* **80** (Nov, 2009) 095019.

[335] XENON1T collaboration collaboration, E. Aprile, *The XENON1T Dark Matter Search Experiment*, 1206.6288.

[336] IceCube Collaboration collaboration, R. Abbasi et al., *Multi-year search for dark matter annihilations in the Sun with the AMANDA-II and IceCube detectors*, *Phys.Rev.* **D85** (2012) 042002, [1112.1840].

[337] P. Smith, G. Arnison, G. Homer, J. Lewin, G. Alner et al., *Improved dark matter limits from pulse shape discrimination in a low background sodium iodide detector at the Boulby mine*, *Phys.Lett.* **B379** (1996) 299–308.

[338] C. Savage, G. Gelmini, P. Gondolo and K. Freese, *Compatibility of DAMA/LIBRA dark matter detection with other searches*, *JCAP* **0904** (2009) 010, [0808.3607].

[339] R. H. Helm, *Inelastic and Elastic Scattering of 187-Mev Electrons from Selected Even-Even Nuclei*, *Phys. Rev.* **104** (1956) 1466–1475.

[340] J. D. Lewin and P. F. Smith, *Review of mathematics, numerical factors, and corrections for dark matter experiments based on elastic nuclear recoil*, *Astropart. Phys.* **6** (1996) 87–112.

[341] G. Duda, A. Kemper and P. Gondolo, *Model independent form factors for spin independent neutralino nucleon scattering from elastic electron scattering data*, *JCAP* **0704** (2007) 012, [hep-ph/0608035].

[342] G. Belanger, E. Nezri and A. Pukhov, *Discriminating dark matter candidates using direct detection*, *Phys.Rev.* **D79** (2009) 015008, [0810.1362].

[343] M. Ressell and D. Dean, *Spin dependent neutralino - nucleus scattering for A approximately 127 nuclei*, *Phys.Rev.* **C56** (1997) 535–546, [hep-ph/9702290].

[344] J. Menendez, D. Gazit and A. Schwenk, *Spin-dependent WIMP scattering off nuclei*, *Phys.Rev.* **D86** (2012) 103511, [1208.1094].

[345] P. Klos, J. Menéndez, D. Gazit and A. Schwenk, *Large-scale nuclear structure calculations for spin-dependent WIMP scattering with chiral effective field theory currents*, *Phys. Rev. D* **88** (Oct., 2013) 083516, [1304.7684].

[346] P. Gondolo, J. Edsjö, P. Ullio, L. Bergström, M. Schelke and E. A. Baltz, *DarkSUSY: Computing supersymmetric dark matter properties numerically*, *JCAP* **0407** (2004) 008, [astro-ph/0406204].

[347] A. Gould, *Resonant Enhancements in WIMP Capture by the Earth*, *Astrophys.J.* **321** (1987) 571.

[348] S. Sivertsson and J. Edsjö, *WIMP diffusion in the solar system including solar WIMP-nucleon scattering*, *Phys.Rev.* **D85** (2012) 123514, [1201.1895].

[349] G. Jungman, M. Kamionkowski and K. Griest, *Supersymmetric dark matter*, *Phys. Rept.* **267** (1996) 195–373, [hep-ph/9506380].

[350] P. Scott, M. Fairbairn and J. Edsjö, *Dark stars at the Galactic centre - the main sequence*, *Mon.Not.Roy.Astron.Soc.* **394** (2009) 82, [0809.1871].

[351] P. D. Serpico and G. Bertone, *Astrophysical limitations to the identification of dark matter: indirect neutrino signals vis-a-vis direct detection recoil rates*, *Phys.Rev.* **D82** (2010) 063505, [1006.3268].

[352] K. Griest and D. Seckel, *Cosmic Asymmetry, Neutrinos and the Sun*, *Nucl.Phys.* **B283** (1987) 681.

[353] P. Gondolo, J. Edsjö, L. Bergström, P. Ullio, M. Schelke, E. A. Baltz et al., "Darksusy: Manual and long description of routines." `http://www.fysik.su.se/~edsjo/darksusy/docs/Manual.pdf`, 2009.

[354] F. Halzen, *Astroparticle physics with high energy neutrinos: from amanda to icecube*, *Eur.Phys.J.* **C46** (2006) 669–687, [`astro-ph/0602132`].

[355] G. Cowan, K. Cranmer, E. Gross and O. Vitells, *Asymptotic formulae for likelihood-based tests of new physics*, *Eur.Phys.J.* **C71** (2011) 1554, [`1007.1727`].

[356] F. Feroz and M. Hobson, *Multimodal nested sampling: an efficient and robust alternative to MCMC methods for astronomical data analysis*, *Mon.Not.Roy.Astron.Soc.* **384** (2008) 449, [`0704.3704`].

[357] F. Feroz, M. Hobson and M. Bridges, *MultiNest: an efficient and robust Bayesian inference tool for cosmology and particle physics*, *Mon.Not.Roy.Astron.Soc.* **398** (2009) 1601–1614, [`0809.3437`].

[358] F. Feroz, K. Cranmer, M. Hobson, R. Ruiz de Austri and R. Trotta, *Challenges of Profile Likelihood Evaluation in Multi-Dimensional SUSY Scans*, *JHEP* **1106** (2011) 042, [`1101.3296`].

[359] R. R. de Austri, R. Trotta and F. Feroz, "`SuperBayeS` package.".

[360] R. Trotta, F. Feroz, M. P. Hobson, L. Roszkowski and R. Ruiz de Austri, *The Impact of priors and observables on parameter inferences in the Constrained MSSM*, *JHEP* **0812** (2008) 024, [`0809.3792`].

[361] C. Arina, J. Hamann and Y. Y. Y. Wong, *A Bayesian view of the current status of dark matter direct searches*, *JCAP* **9** (Sept., 2011) 022, [`1105.5121`].

[362] C. Arina, J. Hamann, R. Trotta and Y. Y. Y. Wong, *Evidence for dark matter modulation in CoGeNT?*, *JCAP* **3** (Mar., 2012) 008, [`1111.3238`].

[363] M. Garny, A. Ibarra, M. Pato and S. Vogl, *On the spin-dependent sensitivity of XENON100*, *Phys. Rev. D* **87** (Mar., 2013) 056002, [`1211.4573`].

[364] IceCube Collaboration, M. G. Aartsen, K. Abraham, M. Ackermann, J. Adams, J. A. Aguilar et al., *Improved limits on dark matter annihilation in the Sun with the 79-string IceCube detector and implications for supersymmetry*, *ArXiv e-prints* (Jan., 2016) , [`1601.00653`].

[365] XENON100 Collaboration collaboration, E. Aprile et al., *Dark Matter Results from 225 Live Days of XENON100 Data*, *Phys.Rev.Lett.* **109** (2012) 181301, [`1207.5988`].

[366] F. Halzen and S. R. Klein, *IceCube: An Instrument for Neutrino Astronomy*, *Rev.Sci.Instrum.* **81** (2010) 081101, [1007.1247].

[367] IceCube Collaboration collaboration, R. Abbasi et al., *The Design and Performance of IceCube DeepCore*, *Astropart.Phys.* **35** (2012) 615–624, [1109.6096].

[368] H. Goldberg, *Constraint on the Photino Mass from Cosmology*, *Phys.Rev.Lett.* **50** (1983) 1419.

[369] D. Hooper and J. Silk, *Searching for dark matter with neutrino telescopes*, *New J.Phys.* **6** (2004) 23, [hep-ph/0311367].

[370] IceCube Collaboration collaboration, P. Scott, C. Savage and J. Edsjö, *Use of event-level neutrino telescope data in global fits for theories of new physics*, *JCAP* **1211** (2012) 057, [1207.0810].

[371] IceCube Collaboration collaboration, M. Danninger, *Searches for dark matter with the IceCube detector*, *J.Phys.Conf.Ser.* **375** (2012) 012038.

[372] IceCube Collaboration collaboration, T. Montaruli, *IceCube and Searches for Astrophysical Sources*, *Nucl.Phys.Proc.Suppl.* **212-213** (2011) 99–108, [1012.0881].

[373] M. Pato, O. Agertz, G. Bertone, B. Moore and R. Teyssier, *Systematic uncertainties in the determination of the local dark matter density*, *Phys.Rev.* **D82** (2010) 023531, [1006.1322].

[374] M. Lisanti, L. E. Strigari, J. G. Wacker and R. H. Wechsler, *The Dark Matter at the End of the Galaxy*, *Phys.Rev.* **D83** (2011) 023519, [1010.4300].

[375] G. Bertone, D. Cerdeno, M. Fornasa, L. Pieri, R. Ruiz de Austri and R. Trotta, *Complementarity of Indirect and Accelerator Dark Matter Searches*, *Phys.Rev.* **D85** (2012) 055014, [1111.2607].

[376] Fermi-LAT Collaboration, M. Ackermann, A. Albert, B. Anderson, W. B. Atwood, L. Baldini et al., *Searching for Dark Matter Annihilation from Milky Way Dwarf Spheroidal Galaxies with Six Years of Fermi Large Area Telescope Data*, *Physical Review Letters* **115** (Dec., 2015) 231301, [1503.02641].

[377] A. Abramowski, F. Aharonian, F. Ait Benkhali, A. G. Akhperjanian, E. Angüner, M. Backes et al., *Search for dark matter annihilation signatures in H.E.S.S. observations of dwarf spheroidal galaxies*, *Phys. Rev. D* **90** (Dec., 2014) 112012, [1410.2589].

[378] MAGIC Collaboration collaboration, J. AleksiÄĞ, S. Ansoldi,

L. Antonelli, P. Antoranz, A. Babic et al., *Optimized dark matter searches in deep observations of Segue 1 with MAGIC*, *JCAP* **02** (2014) 008, [1312.1535].

[379] VERITAS Collaboration collaboration, A. Geringer-Sameth, *The VERITAS Dark Matter Program*, 1303.1406.

[380] CTA Consortium collaboration, M. Doro et al., *Dark Matter and Fundamental Physics with the Cherenkov Telescope Array*, *Astropart. Phys.* **43** (2013) 189–214, [1208.5356].

[381] M. Wood, J. Buckley, S. Digel, S. Funk, D. Nieto et al., *Prospects for Indirect Detection of Dark Matter with CTA*, 1305.0302.

[382] M. Pierre, J. M. Siegal-Gaskins and P. Scott, *Sensitivity of CTA to dark matter signals from the Galactic Center*, *JCAP* **6** (June, 2014) 24, [1401.7330].

[383] CTA Consortium collaboration, M. Actis et al., *Design concepts for the Cherenkov Telescope Array CTA: An advanced facility for ground-based high-energy gamma-ray astronomy*, *Exper. Astron.* **32** (2011) 193–316, [1008.3703].

[384] H.E.S.S. Collaboration collaboration, A. Abramowski et al., *H.E.S.S. constraints on Dark Matter annihilations towards the Sculptor and Carina Dwarf Galaxies*, *Astropart. Phys.* **34** (2011) 608–616, [1012.5602].

[385] K. Bernlöhr, A. Barnacka, Y. Becherini, O. Blanch Bigas, E. Carmona et al., *Monte Carlo design studies for the Cherenkov Telescope Array*, *Astropart. Phys.* **43** (2013) 171–188, [1210.3503].

[386] A. M. Hillas, *Cerenkov light images of EAS produced by primary gamma*, *International Cosmic Ray Conference* **3** (Aug., 1985) 445–448.

[387] J. G. Skellam, *The frequency distribution of the difference between two poisson variates belonging to different populations*, *J. Royal Stat. Soc.* **109** (1946) 296.

[388] J. M. Cline, K. Kainulainen, P. Scott and C. Weniger, *Update on scalar singlet dark matter*, *Phys. Rev. D* **88** (Sept., 2013) 055025, [1306.4710].

[389] Fermi-LAT Collaboration collaboration, M. Ackermann et al., *The Fermi Large Area Telescope On Orbit: Event Classification, Instrument Response Functions, and Calibration*, *ApJS* **203** (2012) 4, [1206.1896].

[390] J. F. Navarro, E. Hayashi, C. Power, A. R. Jenkins, C. S. Frenk, S. D. M. White et al., *The inner structure of ΛCDM haloes - III. Universality and asymptotic slopes*, *MNRAS* **349** (Apr., 2004) 1039–1051, [astro-ph/0311231].

[391] L. Pieri, J. Lavalle, G. Bertone and E. Branchini, *Implications of High-Resolution Simulations on Indirect Dark Matter Searches*, *Phys.Rev.* **D83** (2011) 023518, [0908.0195].

[392] M. Cirelli, G. Corcella, A. Hektor, G. Hutsi, M. Kadastik et al., *PPPC 4 DM ID: A Poor Particle Physicist Cookbook for Dark Matter Indirect Detection*, *JCAP* **1103** (2011) 051, [1012.4515].

[393] Fermi LAT Collaboration collaboration, A. A. Abdo et al., *Measurement of the Cosmic Ray e+ plus e- spectrum from 20 GeV to 1 TeV with the Fermi Large Area Telescope*, *Phys. Rev. Lett.* **102** (2009) 181101, [0905.0025].

[394] H.E.S.S. Collaboration collaboration, F. Aharonian et al., *The energy spectrum of cosmic-ray electrons at TeV energies*, *Phys. Rev. Lett.* **101** (2008) 261104, [0811.3894].

[395] J. R. Hoerandel, *On the knee in the energy spectrum of cosmic rays*, *Astropart. Phys.* **19** (2003) 193–220, [astro-ph/0210453].

[396] D. Fegan, *Gamma/hadron separation at TeV energies*, *J. Phys. G* **23** (1997) 1013–1060.

[397] D. Berge, S. Funk and J. Hinton, *Background Modelling in Very-High-Energy gamma-ray Astronomy*, *Astron.Astrophys.* **466** (2007) 1219–1229, [astro-ph/0610959].

[398] H.E.S.S. Collaboration collaboration, F. Aharonian et al., *Discovery of Very-High-Energy Gamma-Rays from the Galactic Centre Ridge*, *Nature* **439** (2006) 695–698, [astro-ph/0603021].

[399] Fermi-LAT Collaboration collaboration, M. Ackermann et al., *Fermi-lat observations of the diffuse gamma-ray emission: Implications for cosmic rays and the interstellar medium*, *ApJ* **750** (2012) 3, [1202.4039].

[400] Fermi-LAT Collaboration collaboration, M. Ackermann et al., *Dark Matter Constraints from Observations of 25 Milky Way Satellite Galaxies with the Fermi Large Area Telescope*, *Phys. Rev. D* **89** (2014) 042001, [1310.0828].

[401] S. Funk and J. A. Hinton, *Comparison of Fermi-LAT and CTA in the region between 10-100 GeV*, *Astropart. Phys.* **43** (2013) 348–355, [1205.0832].

[402] H. Dickinson and J. Conrad, *Handling Systematic Uncertainties and Combined Source Analyses for Atmospheric Cherenkov Telescopes*, *Astropart.Phys.* **41** (2013) 17–30, [1203.5643].

[403] G. Cowan, K. Cranmer, E. Gross and O. Vitells, *Asymptotic formulae for*

likelihood-based tests of new physics, *Eur. Phys. J. C* **71** (Feb., 2011) 1554, [1007.1727].

[404] G. J. Feldman and R. D. Cousins, *A Unified approach to the classical statistical analysis of small signals*, *Phys.Rev.* **D57** (1998) 3873–3889, [physics/9711021].

[405] I. Cholis and P. Salucci, *Extracting limits on Dark Matter annihilation from gamma-ray observations towards dwarf spheroidal galaxies*, *Phys.Rev.* **D86** (2012) 023528, [1203.2954].

[406] L. Bergstrom, G. Bertone, J. Conrad, C. Farnier and C. Weniger, *Investigating Gamma-Ray Lines from Dark Matter with Future Observatories*, *JCAP* **1211** (2012) 025, [1207.6773].

[407] H.E.S.S. Collaboration collaboration, A. Abramowski et al., *Search for photon line-like signatures from Dark Matter annihilations with H.E.S.S*, *Phys.Rev.Lett.* **110** (2013) 041301, [1301.1173].

[408] V. Lefranc, E. Moulin and for the H. E. S. S. collaboration, *Dark matter search in the inner Galactic halo with H.E.S.S. I and H.E.S.S. II*, *ArXiv e-prints* (Sept., 2015) , [1509.04123].

[409] V. Lefranc, E. Moulin, P. Panci and J. Silk, *Prospects for annihilating dark matter in the inner galactic halo by the Cherenkov Telescope Array*, *Phys. Rev. D* **91** (June, 2015) 122003, [1502.05064].

[410] J. Binney and S. Tremaine, *Galactic Dynamics*. Princeton University Press, 2 ed., 2008.

[411] J. Bovy, H.-W. Rix, C. Liu, D. W. Hogg, T. C. Beers and Y. S. Lee, *The Spatial Structure of Mono-abundance Sub-populations of the Milky Way Disk*, *ApJ* **753** (July, 2012) 148, [1111.1724].

[412] J. Bovy, H.-W. Rix and D. W. Hogg, *The Milky Way Has No Distinct Thick Disk*, *ApJ* **751** (June, 2012) 131, [1111.6585].

[413] I. Minchev, B. Famaey, A. C. Quillen, W. Dehnen, M. Martig and A. Siebert, *Radial Migration Does Little for Galactic Disc Thickening*, *Astron. Astrophys.* **548** (2012) A127, [1205.6475].

[414] C. F. McKee, A. Parravano and D. J. Hollenbach, *Stars, Gas, and Dark Matter in the Solar Neighborhood*, *ApJ* **814** (Nov., 2015) 13, [1509.05334].

[415] J. Read, *The Local Dark Matter Density*, *J.Phys.* **G41** (2014) 063101, [1404.1938].

[416] W. Dehnen and J. Binney, *Mass models of the Milky Way*, *MNRAS* **294** (1998) 429, [astro-ph/9612059].

[417] M. Weber and W. de Boer, *Determination of the Local Dark Matter Density in our Galaxy*, *Astron.Astrophys.* **509** (2010) A25, [0910.4272].

[418] R. Catena and P. Ullio, *A novel determination of the local dark matter density*, *JCAP* **8** (Aug., 2010) 4, [0907.0018].

[419] P. Salucci, F. Nesti, G. Gentile and C. Martins, *The dark matter density at the Sun's location*, *Astron.Astrophys.* **523** (2010) A83, [1003.3101].

[420] P. J. McMillan, *Mass models of the Milky Way*, *MNRAS* **414** (July, 2011) 2446–2457, [1102.4340].

[421] F. Nesti and P. Salucci, *The Dark Matter halo of the Milky Way, AD 2013*, *JCAP* **1307** (2013) 016, [1304.5127].

[422] T. Piffl, J. Binney, P. J. McMillan, M. Steinmetz, A. Helmi, R. F. G. Wyse et al., *Constraining the Galaxy's dark halo with RAVE stars*, *MNRAS* **445** (Dec., 2014) 3133–3151, [1406.4130].

[423] M. Pato and F. Iocco, *The Dark Matter Profile of the Milky Way: A Non-parametric Reconstruction*, *ApJ* **803** (Apr., 2015) L3, [1504.03317].

[424] J. Bovy and H.-W. Rix, *A Direct Dynamical Measurement of the Milky Way's Disk Surface Density Profile, Disk Scale Length, and Dark Matter Profile at 4 kpc $\lesssim R \lesssim$ 9 kpc*, *Astrophys.J.* **779** (2013) 115, [1309.0809].

[425] Y. Huang, X. Liu, H. Yuan, M. Xiang, H. Zhang, B. Chen et al., *The Milky Way's rotation curve out to 100 kpc and its constraint on the Galactic mass distribution*, *ArXiv e-prints* (Apr., 2016) , [1604.01216].

[426] J. H. Oort, *The force exerted by the stellar system in the direction perpendicular to the galactic plane and some related problems*, *Bulletin of the Astronomical Institutes of the Netherlands* **6** (Aug., 1932) 249.

[427] J. N. Bahcall, *K giants and the total amount of matter near the sun*, *"Astrophys.J."* **287** (Dec., 1984) 926–944.

[428] K. Kuijken and G. Gilmore, *The Mass Distribution in the Galactic Disc - II - Determination of the Surface Mass Density of the Galactic Disc Near the Sun*, *MNRAS* **239** (Aug., 1989) 605–649.

[429] K. Kuijken and G. Gilmore, *The galactic disk surface mass density and the Galactic force K(z) at Z = 1.1 kiloparsecs*, *ApJ* **367** (Jan., 1991) L9–L13.

[430] M. Creze, E. Chereul, O. Bienayme and C. Pichon, *The distribution of nearby stars in phase space mapped by Hipparcos. I. The potential well and local dynamical mass*, *A&A* **329** (Jan., 1998) 920–936, [astro-ph/9709022].

[431] S. Garbari, C. Liu, J. I. Read and G. Lake, *A new determination of the local dark matter density from the kinematics of K dwarfs*, *Mon.Not.Roy.Astron.Soc.* **425** (2012) 1445, [1206.0015].

[432] J. Bovy and S. Tremaine, *On the Local Dark Matter Density*, *ApJ* **756** (Sept., 2012) 89, [1205.4033].

[433] M. C. Smith, S. H. Whiteoak and N. W. Evans, *Slicing and Dicing the Milky Way Disk in the Sloan Digital Sky Survey*, *ApJ* **746** (Feb., 2012) 181, [1111.6920].

[434] L. Zhang, H.-W. Rix, G. van de Ven, J. Bovy, C. Liu and G. Zhao, *The Gravitational Potential near the Sun from SEGUE K-dwarf Kinematics*, *ApJ* **772** (Aug., 2013) 108, [1209.0256].

[435] O. Bienaymé, B. Famaey, A. Siebert, K. C. Freeman, B. K. Gibson, G. Gilmore et al., *Weighing the local dark matter with RAVE red clump stars*, *A&A* **571** (Nov., 2014) A92, [1406.6896].

[436] Q. Xia, C. Liu, S. Mao, Y. Song, L. Zhang, R. J. Long et al., *Determining the local dark matter density with LAMOST data*, *MNRAS* **458** (June, 2016) 3839–3850, [1510.06810].

[437] J. Binney and M. Merrifield, *Galactic Astronomy*. 1998.

[438] B. Yanny, C. Rockosi, H. J. Newberg, G. R. Knapp, J. K. Adelman-McCarthy, B. Alcorn et al., *SEGUE: A Spectroscopic Survey of 240,000 Stars with g = 14-20*, *AJ* **137** (May, 2009) 4377–4399, [0902.1781].

[439] S. R. Majewski, R. P. Schiavon, P. M. Frinchaboy, C. Allende Prieto, R. Barkhouser, D. Bizyaev et al., *The Apache Point Observatory Galactic Evolution Experiment (APOGEE)*, *ArXiv e-prints* (Sept., 2015) , [1509.05420].

[440] A. Büdenbender, G. van de Ven and L. L. Watkins, *The tilt of the velocity ellipsoid in the Milky Way disc*, *MNRAS* **452** (Sept., 2015) 956–968, [1407.4808].

[441] E. Høg, C. Fabricius, V. V. Makarov, S. Urban, T. Corbin, G. Wycoff et al., *The Tycho-2 catalogue of the 2.5 million brightest stars*, *A&A* **355** (Mar., 2000) L27–L30.

[442] D. Michalik, L. Lindegren, D. Hobbs and U. Lammers, *Joint astrometric solution of HIPPARCOS and Gaia. A recipe for the Hundred Thousand Proper Motions project*, *A&A* **571** (Nov., 2014) A85, [1407.4025].

[443] D. Michalik, L. Lindegren and D. Hobbs, *The Tycho-Gaia astrometric solution . How to get 2.5 million parallaxes with less than one year of Gaia data*, *A&A* **574** (Feb., 2015) A115, [1412.8770].

[444] G. Gilmore, S. Randich, M. Asplund, J. Binney, P. Bonifacio, J. Drew et al., *The Gaia-ESO Public Spectroscopic Survey*, *The Messenger* **147** (Mar., 2012) 25–31.

[445] G. Dalton, S. Trager, D. C. Abrams, P. Bonifacio, J. A. López Aguerri, K. Middleton et al., *Project overview and update on WEAVE: the next generation wide-field spectroscopy facility for the William Herschel Telescope*, in *Ground-based and Airborne Instrumentation for Astronomy V*, vol. 9147 of *Proc. SPIE*, p. 91470L, July, 2014. 1412.0843. DOI.

[446] R. S. de Jong, S. Barden, O. Bellido-Tirado, J. Brynnel, C. Chiappini, É. Depagne et al., *4MOST: 4-metre Multi-Object Spectroscopic Telescope*, in *Ground-based and Airborne Instrumentation for Astronomy V*, vol. 9147 of *Proc. SPIE*, p. 91470M, July, 2014. DOI.

[447] Ž. Ivezić, S. M. Kahn and P. Eliason, *The Gaia-LSST Synergy*, *ArXiv e-prints* (Feb., 2015) , [1502.06555].

[448] J. I. Read and B. Moore, *Tidal streams in a MOND potential: constraints from Sagittarius*, *MNRAS* **361** (Aug., 2005) 971–976, [astro-ph/0501273].

[449] C. Nipoti, P. Londrillo, H. Zhao and L. Ciotti, *Vertical dynamics of disc galaxies in modified Newtonian dynamics*, *MNRAS* **379** (Aug., 2007) 597–604, [0704.0740].

[450] F. Feroz, M. P. Hobson, E. Cameron and A. N. Pettitt, *Importance Nested Sampling and the MultiNest Algorithm*, *ArXiv e-prints* (June, 2013) , [1306.2144].

[451] S. Garbari, J. I. Read and G. Lake, *Limits on the local dark matter density*, *Mon.Not.Roy.Astron.Soc.* **416** (2011) 2318–2340, [1105.6339].

[452] E. R. Hill, *The component of the galactic gravitational field perpendicular to the galactic plane, K_z*, *Bull. Astron. Inst. Netherlands* **15** (Feb., 1960) 1.

[453] F. Mignard, *Local galactic kinematics from Hipparcos proper motions*, *A&A* **354** (Feb., 2000) 522–536.

[454] R. L. Branham, Jr., *Kinematics and velocity ellipsoid of the F giants*, *MNRAS* **409** (Dec., 2010) 1269–1280.

[455] R. L. Branham, Jr., *The Kinematics and Velocity Ellipsoid of the G III Stars*, *Rev. Mexicana Astron. Astrofis.* **47** (Oct., 2011) 197–209.

[456] C. W. Purcell, J. S. Bullock, E. J. Tollerud, M. Rocha and S. Chakrabarti, *The Sagittarius impact as an architect of spirality and outer rings in the Milky Way*, *Nature* **477** (Sept., 2011) 301–303, [1109.2918].

[457] F. A. Gómez, I. Minchev, B. W. O'Shea, T. C. Beers, J. S. Bullock and C. W. Purcell, *Vertical density waves in the Milky Way disc induced by the Sagittarius dwarf galaxy*, *MNRAS* **429** (Feb., 2013) 159–164, [1207.3083].

[458] C. Faure, A. Siebert and B. Famaey, *Radial and vertical flows induced by galactic spiral arms: likely contributors to our 'wobbly Galaxy'*, *MNRAS* **440** (May, 2014) 2564–2575, [1403.0587].

[459] L. M. Widrow, S. Gardner, B. Yanny, S. Dodelson and H.-Y. Chen, *Galactoseismology: Discovery of Vertical Waves in the Galactic Disk*, *ApJ* **750** (May, 2012) L41, [1203.6861].

[460] W. Dehnen, *The Distribution of Nearby Stars in Velocity Space Inferred from HIPPARCOS Data*, *AJ* **115** (June, 1998) 2384–2396, [astro-ph/9803110].

[461] D. W. Hogg, M. R. Blanton, S. T. Roweis and K. V. Johnston, *Modeling Complete Distributions with Incomplete Observations: The Velocity Ellipsoid from Hipparcos Data*, *ApJ* **629** (Aug., 2005) 268–275, [astro-ph/0505057].

[462] M. Aumer and J. J. Binney, *Kinematics and history of the solar neighbourhood revisited*, *MNRAS* **397** (Aug., 2009) 1286–1301, [0905.2512].

[463] J. Bovy, D. W. Hogg and S. T. Roweis, *The Velocity Distribution of Nearby Stars from Hipparcos Data. I. The Significance of the Moving Groups*, *ApJ* **700** (Aug., 2009) 1794–1819, [0905.2980].

[464] S. Pasetto, E. K. Grebel, T. Zwitter, C. Chiosi, G. Bertelli, O. Bienayme et al., *Thin disk kinematics from RAVE and the solar motion*, *A&A* **547** (Nov., 2012) A71, [1209.0460].

[465] T. Aghajani and L. Lindegren, *Maximum likelihood estimation of local stellar kinematics*, *A&A* **551** (Mar., 2013) A9, [1302.3995].

[466] S. Pasetto, E. K. Grebel, T. Zwitter, C. Chiosi, G. Bertelli, O. Bienayme et al., *Thick disk kinematics from RAVE and the solar motion*, *A&A* **547** (Nov., 2012) A70, [1209.0456].

[467] S. Sharma, J. Bland-Hawthorn, J. Binney, K. C. Freeman, M. Steinmetz, C. Boeche et al., *Kinematic Modeling of the Milky Way Using the RAVE and GCS Stellar Surveys*, *ApJ* **793** (Sept., 2014) 51, [1405.7435].

[468] G. Monari, B. Famaey and A. Siebert, *Modelling the Galactic disc: perturbed distribution functions in the presence of spiral arms*, *MNRAS* **457** (Apr., 2016) 2569–2582, [1601.04714].

[469] C. Flynn, J. Holmberg, L. Portinari, B. Fuchs and H. Jahreiß, *On the mass-to-light ratio of the local Galactic disc and the optical luminosity of the Galaxy*, *MNRAS* **372** (Nov., 2006) 1149–1160, [astro-ph/0608193].

[470] K. Kuijken and G. Gilmore, *The mass distribution in the galactic disc. I - A technique to determine the integral surface mass density of the disc near the sun.*, *Mon.Not.Roy.Astron.Soc.* **239** (Aug., 1989) 571–603.

[471] D. Carollo, T. C. Beers, M. Chiba, J. E. Norris, K. C. Freeman, Y. S. Lee et al., *Structure and Kinematics of the Stellar Halos and Thick Disks of the Milky Way Based on Calibration Stars from Sloan Digital Sky Survey DR7*, *ApJ* **712** (Mar., 2010) 692–727, [0909.3019].

[472] D. I. Casetti-Dinescu, T. M. Girard, V. I. Korchagin and W. F. van Altena, *The Three-dimensional Velocity Structure of the Thick Disk from SPM4 and RAVE DR2*, *ApJ* **728** (Feb., 2011) 7, [1011.6253].

[473] A. Siebert, O. Bienaymé, J. Binney, J. Bland-Hawthorn, R. Campbell, K. C. Freeman et al., *Estimation of the tilt of the stellar velocity ellipsoid from RAVE and implications for mass models*, *MNRAS* **391** (Dec., 2008) 793–801, [0809.0615].

[474] J. Binney, B. Burnett, G. Kordopatis, M. Steinmetz, G. Gilmore, O. Bienayme et al., *Galactic kinematics and dynamics from Radial Velocity Experiment stars*, *MNRAS* **439** (Apr., 2014) 1231–1244, [1309.4285].

[475] M. C. Smith, N. Wyn Evans and J. H. An, *The Tilt of the Halo Velocity Ellipsoid and the Shape of the Milky Way Halo*, *ApJ* **698** (June, 2009) 1110–1116, [0902.2709].

[476] S. R. Loebman, R. Roškar, V. P. Debattista, Ž. Ivezić, T. R. Quinn and J. Wadsley, *The Genesis of the Milky Way's Thick Disk Via Stellar Migration*, *ApJ* **737** (Aug., 2011) 8, [1009.5997].

[477] J. Skilling, *Nested sampling for general bayesian computation*, *Bayesian Anal.* **1** (12, 2006) 833–859.

[478] R. Trotta, *Bayes in the sky: Bayesian inference and model selection in cosmology*, *Contemp. Phys.* **49** (2008) 71–104, [0803.4089].

[479] S. Liem, *Barrett: out-of-core processing of MultiNest output*, *ArXiv e-prints* (Aug., 2016) , [1608.00990].

[480] S. Pearson, A. H. W. Küpper, K. V. Johnston and A. M. Price-Whelan, *Tidal Stream Morphology as an Indicator of Dark Matter Halo Geometry: The Case of Palomar 5*, *ApJ* **799** (Jan., 2015) 28, [1410.3477].

Samenvatting

Het licht dat we zien uit de kosmos wordt gevormd door ongeziene krachten. De bewegingen van de ons omringende sterren in de Melkweg, de interne dynamiek van clusters, de tot een web verweven sterrenstelsels in ons universum, de kleine golven in de 13 miljard jaar geleden gevormde zee van fotonen die nu over ons heen spoelt als de kosmische achtergrondstraling - zij zijn allemaal getekend door een mysterieuze substantie genaamd donkere materie, en vertellen ons veel over wat dit wel en niet kan zijn. De donkere materiedeeltjes kunnen zelf mogelijk ook licht produceren en zo hun aard onthullen: minuscule licht flitsen afkomstig van donkere materiedeeltjes die op atoomkernen botsen in directe detectie experimenten; de Cherenkovstraling in de atmosfeer, geproduceerd door atomen die uit elkaar zijn gescheurd door de gammastraling afkomstig van annihilerende donkere materie, of in het ijs van Antarctica door de muonen die zijn geproduceerd door neutrinos ontsnapt uit de zon alwaar zij zijn gevormd door de daar gevangen donkere materie die met zichzelf annihileert. Ondanks de intense zoektocht is dit licht nog niet gevonden, en de aard van donkere materie blijft, voorlopig, in het ongewisse.

De donkere-materie puzzel bestond al gedurende het grootste deel van de vorige eeuw. Metingen van de interne dynamiek van clusters en de rotatiecurves van sterrenstelsels buiten de Melkweg bevestigden de aanwezigheid van meer en ongeziene materie in deze objecten. Echter bewezen zij niet dat deze massa een nieuwe soort materie moest zijn. Desalniettemin groeide het bewijs dat de deeltjes die bij ons bekend zijn in het Standaardmodel (SM) niet konden voldoen aan de door astronomische observaties opgelegde restricties snel - numerieke simulaties lieten bijvoorbeeld zien dat neutrinos het kosmische web zouden doen vervagen als zij de donkere materiedeeltjes zouden zijn.

Het meest toonaangevende bewijs dat donkere materie iets nieuws moest zijn kwam van de kosmische achtergrondstraling (CMB). Dit licht werd uitgestraald toen het universum een transitie onderging van een ondoorzichtig plasma bestaande uit fotonen,

elektronen, protonen en neutronen, naar een transparant gas van waterstof, helium en een vleugje lithium, waardoor fotonen zich vrijuit konden voortbewegen. Tijdens de transitie oscilleerde het plasma, aangetrokken door het zwaartekrachtsveld van donkere materie-klompen en vervolgens naar buiten gedrukt onder zijn eigen druk. Toen de transitie plaatsvond werden de pieken en dalen van deze oscillaties vastgelegd in de temperatuurdistributie van de fotonen. Nu, miljarden jaren later, zien wij exact dezelfde fotonen als de CMB, met zijn pieken en dalen als warme en koude gebieden op de hemelbol. Uit de patronen in deze gebieden kunnen we de oscillaties van het plasma ontfutselen, en wat we vinden vertelt ons dat slechts 15% van de materie in ons Universum bestaat uit de ons bekende SM deeltjes, zoals protonen, neutronen, elektronen en neutrinos. De overige 85% is donkere materie, bestaande uit tot-op-heden onbekende deeltjes. De Melkweg is gelegen in een grofweg bolvormige halo bestaande uit deze donkere materiedeeltjes, en die bewegen haast zonder wisselwerking door de zon en de aarde heen.

Tegelijkertijd met de roep om nieuwe deeltjes voortkomende uit kosmologische observaties, formuleerden deeltjesfysici hun bestaan als een onderdeel van uitbreidingen op het Standaardmodel van de deeltjesfysica. Veel van deze uitbreidingen zijn een oplossing voor tekortkomingen van het Standaardmodel en produceren tegelijkertijd hypothetische deeltjes welke kunnen fungeren als donkere materie. Een overvloed aan axionen en axion-achtige deeltjes zijn gepostuleerd als oplossing voor het gebrek aan CP-schending in de sterke kernkracht. Steriele neutrinos kunnen de minieme, door oscillatie experimenten aangetoonde, massa's van de normale actieve neutrinos verklaren. Supersymmetrie vormt een oplossing voor het zogenoemde hiërarchieprobleem en kan daarnaast bijdragen aan de vereniging van de sterke- en zwakke kernkracht en elektromagnetische kracht op hoge energie. Supersymmetrie oppert het bestaan van een scala aan nieuwe deeltjes, waarvan de lichtste kan fungeren als donkere materiekandidaat. In de meeste supersymmetrie modellen is dit de neutralino, het meest vooraanstaande lid binnen de groep deeltjes die ook wel bekend zijn als *Weakly Interacting Massive Particles* (zware deeltjes met een zwakke wisselwerking), oftewel WIMPs. Experimenten van over de hele wereld en satellieten in een baan om de aarde zoeken naar zowel axionen, steriele neutrinos alsook WIMPS. WIMPs blijven echter de meest toonaangevende kandidaat-deeltjes, en we focussen op deze deeltjes in Hoofdstuk 2 en 3. Hoofdstuk 4, welke gaat over het bepalen van de donkere materiedichtheid in de nabijheid van de zon doormiddel van de bewegingen van sterren, is agnostisch wat betreft het onderliggende deeltjesfysica-model.

De jacht op donkere materiedeeltjes kan worden onderverdeeld in drie gebieden: directe detectie, indirecte detectie en de zoektocht met deeltjesversnellers. In de laatstgenoemde methode proberen we zelf donkere materiedeeltjes te creëren. En hoewel dit niet één-op-één de donkere materie in de melkweg en de kosmos onderzoekt, kan

het ons in potentie precieze informatie geven over het deeltje en de onderliggende theorieën. Indirecte detectie zoekt naar deeltjes uit het Standaardmodel die zijn geproduceerd door het annihileren van donkere materie in astrofysische structuren, zoals bijvoorbeeld gammastraling en neutrinos uit het centrum van de Melkweg. Daarnaast kan donkere materie verstrooien met atoomkernen in de zon of andere objecten, gevangen worden in hun zwaartekrachtsveld, en steeds weer opnieuw verstrooiing ondergaan totdat ze gevangen zijn in de kern van de zon. Alhier annihileren ze en als er neutrinos overblijven zouden deze uit de zon kunnen ontsnappen en worden waargenomen met neutrino detectoren zoals IceCube op de Zuidpool. Dezelfde verstrooiingen van donkere materie met atoomkernen die leiden tot het vangen van donkere materie in de kern van de zon zijn ook de leidraad voor de laatste groep experimenten, directe detectie. Hier wordt gezocht naar de minuscule hoeveelheden energie die donkere materie achterlaat in de detector als het op een atoomkern botst. Het meest gevoelige experiment is XENON1T, welke binnenkort in werking wordt gezet diep onder de grond in het Gran Sasso laboratorium in Italië.

Desalniettemin, zelfs al wordt WIMP donkere materie ontdekt dan nog zal het lastig zijn om alle eigenschappen te ontrafelen. De signalen die we meten zijn afhankelijk van veel factoren, niet alleen van de aard van het deeltje, maar ook van hun verdeling in de Melkweg. Dit leidt tot veel ontaardingen, een bepaalde hoeveelheid signaal kan bijvoorbeeld worden geproduceerd door een groot aantal deeltjes met zwakke interacties, of door een kleiner aantal deeltjes met sterkere interacties. Echter, door verschillende experimenten te combineren en gebruik te maken van hun verschillende gevoeligheid voor bepaalde eigenschappen wordt het mogelijk om de ontaarding op te heffen. In Hoofdstuk 2 hebben we de uitkomst bestudeert van een hypothetische WIMP donkere materie meting in zowel XENON1T en IceCube. Separate analyses resulteerden in ontaardingen tussen de WIMP massa, de spin-afhankelijke en spin-onafhankelijke WIMP-nucleon wisselwerking. Wij demonstreerden daarentegen dat een gecombineerde analyse, gebruik makende van de verschillende gevoeligheden voor bepaalde processen, deze ontaardingen op kan heffen. Dit is tekenend voor de complementariteit van de experimenten.

De ontdekking van gammastraling afkomstig van WIMP donkere materie die annihileert in de Melkweg is een ander veelbelovend pad voor indirecte detectie. In Hoofdstuk 3 hebben we de vooruitzichten onderzocht voor het aanstaande Cherenkov Telescope Array (CTA) experiment om donkere materie via deze weg te ontdekken. Gammastraling die de bovenste lagen van de atmosfeer treft laat atomen aldaar uiteenvallen en creëert een lawine aan hoog-energetische deeltjes die Cherenkov-licht uitstralen. CTA en soortgelijke experimenten meten deze straling aan de grond met een scala aan telescopen, en reconstrueren vervolgens de richting en energie van de originele gammastraling. Het meest veelbelovende doelwit voor CTA is het centrum

van de Melkweg, en verschillende studies hebben onderzocht hoe sensitief CTA is voor donkere-materie annihilatie aldaar. Echter, voorafgaand aan ons onderzoek had niemand rekening gehouden met de systematische fout in het functioneren van de detector, noch met de diffuse gammastraling-achtergrond welke door bekende astrofysische processen wordt geproduceerd en het donkere materie signaal maskeert. Wij ontdekten dat deze effecten de prestaties van CTA significant doen verslechteren wanneer de conventionele analyse methoden worden gebruikt. Om de impact van de diffuse gammastraling-achtergrond te doen verminderen hebben we een nieuwe analyse methode voorgesteld. Deze maakt gebruik van de verschillende vorm van de achtergrond, welke veelal geconcentreerd is rondom de galactische schijf, en het donkere materie signaal, wat bijna bolvormig is. Hoewel het geen volledige oplossing is, verbetert deze methode de limieten op de annihilatie werkzame doorsnede van donkere materie toch met bijna één orde van grote.

Cruciaal voor alle drie de detectie methodes is de distribute van donkere materie in de Melkweg. De detectie van gammastraling met CTA is afhankelijk van de donkere materie-dichtheid tussen ons en het centrum van de Melkweg. Directe detectie en indirecte detectie door het vangen van donkere materie in de zon en de daaropvolgende annihilatie worden aangedreven door de donkere materie-dichtheid in de buurt van de zon. In Hoofdstuk Chapter 4 hebben we ons verdiept in de bepaling van deze waarde, beter bekend als de lokale donkere materie-dichtheid. Het is belangrijk om deze grootheid te meten met zo min mogelijk aannames, omdat het wordt gebruikt in de analyse van directe en indirecte detectie data, welke vervolgens wordt gebruikt om inzicht te krijgen in theorieën van donkere materie, zoals supersymmetrie. Aannames in de bepaling van de lokale donkere materie-dichtheid sluipen door de experimentele fysica naar de theoretische fysica, en veroorzaken mogelijk onzuiverheden en incorrecte conclusies.

Ter bevordering van dit doel hebben we een nieuwe methode ontwikkeld welke in potentie het aantal aannames in de bepaling van de lokale donkere materie-dichtheid wezenlijk kan verminderen. De bewegingen van de sterren in de melkweg worden gemodelleerd als een botsingloze vloeistof, welke door het zwaartekrachtspotentiaal van de Melkweg stroomt, en aantrekkingskracht van de baryonen alsook van de donkere materie voelt. De dichtheid en stroming wordt beschreven door de botsingloze Boltzmann vergelijking en de Jeans vergelijking, waarop wij onze methode baseren. De data die voor deze en eerdere studies wordt gebruikt bestaat uit de posities en snelheden van een set tracer-sterren boven en onder de galactische schijf. Wij construeerden een model voor de massa distributie in de omgeving van de zon, inclusief het effect van normale en donkere materie, en hebben dit model gefit aan de verticale dichtheid en snelheid dispersie van de tracer-sterren, gebruik makende van de geïntegreerde vorm van de Jeans vergelijking. In de studie gepresenteerd in dit proefschrift hebben we

de methode ontwikkeld en getest op geïdealiseerde modellen, om het te verfijnen voor toekomstig gebruik met echte data.

Onze tests wezen op de cruciale rol van de zogenoemde *kanteling term*, welke de verticale beweging van de sterren omhoog en omlaag door de galactische schijf relateert aan hun radiale beweging naar en weg van het centrum van de Melkweg. Ondanks dat onze methode is gebaseerd op de verticale bewegingen van de sterren, kunnen de radiale bewegingen toch gemodelleerd worden doormiddel van een correctie term. We hebben geïllustreerd dat het weglaten van deze kanteling term lijdt tot een systematische onderschatting van de lokale donkere materie dichtheid. Daarbij komt dat deze term steeds belangrijker wordt op grotere hoogte boven de galactische schijf, precies waar we moeten meten om de invloed van de galactische schijf te vermijden en een duidelijk beeld te krijgen van de donkere materie distributie om ons heen. We hebben ook onderzocht of het haalbaar is om een donkere-schijf detecteren, een extra component van donkere materie welke bijvoorbeeld kan worden gevormd door klompen donkere materie die uit elkaar worden gereten en vervolgens worden aangetrokken tot de baryonische schijf. Hoewel we het totale donkere materie profiel, bestaande uit de bolvormige halo en schijf, kunnen begrenzen, kunnen we tot op heden nog geen onderscheid maken tussen de twee. Dit onderscheid is belangrijk aangezien beide componenten verschillende signalen veroorzaken in directe en indirecte detectie experimenten.

De toekomst is rooskleurig voor het onderzoek naar donkere materie. XENON1T wordt binnenkort in gebruik genomen en gaat opzoek naar de terugslag van atoomkernen die worden geraakt door donkere materiedeeltjes, en grotere experimenten zullen spoedig volgen. IceCube blijft zoeken naar neutrino signalen van donkere materie samen met zijn tegenhanger in de middellandse zee, Antares. Beiden zullen nog dit decennium worden vergezeld door KM3NeT. CTA wordt naar verwachting in 2019 in gebruik genomen en gaat op zoek naar gammastraling van annihilerende donkere materie in het centrum van de Melkweg. Kennis van de verdeling van donkere materie in de Melkweg, welke ten grondslag ligt aan al deze detectie methoden, zal ook snelle ontwikkelingen doormaken met de komst van zeer precieze astrometrische data van de Gaia satelliet. De jacht op donkere materie heeft echter meer nodig dan deze individuele experimenten. Het werk in dit proefschrift overspant directe detectie, indirecte detectie, galacto-dynamica en astrometrie, en voortdurend benadrukken we de samenhang tussen deze gebieden. Donkere materie is een immens vraagstuk dat terugkomt in de deeltjesfysica, astronomie en kosmologie, en alleen doormiddel van een gezamenlijke inspanning kunnen we tot grote hoogte rijken en een alomvattend beeld krijgen van onze Melkweg en ons Universum.

Vertaald door Richard Bartels en Niki Klop.

Summary

The light we see in the cosmos is shaped by unseen forces. The motions of the stars around us in the Milky Way, the internal dynamics of galaxy clusters, the threads of galaxies woven into a web spanning the Universe, the tiny ripples in the sea of photons created 13 billion years ago that now washes over us as the cosmic microwave background - all bear the imprint of a mysterious substance known as *dark matter* and tell us much about what it can or cannot be. The dark matter particles themselves may also produce light and so reveal their nature: tiny flashes of light from dark matter particles striking nuclei in direct detection experiments; or Cherenkov radiation in either the atmosphere, produced by atoms ripped apart by gamma-rays from dark matter annihilating with itself, or in the Antarctic ice by muons created by neutrinos escaping the self-annihilation of dark matter trapped within the Sun. Though much sought after, this light has yet to be seen, and the dark matter remains, for the time being, hidden.

The puzzle of dark matter has been with us for most of the last century. Measurements of the internal motions of galaxy clusters, and the rotations of galaxies outside the Milky Way established the need for additional, unseen mass in those objects, though did not prove that this mass had to be some new type of material. A body of evidence soon grew showing that the particles known to us in the Standard Model could not satisfy the constraints that arose from astronomical observations - for instance numerical simulations showed that neutrinos would dissolve the large scale web of structure we saw throughout the Universe if they were the dark matter particles.

Finally, the most compelling evidence that dark matter was something new came from the cosmic microwave background (CMB). This was emitted when the Universe transitioned from an opaque plasma of photons, electrons, protons, and neutrons, to transparent gas of hydrogen, helium, and a hint of lithium, through which the photons could stream unimpeded. At the point of this transition the plasma was oscillating,

falling into the gravitational wells of dark matter clumps, then being pushed back out by its own pressure. When the transition occurred the peaks and troughs of the oscillations were imprinted onto the temperature distribution of the photons. Billions of years later we see these exact same photons as the CMB, with the peaks and troughs turned into hot and cold patches on the sky. By analysing the patterns of these patches we can extract the oscillations of the plasma, and the harmonies that we find tell us that only 15% of the matter in the Universe is made out of the SM particles known to us, such as protons, neutrons, electrons, photons and neutrinos. The remaining 85% is dark matter, made of as-yet-unknown particles. The Milky Way is embedded in a roughly spherical halo of these particles, which pass through the Sun and the Earth almost entirely unimpeded.

At the same time as new particles were being called for by cosmological observations, particle physicists were formulating them as part of extensions to the Standard Model of particle physics. Many of these extensions solve problems within the Standard Model and also produce hypothetical particles which are candidates for dark matter. A menagerie of axions and axion-like particles have been spawned out of a solution to the lack of CP-violation observed in strong interactions. Sterile neutrinos can explain the small but non-zero masses of the normal active neutrinos observed via neutrino oscillations. Supersymmetry can solve the so-called hierarchy problem and can also assist in unifying the strong, weak, and electromagnetic forces at high energies. Supersymmetry posits the existence of a new set of particles, the lightest of which can be a dark matter candidate. In most supersymmetric scenarios this is the neutralino, the preeminent member of the class of particles known as Weakly Interacting Massive Particles, or WIMPs. Axions, sterile neutrinos, and WIMPS are all being searched for with experiments around the world and satellites in orbit, but WIMPs remain the dominant candidate particle, and we focus on these particles in Chapters 2 and 3. Chapter 4, which is focused on the determination of the dark matter density in the vicinity of the Sun using the motions of stars, is agnostic as to the particular particle physics model.

The hunt for dark matter particles can be divided into three main classes: direct detection, indirect detection, and collider searches. In the latter we endeavour to create the dark matter particles ourselves, and while this does not directly probe the dark matter in the galaxy and cosmos, it can potentially give us precise information on the particle and the theories that underpin it. Indirect detection looks for the Standard Model particles produced by dark matter particles annihilating with one another in astrophysical structures, for instance gamma-rays or neutrinos from the galactic centre. Additionally, dark matter could scatter off nuclei in the Sun or other bodies, and be captured by their gravitational field, interacting again and again until they are captured in the core of the body. There they would annihilate, and any resulting neutrinos could escape and be detected by neutrino detectors such as IceCube, loca-

ted at the South Pole. The same scatterings between dark matter and nuclei that can lead to capture in the Sun also drive the final class of experiments, direct detection, which searches for the minute amounts of energy deposited within a detector volume when a dark matter particle scatters off an atomic nuclei. The most sensitive of these direct detection experiments is XENON1T, which is soon to begin operations deep underground in the Gran Sasso laboratory in Italy.

But even if WIMP dark matter particles are detected, reconstructing their properties will be a difficult task. The signals we detect are dependent on many properties not just of the particle but also their distribution throughout the galaxy. This leads to many degeneracies - for instance a given level of signal could be produced by a larger number of particles with weaker interactions, or a smaller number of particles with stronger interactions. However, different experiments will have different relative sensitivities to each of these properties, and by combining the results of these experiments together it is possible to break these degeneracies. In Chapter 2 we studied the outcome of a hypothetical WIMP dark matter detection in both XENON1T and IceCube. Separate analyses resulted in degeneracies between the WIMP mass, and the spin-dependent and spin-independent WIMP-nucleon interaction strengths. We demonstrated however that a combined analysis can break these degeneracies, exploiting the different relative sensitivities of each experiment and illustrating their complementarity.

The detection of gamma-rays from WIMP dark matter annihilating in the Milky Way is another promising avenue for indirect detection. In Chapter 3 we investigated the prospects of detecting dark matter via this method using the upcoming Cherenkov Telescope Array (CTA). Gamma-rays striking the upper atmosphere rip apart atoms and initiate cascades of high-energy particles which emit Cherenkov radiation. CTA and other experiments like it work by detecting this radiation with an array of telescopes on the ground, and then reconstructing the direction and energy of the original gamma-ray. The most promising target for CTA is the centre of the Milky Way, and several works estimate the sensitivity of CTA to dark matter annihilating there. However prior to our work none had taken into account systematic uncertainties in the performance of the detector, nor the diffuse gamma-ray background produced through normal astrophysical processes which would mask any signal from dark matter. We found that including these effects significantly degraded the performance of CTA when using standard analysis techniques. To remedy the impact of the diffuse gamma-ray background we proposed a new analysis method, which exploited the difference in shape between the background, which would be concentrated around the disc, and the dark matter signal, which would be close to spherically symmetric. While not a total panacea, this method improved the limits on the self-annihilation cross section by up to an order of magnitude.

Crucial to all three of these detection methods is the distribution of dark matter in the Galaxy. Detection of gamma-rays with CTA is dependent on the dark matter density between us and the galactic centre. Direct detection and indirect detection via solar capture and annihilation are driven by the density of dark matter within a small region around the Sun. In Chapter 4 we delved into the determination of this quantity, known as the local dark matter density. It is important to measure this quantity with as few assumptions as possible, as it is used in the analysis of direct and indirect detection data, which in turn are used to explore dark matter theories such as supersymmetry. Assumptions in the determination of the local dark matter density will flow through experimental physics to theoretical physics, potentially causing biases and incorrect conclusions.

To further this goal, we developed and presented a new method which has the potential to greatly reduce the number of assumptions made when determining the local dark matter density. The motions of stars moving in the galaxy are modelled as a collisionless fluid, flowing through the gravitational potential of the Milky Way, feeling the pull of both normal baryonic matter and dark matter. Their density and flow is described by the collisonless Boltzmann equation and the Jeans equations, on which we built our method. The data used for this and previous studies consists of the positions and velocities of a set of tracer stars up and down out of the disc plane. We constructed a model of the mass distribution near the Sun, including both normal matter and dark matter, and, using an integrated form of the Jeans equations, fitted this model to the vertical density and velocity dispersion of the tracer star population. In the work presented in this thesis we developed the method and tested it on idealised mock data, honing and improving it before its future application to real data.

Our tests illustrated the crucial importance of the so-called *tilt term*, which links the vertical motions of stars up and down in the baryonic disc plane of the Milky Way with their radial motions towards or away from the galactic centre. While our method is based on the vertical motions of stars, it is able to account for these radial motions through a correction term. We have demonstrated here that ignoring the tilt term leads to a systematic underestimation of the local dark matter density. Moreover, this term becomes more important at greater heights above the disc plane, which is where we must reach if we want to avoid the effects of the baryonic disc and gain a clear picture of the distribution of dark matter around us. We also explored the detection of dark discs, an extra dark matter component which can be formed, for instance, by clumps of dark matter being torn apart by and then accreting onto the baryonic disc. While we can constrain the total dark matter profile, consisting of the spherical halo and dark disc, we cannot yet distinguish the two, which is important given they each generate different signals in direct and indirect detection experiments.

The future of dark matter research is promising. XENON1T will soon be in operation, looking for the recoils of nuclei struck by dark matter particles, and even larger detectors will follow. IceCube continues to hunt for neutrino signals from dark matter annihilations alongside its Mediterranean counterpart ANTARES, and both will be joined by KM3NeT within the decade. CTA is expected to start operations in 2019, searching for gamma-rays from dark matter annihilating throughout the Milky Way. Knowledge of the distribution of dark matter in the Milky Way, which underpins all of these detection methods, will also undergo rapid advancement with the advent of high precision astrometric data from the Gaia satellite. But the pursuit of dark matter will require more than just the progress of individual experiments. The work presented in this thesis extends across direct detection, indirect detection, galactic dynamics and astrometrics, and throughout we have highlighted the rich interplay between these areas. Dark matter is a daunting problem that spans particle physics, astronomy, and cosmology, and only through a united effort will we scale the heights to attain a commanding view of our Galaxy and our Universe.

Acknowledgements

Firstly, I owe tremendous thanks and gratitude to my supervisor, Gianfranco Bertone. Over the past four years I've learnt an enormous amount from Gianfranco not only about dark matter, but also about how to be an academic. For your time, guidance, wisdom and support through three research projects, numerous conferences, and this thesis, grazie di cuore.

Thank you also to my promoter, Jan de Boer, for advice and counsel, especially during the process of thesis writing and submission, and my committee, for reading this thesis and for their forbearance while I negotiated the Byzantine process of organizing a defence date.

Backing up a little bit, the start of this PhD goes back to November 2011, at the University of Canterbury in New Zealand. Pat Scott, with whom I was working with for my master's research project, was visiting, and I asked him if he knew of any PhD positions in Europe or North America. Yes, he said, Gianfranco Bertone has just started at this new place called GRAPPA in Amsterdam, he has an ERC grant, and might be looking for PhD students, so you should send him an email. So I sent Gianfranco an email asking about PhD positions, and here I am, four and a bit years later. Pat, thanks for not only setting me on the path to Amsterdam, but also your continued support while I've been here.

I arrived in Amsterdam on the same day as Chiara Arina and Christoph Weniger, two new GRAPPA post-docs, both of whom I'd go on to write papers with. I'd like to thank them both for the knowledge they passed on to me, and their patience as I learned the tools of the trade they had long ago mastered.

The local dark matter density project that features in Chapter 4 has been ongoing since early in my PhD. My collaborator throughout this work has been Sofia Sivertsson, who I first met in Stockholm in 2011. I was visiting there to work with Pat on

my masters project, and for Midsummer I headed out to the archipelago with a group of locals, including Pat and Sofia. Embarrassingly when she first arrived in Amsterdam I completely forgot that we'd met, and re-introduced myself. Sofia, however, did remember... It's been great to work with you Sofia and I wish you all the best for your future endeavours. Specific thanks are in order for the baryon model featured in Fig. 4.2, and the bias correction discussed in Sec. 4.8.1 and reproduced in Appendix B.

Since starting my masters thesis project at Canterbury I have been transitioning slowly from theoretical physics to astrophysics, and now towards astronomy. As I entered the realm of astrometrics and galactic dynamics I've been lucky enough to have Justin Read as teacher, guide and collaborator. Thank you Justin for all your help over the past few years, and I look forward to continue working with you in the future.

Many thanks to Sebastian Liem and Michael Feyereisen, my paranymphs and statistical fairy godparents. I've learned a huge amount from both of you, and I am deeply indebted. As no doubt many of you readers out there have skipped most of the thesis and come right to the acknowledgements, I'll put the advertisement for Sebastian's brilliant software here: Are you working with MultiNest chains, but sick of wasting time with Matlab based codes? Try Barrett, the 100% Python code for analysing and plotting MultiNest posteriors [479].

Thanks and recognition are also owed to Richard Bartels for translation of my English Summary to the Dutch Samenvatting and Niki Klop for editing work on it, Francesca Calore for the DM profiles from the EAGLE HR and APOSTLE IR simulations shown in Fig. 1.6 and for discussions on gamma-rays while cooking in the flat, Nassim Bozorgnia for discussions on direct detection and the dark disc, Daniele Gaggero for advice on cosmic rays in dwarf spheroidals, Christopher McCabe for help with SUSY and the hierarchy problem, Tom Edwards for proofreading, and Ioanna Papavergou for checking through my derivations of the Jeans Equations. For the innumerable chats, seminars, and discussions that make GRAPPA and AmsterDark such an outstanding and energetic environment in which to work, in addition to the aforementioned I'd like to thank further members, past and present: Shin'ichiro Ando, Arnim Balzer, David Berge, Mark Bryan, Maria Cabrera Catalan, Patrick Decowski, Ben Freivogel, Mattia Fornasa, Jennifer Gaskins, Suraj Krishnamurthy, Mark Lovell, Sera Markoff, David Salek, Djoeke Schoonenberg, Doug Spolyar, Emma Storm, Irene Tambora, Chris Tunnel, Jaco Vink, Michael Wiechers, Fabio Zandanel, and my flatmate, officemate, and now Spanish teacher, Roberta Diamanti. And I guess also that rapscallion Fotis Dimitrakopoulos, even though he did play for the string theory football team.

To my doctoral predecessors and former officemates Daniel Mayerson, Ben Mosk, and Natascia Pinzani Fokeeva - thank you for the support and advice as I navigated the maze of thesis writing, and special thanks to Natascia, upon whose LaTeX code template this thesis was written.

Thanks to Pascal Steger, from whose code Sofia and I developed our analysis tools, and who introduced me to the wonder of `pdb.set_trace`.

Throughout this PhD I've visited several institutions around the world, and I'd like to thank Scott Tremaine at the IAS in Princeton, Tracy Slatyer at MIT in Boston, the Mainz Institute for Theoretical Physics, and again Pascal and Justin at ETH Zürich and University of Surrey, for their hospitality.

Humble thanks and homage to the fonts of knowledge and wielders of power in the Institute of Physics and Anton Pannekoek Institute administration; Anne-Marieke Crommentuijn (HRH), Natalie Wells (HRH), Joost van Mameren, Rita Vinig, Fatima Ouazza, Kim Rijsdijk, Susan Franzen, and Milena Hoekstra. From my first arrival all the way through thesis writing their help has been invaluable. Thank you also to my colleagues on the IoP PhD-Postdoc Council, with whom I've poured beers, drank beers, and organized beer consumption (with some science on the side): Rogier Vlijm, Rens Limpens, Nick de Jong, Julie Desarnaud, Daniel Miedema, Maureen Dinkgreve, Laurens Kabir, Niki Klop, Georgios Skantzaris, and Antonio Capretti.

GRAPPA sits between the Institute of Physics, the Anton Pannekoek Institute for Astronomy, and NIKHEF, and from First Thursday beers to Whisky Break and Sinterklaas to Brouwerij 't IJ, I've always felt welcome. From string theory to soft matter to supernova shockwaves, XENON to x-ray astronomy, cold atoms to CTA to condensed matter theory and experiment, AdS/CFT and accreting and merging black holes; thank you all.

Finally, a thank you to all my family and whānau back home in New Zealand from whence I started this journey, and especially my big sister, Monica. Far away, but always present. Thanks.